Oceanologia

Official Journal of the Polish Academy of Sciences: Institute of Oceanology and Committee on Maritime Research

This journal is supported by the Ministry of Science and Higher Education, Warsaw, Poland

Indexed in: ISI Journal Master List, Science Citation Index Expanded, Scopus, Current Contents, Zoological Record, Thomson Scientific SSCI, Aquatic Sciences and Fisheries Abstracts, DOAJ

IMPACT FACTOR ANNOUNCED FOR 2016 IN THE 'JOURNAL CITATION REPORTS' IS 1.500; 5-year IF is 1.341

Publisher
Elsevier Sp. z o.o.
22, Jana Pawła II Avenue
00-133 Warsaw, Poland

Associate Publisher
Justyna Kasprzycka
j.kasprzycka@elsevier.com
+31 20 485 3846

ISSN 0078-3234

Oceanologia (2018) 60, 1—15

Available online at www.sciencedirect.com

ScienceDirect

journal homepage: www.journals.elsevier.com/oceanologia/

ORIGINAL RESEARCH ARTICLE

Total suspended particulate matter in the Porsanger fjord (Norway) in the summers of 2014 and 2015

Jagoda Białogrodzka [a,b,*], Małgorzata Stramska [a,b], Dariusz Ficek [c], Marzena Wereszka [a]

[a] *Department of Earth Sciences, Szczecin University, Szczecin, Poland*
[b] *Institute of Oceanology, Polish Academy of Sciences, Sopot, Poland*
[c] *Department of Environmental Physics, Pomeranian University in Słupsk, Słupsk, Poland*

Received 29 December 2016; accepted 19 June 2017
Available online 6 July 2017

KEYWORDS
Arctic;
Porsanger fjord;
Suspended matter;
Optical measurements

Summary High-latitude fjords, very vulnerable to global change, are impacted by their land and ocean boundaries, and they may be influenced by terrestrial water discharges and oceanic water inputs into them. This may be reflected by temporal and spatial patterns in concentrations of biogeochemically important constituents. This paper analyses information relating to the total suspended matter (TSM) concentration in the Porsanger fjord (Porsangerfjorden), which is situated in the coastal waters of the Barents Sea. Water samples and a set of physical data (water temperature, salinity, inherent optical properties) were obtained during two field expeditions in the spring and summer of 2014 and 2015. Bio-optical relationships were derived from these measurements, enabling optical data to be interpreted in terms of TSM concentrations. The results revealed significant temporal variability of TSM concentration, which was strongly influenced by precipitation, terrestrial water discharge and tidal phase. Spatial distribution of TSM concentration was related to the bathymetry of the fjord, dividing this basin into three subregions. TSM concentrations ranged from 0.72 to 0.132 g m^{-3} at the surface (0—2 m) and from 0.5 to 0.67 g m^{-3} at 40 m depth. The average mineral fraction was estimated to be 44% at surface and 53% at 40 m.

* Corresponding author at: Department of Earth Sciences, Szczecin University, Mickiewicza 16, Szczecin 70-383, Poland. Tel.: +48 58 73 11 600; fax: +48 58 55 12 130.
E-mail addresses: jbialogrodzka@iopan.gda.pl, jagoda.bialogrodzka@gmail.com (J. Białogrodzka).
Peer review under the responsibility of Institute of Oceanology of the Polish Academy of Sciences.

Production and hosting by Elsevier

http://dx.doi.org/10.1016/j.oceano.2017.06.002

1. Introduction

Important oceanic processes, such as the export of carbon and other biogeochemically important material are closely associated with the spatial and temporal variability of suspended particulate matter. The quantity and quality of suspended matter in the water column govern light transfer in surface waters and its availability to primary production, strongly influencing the euphotic depth (Kirk, 2011; Mobley, 1994). In extreme situations, the within-day variability of total suspended matter (TSM) in coastal waters may encompass several orders of magnitude due to the combined effects of physical (*e.g.*, terrestrial water runoff, tidal mixing, aerial deposition of dust) and biological processes (*e.g.*, biological production, aggregation, Montes-Hugo et al., 2012). The high-latitude fjords are among the regions where TSM dynamics is still poorly understood. This is because of the relatively large number of fjords, in which conditions can differ significantly. Traditional shipboard surveys have been sporadic and so far supplied very limited biogeochemical data sets in only a few fjords. In addition, because regional coastal algorithms are non-existent, a quantitative interpretation of the ocean colour data provided by satellite sensors in such locations is not possible.

In general, delivery of suspended matter to Arctic fjords involves four major processes (Syvitski, 1989; Winters and Syvitski, 1992): (1) ice-contact processes associated with tidewater glaciers, (2) rafting by icebergs and sea ice, (3) fluvial discharge of sediment and (4) exchanges of water masses, for example, as a result of oceanic inflows. To extend knowledge of TSM concentrations in high-latitude fjords, *in situ* experiments were carried out in the Porsanger fjord (Porsangerfjorden), one of the largest fjords in northern Norway (Fig. 1). There are no glaciers around the Porsanger fjord, so one would expect TSM concentrations in this fjord to be lower than, for example, in some Greenland and Spitsbergen fjords, where glaciers are present. Nevertheless, it is important to collect information in all types of fjords in order to understand more about how TSM concentrations (both organic and mineral fractions) vary across different time and spatial scales in the Arctic and to enable future extrapolation of this knowledge to large-scale and global estimates.

This paper describes the preliminary results of experiments carried out in the Porsanger fjord. The primary objective was to develop and validate local bio-optical relationships for estimating TSM concentrations from *in situ* optical data and to describe the spatial and temporal variability of TSM concentrations in the Porsanger fjord based on water samples and optical surveys. Traditionally, laboratory biogeochemical analyses of discrete water samples collected at sea have been used to determine the concentrations of suspended material in seawater. However, such analyses are time-consuming and difficult to apply on a large scale. More recently, optical instruments have become popular tools for ocean monitoring (Zaneveld et al., 1994). Unlike classic laboratory analyses of discrete water samples, *in situ* optical measurements provide information about the marine environment at larger spatial and temporal scales. This was the approach taken in the present research.

2. Study region

There are a great many fjords along the Norwegian coast with large variations in topography and dynamics. This paper focuses on the Porsanger fjord, which is located in the in the vicinity of the Barents Sea (Fig. 1) (*ca* 70.0–71.0°N, 25.0–26.5°E). Approximately 100 km long and 15–23 km wide, it has a maximum depth of more than 230 m and extends south-westwards from the northern tip of Norway (North Cape – Nordkapp). It is surrounded by mountains (Fig. 2) that rise to altitudes of more than one thousand metres (Mt. Cahkarassa, 1139 m) on the south-western side

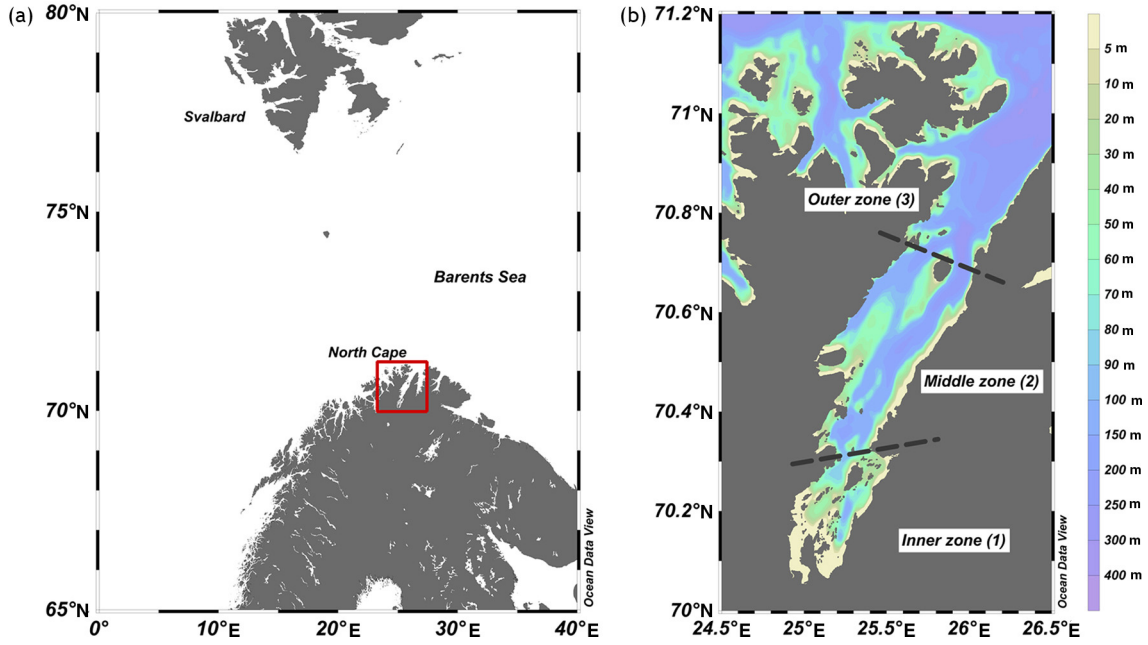

Figure 1 Geographical location of the Porsanger fjord (left panel, red rectangle); fjord bathymetry showing the three subregions investigated (right panel).

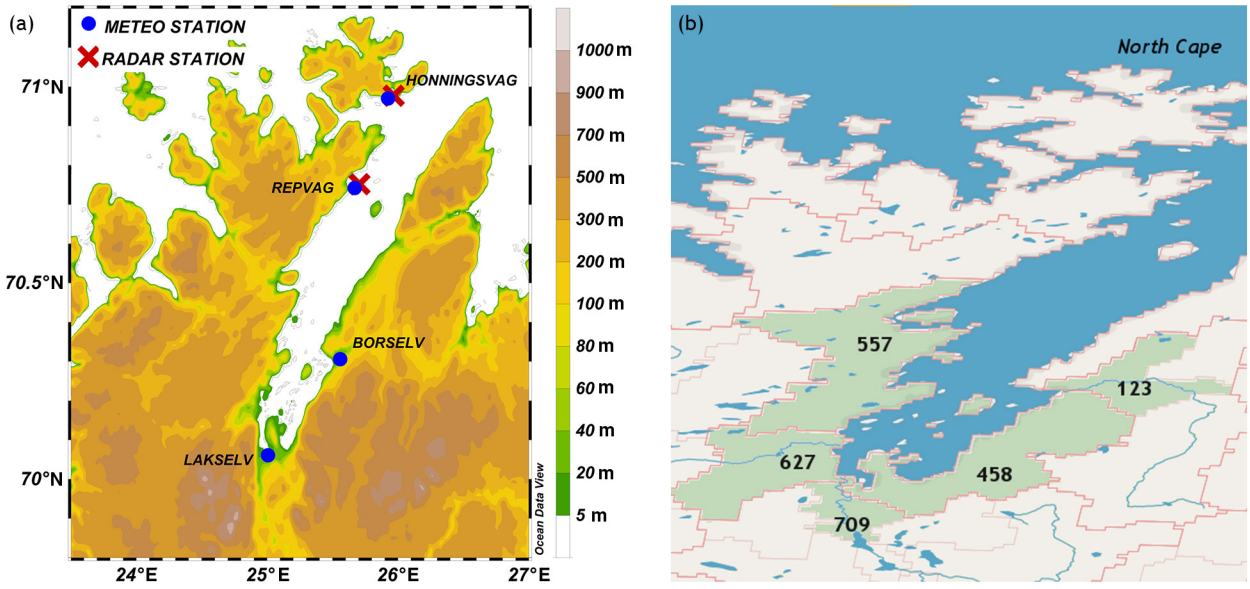

Figure 2 (a) Topography of the land surrounding the Porsanger fjord showing the location of the meteorological and radar stations; (b) E-Hype sub-basins used for water discharge estimates (based on map provided by SMHI HypeWeb).

of the fjord. The land around the fjord, part of the Finnmarksvidda plateau, is mostly about 400 m above sea level.

The land cover varies. Moreover, the region is sparsely populated: only two communities — Honningsvåg and Lakselv — have more than 2000 inhabitants. Farming areas are rather small and are situated mostly around the inner part of the fjord. On the south-eastern, north-western, and north-eastern sides of the fjord there are mostly rocks and tundra vegetation. There is woodland on either side of the middle part of the fjord, but tree growth is stunted as a result of low temperatures and short growing seasons. There are peat bogs all around the fjord.

According to Cushman-Roisin et al. (1994), the width of the Porsanger fjord is approximately three times the deformation radius, so it can be classified as a broad fjord. These same authors reported that the combination of vertical stratification and fjord width can lead, under typical wind stresses, to the development of upwelling on one side of the fjord and downwelling on the other. In line with the classification proposed by Svendsen (1995), Porsanger can be described as a fjord with relatively little water runoff in comparison to other Norwegian fjords, except for the spring and summer seasons, when freshwater runoff significantly influences its hydrography.

With regard to its bathymetry, the Porsanger fjord can be divided into three zones (Fig. 1): an inner zone (subregion 1, extending 0—30 km from the head), a middle zone (subregion 2, located 30—70 km from the head) and an outer zone (subregion 3, 70—100 km from the head). The inner zone is separated from the remainder of the fjord by a 60 m deep sill, situated approximately 30 km from the fjord head: this significantly inhibits water exchange between the inner and outer parts of the fjord. The inner zone environment is very different from the rest of the fjord and supports a unique Arctic ecosystem (Eilertsen and Frantzen, 2007). Beyond the internal sill is the middle part of the fjord: this is separated from the outer zone by the island of Tamsøya, which lies about 70 km from the head of the fjord. Finally, the outer zone ends in a deep sill (180 m); this does not constrain the movements of waters between the fjord and the coastal region of the Barents Sea. Historical observations show evidence of two prevailing wind directions—southerly and northerly—along the fjord's axis. The Porsanger fjord is stratified from May to October as a result of seasonal river runoff and surface warming (Svendsen, 1995). The sea level variability due to tides is significant (about 3 m). The most important tidal component in the surface currents is the semidiurnal one (M2), but winds also have a strong impact on surface currents (Stramska et al., 2016).

3. Methods

Data were collected from June 06 to 29, 2014 and from May 29 to June 18, 2015 during two field expeditions in the Porsanger fjord. Fig. 3a and b shows the sampling stations in 2014 and 2015. At some stations, discrete water samples were collected for TSM determinations, usually near the surface, but also from one or two depths (most often 5 m and 40 or 50 m). The number of water levels sampled at each station depended on the weather conditions, as only a small boat was available for the fieldwork. When the sea was too rough, it was only possible to collect water samples from the surface. In addition to water samples, vertical profiles of inherent optical properties (IOPs) were measured with ac-9 and/or ac-s instruments (WETLabs). More stations were done with the ac-9 in 2014 — this was before a new ac-s instrument was purchased. At some stations data were collected with both instruments, so the different data sets could be compared. The depth range for the profiles was usually 0—50 m, since it was difficult to deploy the instrument packages from that small boat. However, the mixed layer depth varied between 10 and 30 m, so it was usually possible to collect water samples representing both the surface and the deeper water masses. More stations were covered in 2015 than in 2014 (Fig. 3), following some modifications made to the boat to facilitate the deployment of equipment.

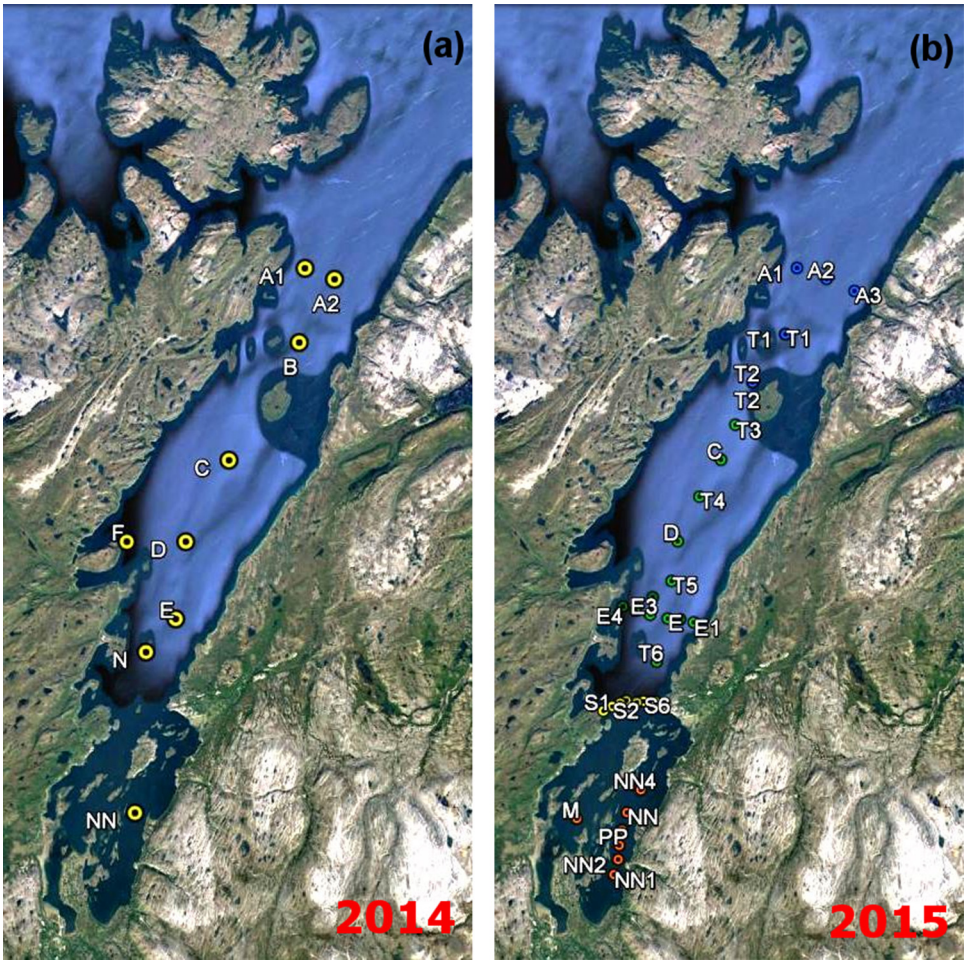

Figure 3 Hydrographic stations visited in (a) 2014 and (b) 2015 (prepared with Google Earth software; Image Landsat, Image IBCAO).

After collection, the water samples were brought to the coastal station laboratory for analysis. The TSM concentration (in g m^{-3}), defined as the dry mass of particles per unit volume of water, was determined using a standard gravimetric technique (Stavn et al., 2009; Woźniak et al., 2011). The water samples were passed through specially prepared GF/F filters (25 mm in diameter). Before filtration, these filters were precombusted for 4 h at 450°C, pre-washed with pure deionized and particle-free water (to prevent the loss of filter material during the filtration of the main sample), dried and pre-weighed. Volumes of seawater samples varied between 250 and 2500 ml, depending on the water turbidity. The samples were filtered as soon as possible after collection. When filtration was completed, the filters were rinsed with about 60 ml purified deionized water to remove sea salt. Next, the filters with their particle load were dried. The dry mass of particles collected on the filters was measured with a Radwag XA 82/220.R2 microbalance (resolution 0.01 mg). Three replicate filters were weighed for each water sample, the reproducibility generally being within ±8%. Thereafter, the filters were combusted for 4 h at 450°C to remove the organic particle fraction (loss on ignition (LOI) technique; Pearlman et al., 1995) and reweighed. The concentration of particulate organic matter (TSM_{org}) was calculated (in g m^{-3}) from the difference in weight before and after combustion. The ac-9 and ac-s data were processed according to procedures described in Pegau et al. (1997). After applying the corrections for water temperature and salinity, the data were carefully inspected for large spikes, most likely present because of the air bubbles in surface waters. For the final data set, data from the upper sections of the profiles were used, which were averaged into 1 m bins in order to average the instrumental noise. Finally, the values from the water sample analysis were matched with simultaneous determinations of beam attenuation coefficient (c_p at 650 nm and 648.8 nm for the ac-9 and ac-s instruments, respectively). These data yielded statistical relationships between the optical and water sample data (Fig. 4). There was a small but systematic difference between the values of $c_p(650)$ recorded by the ac-9 instrument and those of $c_p(648.8)$ recorded by the ac-s. For consistency, therefore, the ac-9 data were converted to the ac-s measurements in accordance with the relationship shown in Fig. 4a. This was done because (1) more data were collected with the ac-s, and (2) the ac-s was new and was calibrated immediately prior to the experiments. Although the correction was relatively small, the vertical profiles measured at the same station with the ac-9 and ac-s were almost identical after it had been applied. In the second step, the relationship based on the comparison between c_p and TSM determined from the water samples shown in Fig. 4b was applied to all the vertical optical profiles of c_p collected *in situ* (converted ac-9 and ac-s data). This

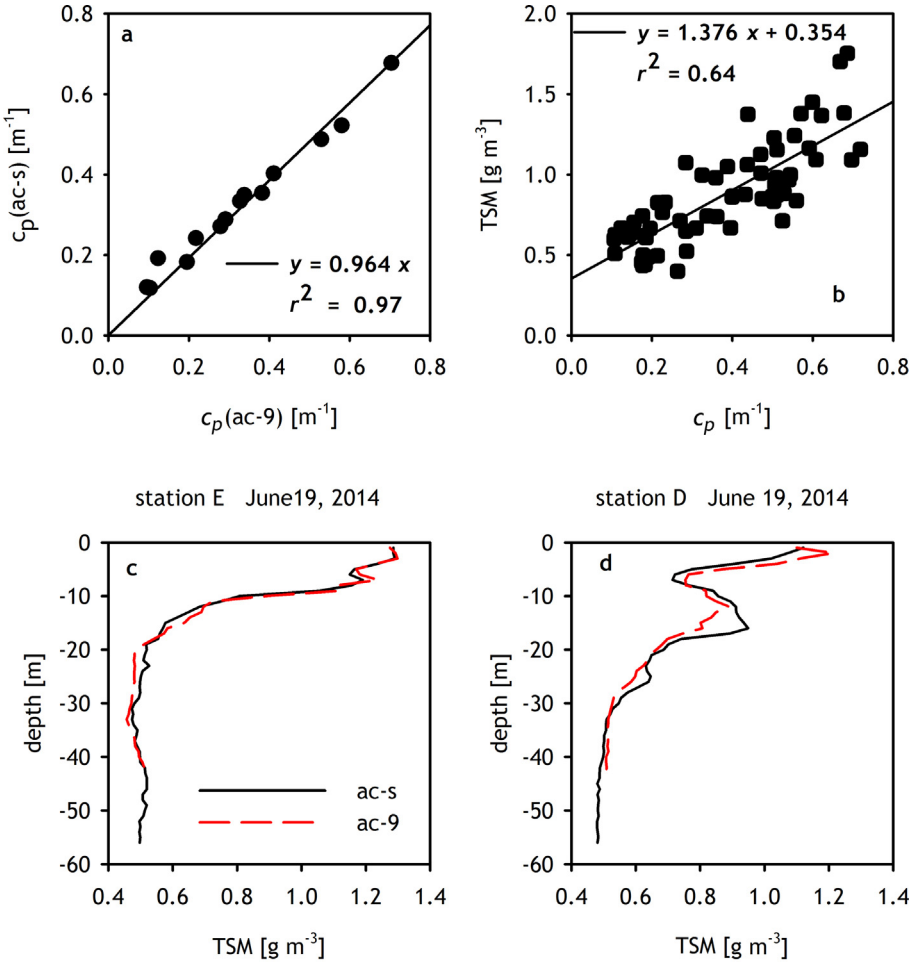

Figure 4 (a) Regression used to convert ac-9 c_p(650) data to c_p(648.8) ac-s values; (b) regression between in water c_p measurements and TSM concentrations determined on water samples; (c) and (d) comparison of example TSM vertical concentration profiles determined from ac-9 and ac-s measurements.

yielded information about the vertical distribution of TSM concentrations. Vertical profiles of TSM derived from ac-9 and ac-s measurements at the same station are exemplified in Fig. 4c and d. The experimental data also contain two samples of water taken from the Rivers Børselva and Lakselva in 2015.

Vertical profiles of water temperature (T) and salinity (S) were collected during the experiment with an SBE 49 FastCAT (Seabird Electronics) CTD Sensor interfaced with the ac-s.

In addition to the boat surveys, surface currents were monitored using the high-frequency (HF) radar system operating in the Porsanger fjord (the radar site's location is shown in Fig. 2a) from June 10 (year day 161) to October 11 (year day 284) in 2014 and from May 28 (year day 148) to August 17 (year day 229) in 2015. More details on the data sets collected are available in a separate paper (Stramska et al., 2016).

In our paper we have also used additional data sets. Wind data from Honningsvåg and Lakselv with hourly resolution, and precipitation data from Honningsvåg, Børselv and Repvåg with daily resolution, were obtained from the Norwegian Meteorological Institute (http://www.yr.no). Fig. 2a shows the geographical positions of Honningsvåg, Lakselv, Børselv and Repvåg. Daily data of water discharge to the fjord based on the E-Hype numerical model (http://hypeweb.smhi.se/europehype/time-series/) from the model subregions indicated in Fig. 2b are also used. That model was extensively validated with observational data (Donnelly et al., 2011, 2015). Water runoff is given as daily averaged water discharge (in $m^3\ s^{-1}$).

4. Results

4.1. Weather conditions

The weather data are summarized in Figs. 5 and 6. Figs. 5a and 6a show time series of wind speed data from the Honningsvåg and Lakselv weather stations in 2014 and 2015 respectively, while Figs. 5b and 6b display the precipitation data from Honningsvåg, Børselv and Repvåg. The bio-optical experiments lasted only few weeks (June 6—29 in 2014 and May 29—June 18 in 2015) but the meteorological data presented in Figs. 5 and 6 start on year day 140 (mid-May) in order to provide background information from the time before the experiments commenced. For example, Fig. 6 shows that around May 24—25, 2015, several days before the experiment started, there was a strong wind

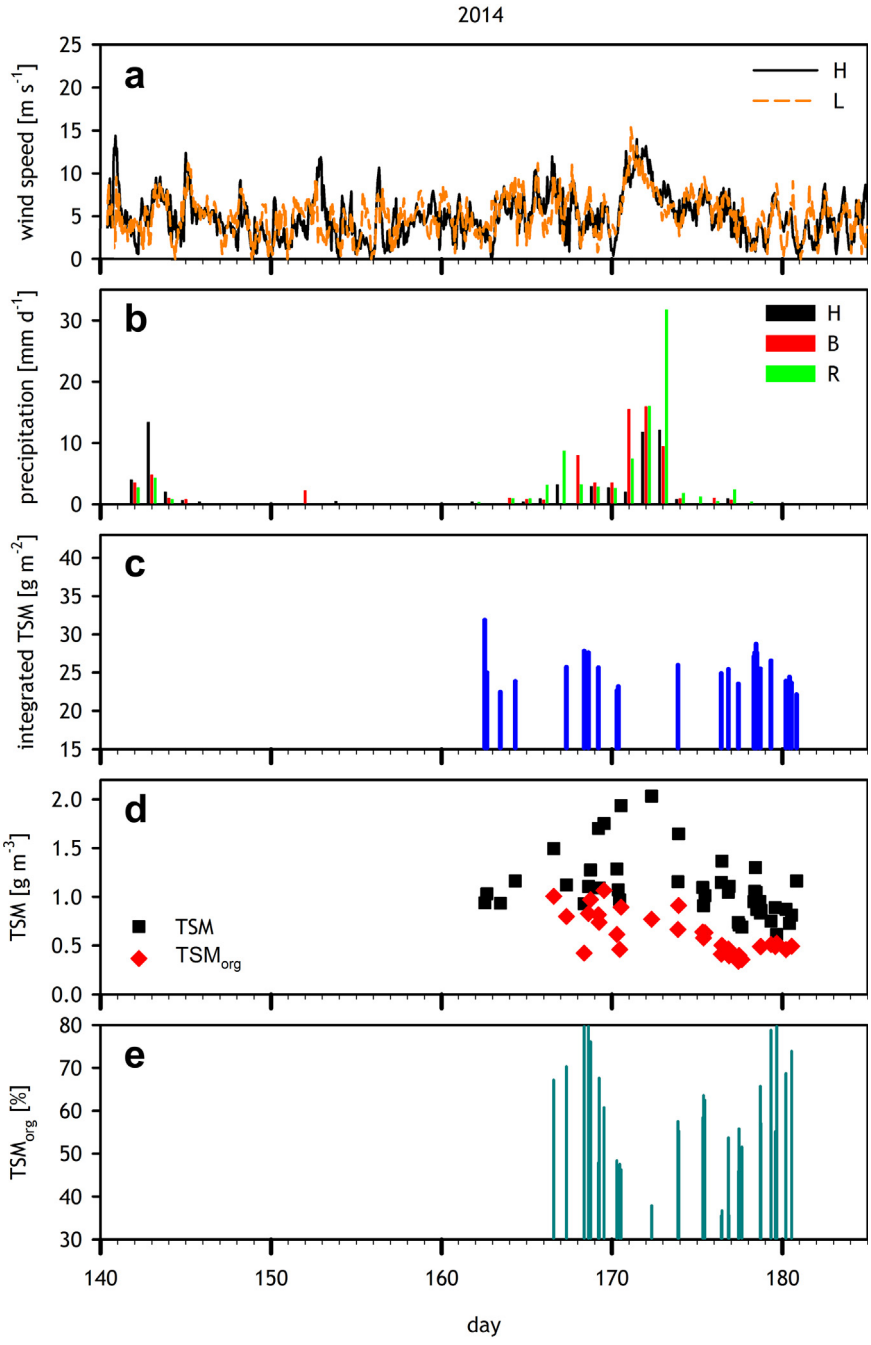

Figure 5 Summary of TSM data collected in 2014. (a) Wind speed recorded at Honningsvåg (H) and Lakselv (L); (b) precipitation at Honningsvåg (H), Børselv (B) and Repvåg (R); (c) TSM integrated over the 0–30 m water layer; (d) concentrations of total TSM and the organic fraction TSM_{org} in surface waters; (e) organic fraction of TSM (in %) in surface waters.

event accompanied by significant precipitation. In May 2014, by contrast, there was much less precipitation and winds were weaker than in May 2015. The lower panels in Figs. 5 and 6 present the results from boat experiments – TSM data from all the stations combined and plotted as a function of time. The water-column-integrated TSM in the top 30 m of the surface water is shown in panels (c), TSM and TSM_{org} concentrations measured in surface waters (0–2 m) are displayed in panels (d), and the percentage of the organic fraction present in surface water TSM is plotted in panels (e). The data shown in panels (c) are based on TSM profiles derived from optical data, the data in panels (d) are a combination of water samples and optical data, while the data in panels (e) refer only to water sample determinations. From Figs. 5 and 6 it becomes clear that the highest TSM values (water-column-integrated and surface concentrations) corresponded to significant precipitation events. These events happened around June 22 (year day 173) in 2014 and around May 25 (day 145) in 2015. Precipitation presumably led to increased water runoff from the coast into the fjord, thereby supplying large amounts of suspended particles to its waters.

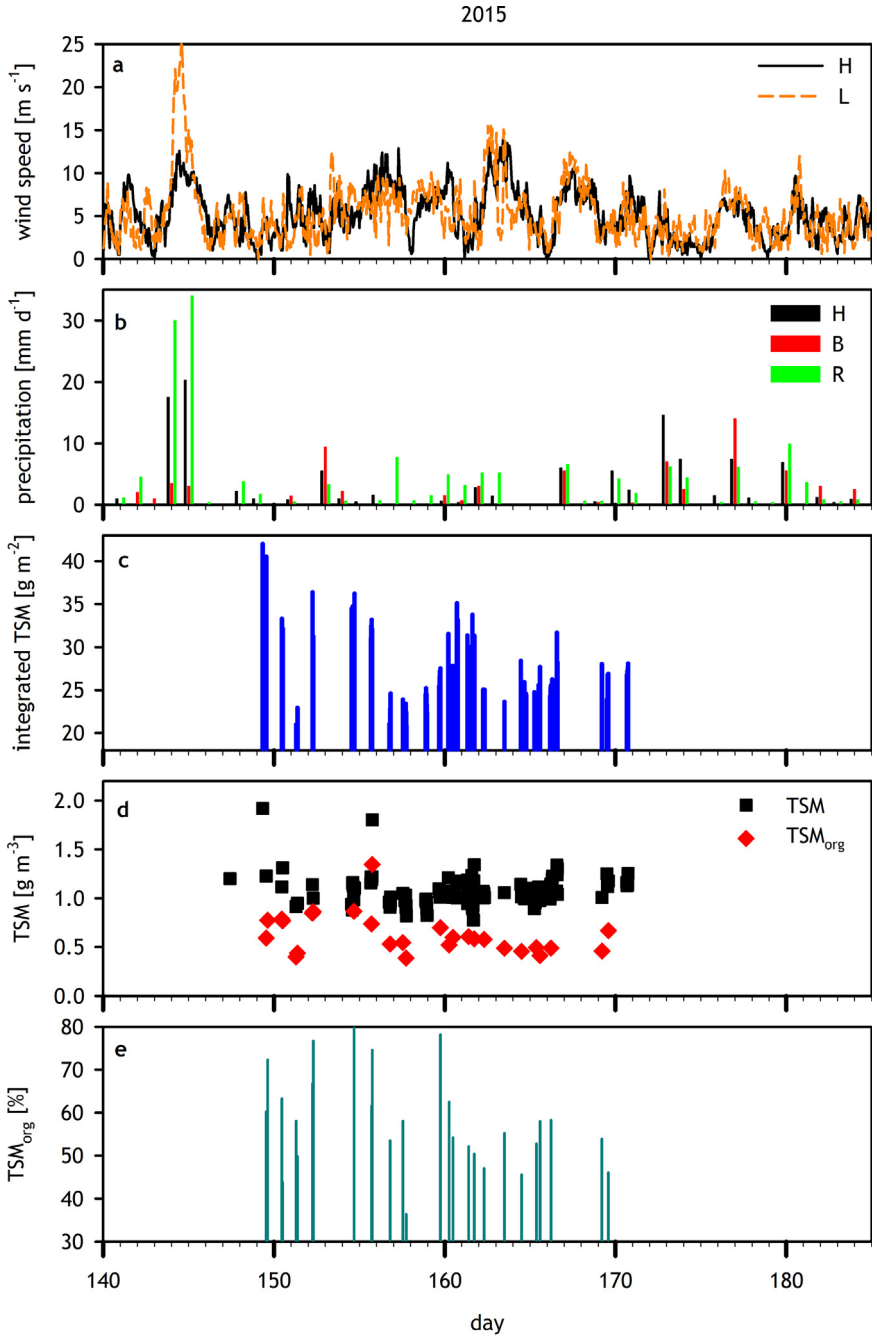

Figure 6 Summary of TSM data collected in 2015. (a) Wind speed recorded at Honningsvåg (H) and Lakselv (L); (b) precipitation at Honningsvåg (H), Børselv (B) and Repvåg (R); (c) TSM integrated over the 0—30 m water layer; (d) concentrations of total TSM and the organic fraction TSM_{org} concentration in surface waters; (e) organic fraction of TSM (in %) in surface waters.

4.2. Terrestrial water discharge

The 2014 and 2015 time series of water discharge in the five subregions of the E-HYPE model for which all runoff is supplied to the Porsanger fjord are shown in Fig. 7 (the locations of the subregions are shown in Fig. 2b). The results from the HYPE model indicate that the average water runoff in this region reaches its annual maximum in June. According to these data, the runoff in subregion 709, where the mouth of the River Lakselva is situated, makes the most important contribution to the total runoff (Fig. 7). Moreover, the temporal distribution of the total discharge was quite different in 2014 and 2015. For better comparison of the data, Fig. 7c shows not only the time series for both years, but also the 36-year averaged values for the period with significant discharge (year days from 100 (April 10) to 200 (July 19)). The total discharge until day 145 was similar in both 2014 and 2015, but the temporal distribution was quite different. For example, on days 120—155 in 2015 the total discharge was about 40% greater than during the same period in 2014. Therefore, the relatively high TSM concentrations measured at the start of the experiment in May 2015

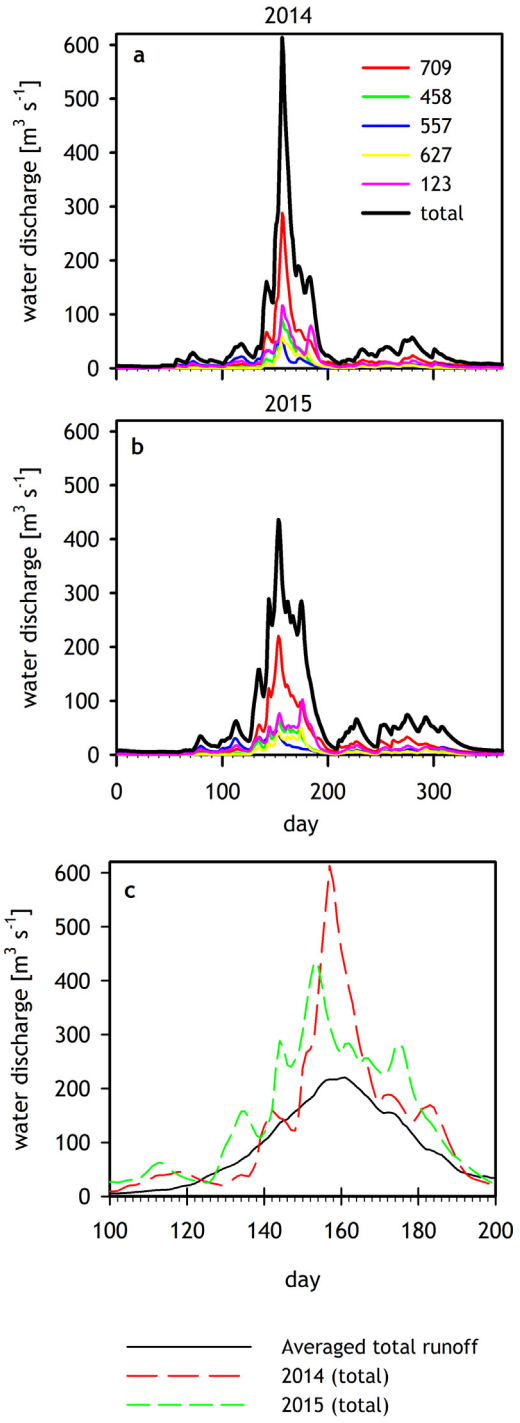

Figure 7 Annual time series of water discharge estimated from the E-Hype model in the subregions marked on the map in Fig. 2, and total runoff estimated as the sum of the water discharge in all the subregions. (a) 2014; (b) 2015; (c) comparison of total runoff in the spring/summer seasons of 2014, 2015, and the 36-year average.

(day 149) were most likely related to both the seasonal runoff of meltwater and the increased runoff due to the precipitation event on days 144–145. In contrast, surface TSM concentrations were lower at the start of the experiment in June 2014 (day 163). According to the data shown in Fig. 7, the total water runoff was also significant at this time, but there were no precipitation events.

At the beginning of the experiment in 2014, the snow near the coast of the fjord had already melted, but some was still melting in the higher mountains in June of that year. The water supplied by the rivers at this time may have contained lower levels of TSM. However, TSM levels inside the fjord increased in 2014 around day 171–173 (June 20–22), most likely due to the storm event with precipitation that occurred around that time. As a result of that event, water was discharged not only by the larger rivers, but also in the form of "no point source water runoff", which could have supplied larger quantities of TSM. The water-column-integrated TSM values were generally higher in 2015 than in 2014, most probably because precipitation was more frequent in 2015. These observations lead to the conclusion that terrestrial water runoff was very likely the most important phenomenon affecting variability of TSM concentrations during this experiment. Table 1 provides detailed statistical information on the TSM concentrations recorded in the Porsanger fjord.

In 2015 data from two rivers (Lakselva and Børselva) were also collected. Measured TSM levels were 11 and 3 g m^{-3} respectively. About 20% of the TSM was organic. Because of insufficient manpower, more regular measurements in the rivers could not be carried out in addition to oceanographic surveys, but the river data do underline the strong variability in TSM concentrations in their waters, and also show that a significant fraction is made up of organic particles (although this fraction was smaller in the rivers than that the average value measured in the fjord waters).

4.3. Water temperature and salinity distribution

There are significant differences between the vertical distribution of water temperature and salinity in subregions 1 and 2, as illustrated in Fig. 8 and in the subsequent figures. The salinity in subregion 1 is quite low at the top of the water column, with values increasing from about 27 at the surface to about 33 at 10 m. It then continues to increase with depth below 20 m, albeit more slowly, to about 34 at depths below 40 m. Since on May 30, 2015, the surface water salinity was the lowest measured by us in this region, it is most likely that large volumes of terrestrial freshwater were also supplied to subregion 1. The surface water temperature (about 8°C) in subregion 1 was generally higher than in subregion 2 (see also Table 2). However, it decreased rapidly with depth to about 4°C or less at 40 m and 2°C at 50 m. The water temperature measured on several occasions in this region at depths below 60 m was only about 0°C (data not shown in Fig. 8 or in Table 2). In contrast, surface (0–2 m) water salinity in subregion 2 varied between 29.13 and almost 33 during this experiment (see Table 2) and depended on the phase of the tide: waters were less saline at low tides (surface water flowing to subregion 2 from subregion 1) but more saline at high tides. The lowest S of 29 was recorded on day 170 in 2014 at station E in the surface waters of subregion 2. Below 40 m in subregion 2 the salinity was always above 34. Also, in contrast to subregion 1, the subsurface water temperature measured during this experiment in subregion 2 (even at 40 m, see Table 2) was always above 4°C. The surface water temperature recorded on May 29 and 30 in subregion 2 was

Table 1 Basic statistics (mean, minimum, maximum, and standard deviation (*SD*) values) of TSM concentrations in three subregions of Porsangerfjorden. *N* stands for number of data taken for the analysis. IN – subregion 1, MID – subregion 2, OUT – subregion 3.

TSM [g m^{-3}]	Mean			Minimum			Maximum			*SD*			*N*		
	IN	MID	OUT	IN	MID	OUT	IN	MID	OUT	IN	MID	OUT	IN	MID	OUT
2014															
0–2 m	1.08	0.96	1.03	0.95	0.72	0.91	1.19	1.32	1.30	0.09	0.20	0.11	6	22	7
40 m	0.58	0.54	0.55	0.55	0.50	0.50	0.64	0.67	0.65	0.04	0.05	0.05	6	22	7
Sum in 30 m	23.99	24.23	27.27	22.14	19.62	24.31	25.85	27.63	31.90	1.46	1.93	2.54	5	19	6
2015															
0–2 m	1.06	1.05	1.10	0.78	0.78	0.88	1.25	1.92	1.31	0.14	0.13	0.12	12	108	14
40 m	0.62	0.63	0.68	0.45	0.47	0.41	0.93	1.08	0.97	0.11	0.08	0.16	12	95	14
Sum in 30 m	24.74	26.48	30.78	17.24	20.92	23.47	28.08	43.15	39.99	3.74	4.28	4.51	12	109	14

Table 2 Basic statistical analysis (mean, minimum, maximum, and standard deviation (*SD*) values) of temperature and salinity in three subregions of Porsangerfjorden. *N* stands for number of data taken for the analysis. IN – subregion 1, MID – subregion 2, OUT – subregion 3.

	Mean			Minimum			Maximum			*SD*			*N*		
	IN	MID	OUT	IN	MID	OUT	IN	MID	OUT	IN	MID	OUT	IN	MID	OUT
Temperature [°C]															
2014															
0–2 m	7.84	7.57	6.75	7.29	6.69	6.62	9.45	8.38	7.06	1.08	0.46	0.15	2	10	4
40 m	4.03	5.27	5.91	2.90	4.15	5.31	5.14	6.09	6.42	1.27	0.54	0.44	2	12	4
2015															
0–2 m	7.55	6.63	6.32	6.22	5.46	5.77	8.18	7.67	7.12	0.48	0.43	0.45	8	103	12
40 m	2.46	4.97	5.67	1.66	4.56	5.04	4.35	5.59	6.18	0.68	0.19	0.39	11	92	12
Salinity															
2014															
0–2 m	29.52	31.35	33.71	26.90	29.13	33.53	30.41	32.81	33.94	1.75	0.68	0.15	2	10	4
40 m	33.85	34.06	34.14	33.69	33.87	34.00	34.02	34.12	34.26	0.19	0.07	0.13	2	12	4
2015															
0–2 m	28.91	31.75	33.79	27.10	25.82	33.37	29.96	33.94	34.15	0.97	1.29	0.20	8	103	12
40 m	33.70	34.12	34.20	33.59	33.95	34.06	33.95	34.23	34.29	0.09	0.05	0.07	11	92	12

lower than that measured in subregion 1. In general (Table 2), the salinity was the highest in subregion 3 owing to significant advection of oceanic water masses. The surface temperature was the highest in subregion 1, whereas the highest temperature at 40 m was noted in subregion 3.

4.4. Temporal and spatial TSM distribution

Since the high TSM concentrations measured at the end of May 2015 produced the most interesting event in this TSM data set, some more data from this period will now be discussed. Fig. 8 presents a few examples of TSM, T and S profiles measured at the end of May 2015. The left-hand side of Fig. 8(plots a–c) presents data from subregion 1, while the right-hand side of Fig. 8(plots d–f) displays data from subregion 2. Unfortunately, it is not possible to state exactly when the TSM concentration reached these elevated levels, because concentrations of about 2 g m^{-3} were already being detected when the first stations has been set up in 2015 (after May 29, Fig. 8). Interestingly, this increase in TSM did not happen at the same time in subregion 1 (see Fig. 8a–c). This is difficult to explain, but it may have been due to larger volumes of runoff water from snow melt being delivered to subregion 2 or because the concentration of suspended matter was higher in the runoff water supplied to subregion 2.

The seasonal increase in TSM concentrations measured along the entire fjord on June 3, 2015 is shown in Fig. 9(a–c). Note that a significant period of time elapsed between the visits to the first station (A2) and the last one (T5) on that day, because of the quite considerable distance (45 km) between them. Station A2 was thus visited as the tide was rising, but T5 was reached at high tide. This implies that some of the variability displayed in Fig. 9 in TSM, T, and S data must be due to spatial patterns and some to the temporal variability associated with tides. Nevertheless, it is clear that elevated TSM concentrations were also recorded in subregion 3 (station A2). In comparison to June 3 (Fig. 9a–c), TSM concentrations on June 10 were somewhat lower (Fig. 9d–f); on that

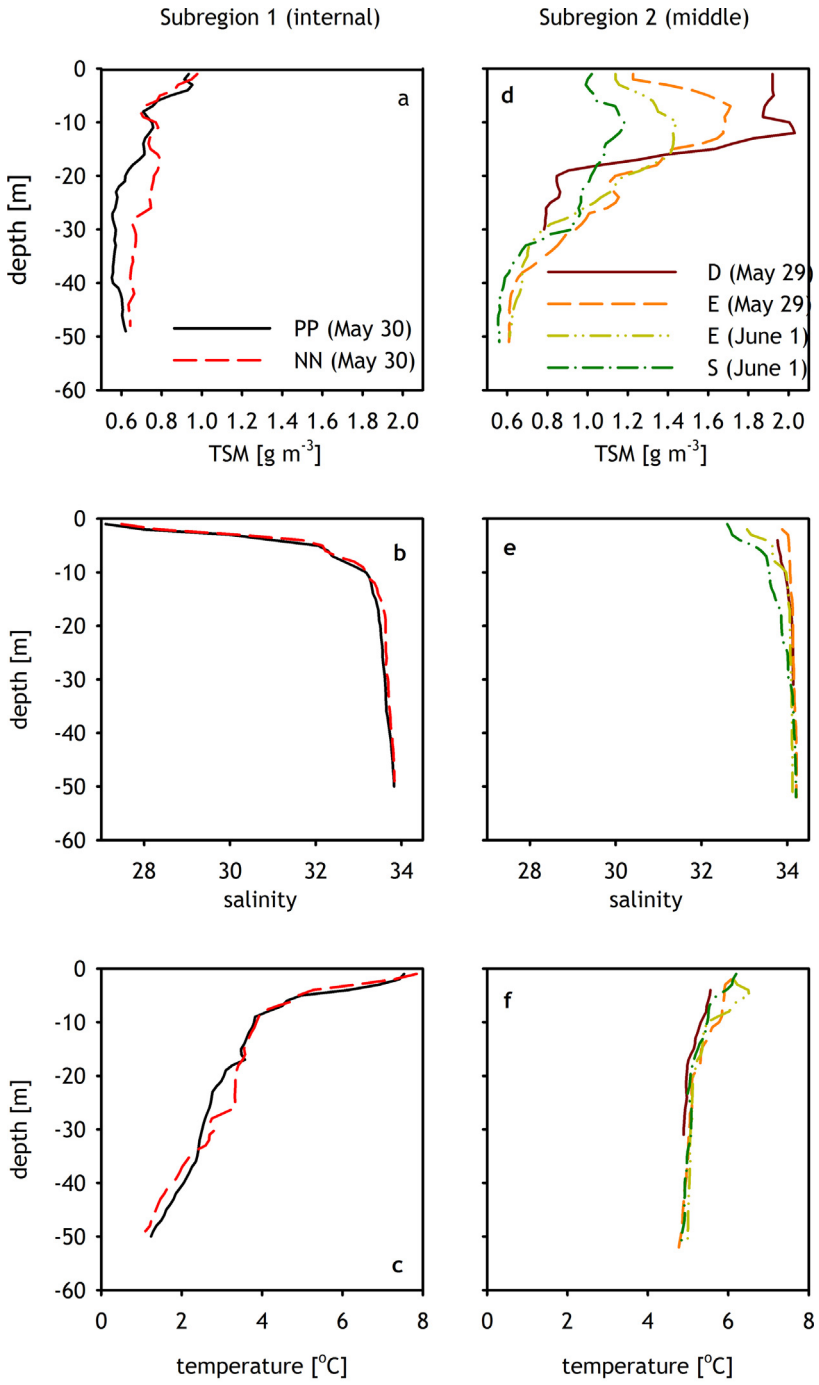

Figure 8 Examples of TSM, water temperature and salinity profiles measured on May 29—June 30, 2015. Note that the range of values for TSM concentration, salinity and temperature is different in each plot.

day, TSM levels were lower in the inner part of the fjord, increasing towards its mouth.

During our experiment it was observed that the spatial variability of TSM documented over a single day was the strongest in the outer part of the fjord (Fig. 10). Fig. 10a shows considerable variability of TSM along transect A in the outer part of the fjord. This was expected, since interaction between oceanic and fjord water masses in subregion 3 is very intensive (see also Table 1). Moreover, the water column in subregion 3 contains at least two water masses with different temperatures—this is also reflected by the TSM concentration profiles. Fig. 11a—f shows examples of data collected across the fjord at similar phases of the tide along transect E in the morning and afternoon of June 9. The vertical TSM profiles at the different stations were quite similar, and the overall pattern did not change much between the morning and afternoon. TSM concentrations were somewhat higher (more than 1.2 g m^{-3}) at about 10 m depth, most likely because water was advected westwards (from station E to station E3). The differences are greater if the same

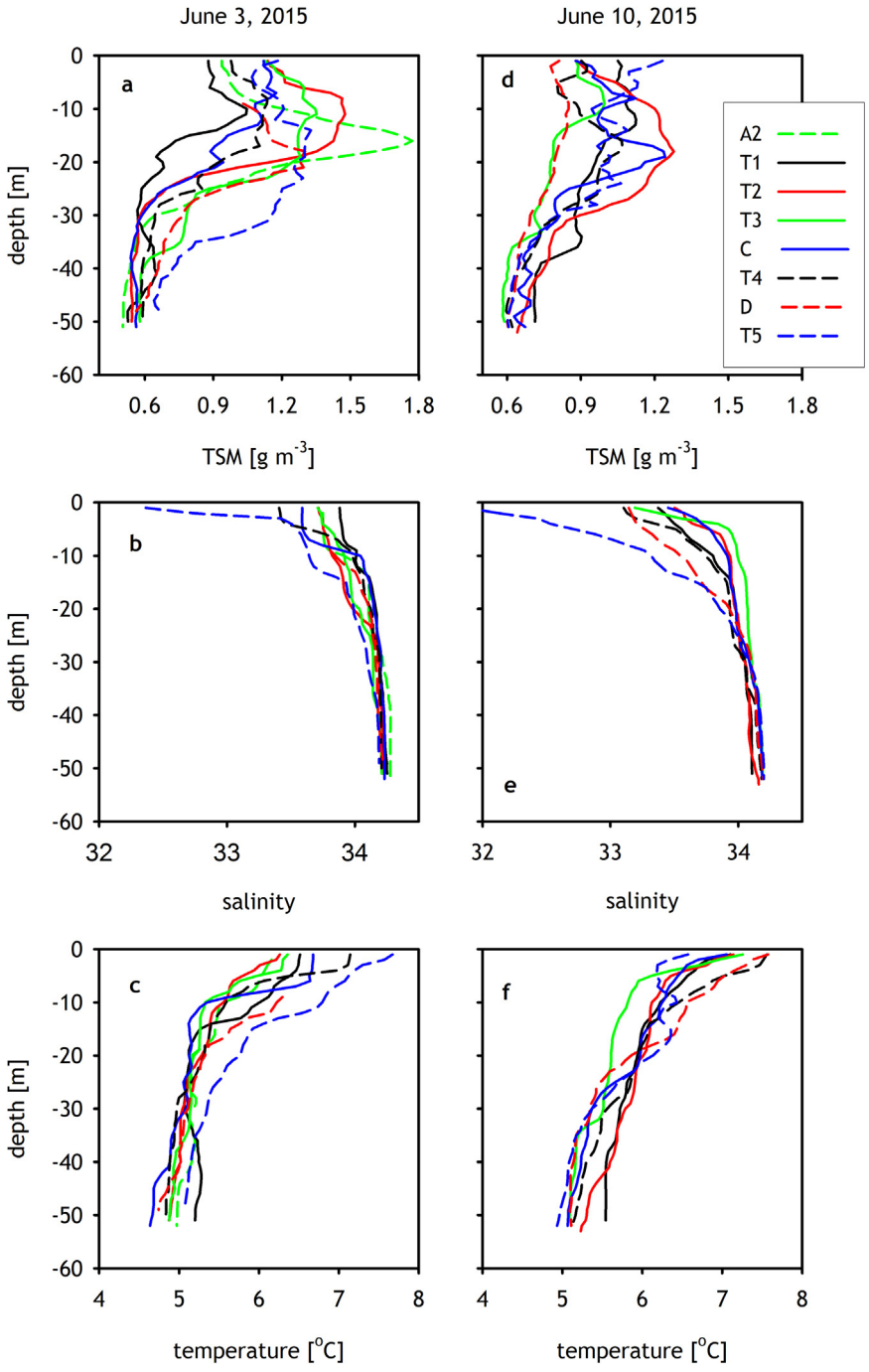

Figure 9 Comparison of example TSM, water temperature and salinity profiles measured at stations located along the fjord (transect T) on June 3 and June 10, 2015.

transect is compared at different phases of the tide (compare Fig. 11a and d with Fig. 11g). The spatial variability of the TSM concentration in the surface waters of subregion 1 appears to be relatively small (Fig. 12).

In general (Table 1), the range of TSM concentrations is the largest in the middle part of the fjord. The mean TSM concentrations at 40 m were 54% and 60% of the surface TSM concentrations recorded in 2014 and 2015 respectively. The mean TSM concentrations were the highest in the inner region in 2014, but in the outer region in 2015. In both years the deep water TSM concentrations were the greatest in subregion 3, which is consistent with the fact that the vertical water density gradient is the smallest in this region and that vertical mixing is expected to play a more significant role in transporting particles to greater depths.

4.5. Suspended organic and inorganic matter

In general, more than half of the suspended matter in the surface waters was organic (on average 55% in 2014 and 59%

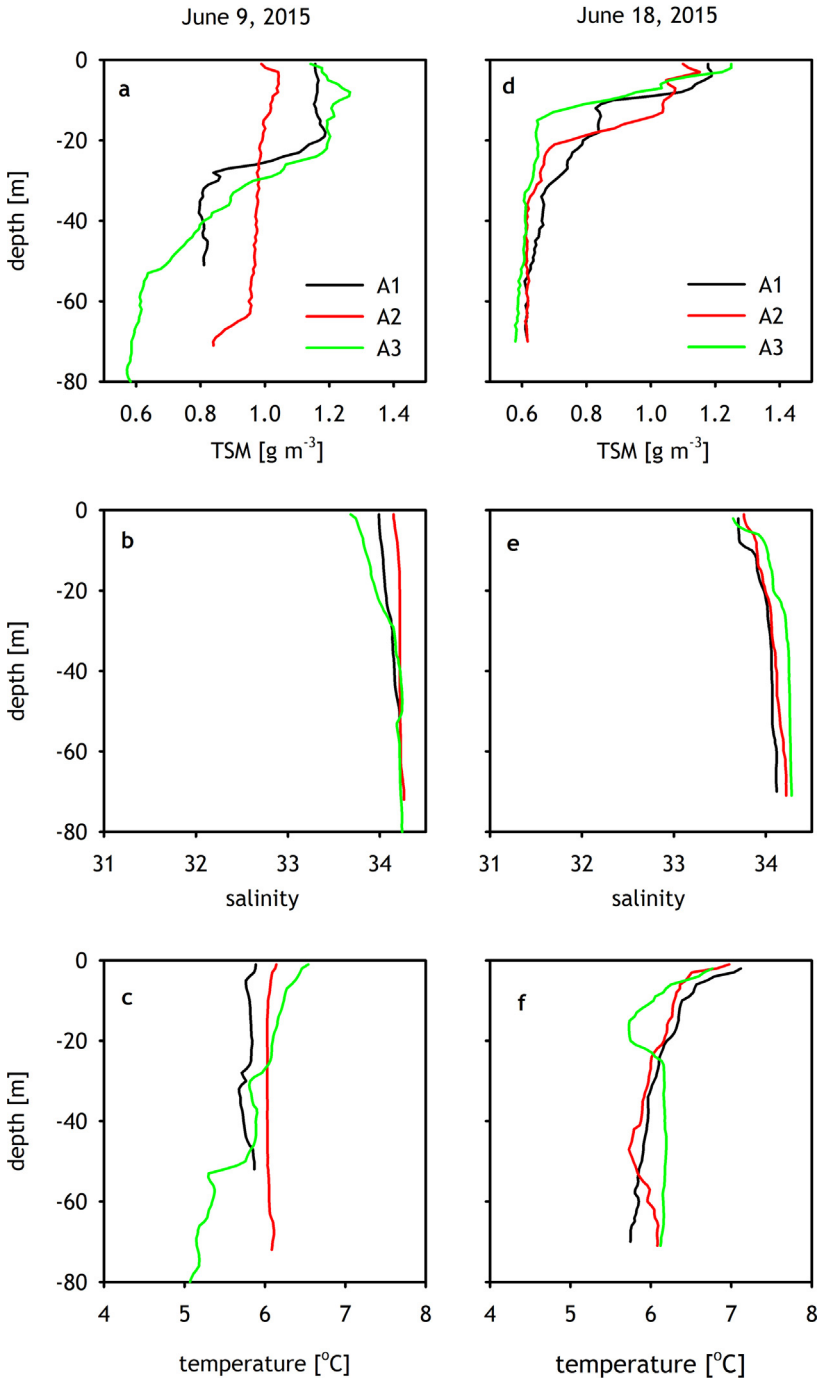

Figure 10 Comparison of example TSM, water temperature and salinity profiles measured at stations located in the outer part the fjord (subregion 3) on June 9 and June 18, 2015.

in 2015). At 40 m and below, this decreased to less than 50% (*e.g.*, June 14 2015, station M) and in some cases even less than 30% (see Figs. 5 and 6). This shows that in the Porsanger fjord, where one would expect relatively low particulate matter concentrations because of the low level of primary productivity and absence of glaciers, TSM concentrations are quite significant and the proportion of mineral particles is relatively high. This is consistent with our observations that rivers supply a large amount of suspended matter, only 20% of which is organic.

5. Discussion

The TSM concentrations measured in the Porsanger fjord (Table 1) are generally high in comparison to other, similar data sets gathered in open ocean regions, but lower than in some fjords, in particular those with glacial runoff. For example, Lund-Hansen et al. (2010) reported TSM concentrations of the order of 300 g m^{-3} in the internal part of the Kangerlussuaq fjord in Greenland. Similar TSM concentrations were measured by Zhu et al. (2016) in Kongsfjorden,

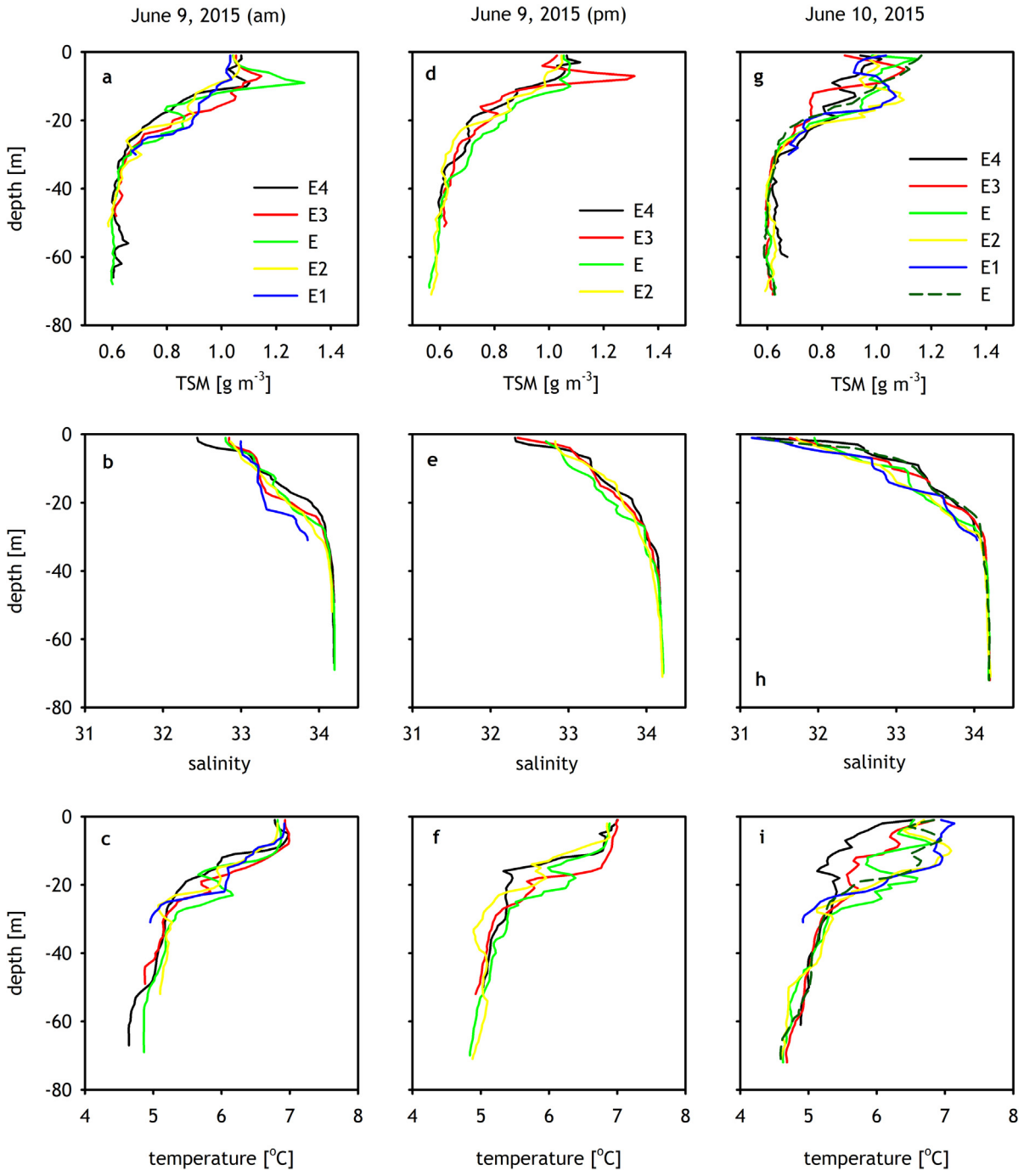

Figure 11 Comparison of example TSM, water temperature and salinity profiles measured at stations located across the middle part of the fjord (subregion 2) on June 9 and June 10, 2015.

Svalbard. In the Baltic Sea (Lund-Hansen and Christianses, 2008; Woźniak et al., 2016) TSM concentrations can also reach high values, for example, more than 15 g m^{-3} in the Gulf of Gdańsk. In the open Baltic Sea TSM concentrations vary between 0.1 and 10 g m^{-3}. The organic fraction in the Baltic Sea is higher (about 80% of TSM there consists of organic particles). The same order of TSM concentrations was recorded in Chesapeake Bay (Ondrusek et al., 2012). In some other coastal regions TSM concentrations are similar to those recorded in this work in the Porsanger fjord (Babin et al., 2003; Faust et al., 2014; Kiyomoto et al., 2001). The mineral content in some coastal regions in the Mediterranean Sea, English Channel or glacial fjords is higher (80, 64, and 81% respectively) than in the Porsanger fjord.

Finally, it has to be noted that our measurements covered only a small part of the year, so no inferences can be drawn regarding the entire annual cycle or the annual range of TSM variability. Nevertheless, considering that this experiment was scheduled for late spring/early summer, when water runoff in the Porsanger fjord is at its most intense, one

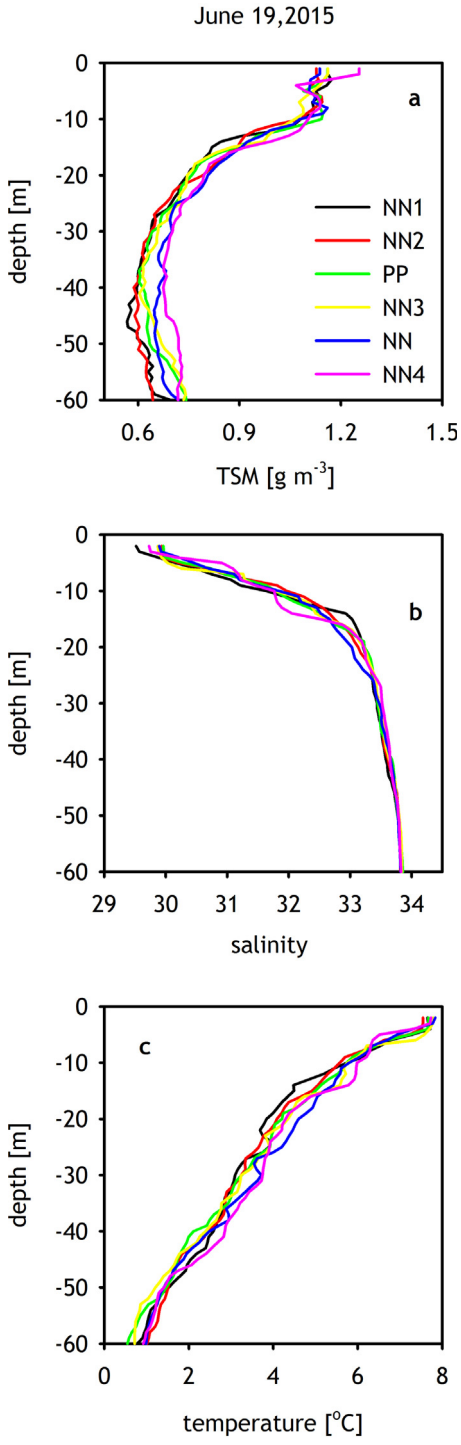

Figure 12 Comparison of example TSM, water temperature and salinity profiles measured at stations located in the inner part the fjord (subregion 1) on June 19, 2015.

can assume that the seasonal increase in TSM concentrations directly related to terrestrial water runoff was reliably documented. One would also expect TSM to increase during summer as a result of seasonal phytoplankton blooms, but this increase would involve mostly the organic fraction of TSM, with the inorganic fraction remaining rather stable. It would be interesting to perform similar experiments in other fjords in order to acquire a better understanding of the range and variability of TSM concentrations in somewhat different environmental settings.

6. Conclusions

On the basis of the *in situ* data presented here, regional bio-optical relationships were derived, enabling optical data (beam attenuation coefficient c_p) to be interpreted in terms of the TSM concentration in the Porsanger fjord. The relationships, similar for the data sets collected in 2014 and 2015, were used to convert *in situ* vertical c_p profiles to TSM concentrations. The results indicate that TSM concentrations lie within the range of values found in other coastal regions, but that they are lower than in fjords where glacial activity supplies large amounts of terrigenous particulate matter. Nevertheless, the present data also indicate that significant amounts of such material are delivered to fjord waters during precipitation events. The optical properties of the fjord waters are most likely affected by this presence of mineral particles, which efficiently scatter underwater light.

A significant temporal variability in TSM concentrations was documented. TSM concentrations in surface waters were the highest during the periods when precipitation events were recorded in the meteorological data. There was also temporal variability in relation to water mass movements associated with tides. Spatial variability was more pronounced when different subregions of the fjord were compared but less so when data from stations located on transects across the fjord were compared. There was a significant decrease in TSM concentration from surface to deep waters. On average, the organic fraction was 56% at the surface and 47% at 40 m depth. The mineral fraction made up some 80% of the TSM delivered to the Porsanger fjord with runoff.

Acknowledgements

The authors express their gratitude to Knut Yngve Børsheim, Hans Kristian Strand, and Henrik Søiland from the Norwegian Institute of Marine Research, for their help with the experiment logistics. Many thanks go to Mateusz Jakowczyk, Daniel Materka, Roman Majchrowski, Roman Marks, Marek Świrgoń and Tomasz Żmójdzin for their participation in the NORDFLUX field experiments. The authors are grateful to all the persons involved in the programmes providing free access to the data sets used in the study. Meteorological data from Honningsvåg were made available by the Norwegian Meteorological Institute (http://www.yr.no). E-Hype model water discharge data were obtained from SMHI (hypeweb.smhi.se). Some of the figures were prepared with Ocean Data View software (Schlitzer, R., Ocean Data View, http://odv.awi.de, 2015), and some maps were prepared using Google Earth software.

This work was funded by the Norway Grants through the Polish-Norwegian Research Programme operated by the National Centre for Research and Development (NCBR contract No. 201985 entitled 'Application of *in situ* observations, high frequency radars, and ocean colour, to study suspended matter, particulate carbon, and dissolved organic carbon fluxes in coastal waters of the Barents Sea'). Partial support for JB and

MS also came from the statutory funds of the Institute of Oceanology of the Polish Academy of Sciences (IO PAN).

References

Babin, M., Morel, A., Fournier-Sicre, V., Fell, F., Stramski, D., 2003. Light scattering properties or marine particles in coastal and open ocean waters as related to the particle mass concentration. Limnol. Oceanogr. 48 (2), 843—859.

Cushman-Roisin, B., Asplin, L., Svendsen, H., 1994. Upwelling in broad fjords. Cont. Shelf Res. 14, 1701—1721.

Donnelly, C., Stromqvist, J., Arheimer, B., 2011. Modelling climate change effects on nutrient discharges from the Baltic Sea catchment: processes and results. IAHS Publ. 348, 145—150.

Donnelly, C., Andersson, J.C.M., Arheimer, B., 2015. Using flow signatures and catchment similarities to evaluate the E-HYPE multi-basin model across Europe. Hydrol. Sci. J. 61 (2), 255—273, http://dx.doi.org/10.1080/02626667.2015.1027710.

Eilertsen, H.C., Frantzen, S., 2007. Phytoplankton from two sub-Arctic fjords in northern Norway 2002—2004: I. Seasonal variations in chlorophyll *a* and bloom dynamics. Mar. Biol. Res. 3, 319—332.

Faust, J.C., Knies, J., Slagstad, T., Vogt, Ch., Milzer, G., Giraudeau, J., 2014. Geochemical composition of Trondheimsfjord surface sediments: sources and spatial variability of marine and terrigenous components. Cont. Shelf Res. 88, 61—71.

Kirk, J.T.O., 2011. Light and Photosynthesis in Aquatic Ecosystems, 3rd ed. Cambridge Univ. Press, 662 pp.

Kiyomoto, Y., Iseki, K., Okamura, K., 2001. Ocean color satellite imagery and shipboard measurements of chlorophyll *a* and suspended particulate matter distribution in the East China Sea. J. Oceanogr. 57, 37—45.

Lund-Hansen, L.C., Christianses, C., 2008. Suspended particulate matter (SPM) in the North Sea-Baltic Sea transition: distributions, inventories, and the autumn 2002 inflows. Danish J. Geogr. 108 (2), 37—47.

Lund-Hansen, L.C., Andersen, T.J., Nielsen, M.H., Pejrup, M., 2010. Suspended matter, Chl-*a*, CDOM, grain sizes, and optical properties in the Arctic Fjord-type Estuary, Kangerlussuaq, West Greenland during summer. Estuar. Coast. 33 (6), 1442—1451.

Mobley, C.D., 1994. Light and Water: Radiative Transfer in Natural Waters. Acad. Press, San Diego, 592 pp.

Montes-Hugo, M., Gagne, J.P., Demers, S., Cizmeli, S., Mas, S., 2012. Ocean colour and distribution of suspended particles in the St. Lawrence Estuary. EARSeL eProc. 11, 1—11.

Ondrusek, M., Stengel, E., Kinkade, C., Vogel, R., Keegstra, P., Hunter, C., Kim, C., 2012. The development of a new optical total suspended matter algorithm for the Chesapeake Bay. Remote Sens. Environ. 119, 243—254, http://dx.doi.org/10.1016/j.rse.2011.12.018.

Pearlman, S.R., Costa, H.S., Jung, R.A., Mckeown, J.J., Pearson, H. E., 1995. Solids (section 2540). In: Eaton, A.D., Clesceri, L.S., Greenberg, A.E. (Eds.), Standard Methods for the Examination of Water and Wastewater. American Publ. Health Assoc, 2-53—2-64.

Pegau, W.S., Gray, D., Zaneveld, J.R., 1997. Absorption and attenuation of visible and near-infrared light in water: dependence on temperature and salinity. Appl. Opt. 36 (24), 6035—6046.

Stavn, R.H., Rick, H.J., Falster, A.V., 2009. Correcting the errors from variable sea salt retention and water of hydration in loss on ignition analysis: implications for studies of estuarine and coastal waters. Estuar. Coast. Shelf Sci. 81 (4), 575—582.

Stramska, M., Jankowski, A., Cieszyńska, A., 2016. Surface currents in the Porsangerfjorden. Pol. Polar Res. 37 (3), 337—360, http://dx.doi.org/10.1515/popore-2016-0018.

Svendsen, H., 1995. Physical oceanography of coupled fjord-coast systems in northern Norway with special focus on dynamics and tides. In: Ecology of Fjords and Coastal Waters. Proc. Mare Nor Symposium on the Ecology of Fjords and Coastal Waters, Tromsø, Norway, 5—9 December 1994, Elsevier, 149—164.

Syvitski, J.P.M., 1989. On the deposition of sediment within glacier-influenced fjords: oceanographic controls. Mar. Geol. 85, 301—329.

Winters, G.V., Syvitski, J.P.M., 1992. Suspended sediment character and distribution in MacBeth Fiord, Baffin Island. Arctic 45, 25—35.

Woźniak, S.B., Meler, J., Lednicka, B., Zdun, A., Stoń-Egiert, J., 2011. Inherent optical properties of suspended particulate matter in the southern Baltic Sea. Oceanologia 53 (3), 691—729, http://dx.doi.org/10.5697/oc.53-3.691.

Woźniak, S.B., Darecki, M., Zabłocka, M., Burska, D., Dera, J., 2016. New simple statistical formulas for estimating surface concentrations of suspended particulate matter (SPM) and particulate organic carbon (POC) from remote-sensing reflectance in the southern Baltic Sea. Oceanologia 58 (3), 161—175, http://dx.doi.org/10.1016/j.oceano.2016.03.002.

Zaneveld, J.R.V., Kitchen, J.C., Moore, C.C., 1994. Scattering error correction of reflecting-tube absorption meters. Proc. SPIE. 2258. Ocean Optics XII 44, http://dx.doi.org/10.1117/12.190095.

Zhu, Z.Y., Wu, Y., Liu, S.M., Wenger, F., Hu, J., Zhang, J., Zhang, R.F., 2016. Organic carbon flux and particulate organic matter composition in Arctic valley glaciers: examples from the Bayelva River and adjacent Kongsfjorden. Biogeosciences 13, 975—987.

Oceanologia (2018) 60, 16—31

Available online at www.sciencedirect.com

ScienceDirect

journal homepage: www.journals.elsevier.com/oceanologia/

ORIGINAL RESEARCH ARTICLE

Attributing mean circulation patterns to physical phenomena in the Gulf of Finland

Antti Westerlund [a,*], **Laura Tuomi** [a], **Pekka Alenius** [a], **Elina Miettunen** [b], **Roman E. Vankevich** [c]

[a] *Finnish Meteorological Institute, Marine Research, Helsinki, Finland*
[b] *Finnish Environment Institute/Marine Research Centre, Helsinki, Finland*
[c] *Russian State Hydrometeorological University, Saint Petersburg, Russia*

Received 15 September 2016; accepted 19 May 2017
Available online 12 June 2017

KEYWORDS
Circulation;
Upwelling;
Modelling;
Baltic Sea;
Gulf of Finland

Summary We studied circulation patterns in the Gulf of Finland, an estuary-like sub-basin of the Baltic Sea. According to previous observations and model results, the long-term mean circulation in the gulf is cyclonic and mainly density driven, whereas short-term circulation patterns are wind driven. We used the high-resolution 3D hydrodynamic model NEMO to simulate the years 2012—2014. Our aim was to investigate the role of some key features, like river runoff and occasional events, in the formation of the circulation patterns. Our results show that many of the differences visible in the annual mean circulation patterns from one year to another are caused by a relatively small number of high current speed events. These events seem to be upwelling-related coastal jets. Although the Gulf of Finland receives large amounts of fresh water in river runoffs, the inter-annual variations in runoff did not explain the variations in the mean circulation patterns.

* Corresponding author at: Finnish Meteorological Institute, Erik Palménin aukio 1, P.O.Box 503, FI-00101 Helsinki, Finland. Tel.: +358 29 539 1000
E-mail address: antti.westerlund@fmi.fi (A. Westerlund).
Peer review under the responsibility of Institute of Oceanology of the Polish Academy of Sciences.

Production and hosting by Elsevier

1. Introduction

The Gulf of Finland (GoF) in the Baltic Sea is a long, estuary-like sea area that is a direct continuation of the Baltic Proper. Short-term surface circulation in the gulf is mainly wind driven. The stability of currents varies from season to season. The relatively large freshwater input from the eastern end and the more saline deep water flow from the main basin at the western end maintain horizontal density gradients. The

http://dx.doi.org/10.1016/j.oceano.2017.05.003

dominating south-westerly winds, freshwater input locations and the rotation of the Earth lead one to expect that the long-term mean circulation pattern would be cyclonic. Such residual circulation in the gulf was already described by Witting (1912) and later by Palmén (1930) in his classical study of circulation in the sea areas around Finland. For in-depth descriptions of the gulf, see e.g. Alenius et al. (1998), Soomere et al. (2008, 2009), Leppäranta and Myrberg (2009), and Myrberg and Soomere (2013).

In recent years, the circulation patterns in the gulf have been studied in many numerical model studies. While the model results have generally agreed with the features described by Witting, the results of the model studies vary somewhat from each other. For example, Maljutenko et al. (2010), Elken et al. (2011), Soomere et al. (2011) and Lagemaa (2012) show stronger mean currents west of Narva Bay on the southern coast than what was reported earlier by Andrejev et al. (2004). Also, the intensity of the outflow from the gulf seems to differ from one study to another and from one year to another. Where Andrejev et al. (2004) and Elken et al. (2011) observed a clear outflow in the subsurface layer, Maljutenko et al. (2010) did not. Lagemaa (2012) found the outflow to differ significantly from one year to another.

There are some obvious reasons for the differences between model results. Different studies have simulated different years, and model setups have been different. Also, there is significant inter-annual variability in the mean circulation. But these differences in results may also indicate that the reasons why such a statistical mean circulation pattern emerges are still not fully understood. By studying the physical mechanisms underlying the mean circulation pattern, we can also better understand the relative strengths and weaknesses of different hydrodynamic models and model configurations. For example, if we find that models overestimate or underestimate the effect of certain forcing inputs to the mean circulation, we know those processes need further attention in the model.

Suhhova et al. (2015) speculated that the role of upwelling-related coastal jets may be significant for the mean circulation in the gulf. Coastal upwelling is prevalent in the Gulf of Finland (Lehmann and Myrberg, 2008). Because the dominating wind direction in the GoF is from the south-west, upwelling events are expected to be more common in the northern (Finnish) side of the gulf than in the southern (Estonian) side. A coastal jet is developed simultaneously with the upwelling event. In the GoF, these jets have been both directly observed (e.g. Suursaar and Aps, 2007) and modelled (Zhurbas et al., 2008).

The effects of the residual circulation pattern can be indirectly seen, for example, in the intensity and whereabouts of the salinity gradients across the gulf. The salinity field in the gulf varies significantly both in space and in time. The four largest rivers in the area flow to the eastern gulf. The GoF receives the largest single freshwater input of the whole Baltic Sea from the river Neva at its eastern end. One way to view the gulf is to think of it as a transition zone between the fresh waters of the Neva and the brackish waters of the Baltic Proper (Myrberg and Soomere, 2013). The surface salinity decreases from 5 to 6.5 in the western part of the GoF to about 0 to 3 in the easternmost part of the gulf (Alenius et al., 1998).[1] In the western part of the GoF, a quasi-permanent halocline is located at the depth of 60–80 m and the bottom salinity can reach values up to 8–10 when more saline water masses advect from the Baltic Proper. In the eastern part of the GoF, there is no permanent halocline and the salinity typically increases linearly with depth. Changes in circulation patterns are relatively quickly reflected in the mean salinities, especially in the volatile upper layers. This means that it is possible to indirectly validate the mean circulation field of the gulf by investigating the patterns of salinity in the gulf. This method has been previously employed by e.g. Myrberg et al. (2010) and Leppäranta and Myrberg (2009).

The residual mean circulation must be distinguished from the instantaneous or short-term circulation patterns. It lies more behind the scenes but is nevertheless important for many applications, such as estimating the transport, distribution and residence times of substances discharged to the sea. These substances can be, for instance, nutrients from the land or oil and chemicals from accident sites. Improving substance transport estimates is a high priority task in the area as the coastline is densely populated and ship fairways are highly trafficked. When high-resolution numerical models are used in these tasks, they must be able to faithfully reproduce the mean circulation patterns. Correctly working numerical models can bring significant added value to decision support systems that are built to evaluate the effects of environmental protection measures on marine systems. Unfortunately, evaluating model performance is not straightforward. Where current measurements exist, they lack coverage, both spatial and temporal. Thus, questions remain about the accuracy of modelled circulation patterns.

Our objective is to study how physical processes are attributed to features that are observed in mean circulation patterns. We use the numerical 3D model NEMO (Madec and the NEMO team, 2008), an increasingly popular model in the investigations of the Baltic Sea, to calculate the mean circulation pattern in the Gulf of Finland for the years 2012–2014. We use two setups of the model, one fine resolution and one of coarser resolution, which are validated against observations and benchmarked against other model data. We analyse some of the key circulation features and especially the contribution that high current speed events make to the longer term averages. Finally, we investigate how these details relate to specific phenomena such as upwelling.

2. Material and methods

2.1. Modelling

2.1.1. NEMO

We used two setups of the NEMO 3D ocean model (V3.6), a coarse resolution setup with a two nautical mile (NM) horizontal resolution covering the Baltic Sea and the North Sea area, and a fine resolution setup for the Gulf of Finland with 0.25 NM horizontal resolution. We ran the model from the

[1] All salinities in this paper are on the practical salinity scale.

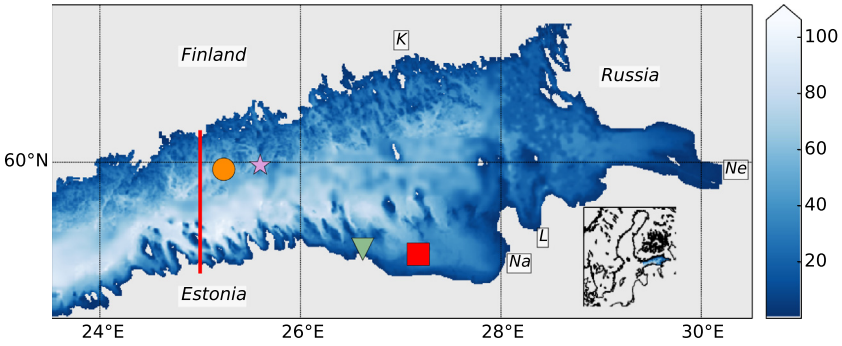

Figure 1 The model domain and bathymetry (in metres) from the fine resolution 0.25 NM NEMO setup. Stations and sites referenced in the article (from the west): H (orange circle), Kalbådagrund (magenta star), G (green triangle) and 15 (red square). The thin red line shows the location of the 25°E transect. Also indicated on the map are the approximate locations of the Neva (Ne), Narva (Na), Luga (L) and Kymi (K) river mouths. Inset is the location of the model domain on a map of the Baltic Sea. (For interpretation of the references to color in this figure legend, the reader is referred to the web version of the article.)

beginning of 2011 to the end of 2014. We considered the results from 2011 as the stabilisation of the model and chose the years 2012–2014 for closer analysis. The model saved daily mean values of temperature, salinity and current fields.

The horizontal resolution of the fine resolution setup, approximately 500 m, is well below the typical range of internal Rossby radius (2–4 km) in the GoF (Alenius et al., 2003). This configuration is based on the setup by Vankevich et al. (2016) with some modifications related to atmospheric forcing and boundary conditions. The model domain covers the GoF east from longitude 23.5°E, where an open boundary to the Baltic Proper is located (see Fig. 1). Model bathymetry is based on Andrejev et al. (2010). This setup has 94 z-coordinate (with partial step) vertical layers. The topmost vertical layers are 1 m thick, and the layer thickness slightly increases with depth, being about 1.08 m at the lower bound of the z-axis. The time step of the model was 100 s. The ice model LIM3 was included in the setup (Vancoppenolle et al., 2009). Due to the high computational requirements of the configuration, and since the focus of this study is on the ice-free period, the ice model was only run with a thermodynamical formulation. Like Vankevich et al. (2016), we used initial conditions for the beginning of 2011 from the operational version of HIROMB (High Resolution Operational Model for the Baltic). The lateral boundary condition on the open boundary was taken from the coarser setup. Flather boundary conditions were used for barotropic velocities and sea surface height; flow relaxation was used for temperature and salinity.

The coarser 2 NM NEMO setup for the Baltic Sea and the North Sea was also used for analyses. This setup was documented and validated in Westerlund and Tuomi (2016) and is based on the NEMO Nordic configuration by Hordoir et al. (2013a, 2013b, 2015). The layer thickness of this setup starts from 3 m in the surface layer, growing with depth. Unlike in Westerlund and Tuomi (2016), the boundary condition of the coarse setup was updated to use Copernicus Marine Environment Monitoring Service (CMEMS) Global Ocean Reanalysis product (Ferry et al., 2016) to improve the representation of sea levels in the model. Furthermore, the additional strong isopycnal diffusion that was previously applied in the Neva estuary, described in Hordoir et al. (2015), was turned off in order to make the description of currents in the eastern part of the GoF more realistic. The bathymetry of the setup was updated to the latest version of the NEMO Nordic bathymetry and the ice model of the coarser setup was turned off to improve run times.

2.1.2. Meteorological forcing

We used forecasts from the HIRLAM (High Resolution Limited Area Model) numerical weather prediction system (HIRLAM-B, 2015) of the Finnish Meteorological Institute (FMI) for atmospheric forcing. Its domain covers the European region with a horizontal resolution of 0.15° (V73 and earlier; before 6 March 2012) or 0.068° (V74; after 6 March 2012). Vertically the domain is divided into 60 (V73) or 65 (V74) terrain-following hybrid levels, the lowest level being about 12 m above the sea surface. The forecasts are run four times a day (00, 06, 12, and 18 UTC) using boundary conditions from the Boundary Condition Optional Project of the ECMWF (European Centre for Medium-Range Weather Forecasts). Each day of forcing was extracted from the 00 forecast cycles with the highest available temporal resolution in the model archive, varying from 1 to 6 h.

Forcing taken from HIRLAM includes the two-metre air temperature, total cloud cover, mean sea-level pressure and 10-m winds, and either the two-metre dew point temperature or relative humidity, depending on the availability in the model archive. Forcing was read into the NEMO run with CORE bulk formulae (Large and Yeager, 2004).

2.1.3. River runoff and precipitation data

River runoff forcing for the four main rivers running into the GoF was based on data obtained from two sources. For the river Kymi, we used the same climatological runoff data from Stålnacke et al. (1999) as was used in Vankevich et al. (2016). The discharges for the Neva, Narva and Luga rivers were from HydroMet, received as a part of the Gulf of Finland Year 2014 (GoF2014) project.

The sensitivity of the model configuration to changes in the river runoff forcing was evaluated by running experiments for the years 2013–2014 with modified runoffs. The first experiment had no river runoffs and the second experiment had runoff volume multiplied by two.

Precipitation fields were climatological and based on downscaling of the ERA40 reanalysis for the period 1961—2007 (cf. Hordoir et al., 2015).

2.1.4. CMEMS reanalysis product

In addition to NEMO, we used CMEMS Baltic Sea Reanalysis (Axell, 2016) to further analyse the circulation in the gulf. This product is based on the HIROMB model with the horizontal resolution of approximately 3 NM, with 51 vertical levels. The top layer in this model is 4 m thick and layer thickness increases with depth. This product implements a data assimilation algorithm for salinity, temperature, and ice concentration and thickness.

2.2. Measurements

2.2.1. CTD

Usually model development and evaluation are limited by the availability of measured datasets with sufficient temporal and spatial resolutions. We hoped to be a little bit better off with the GoF2014 dataset. The official GoF2014 data covers the whole gulf with data from 1996 to 2014 from Estonia, Finland and Russia. This dataset consists of almost 38,500 depth observations with several parameters from 53 different observation stations covering the whole gulf. The number of visits to stations varies and only some of them can be considered to be like a time series.

Additionally, the FMI did three one-week CTD surveys with over 80 stations each in the western gulf, in Finnish and Estonian waters. One of these was done in 2013 and two were done in 2014. These surveys were planned to collect data on temperature, salinity and density fields for model development. The horizontal spacing of the stations was around 4 NM across the gulf and around 9 NM along the gulf. The observation grid was a compromise between the needed resolution (the Rossby radius of deformation is of the order of 2—4 km), the available ship time and the area that we wanted to cover. CTD casts were done at every station with SeaBird SBE911 ctd.

The 2013 observations were made 3—7 June 2013, from east to west. In 2014 there were two cruises, the first 15—19 June, from west to east, and the second 8—12 September, from west to east. The duration of each cruise was five days. Thus, the whole grid may not be considered synoptic. The time of each section across the gulf was of the order of 6 h and those sections may be considered rather synoptic, though the transversal Seiche period of the gulf is of the same order. For analysis, the cruise data was then interpolated to a 3D grid using the DIVA (Data-Interpolating Variational Analysis) interpolation method (Troupin et al., 2012).

2.2.2. Weather stations

We used wind measurements from the FMI's coastal weather station Kalbådagrund (location shown in Fig. 1) in order to evaluate the accuracy of the meteorological forcing. This weather station is considered to be representative for open sea weather conditions in the Gulf of Finland and it has been used in many earlier studies (e.g. Lips et al., 2011; Tuomi et al., 2012). At Kalbådagrund, wind measurements are made at 32 m height. From this station, we have data for the main meteorological parameters at 10-min intervals.

3. Results

3.1. The mean circulation field in the Gulf of Finland in the NEMO model

In the Gulf of Finland, the persistency of the circulation field (defined as the ratio of the vector velocity to scalar speed) is known to be rather low. Alenius et al. (1998), among others, cite Palmén's estimates, which ranged from 6% to 26% for long-term persistency. This means that the current field is very variable in time (and space). Therefore it is to be expected that the residual circulation pattern is different from year to year too. We present here the mean circulation patterns from the two NEMO model setups, averaged over time and depth. Depth averaging was done from the surface to 7.5 m depth. These limits for averaging were chosen to make sure that averaging does not include the thermocline, which can at times be shallower than 10 m.

The annual mean circulation, modelled with 2 NM NEMO, was quite different for the years 2012—2014 (Fig. 2). Of these years, 2012 resembles most the traditional mean circulation patterns, while the years 2013 and 2014 showed quite different mean circulation fields. In 2012, there was a westward residual current on the northern coast (also called the Finnish Coastal Current, Stipa, 2004) with speeds of a few centimetres per second and a relatively strong jet with top speeds over 10 cm s^{-1} along the south-eastern coast, west of Narva Bay. In 2013, the residual in the northern coast is eastward and the jet on the southern coast is even stronger than in 2012. In 2014, the residual in the northern gulf is weak, only a few centimetres per second, but the jet on the southern coast exists still.

The annual mean circulation from the fine resolution 0.25 NM setup showed similar results to the 2 NM setup, as shown in Fig. 3. However, as this setup also resolves the submesoscale, the overall picture is much more detailed. While the circulation direction is similar to that in the coarser NEMO setup, the 0.25 NM NEMO setup generally simulated higher mean current speeds. Contrary to the 2 NM NEMO setup, there was no clear outflow on the northern coast in 2012, albeit the general flow direction was the same. In 2013 and 2014, the residual circulation patterns were mostly similar to those in the coarser run.

The mean circulation for the whole period 2012—2014 shows four circulation loops in the gulf (Fig. 4). The centre of the first loop is located at approximately 23.5°E (loop A, in the nomenclature of Lagemaa, 2012). As this loop is very close to our 0.25 NM setup domain boundary, we only capture it fully in the coarser model. The second loop (B) is roughly at 25°E. The third loop (C), at 27°E, includes the coastal current west of Narva Bay. The fourth loop (D), at 28.5°E, is located in the Neva estuary.

The wind measurements at the Kalbådagrund weather station were used, along with corresponding HIRLAM model data, to evaluate whether the differences in the annual mean circulation patterns could be linked to differences in the wind conditions in 2012—2014. All the years have a dominating wind component from the south-southwest (Fig. 5). There are, however some differences in the frequency and magnitude of the easterly winds between the years. In 2012, the

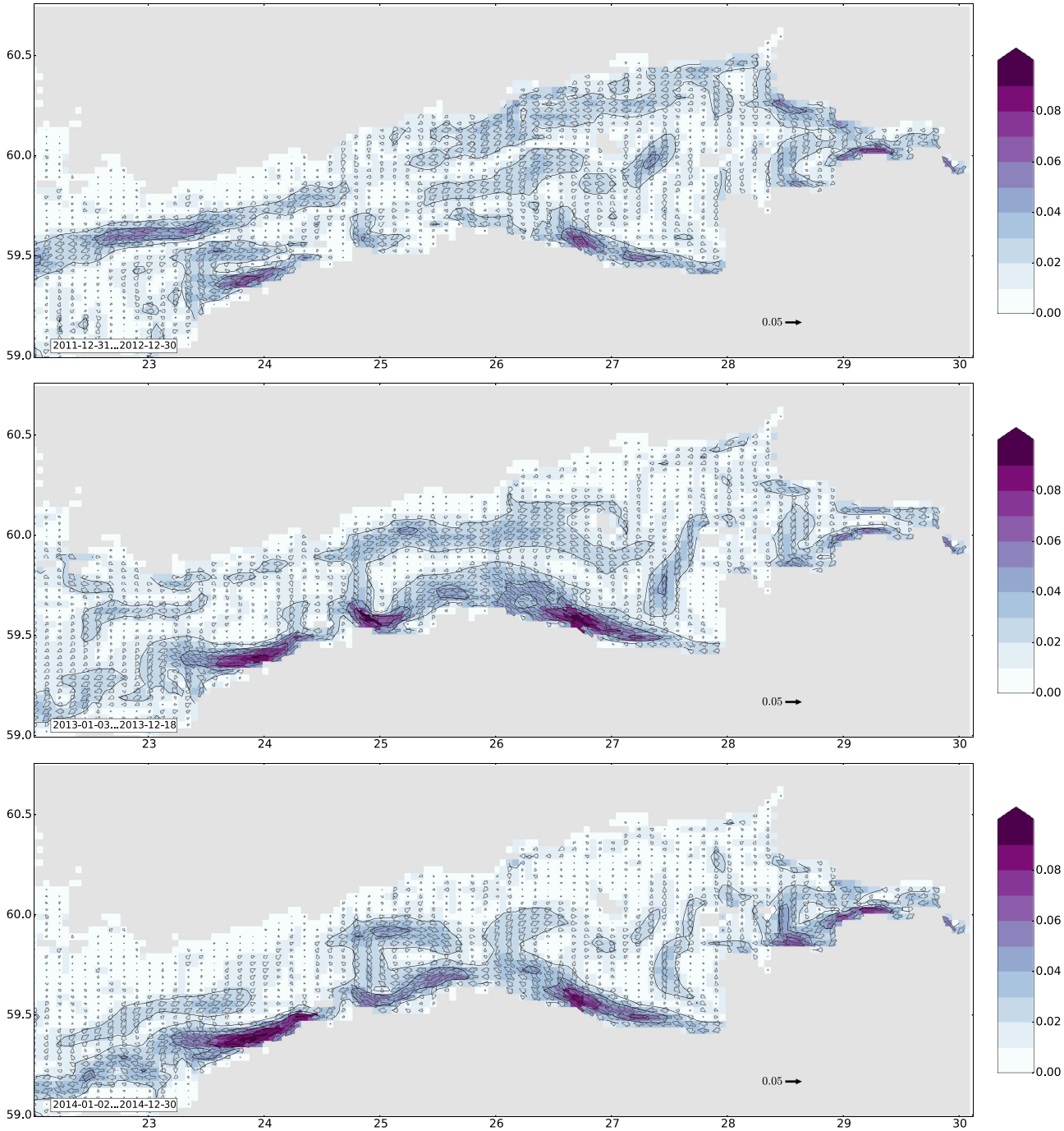

Figure 2 Annual mean circulation in the 2 NM setup averaged from 0 m to 7.5 m depth for the years 2012 (top), 2013 (middle) and 2014 (bottom). Velocities are in m s^{-1}. Vector arrows are drawn for every other grid point in the longitudinal direction and for every grid point in the latitudinal direction.

quantity of easterly winds is smallest and in 2014 it is largest. In 2013, there is also a significant component of high wind speeds from the west, contrary to the other years. We also compared the forcing wind field to the measured values at Kalbådagrund and found that HIRLAM forecast the wind speed and direction fairly well. In 2012, there were relatively few differences, although the forcing data shows weaker south-eastern winds than the measurements. In 2013, the forcing data has a stronger component of northerly winds than the measurements. In 2014, easterly winds are not as well represented in the forcing data.

3.2. Benchmarking the circulation field

As validation of the whole circulation field is difficult and spatial coverage of measurements is sparse, we instead

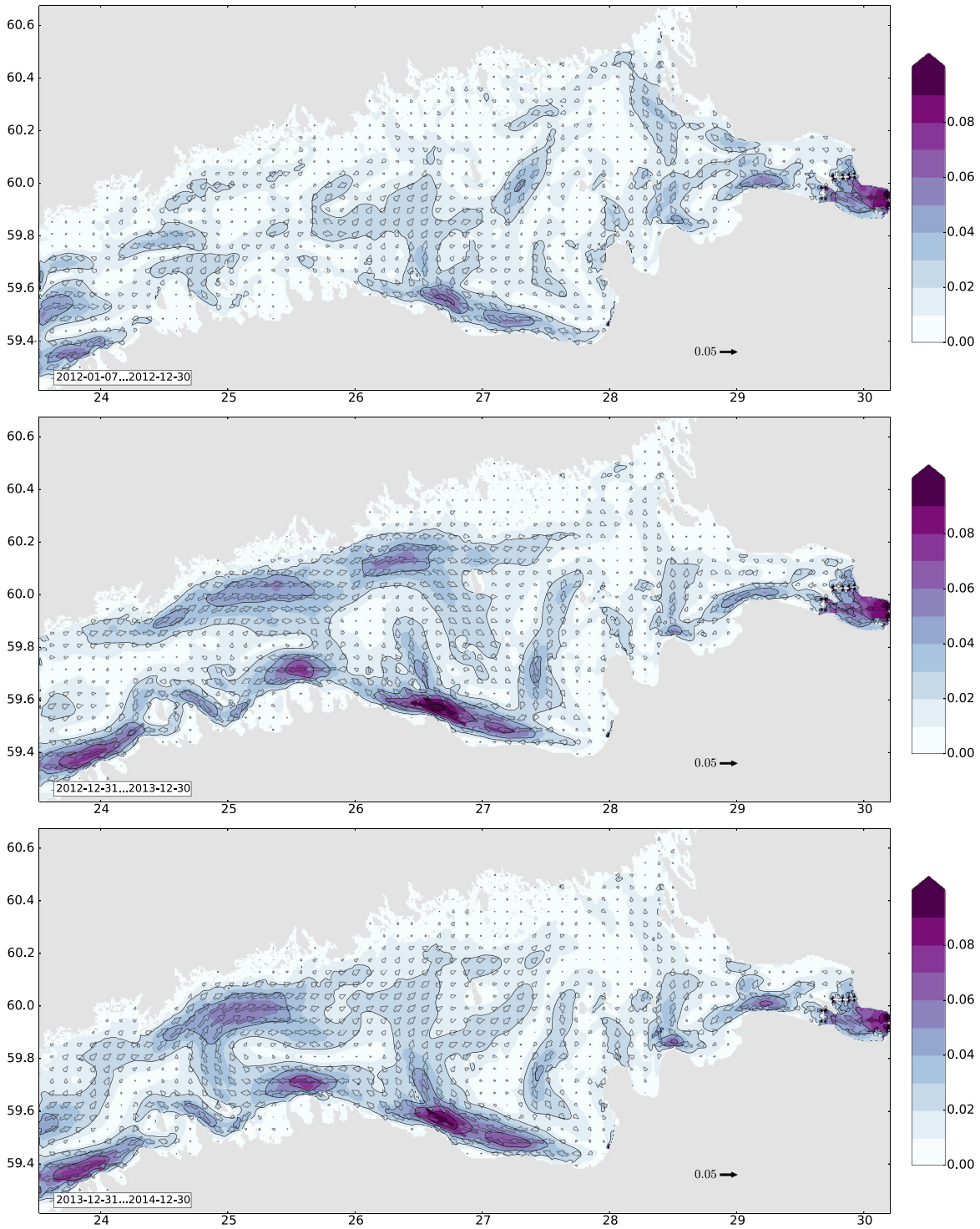

Figure 3 Annual mean circulation in the 0.25 NM setup averaged from 0 m to 7.5 m depth for the years 2012 (top), 2013 (middle) and 2014 (bottom). Velocities are in m s^{-1}. Vector arrows are drawn for every 13th grid point in the longitudinal direction and in every 11th grid point in the latitudinal direction.

benchmark the two NEMO setups against the HIROMB-based CMEMS product. We consider this model indicative of the general performance of hydrodynamic models in the area (cf. Myrberg et al., 2010). In the HIROMB results, the outflow in the northern gulf is clearly visible in 2012, almost non-existent in 2013 and reversed in 2014 (Fig. 6). The direction of flow is more uniform and the field is smoother than in NEMO. Furthermore, HIROMB does not show a clear coastal current on the southern coast in 2012. The years before 2012 had a similar mean circulation pattern as the

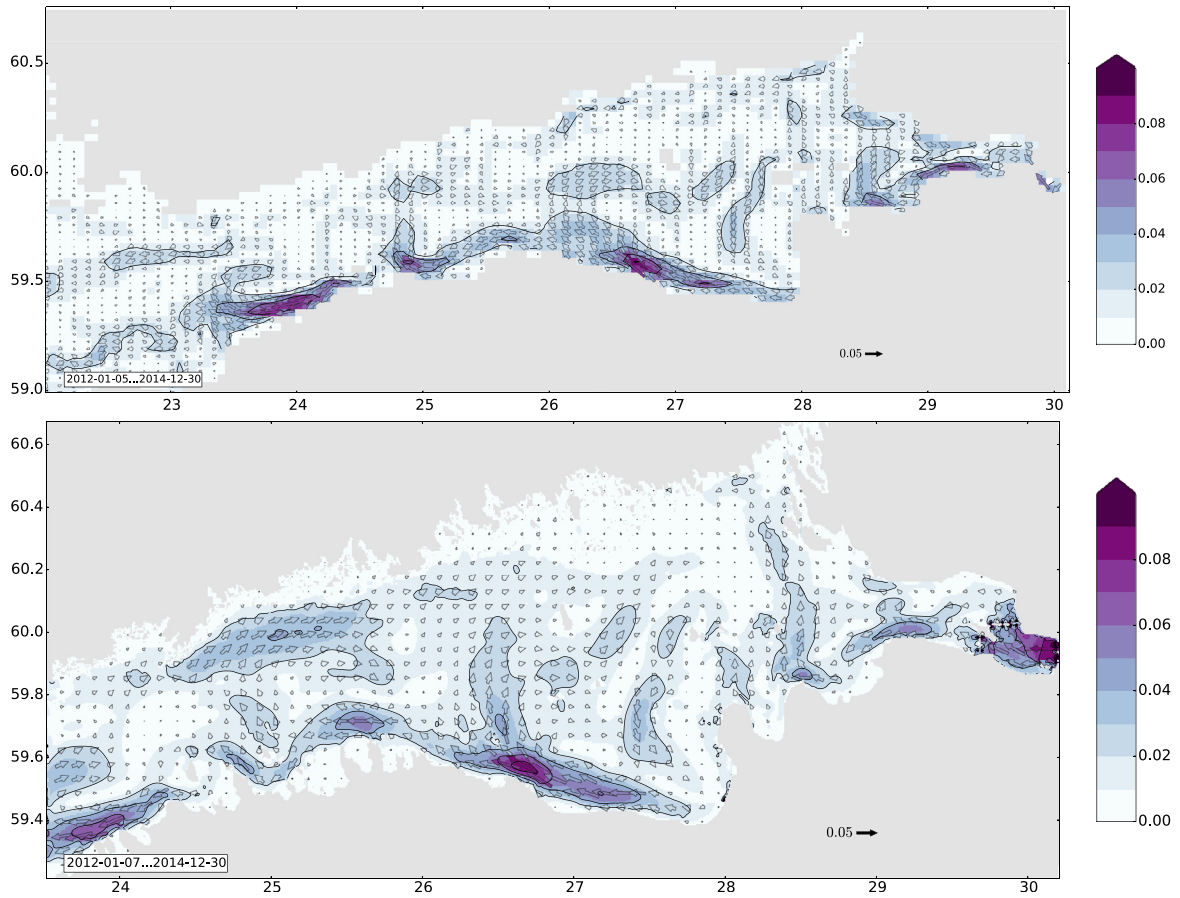

Figure 4 Mean circulation for 2012—2014 averaged from 0 m to 7.5 m depth in the 2 NM (top) and the 0.25 NM (bottom) setup. Velocities are in m s^{-1}. For the upper figure, vector arrows are drawn for every other grid point in the longitudinal direction and for every grid point in the latitudinal direction. For the lower figure, vector arrows are drawn for every 13th grid point in the longitudinal direction and in every 11th grid point in the latitudinal direction.

year 2012 (not shown here). In the 2013 results there is a marked difference: in NEMO the residual current in the Finnish coast is mainly to the east, while in HIROMB it is to the west. In other areas the speeds in NEMO are stronger but the directions are similar to those of HIROMB. The reversal of the outflow in 2014 from that of 2012 is more or less similar in the coarser NEMO model and in HIROMB. All the models show a clear alongshore current on the southern coast in 2014 too.

3.3. Salinity validation

We compared the model salinity with observations, as the mean salinity field can be used as a proxy for the mean circulation field. In these comparisons we used the CTD survey data from 2013 to 2014. Model data has been averaged over the span of the cruises (cf. Section 2.2.1). North—south salinity cross-sections show that the 0.25 NM NEMO model is able to describe the vertical structure of the water column rather well (Fig. 7). In the near-surface layers, however, the freshest water is somewhat incorrectly placed in each case in both NEMO and HIROMB. In 2013, the surface layer in NEMO was less saline than in the observations. In 2014, the observations show less saline water on the northern coast. The model shows the opposite.

3.4. Attributing the features of the mean circulation field with physical phenomena

3.4.1. River runoff

As the Gulf of Finland is in many ways like a large estuary, the density gradients are significant for the mean currents in the gulf. Therefore, correctly prescribing river runoff forcing is even more important than in the other sub-basins of the Baltic Sea. Runoff data with high enough temporal resolution is still inaccessible or sometimes non-existent for many rivers. Therefore it is common to use data from hydrological models, such as E-HYPE (Donnelly et al., 2016) or climatological runoff data (e.g. Bergström and Carlsson, 1994).

The datasets gathered during the GoF2014 include monthly mean runoffs from the Neva, Narva and Luga rivers from recent years. This allowed us to compare them to respective values from E-HYPE. The comparison showed that the modelled runoffs often differ significantly from the observed ones. For example, for the GoF2014 study period

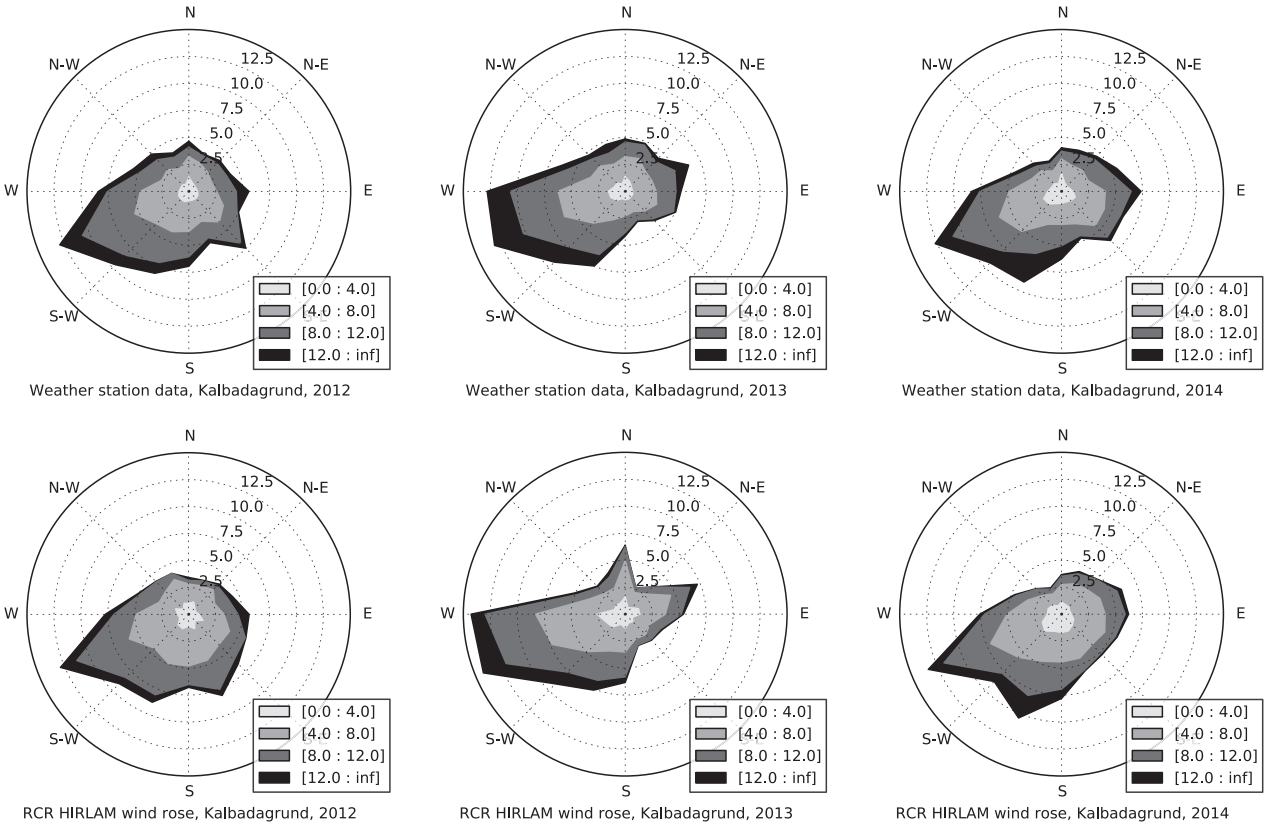

Figure 5 Annual wind roses at Kalbådagrund meteorological station in 2012, 2013 and 2014. Top: observation; bottom: HIRLAM model 10 m winds. Wind speeds are in m s^{-1}, frequencies are in percent.

1996–2014, the mean observed runoff from the Neva was 2345 m^3 s^{-1} (about 73 km^3 a^{-1}, which is in one year almost 7% of the volume of GoF: 1090 km^3). The mean runoff from E-HYPE was 1881 m^3 s^{-1}, which means almost a 28% difference from the observed value. More detailed information about GoF2014 and the dataset can be found in Raateoja and Setälä (2016).

To investigate how incorrectly estimated river runoffs could affect the modelled circulation patterns, we performed two simulations with the 0.25 NM NEMO setup using modified runoff forcing, namely (1) no runoff from the four major rivers into the gulf and (2) doubled runoff from the four major rivers into the gulf. Although, this approach is somewhat artificial, it shows how sensitive the modelled near-surface current fields are to river runoff forcing. The changes in the river runoff mainly affected the magnitude of the near-surface currents, as shown in Fig. 8. There were hardly any changes in the direction of the mean currents. When the runoffs are doubled, the Neva river plume became very easily identifiable. Compared to the reference run (Fig. 4), the highest mean current speeds increased by roughly half.

3.4.2. High flow speed events

The averaging of variable currents over time periods of years can hide different kinds of physical situations. Rare high energy events can show up and even dominate averages in certain areas. A relatively small number of days with high current speeds can contribute to the mean circulation field in a significant way. We demonstrate this using the coastal flow near the northern coast of the gulf as an example.

To quantify the contribution of days with high current speeds, we divided the model dataset into two parts based on the modelled current speed at a point near the Finnish coast. This point is indicated in Fig. 1 as site H. It was chosen because it is in an area where strong coastal currents were seen in the NEMO results (Fig. 4).

We found that strong current episodes contributed significantly to the formation of the jet in the residual pattern of currents on the Finnish coast (Fig. 9). Even though days with high current speeds are only 18% of all days in 2012–2014 (when the criterion for high current speed is 10 cm s^{-1} daily mean speed), they still are a major contribution to the overall mean circulation field. If we removed the days with strong currents from the analysis, the magnitude of the eastward current in the Finnish coast was smaller, but the direction was still towards the east. For example, mean current speed was approximately 3.3 cm s^{-1} at site H in 2012–2014. If we include only days with strong currents in the calculation, the magnitude of the current was 1.3 cm s^{-1}, which is around 41% of the total. The direction of the current in both cases was nearly the same. On the southern coast, a similar analysis revealed the same, with high current speed days contributing significantly to the coastal current visible in the annual mean circulation field (not shown).

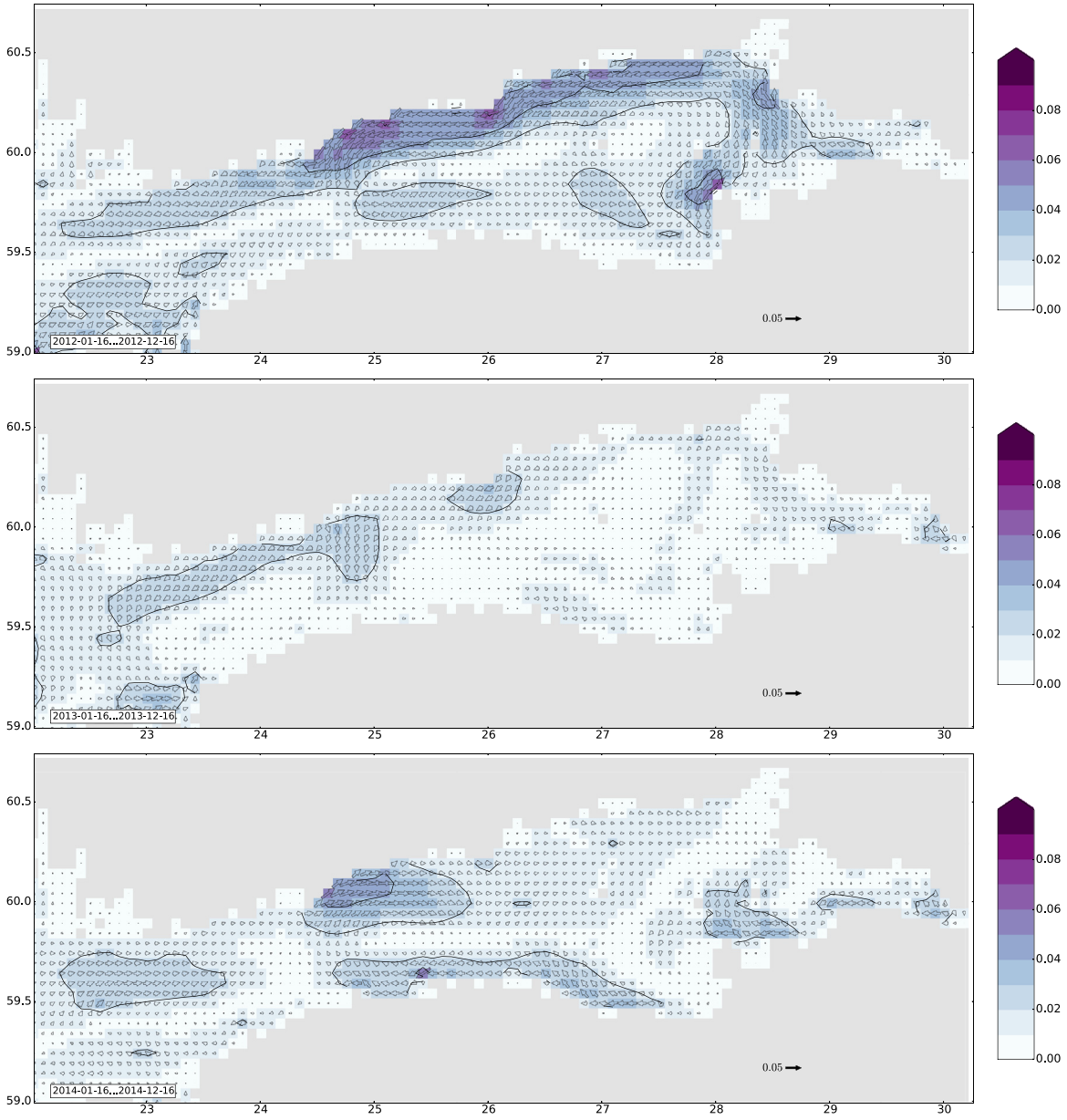

Figure 6 Annual mean circulation in the CMEMS product averaged from 0 m to 7.5 m depth for the years 2012 (top), 2013 (middle) and 2014 (bottom). Velocities are in m s^{-1}. Vector arrows are drawn for every grid point.

3.4.3. Upwelling-related jets

To further understand what sort of events contribute to the strong coastal currents in the annual mean current fields in different years, we investigated how these high-speed events relate to coastal upwelling. We selected an area in the south-eastern GoF, west of Narva Bay, for closer inspection. In this area the annual mean current fields of the 0.25 NM NEMO run showed high-speed westward currents, especially in the years 2013 and 2014 (Fig. 3). We chose the nearshore station 15 (location shown in Fig. 1) from which there were several temperature measurements available during 2012–2014. On a number of occasions, the modelled temperature decreased rapidly within a short time period during the summer stratified season, indicating a possible upwelling event (Fig. 10, upper panel). Many of the temperature drops, including the two events with the highest current speed at this station, can be associated with high-speed alongshore currents, visible in the modelled current speeds at the nearby station 15 (Fig. 10, lower panel). Similar analysis for two stations near the northern coast gave concurring results (not shown).

The model reproduced the seasonal temperature cycle in the surface layer fairly well (Fig. 10). During two of the possible upwelling events, the measured temperature also shows lower values. However, the temporal resolution of the measurements is not sufficient enough to differentiate between upwelling and cooling of surface water due to other processes.

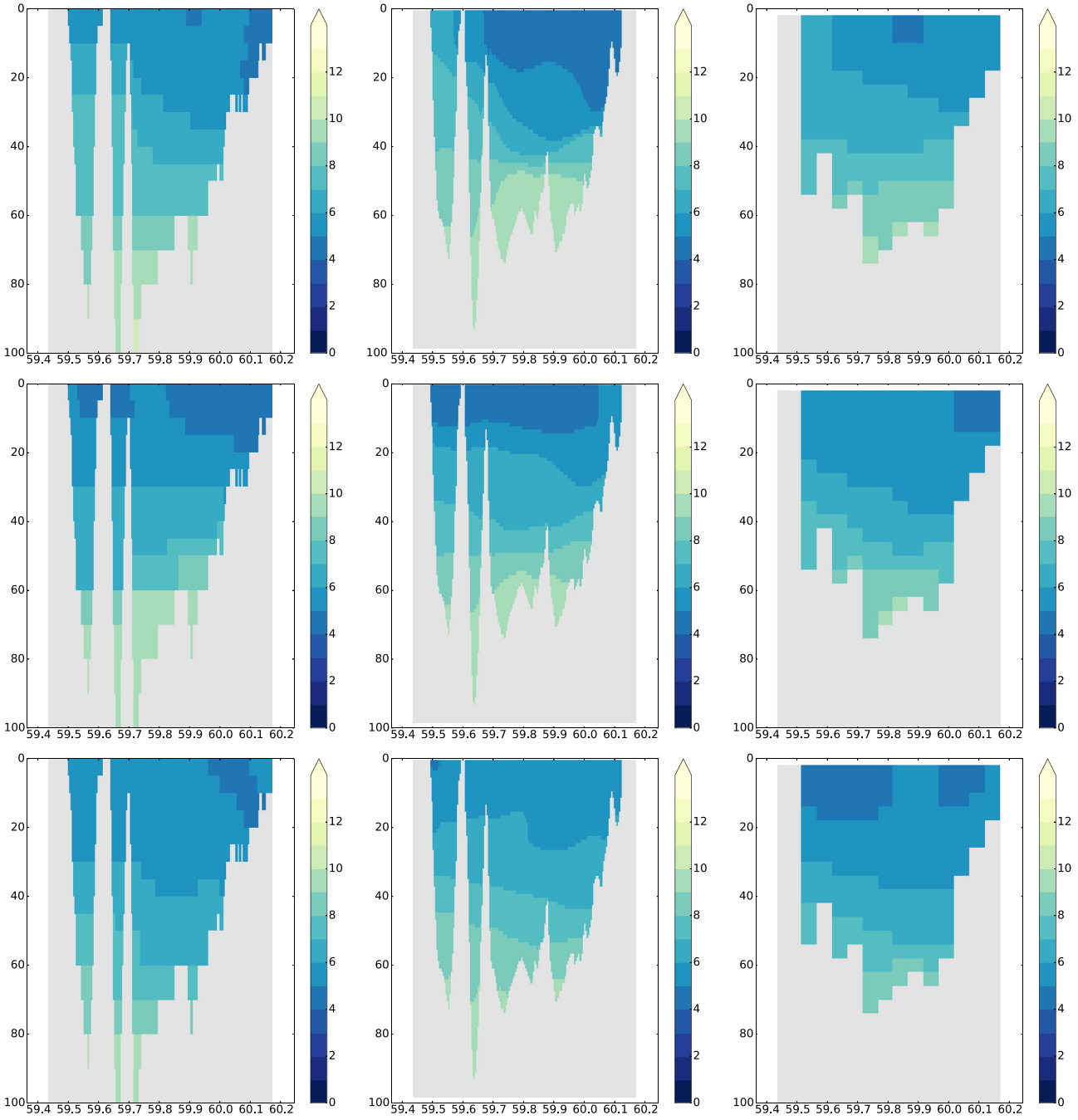

Figure 7 A south–north salinity cross-section at 25°E from gridded observations (left) and the 0.25 NM NEMO model averaged over the time span of the cruise (middle). For reference, the monthly mean from the 3 NM HIROMB-based CMEMS product is also provided (right). The June 2013 cruise (top), the June 2014 cruise (middle) and the September 2014 cruise (bottom) are shown. The south coast is on the left-hand side.

For a rough quantitative estimate of the effect that these possible upwelling events have on the annual mean current speed in this area, we focused on one specific event at station 15 in September 2013. Like in the previous section, we take the average speed of 10 cm s^{-1} as the lower limit of a high current speed day, since during these possible upwelling events the current speed peaks are clearly higher than 10 cm s^{-1} and in most of the other higher current speed events the peaks are around or smaller than 10 cm s^{-1}. This event had 15 high-speed days (from 11 to 25 Sep 2013) with a mean velocity of 18 cm s^{-1}. Averaged over the year, if we assume that the flow direction stays the same during this event, this single event contributes approximately 0.7 cm s^{-1} to the yearly mean. As the yearly mean velocity for this station was 6 cm s^{-1} in 2013, it means that this single event contributed over 10% of that figure. As there were five events in

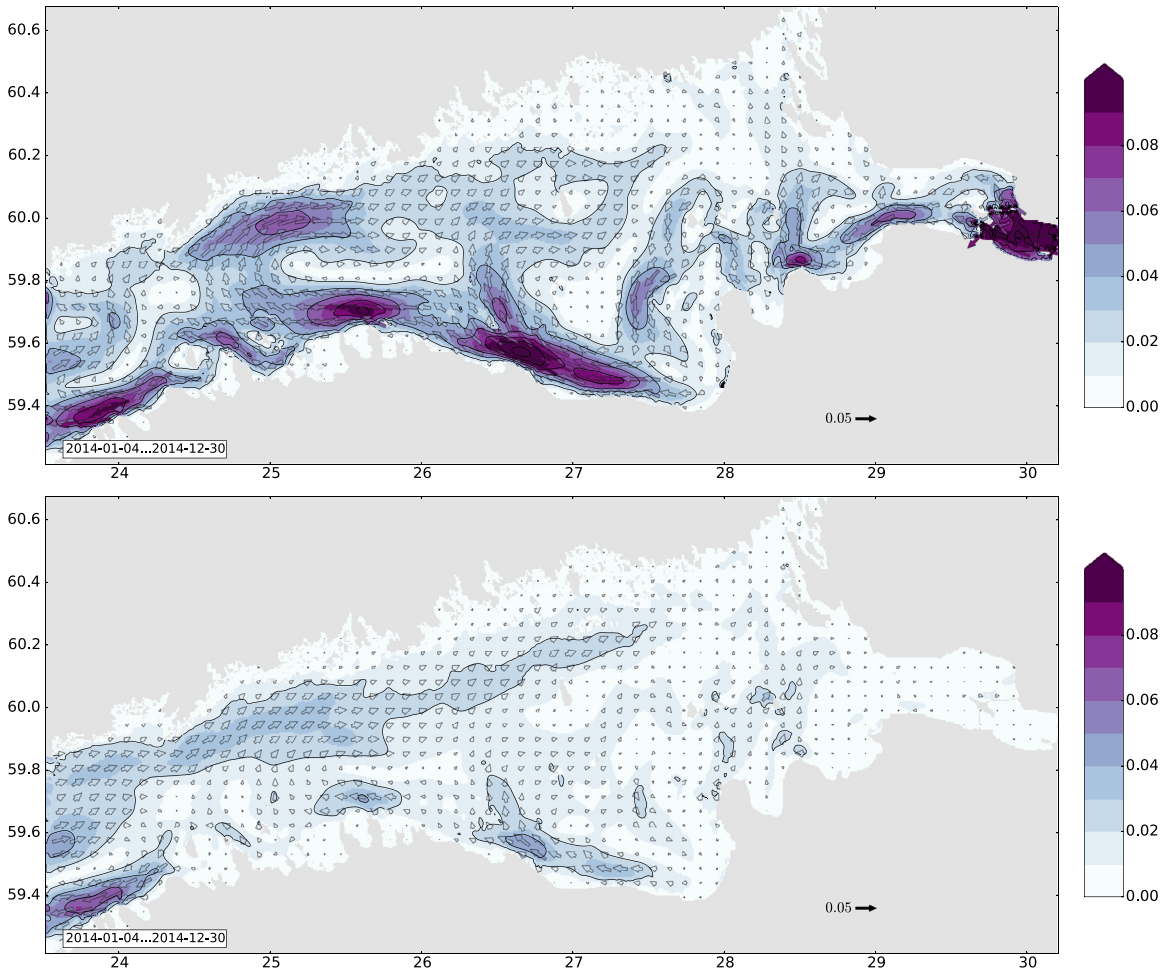

Figure 8 Mean circulation in 2014 averaged from 0 m to 7.5 m depth in two runs of the NEMO 0.25 NM setup. The top figure shows the run with double volume runoffs, the bottom run is the one without river runoff. Velocities are in m s^{-1}. Vector arrows are drawn for every 13th grid point in the longitudinal direction and in every 11th grid point in the latitudinal direction.

2013 where the current speed exceeded this threshold of 10 cm s^{-1}, these high-speed events were reflected in a significant way in the annual mean current field at this point.

The modelled surface temperature field shows that this event displays the characteristics of an upwelling event along the southern coast of the Gulf of Finland (Fig. 11). The modelled mean surface salinity field from the same day confirmed that this cooler water originated from deeper layers with more saline water. The salinity field also shows how the freshwater plume from the Neva estuary is directed towards the south-west, towards the southern coast. The extent of this event in September 2013 suggests that coastal jets might emerge further west on the southern coast, thus contributing highly to the annual mean values, as in the case of station 15.

4. Discussion

The horizontal resolution of the 3D hydrodynamic model, as well as that of the meteorological forcing, have a large effect on the modelled surface and near-surface current fields. Andrejev et al. (2010) have shown that the trajectories of Lagrangian tracers in the Gulf of Finland are much affected by the horizontal resolution of the circulation model. Of the two NEMO setups we used, the fine resolution setup (0.25 NM) has sufficient scale to solve the Rossby radius of deformation in the gulf. Compared to the 2 NM NEMO setup or the HIROMB model, the 0.25 NM setup gave more detailed mean circulation fields, as expected, but also produced somewhat different circulation in the middle part of the GoF than the coarse resolution setups. Unfortunately, the good quality datasets that are presently available are not sufficient to validate the accuracy of the simulated circulation patterns in detail.

Meteorological forcing is one of the key factors in the ability of a 3D hydrodynamic model to simulate the surface and near-surface current fields. In relatively small basins these currents are mainly driven by wind stress. In the GoF, long-term runs tend to produce a cyclonic mean surface circulation pattern as a result of the prevailing south-westerly winds, density-driven circulation, Coriolis force and topographic steering. But, the variable wind conditions have a large effect on the annual circulation patterns, as can be seen from the previous studies of Andrejev et al. (2004), Maljutenko et al. (2010), Elken et al. (2011), Soomere et al. (2011), and Lagemaa (2012).

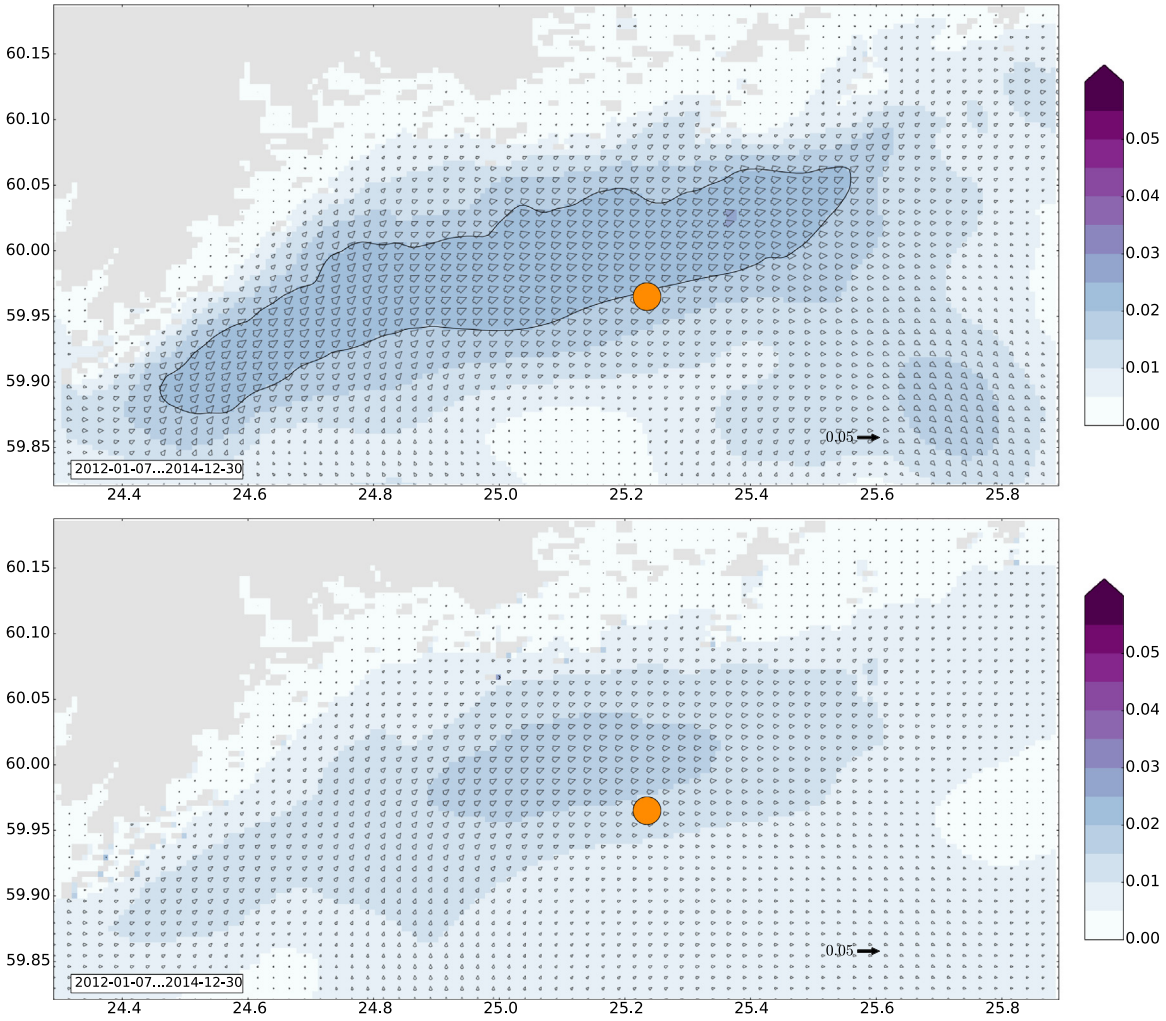

Figure 9 Mean circulation 2012–2014 off Helsinki, split into the contribution of low and high current speed days. The modelled circulation field from the 0.25 NM NEMO setup has been averaged from 0 m to 7.5 m depth. The upper panel shows the contribution of days with low modelled current speed at a chosen location (site H, indicated with an orange circle, cf. Fig. 1). The lower panel shows the contribution of days with the high current speed at the same site. The mean circulation field is the vector sum of the two figures. The limit for high-speed days was 0.1 m s^{-1}, which means that the upper figure has approximately 82% of days and the lower figure 18%. Velocities are in m s^{-1}. Vector arrows are drawn for every third grid point in the longitudinal direction and in every second grid point in the latitudinal direction. Note the colour scale, which is different from the other figures. (For interpretation of the references to color in this figure legend, the reader is referred to the web version of the article.)

The wind roses from Kalbådagrund station show some variability in the directionality of the wind field over the years. Especially the proportion and magnitude of easterly winds varied. This could have a large effect on the frequency and location of the upwelling events in the gulf and influence the annual mean surface and near-surface current fields significantly. For instance, in 2013 and 2014, when the easterly winds were stronger compared to those of 2012, there were much higher current speeds on the southern coast of the GoF which we associated with coastal currents.

The meteorological forcing used in this study had a resolution of c. 7.5 km, except for the two first months of 2012 when it was coarser. This resolution is high enough to produce a wind field and other meteorological parameters in the GoF with sufficient accuracy for marine modelling. The peak of the high-wind situations is predicted more accurately than in some of the earlier modelling studies that have utilised the SMHI (Swedish Meteorological and Hydrological Institute) gridded meteorological dataset with one-degree resolution (Andrejev et al., 2004; Tuomi et al., 2012). However, a comparison of the wind roses at Kalbådagrund showed that HIRLAM was not able to describe the directional properties of the wind field in full detail. Furthermore, HIRLAM slightly underestimates higher wind speeds (of over 12 m s^{-1}). This affects the ability of NEMO to simulate the intensity of the upwelling events and the resulting coastal jets.

The upwelling-related alongshore coastal jets west of Narva Bay have been earlier presented by Suursaar and Aps (2007), who analysed RDCP (Recording Doppler Current Profiler) measurements from summer 2006 west of Narva Bay during an upwelling event. Also, Suhhova et al. (2015) have

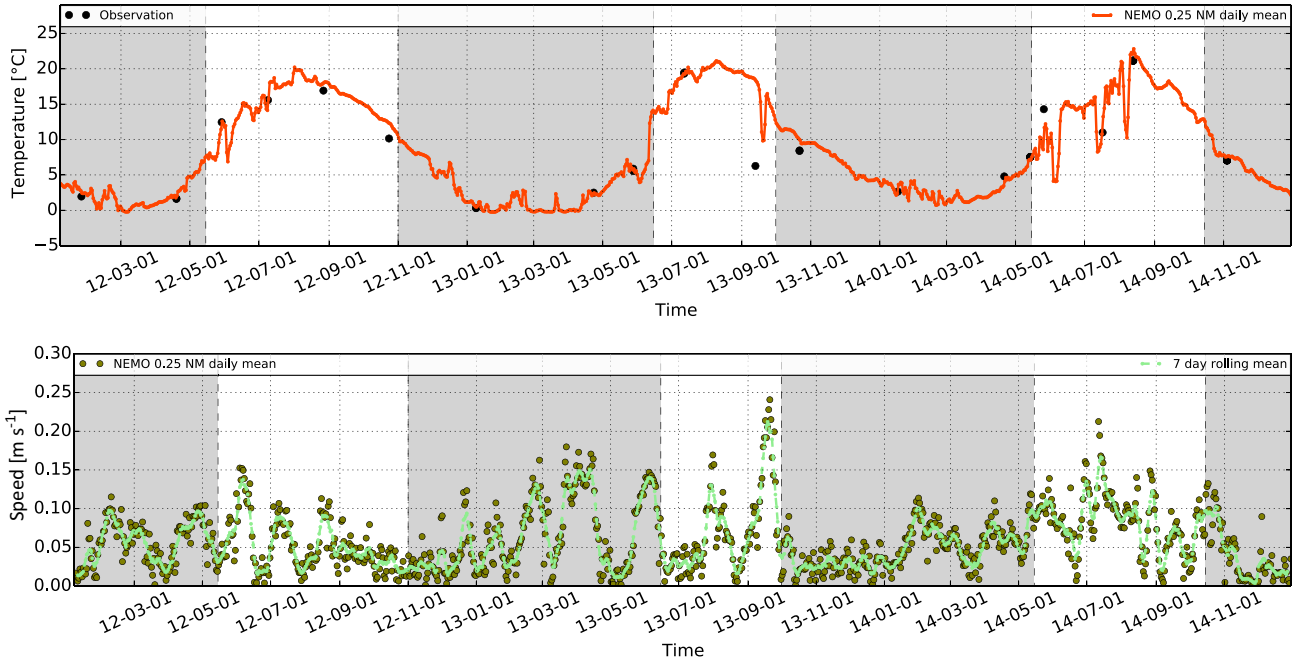

Figure 10 Top: a time series of water temperature at 5 m depth (station G). The red line is from the 0.25 NM NEMO setup and black dots are observations. Bottom: a time series of horizontal current speed at 10 m depth (station 15). Dark green dots are from the 0.25 NM setup and light green dashed line is the seven-day moving average. A shaded background indicates the approximate time intervals when there was no seasonal thermocline in the water column. The results cover 2012—2014, the date is given in the YY-MM-DD format. (For interpretation of the references to color in this figure legend, the reader is referred to the web version of the article.)

investigated the westward surface currents off the Estonian coast near the Pakri Peninsula, based on approximately four months of ADCP (Acoustic Doppler Current Profiler) measurements made in 2009 and HIROMB simulations. They found that upwelling-related jets were mainly responsible for the westward current in this area.

The ability of the model to simulate coastal upwelling events and their extent and magnitude greatly affects how the model simulates the alongshore coastal jets. For example, Lagemaa (2012) has shown that HIROMB model generally overestimates currents in the Estonian coast compared to ADCP measurements. He discussed that incorrectly described upwelling and downwelling jets may be one of the reasons for the overestimation. Vankevich et al. (2016) have shown that a fine resolution NEMO setup, which is similar to our setup, simulates the spatial patterns of an upwelling event well. However, further investigation of the link between the scale of the upwelling events and the magnitude of the coastal jet simulated by NEMO would be beneficial.

There are also measurements that indirectly allow us to gain some understanding about the circulation field. The profiles measured during the Gulf of Finland year 2014 gave a possibility to analyse the horizontal and vertical extent of the salinity stratification in the gulf. As our results showed, there was diversity in the ability of the models to simulate this. A situation in which less saline water is found in the southern coast of the gulf suggests that circulation has been more or less anti-cyclonic around that time. Although that situation might be rare, it has been observed several times in ferrybox measurements on the Helsinki—Tallinn route (Kikas and Lips, 2016).

Several questions remain. For example, the intensity and direction of the outflow at the northern side of the gulf differs between the models and should be investigated further. In our model runs the direction and intensity of the outflow at the Finnish coast is greatly influenced by the high current speed situations. To determine if this response is correctly estimated, the results need to be verified against current measurements. The FMI has made ADCP measurements in 2009—2014 on the Finnish coast but those datasets need further processing before they can be used for analyses. Also, more observations are needed from the Narva estuary and its vicinity. Further study is also required to quantify the impact of upwelling-related jets in the longer term. It is clear that our three-year runs do not as such represent the same thing as, say, a 30-year climatological run. If such high-resolution runs were feasible at this point in time, they would surely prove informative.

Further effort and observations are also required to understand if parameterisations in hydrodynamic models that are currently used allow the frequency and intensity of these events to be modelled correctly. For example, a more detailed investigation of the sensitivity of model results to river runoff variance might help us understand how to better capture the Neva river plume correctly after it enters the gulf. Another subject area worthy of attention is current-induced substance transport and its relation to the mean circulation field. From our results, it is clear that single high-energy events can strongly affect the mean circulation. But what this means for simulations of substances leaked into the sea is an open question still.

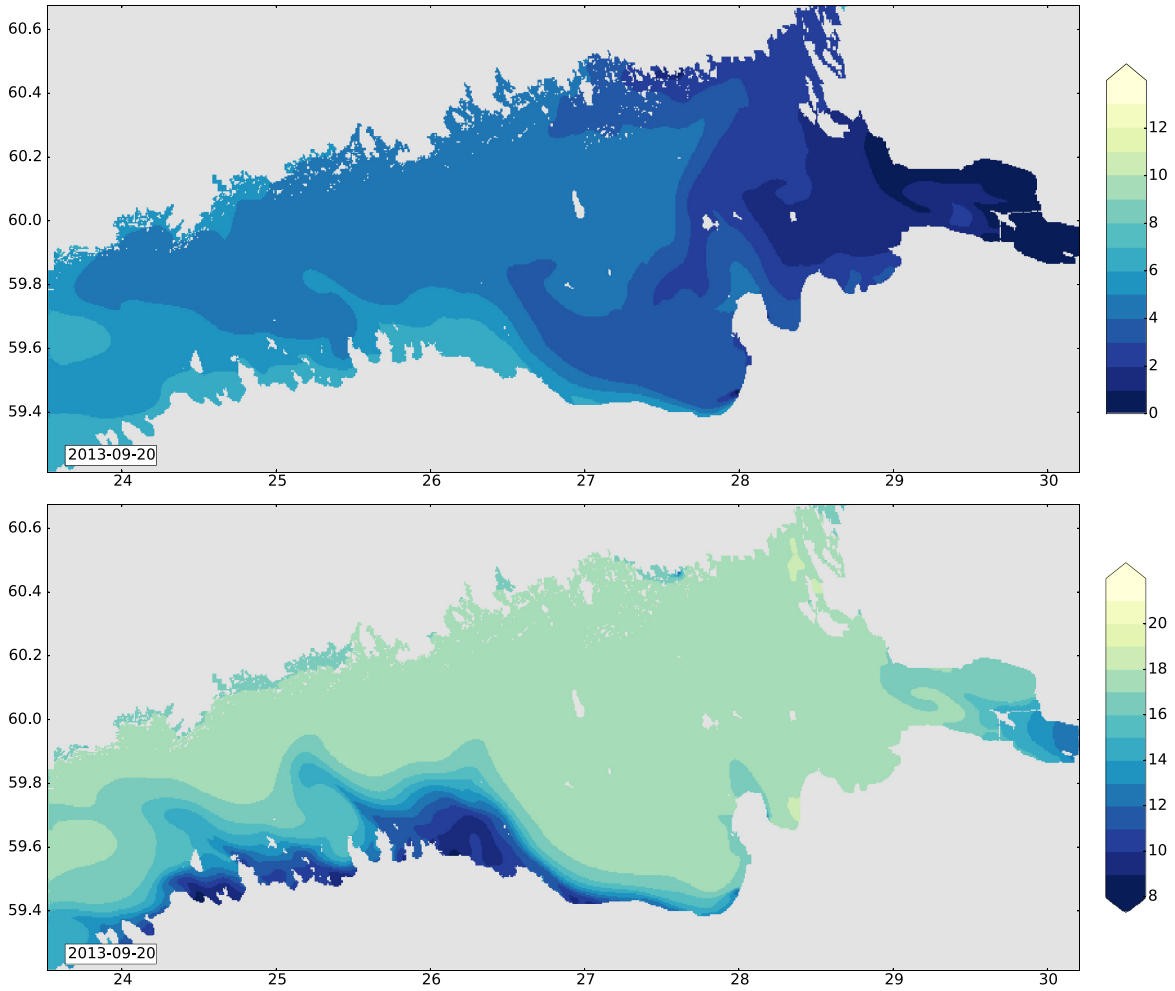

Figure 11 The surface salinity (top) and temperature (°C, bottom) fields from the 0.25 NM NEMO model run on the 20 September 2013 during an upwelling event on the southern coast of the Gulf of Finland.

5. Conclusions

In this study we analysed circulation patterns in the Gulf of Finland with two setups of the NEMO 3D hydrodynamic model.

We found that our model produces notable differences in the residual circulation patterns from year to year and from one model setup to another. Benchmarking the results to the HIROMB-based CMEMS product showed that the overall pattern was similar in both models. Comparison to salinity observations from the area revealed that vertical salinity structure was well represented. There were differences in the surface salinities, however, as is often the case for hydrodynamic models of this area. The models seem to need further development before they are able to capture the location of the surface salinity gradients in the Gulf of Finland.

We found that days with strong currents contribute significantly to the mean flow west of Narva Bay and off the Finnish coast, causing relatively strong coastal currents. We also found that most notable high-speed events were associated with upwelling.

Further, we found that the variations in runoff mainly affected the magnitude of near-surface currents. The directions of the currents seemed less sensitive to the changes. It is unlikely that runoff changes have a major effect on the year-to-year variations in the mean circulation patterns.

The experiments with the NEMO model have been beneficial to understanding the model behaviour in the area. The dynamics of the Gulf of Finland will continue to be a worthwhile topic of study as the gulf is vulnerable to accidents, and marine traffic is heavy both along and across the gulf. Also, further studies will advance the development of the high-resolution NEMO configurations for the gulf as an operational tool for everyday predictions and an aide when compiling environmental assessments of the possible changes in the gulf.

Acknowledgements

This work has been partly financed by the Maj and Tor Nessling Foundation [grant numbers 201500179, 201600161, 201700056]; the EXOSYSTEM RUSPLUS_S&T_FULL-240 project; and the Finnish Ministry of Environment. Roman Vankevich was supported by the Russian Foundation for Basic Research

[grant N 16-55-76021]. The authors would like to thank Robinson Hordoir and others at SMHI for their work on the NEMO Nordic configuration and their support for our efforts. Sami Niemelä and the FMI-HIRLAM team are acknowledged for providing the FMI-HIRLAM data and useful advice. Continued work on Baltic Sea NEMO has been possible over the years thanks to Jari Haapala and other colleagues at FMI. This study has been conducted using E.U. Copernicus Marine Service Information. The Gulf of Finland Year 2014 data providers include Estonian Marine Institute (EMI); Marine Systems Institute (MSI); Finnish Environment Institute (SYKE); Uusimaa and South-East Finland Centres for Economic Development, Transport and the Environment (UUDELY and KASELY); City of Helsinki Environment Centre (HELSINKI); and North-West Interregional Territorial Administration for Hydrometeorology and Environmental Monitoring (HYDROMET).

References

Alenius, P., Myrberg, K., Nekrasov, A., 1998. The physical oceanography of the Gulf of Finland: a review. Boreal Environ. Res. 3, 97—125.

Alenius, P., Nekrasov, A., Myrberg, K., 2003. Variability of the baroclinic Rossby radius in the Gulf of Finland. Cont. Shelf Res. 23, 563—573.

Andrejev, O., Myrberg, K., Alenius, P., Lundberg, P.A., 2004. Mean circulation and water exchange in the Gulf of Finland — a study based on three-dimensional modelling. Boreal Environ. Res. 9, 1—16.

Andrejev, O., Sokolov, A., Soomere, T., Värv, R., Viikmäe, B., 2010. The use of high-resolution bathymetry for circulation modelling in the Gulf of Finland. Est. J. Eng. 19, 187—210, http://dx.doi.org/10.3176/eng.2010.3.01.

Axell, L., 2016. Baltic Sea Physics Reanalysis from SMHI. [WWW Document], http://marine.copernicus.eu/documents/PUM/CMEMS-BAL-PUM-003-008.pdf.

Bergström, S., Carlsson, B., 1994. River run-off to the Baltic Sea: 1950—1990. Ambio 23, 280—287.

Donnelly, C., Andersson, J.C.M., Arheimer, B., 2016. Using flow signatures and catchment similarities to evaluate the E-HYPE multi-basin model across Europe. Hydrol. Sci. J. 61, 255—273.

Elken, J., Nomm, M., Lagemaa, P., 2011. Circulation patterns in the Gulf of Finland derived from the EOF analysis of model results. Boreal Environ. Res. 16, 84—102.

Ferry, N., Parent, L., Masina, S., Storto, A., Zuo, H., Balmaseda, M., 2016. Global Ocean Physics Reanalysis Glorys2V3. [WWW Document], http://marine.copernicus.eu/documents/PUM/CMEMS-GLO-PUM-001-009-011-017.pdf.

HIRLAM-B, 2015. System Documentation. [WWW Document], http://www.hirlam.org/.

Hordoir, R., An, B.W., Haapala, J., Meier, H.E.M., 2013a. A 3D Ocean Modelling Configuration for Baltic and North Sea Exchange Analysis. [WWW Document], http://www.smhi.se/polopoly_fs/1.28758!RO_48.pdf.

Hordoir, R., Dieterich, C., Basu, C., Dietze, H., Meier, H.E.M., 2013b. Freshwater outflow of the Baltic Sea and transport in the Norwegian current: a statistical correlation analysis based on a numerical experiment. Cont. Shelf Res. 64, 1—9, http://dx.doi.org/10.1016/j.csr.2013.05.006.

Hordoir, R., Axell, L., Löptien, U., Dietze, H., Kuznetsov, I., 2015. Influence of sea level rise on the dynamics of salt inflows in the Baltic Sea. J. Geophys. Res. Ocean. 120, 6653—6668, http://dx.doi.org/10.1002/2014JC010642.

Kikas, V., Lips, U., 2016. Upwelling characteristics in the Gulf of Finland (Baltic Sea) as revealed by Ferrybox measurements in 2007—2013. Ocean Sci. 12, 843—859, http://dx.doi.org/10.5194/os-12-843-2016.

Lagemaa, P., 2012. Operational Forecasting in Estonian Marine Waters. TUT Press, Tallinn, http://digi.lib.ttu.ee/i/?714.

Large, W.G., Yeager, S.G., 2004. Diurnal to decadal global forcing for ocean and sea-ice models: the data sets and flux climatologies. In: NCAR Technical Note, NCAR/TN-460+STR, CGD Division of the National Center for Atmospheric Research. , http://dx.doi.org/10.5065/D6KK98Q6 PDF 112 pp.

Lehmann, A., Myrberg, K., 2008. Upwelling in the Baltic Sea — a review. J. Mar. Syst. 74, S3—S12, http://dx.doi.org/10.1016/j.jmarsys.2008.02.010.

Leppäranta, M., Myrberg, K., 2009. Physical Oceanography of the Baltic Sea. Springer-Verlag, 378 pp.

Lips, U., Lips, I., Liblik, T., Kikas, V., Altoja, K., Buhhalko, N., Rünk, N., 2011. Vertical dynamics of summer phytoplankton in a stratified estuary (Gulf of Finland, Baltic Sea). Ocean Dyn. 61, 903—915, http://dx.doi.org/10.1007/s10236-011-0421-8.

Madec, G., the NEMO team, 2008. NEMO Ocean Engine, Institut Pierre-Simon Laplace (IPSL), France, note du Pôle de modélisation, No 27, 386 pp., https://www.nemo-ocean.eu/bibliography/documentation/.

Maljutenko, I., Laanemets, J., Raudsepp, U., 2010. Long-term high-resolution hydrodynamical model simulation in the Gulf of Finland. In: Baltic International Symposium (BALTIC), 2010 IEEE/OES US/EU. 1—7, http://dx.doi.org/10.1109/BALTIC.2010.5621641.

Myrberg, K., Soomere, T., 2013. The Gulf of Finland, its hydrography and circulation dynamics. In: Preventive Methods for Coastal Protection, Springer, 181—222.

Myrberg, K., Ryabchenko, V., Isaev, A., Vankevich, R., Andrejev, O., Bendtsen, J., Erichsen, A., Funkquist, L., Inkala, A., Neelov, I., Rasmus, K., Medina, M.R., Raudsepp, U., Passenko, J., Söderkvist, J., Sokolov, A., Kuosa, H., Anderson, T.R., Lehmann, A., Skogen, M.D., 2010. Validation of three-dimensional hydrodynamic models of the Gulf of Finland. Boreal Environ. Res. 15, 453—479.

Palmén, E., 1930. Untersuchungen über die Strömungen in den Finnland umgebenden Meeren. Soc. Scient. Fenn., Comm. Phys.-Math. 12, 1—94, (in German).

Raateoja, M., Setälä, O. (Eds.), 2016. The Gulf of Finland Assessment. Rep. Finnish Environ. Insti., Helsinki PDF 368 pp., http://hdl.handle.net/10138/166296.

Soomere, T., Myrberg, K., Leppäranta, M., Nekrasov, A., 2008. The progress in knowledge of physical oceanography of the Gulf of Finland: a review for 1997—2007. Oceanologia 50 (3), 287—362.

Soomere, T., Leppäranta, M., Myrberg, K., 2009. Highlights of the physical oceanography of the Gulf of Finland reflecting potential climate changes. Boreal Environ. Res. 14, 152—165.

Soomere, T., Delpeche, N., Viikmäe, B., Quak, E., Meier, H.E.M., Doos, K., 2011. Patterns of current-induced transport in the surface layer of the Gulf of Finland. Boreal Environ. Res. 16, 49—63.

Stålnacke, P., Grimvall, A., Sundblad, K., Tonderski, A., 1999. Estimation of riverine loads of nitrogen and phosphorus to the Baltic Sea, 1970—1993. Environ. Monit. Assess. 58, 173—200.

Stipa, T., 2004. Baroclinic adjustment in the Finnish Coastal Current. Tellus A 56, 79—87.

Suhhova, I., Pavelson, J., Lagemaa, P., 2015. Variability of currents over the southern slope of the Gulf of Finland. Oceanologia 57 (2), 132—143, http://dx.doi.org/10.1016/j.oceano.2015.01.001.

Suursaar, Ü., Aps, R., 2007. Spatio-temporal variations in hydrophysical and-chemical parameters during a major upwelling event off the southern coast of the Gulf of Finland in summer 2006. Oceanologia 49 (2), 209—228.

Troupin, C., Barth, A., Sirjacobs, D., Ouberdous, M., Brankart, J.-M., Brasseur, P., Rixen, M., Alvera-Azcárate, A., Belounis, M., Capet, A., Lenartz, F., Toussaint, M.-E., Beckers, J.-M., 2012. Generation

of analysis and consistent error fields using the Data Interpolating Variational Analysis (Diva). Ocean Model. 52—53, 90—101, http://dx.doi.org/10.1016/j.ocemod.2012.05.002.

Tuomi, L., Myrberg, K., Lehmann, A., 2012. The performance of the parameterisations of vertical turbulence in the 3D modelling of hydrodynamics in the Baltic Sea. Cont. Shelf Res. 50, 64—79.

Vancoppenolle, M., Fichefet, T., Goosse, H., Bouillon, S., Madec, G., Maqueda, M.A.M., 2009. Simulating the mass balance and salinity of Arctic and Antarctic sea ice. 1. Model description and validation. Ocean Model. 27, 33—53.

Vankevich, R.E., Sofina, E.V., Eremina, T.E., Ryabchenko, V.A., Molchanov, M.S., Isaev, A.V., 2016. Effects of lateral processes on the seasonal water stratification of the Gulf of Finland: 3-D NEMO-based model study. Ocean Sci. 12, 987—1001, http://dx.doi.org/10.5194/os-12-987-2016.

Westerlund, A., Tuomi, L., 2016. Vertical temperature dynamics in the Northern Baltic Sea based on 3D modelling and data from shallow-water Argo floats. J. Mar. Syst. 158, 34—44, http://dx.doi.org/10.1016/j.jmarsys.2016.01.006.

Witting, R., 1912. Zusammenfassende Uebersicht der Hydrographie des Bottnischen und Finnischen Meerbusens und der Nördlichen Ostsee nach den Untersuchungen bis Ende 1910. Soc. Sci. Fenn. Finländische Hydr.-Biol. Untersuchungen, No. 7.

Zhurbas, V., Laanemets, J., Vahtera, E., 2008. Modeling of the mesoscale structure of coupled upwelling/downwelling events and the related input of nutrients to the upper mixed layer in the Gulf of Finland, Baltic Sea. J. Geophys. Res. Ocean. 113 (C5), C05004, http://dx.doi.org/10.1029/2007JC004280.

Oceanologia (2018) 60, 32—51

Available online at www.sciencedirect.com

ScienceDirect

journal homepage: www.journals.elsevier.com/oceanologia/

ORIGINAL RESEARCH ARTICLE

Modeling the ecosystem response to summer coastal upwelling in the northern South China Sea

Rui Jiang [a,b], **You-Shao Wang** [a,c,*]

[a] *State Key Laboratory of Tropical Oceanography, South China Sea Institute of Oceanology, Chinese Academy of Sciences, Guangzhou, China*
[b] *University of Chinese Academy of Sciences, Beijing, China*
[c] *Daya Bay Marine Biology Research Station, Chinese Academy of Sciences, Shenzhen, China*

Received 19 October 2016; accepted 19 May 2017
Available online 15 June 2017

KEYWORDS
The northern South China Sea;
NPZD ecosystem model;
Summer coastal upwelling;
Coastal ecosystem

Summary A coupled three-dimensional physical model and a nitrogen-based nutrient, phytoplankton, zooplankton, and detritus (NPZD) ecosystem model were applied to simulate the summer coastal upwelling system over the continental shelf of northern South China Sea (NSCS) and its impact on hydrographic conditions and ecosystem. The simulated results were comprehensively validated against field and satellite measurements. The model results show that the near shore ecosystem of NSCS has significant responses to the summer coastal upwelling system. The Shantou Coast to the Nanri Islands of Fujian province (YD) and the east of the Leizhou Peninsula (QD) are two main regions affected by NSCS summer coast upwelling. During summer, these two coastal areas are characterized by nearshore cold and high salinity upwelling current. Further, the summer coastal upwelling serves as a perfect nutrient pump, which lifts up and advects nutrient-rich current from deep to surface, from inner shelf to about 30 km outer shelf. This nutrient source reaches its maximum in the middle of July and then begins to decrease. However, the maximum phytoplankton and chlorophyll *a* do not coincide with the maximum nutrients and delay for about 10 days. Because of the intensive seasonal thermocline and the complicated current transporting through Qiongzhou strait, the ecological responding of QD is less pronounced than YD. This study has a better understanding of the physically modulated ecological responses to the NSCS summer coastal upwelling system.

* Corresponding author at: State Key Laboratory of Tropical Oceanography, South China Sea Institute of Oceanology, Chinese Academy of Sciences, Guangzhou 510301, China. Tel.: +86 20 8902 3102; fax: +86 20 8902 3102.
E-mail address: yswang@scsio.ac.cn (Y.-S. Wang).
Peer review under the responsibility of Institute of Oceanology of the Polish Academy of Sciences.

Production and hosting by Elsevier

http://dx.doi.org/10.1016/j.oceano.2017.05.004

1. Introduction

Coastal upwelling is one of the most prominent marine physical processes involving biogeochemical cycles, primary productivity, and fisheries (Prego et al., 2007). Coastal upwelling system is commonly produced by the interaction between favorable winds and the topography (Woodson et al., 2007) and is characterized by bringing cold and nutrient-rich deep water toward the surface while influencing the transport of suspended matters (Freon et al., 2009). Because of its important role in the marine ecosystem, coastal upwelling has been studied worldwide (González-Gil et al., 2015; Ruzicka et al., 2016).

The South China Sea (SCS) is located in the southeast of Asia with an average depth of about 1350 m. It is the largest marginal sea in the world, which stretches 3.5×10^6 km^2 from 23°57′N in the north to the 3°00′N in the south and from 99°10′E in the west to the 122°10′E in the east (Chen et al., 2006). The SCS also supports the most frequent human activity (Li et al., 2014). Our study area — northern South China Sea (NSCS) (Fig. 1) is affected by both natural environment and human activities year-round. In the northern shelf of the NSCS, there are many rivers which input fresh water into it (such as the Pearl River), while the south of the NSCS joins to the SCS. The occurrence of summer coastal upwelling is a regular phenomenon during June to September in the NSCS, and there are two main coastal upwelling regions: Shantou Coast to the Nanri Islands of Fujian province (YD), and the east of the Leizhou Peninsula (QD) (Jing et al., 2008). All of these days, temperature, salinity, dissolved oxygen (DO) and chlorophyll *a* have been regarded as four main indicators for NSCS summer coastal upwelling (Wang, 2013). In order to explore the corresponding environmental changes, a lot of research techniques have been used, such as remote sensing, multivariate statistical analysis, and indicator (silicate) method (Ehlert et al., 2013). However, the influence of the coastal upwelling system on the NSCS ecosystem is still not well understood because of the complex topography, currents and the dynamic climatology (Morton and Blackmore, 2000).

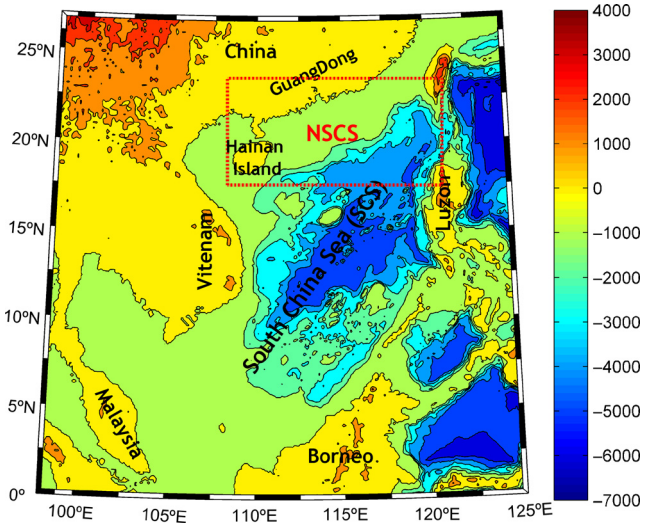

Figure 1 The northern South China Sea (NSCS) and its physiography; different colors represent the bathymetry of the South China Sea [altitude: m]. (For interpretation of the references to color in this figure legend, the reader is referred to the web version of this article.)

With increasing pressure for a profound understanding of marine ecosystems, numerical modeling becomes a powerful tool for research. Ecological models are ecosystem-based management tools that can be used to forecast ecological impacts. Through their ability to integrate into in situ measurements with the theoretical assumptions of ecosystem response, ecological models can be an effective tool for developing strategies for simulating the environmental changes (Cropper and DiResta, 1999). Coupled physical-biological model can be an efficient approach to study the time dependent three-dimensional responses of the marine ecosystem to the coastal upwelling system, and it can also compensate the time-space restrictions of the earlier studies.

In the paper, the Regional Ocean Model System (ROMS) coupled with a nitrogen-based nutrient, phytoplankton, zooplankton, and detritus (NPZD) ecosystem model was given in the NSCS, and was also constructed and analyzed by discretization, driven condition, and validation methods.

2. Material and methods

2.1. Model description

The first generation of marine ecosystem models was put forward by Riley (Riley and Stommel, 1949), and constructed as a one-dimensional NP ecological model, which not only put phytoplankton, zooplankton as state variables, but also took photosynthesis, predator-prey relationship, and mineralization into account. It is also the foundation of the NPZD ecological model used in this paper. Compared with the NP model, this NPZD model describes ecosystem structure and functions in more detail, in addition, it is three-dimensional.

The NPZD ecological model is one of the most popular models by virtue of its fewer requirements for parameters and observation data (Heinle and Slawig, 2013). It has successfully simulated many ecological and physical processes in different seas, for instance, the NPZD model was used to illustrate the relationship between changes in the intensity of the spring bloom and changes in the physical forcing in the northeast Atlantic Ocean (Waniek, 2003) and it was also used for simulating the long-term change of planktonic ecosystems in the upstream Kuroshio Current (Li et al., 2015).

The schematic of the NPZD ecological model is presented here (Fig. 2). It describes the evolution of nutrients (*N*), phytoplankton (*P*), zooplankton (*Z*) and detritus (*D*) (Powell et al., 2006). Furthermore, it is a nitrogen-based model and each square in it represents an ecological variable. These ecological variables belong to four submodules corresponding to *N* submodule, *P* submodule, *Z* submodule, and *D* submodule, respectively, and the arrows between the squares indicate directions of energy flows. Nutrients enter the sea through rivers and atmospheric precipitation transport. On one hand, phytoplankton utilizes photosynthesis for compounding organics for its autotrophic growth. But on the other hand, its growth is also limited by light, nutrients, and temperature, etc. Zooplankton is an important linkage

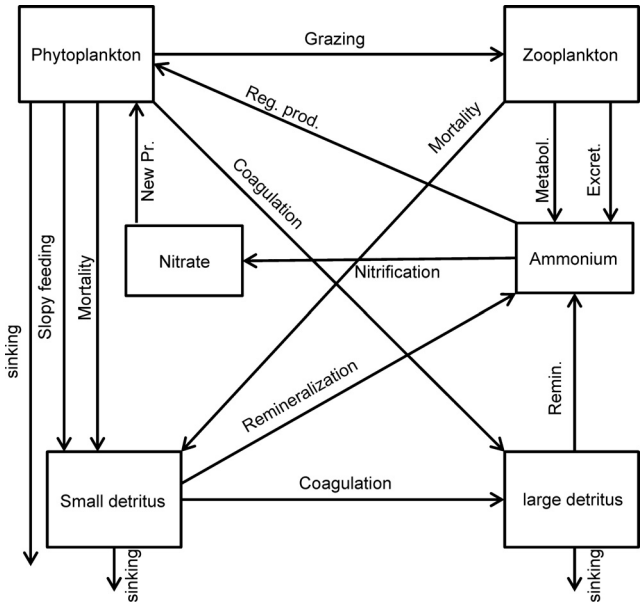

Figure 2 Schematic representation of the NPZD ecological model.

for energy transfer within the trophic structure of marine ecosystems (Turner and Tester, 1997). Zooplankton grazes the living phytoplankton and then assimilates it as its own organics. The unassimilated part, dead phytoplankton, dead zooplankton, and its excrement convert into detritus. As the last part, the new round of marine ecological cycle begins with detritus breaking down into nutrients.

2.2. NPZD model set-up

In this paper, the ecological model over the NSCS is the Fasham-type model (Fasham et al., 1990), which is embedded in the Regional Ocean Modeling System (ROMS). It is a nitrogen-based ecosystem model, which includes six prognostic variables: nitrate (NO_3), ammonium (NH_4), phytoplankton (*Phyto*), zooplankton (*Zoo*), large detritus (*LDetN*), and small detritus (*SDetN*). The NPZD model equations used in the paper can be written as follows:

$$\frac{\partial[NO_3]}{\partial t} = -t_{pp_{\max}}\cdot Q_{NP}\cdot[Phyto] + Q_{nitr}\cdot[NH_4], \tag{1}$$

$$\frac{\partial[NH_4]}{\partial t} = -t_{pp_{\max}}\cdot Q_{RP}\cdot[Phyto] - Q_{nitr}\cdot[NH_4] + (t_{Zbmet} + Q_{excr})\cdot[Zoo] + t_{SDremin}\cdot[SDetN] + t_{LDremin}\cdot[LDetN], \tag{2}$$

$$\frac{\partial[Phyto]}{\partial t} = t_{pp_{\max}}\cdot(Q_{NP} + Q_{RP})\cdot[Phyto] - t_{P_{mort}}\cdot[Phyto] - Q_{coag}\cdot[Phyto] - Q_{graze}\cdot[Zoo] + L_{vs}, \tag{3}$$

$$\frac{\partial[Zoo]}{\partial t} = Q_{graze}\cdot AE_N\cdot[Zoo] - t_{Zbmet}\cdot[Zoo] - t_{Zmort}\cdot[Zoo] - Q_{excr}\cdot[Zoo], \tag{4}$$

$$\frac{\partial[LDetN]}{\partial t} = t_{coag}\cdot([SDetN] + [Phyto])\cdot([SDetN] + [Phyto]) - t_{LDremin}\cdot[LDetN] + L_{vs}, \tag{5}$$

$$\frac{\partial[SDetN]}{\partial t} = Q_{graze}\cdot(1 - AE_N)\cdot[Zoo] + t_{pmort}\cdot[Phyto] + t_{Zmort}\cdot[Zoo] - t_{coag}\cdot([SDetN] + [Phyto])\cdot[SDetN] - t_{SDremin}\cdot[SDetN] + L_{vs}, \tag{6}$$

$$\frac{\partial(\theta)}{\partial t} = t_{PP_{\max}}\cdot(Q_{NP} + Q_{RP})\cdot\left(\frac{\theta_m\cdot V_p\cdot(Q_{NP} + Q_{RP})}{\sqrt{V_p^2 + \alpha^2\cdot\theta^2\cdot PAR^2}} - \theta\right) + L_{vs}, \tag{7}$$

$$Q_{NP} = \frac{([NO_3]/K_{NO_3})\cdot I_{NH_4}}{1 + [NO_3]/K_{NO_3}}, \tag{8}$$

$$Q_{RP} = \frac{[NH_4]/K_{NH_4}}{1 + [NH_4]/K_{NH_4}}, \tag{9}$$

$$Q_{nitr} = t_{nitri}\cdot\left(1 - \max\left[0, \frac{PAR - I_{thNH_4}}{D_{p5NH_4} + PAR - 2\cdot I_{thNH_4}}\right]\right), \tag{10}$$

$$Q_{graze} = t_{Z_{graze}}\cdot\frac{[Phyto]}{K_P + [Phyto]}, \tag{11}$$

$$Q_{excr} = Q_{graze}\cdot r_{C:N,phyto}\cdot AE_N\cdot\left(\frac{1}{r_{C:N,phyto}} - \frac{GGE_C}{AE_N\cdot r_{C:N,zoo}}\right), \tag{12}$$

$$I_{NH_4} = \frac{1}{1 + [NH_4]/K_{NH_4}}, \tag{13}$$

$$t_{PP_{\max}} = \frac{V_P\cdot\alpha\cdot PAR\cdot\theta}{\sqrt{V_p^2 + \alpha^2\cdot\theta^2\cdot PAR^2}}, \tag{14}$$

$$V_p = 0.59\cdot 1.066^T. \tag{15}$$

The parameters in these equations can be checked in Table 1. L_{vs} represents the vertical sinking terms, which affects phytoplankton, small and large detritus (ω_{Phyt}, ω_{SD}, ω_{LD}). All source terms ($Q\ldots$) are written such that they are non-dimensional.

Within the biology routine, the photosynthetically active radiation (*PAR*) for each cell is successively calculated. The loop starts at the top cell. For each cell, the *PAR* in the center of the cell is calculated with:

$$PAR_k = PAR_{k+1}\cdot e^{-0.5\cdot\left(k_{water} + k_{Chla}\cdot\lfloor Chla\rfloor_k\cdot\Delta z_k\right)},$$

k is the cell index (from 1 at the bottom to N at the top). PAR_{N+1} is the surface *PAR*, k_{water} and k_{Chla} are attenuation coefficient for water and chlorophyll, [*Chla*] is the chlorophyll

Table 1 List of parameters used in the biogeochemical model.

Variable	Description	Value	Unit
k_{water}	Light attenuation due to sea water	0.04	[m^{-1}]
K_{Chla}	Light attenuation by chlorophyll	0.024	[(m^2 mg *Chla*)$^{-1}$]
A	Initial slope of the *P–I* curve	1	[mg C (mg *Chla* W m^{-2} d)$^{-1}$]
$r_{C:N,phyto}$	C:N ratio for phytoplankton	6.625	[mol C (mol N)$^{-1}$]
$r_{C:N,zoo}$	C:N ratio for zooplankton	5	[mol C (mol N)$^{-1}$]
θ_m	Maximum cellular chlorophyll:C ratio	0.053478	[mg *Chla* (mg C)$^{-1}$]
K_{NO_3}	Half-saturation for phyto. NO_3 uptake	1.0/0.75	[mmol N m^{-3}]
K_{NH_4}	Half-saturation for phyto. NH_4 uptake	1.0/0.5	[mmol N m^{-3}]
t_{Pmort}	Phyt mortality to SDetN rate	0.072	[d^{-1}]
t_{Zgraze}	Zoo-specific maximum grazing rate	0.6	[d^{-1}]
AE_N	Zoo assimilation efficiency for N	0.75	[–]
K_P	Zoo half-saturation const. for ingestion	3	[mmol N m^{-3}]
t_{Zbmet}	Zoo specific excretion rate	0.1	[d^{-1}]
t_{Zmort}	Zoo quadratic mortality to Detritus	0.025	[d^{-1} (mmol N m^{-3})$^{-1}$]
$t_{SDremin}$	Small detrital breakdown to NH_4 rate	0.03	[d^{-1}]
$t_{LDremin}$	Specific rate of LDetN recycling to NH_4	0.01	[d^{-1}]
ω_{SD}	Sinking velocity for SDetN	1.0	[m d^{-1}]
ω_{LD}	Sinking velocity for LDetN	10	[m d^{-1}]
ω_{Phyto}	Sinking velocity for Phyt	0.5	[m d^{-1}]
t_{nitri}	Nitrification of NH_4 to NO_3	0.05	[d^{-1}]
D_{p5NH_4}	0.5 dose for nitrification inhibition	0.036	[W m^{-2}]
I_{thNH_4}	Threshold PAR for nutrition inhib	0.0095	[W m^{-2}]
t_{coag}	Specific (per unit Phyt + SDetN) aggregation rate	0.01	[(mmol N m^{-3})$^{-1}$ d^{-1}]
GGE_C	Zoo gross growth efficiency for C	0.65	[–]

concentration in this cell, and Δ_{zk} is the height of the cell. After the calculation of the newly generated production, PAR_k is multiplied again with the same attenuation factor.

2.3. Coupling NPZD ecological model with physical model

The adopted physical model — ROMS is a new generation ocean circulation model (Shchepetkin and McWilliams, 2005) that has been specially designed for accurate simulations of regional oceanic systems.

ROMS is discretized in coastline and terrain-following curvilinear coordinates using high-order numerical methods. It is a split-explicit, free-surface ocean model, where short time steps are used to advance the surface elevation and barotropic momentum, with a much larger time step used for temperature, salinity, and baroclinic momentum. The model has a 2-way time-averaging procedure for the barotropic mode, which satisfies the 3D continuity equation. The specially designed 3rd order predictor-corrector time step algorithm allows a substantial increase in the permissible time-step size (Shchepetkin and McWilliams, 1998). To address the challenge of bridging the gap between near-shore and off-shore dynamics, a nesting capability has been added to ROMS and tested for the California Upwelling System (Davenport et al., 2012; Penven et al., 2006).

ROMS can be used to process the initial conditions and lateral boundary conditions for biogeochemical tracer. It can assist in adding initial and lateral conditions for biogeochemical variables of the NPZD model.

2.4. Data

In this paper we use World Ocean Altas 2009 (WOA2009) global dataset (monthly climatology at 1° resolution), CSIRO Atlas of Regional Seas (CARS2009) database (annual, seasonal and monthly climatology for temperature, salinity, nitrate, phosphate, and oxygen), and COADS05 (directory of the surface fluxes global monthly climatology at 0.5° resolution). Besides, surface chlorophyll *a* climatology is based on SeaWiFS observation.

WOA2009 or CARS2009 provides a monthly, seasonal and annual climatology for nitrate concentration, phosphate, silicate, and oxygen. WOA or SeaWiFS can then be used to obtain climatology of surface chlorophyll concentration. Phytoplankton is estimated by a constant chlorophyll/phytoplankton ratio derived from previous simulations, and zooplankton is estimated in a similar way ($Chla/P = 1.59$; $Z/P = 0.3$) (Gan et al., 2009a,b).

3. Model discretization and the driven condition

3.1. Model discretization

In this study, the model was run for 3 years and initialized after a 10-year long spin-up (Powell et al., 2006) to ensure a steady state. The model was configured over the NSCS region (107°00′–121°E; 17°00′–23°30′N) and open boundaries were given in east, west and south boundaries of the domain

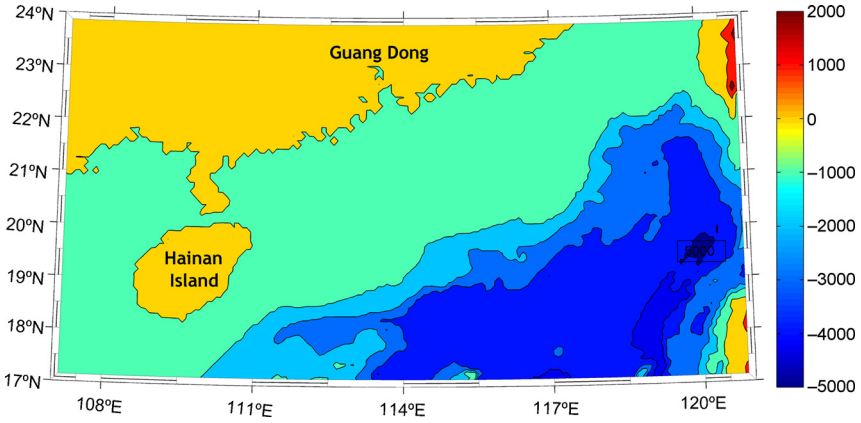

Figure 3 The northern South China Sea (NSCS) model domain and bathymetry; different colors represent the bathymetry of the NSCS [altitude: m]. (For interpretation of the references to color in this figure legend, the reader is referred to the web version of this article.)

(Fig. 3); meanwhile, the radiation open boundary conditions for barotropic velocities and mass conservation enforcement were used. The horizontal resolution of the model is 20.8 km, which is enough to resolve the first and second baroclinic Rossby deformation radius in the basin (Chelton et al., 1998). In vertical, the simulated domain is discretized into 32 vertical levels. Furthermore, the spatial resolution of the model is 1/5 and the time step is 3600 s.

3.2. Model driven condition

The model driven condition contains different surface fluxes, such as wind stress, surface net heat flux, surface freshwater flux, sea surface temperature, solar shortwave radiation, and sea surface salinity, etc.

The wind stress vectors and wind stress norm were obtained from the global atlas of surface marine data at 1/2° resolution at 4 different periods of the year (Fig. 4b). Sea surface temperature (SST) is used for the restoring term in the heat flux calculation (Fig. 4a). To improve the model solution, it is possible to use SST climatology at a finer resolution (9.28 km) (Casey and Cornillon, 1999). For the surface forcing, instead of directly prescribing the fluxes, it is possible to use a bulk formula to generate the surface fluxes from atmospheric variables during the model run.

4. Model validation procedure and criteria

As the basis of this coupled model, the accuracy of the hydrodynamic model is of great importance to the NPZD model. To assess it, the hydrodynamic model results were compared with Simple Ocean Data Assimilation analytic system (https://climatedataguide.ucar.edu/climate-data/soda-simple-ocean-data-assimilation) (SODA-an ocean reanalysis database). The simulated seasonal changes of sea surface temperature and flow field show a reasonable agreement with SODA (Figs. 5 and 6). Furthermore, to give this hydrodynamic model a quantitative validation, the Root Mean Square Error (RMSE) and correlation coefficient (Corrcoef) of the sea surface flow velocities (X direction of the flow in YD (u(YD)) and QD (u(QD)), Y direction of the flow in YD (v(YD)) and QD (v(QD))) between the model and SODA were calculated (Table 2).

And then, to assess the ability of the coupled ROMS-NPZD model to reproduce realistic chlorophyll patterns and nutrients over the NSCS, the mean surface chlorophyll a and NO_3 concentrations during September to October derived from the NPZD model were compared with the data measured during September to October in 2004, which partly coincided with the summer coastal upwelling in NSCS (Fig. 8). Moreover, satellite-derived high-resolution of surface chlorophyll from the Moderate Resolution Imaging Spectro-radiometer (MODIS) was also compared with the simulated chlorophyll (Fig. 7), which reflects a pretty good match.

Here, a Taylor diagram (Taylor, 2001) was constructed to statistically summarize how closely the simulated results match observations in terms of the standard deviations, the centered root mean square difference and the correlation (Fig. 9).

RMSE and Corrcoef of chlorophyll a and NO_3 concentrations between the model and the measured data were also calculated (Table 2) in order to evaluate the usability of the NPZD model. RMSE value and Corrcoef reflect the forecast accuracy of a model (Park et al., 2009). The smaller RMSE value it is, the higher accuracy of the model results we get. Corrcoef (Ogasawara, 2010) is a kind of value set at $[-1, 1]$, and the closer absolute Corrcoef value approaches to 1, the better-simulated results they would be. Specifically speaking, the simulated results generally well reproduce the observations with the Corrcoef ranging from 0.7 to 0.9, and the normalized standard deviation (NSD) from 0.5 to 0.8 (normalized by the standard deviation of the corresponding observed field, Taylor, 2001). In addition, observing the two line charts (Fig. 10) we can see that the variation trend and the range of concentration are roughly the same.

However, the simulated results of some nearshore stations have relatively large errors, such as station 1 and station 33. After analyzing the causes, we find that these stations located in the Pearl River estuary are affected by the strong Pearl River diluted water, which reflects that there may exist some shortcomings in simulated freshwater flux of the

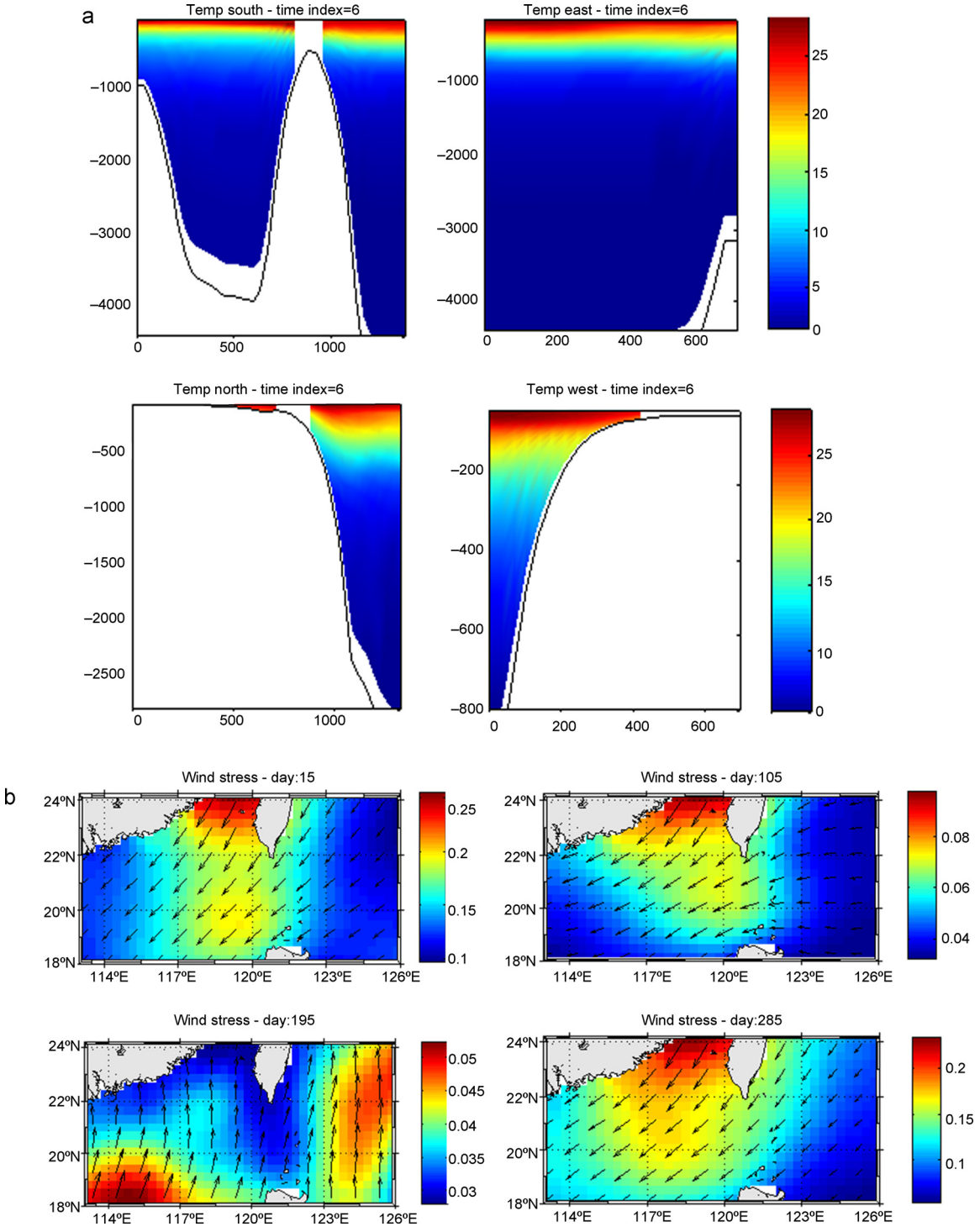

Figure 4 Four different sections of temperature [°C] for initial condition (a), the sections are in the *X*-direction (East—West), the first section is for the southern part of domain and the last one is for the northern part of the domain. The wind stress vectors and wind stress norm (b) obtained from the global atlas of surface marine data at 1/2° at 4 different periods of the year [N m^{-2}].

physical model. On account of the simulated results being climatic, and yet the measured results being discontinuous, interannual variations are allowed; so the differences between them are understandable. Beyond that, the most of the simulated results conform to the measured and satellite data. In sum, this coupled ROMS-NPZD model can be used as the basis of quantitative ecological research. To ensure the accuracy of our study, model results of the third year, which are the most steady simulated results among all the model data, are used to illustrate ecosystem response mechanism.

5. Results description

Coastal upwelling is one of the most important physical processes which has a significant influence on the distribution of nutrients and hence affecting primary production (Krishna, 2008). Upwelling is responsible for transporting higher-salinity and nutrient-rich deeper water to the surface layer. The previous ecological studies on summer upwelling system over the northern continental shelf of SCS were mainly carried out by ship drift data (Cai et al., 2002; Song et al., 2012), and the interannual variation may have a marked impact on the universality of the data. Since this coupled ROMS-NPZD model simulations were climatologically forced runs, the simulated data do not correspond to a specific year.

5.1. Hydrographic conditions response to YDU and QDU

The coastal upwelling in YD and QD are characterized by the flow responding to the southwesterly winds on the shelf. The surface water shows obvious continental shelf upwelling characteristics (Fig. 11), such as low temperature, high salinity in the east of the Leizhou Peninsula (noted as Qiongdong-QD upwelling-QDU), and the inshore areas from the Shantou Coast to the Nanri Islands of Fujian province (noted as Yuedong – YD upwelling – YDU) (Jing et al., 2008). The typical mature upwelling regions of the study areas are characterized by nearshore cold and high-salinity layer, which is surrounded by an offshore warm and low salinity layer, in summer. As the cold upwelling water which is generated near the coast spreads and advects offshore, it pushes warm water far from the coast (Gan et al., 2009a,b). Comparing these two coastal upwelling regions, the salinity of YD is not as high as QD, but it is much higher compared to other coasts around.

The summer coastal upwelling is a regular phenomenon during June to September in NSCS (Yu, 1987). Low temperature in the surface water can be detected clearly in both QD and YD, and it can be about 2–3°C lower than the offshore water (Figs. 12a and b, 13a and b). The variations of temperature in QD (Fig. 12a) and in similar latitudes elsewhere (the region around 113°E) (Fig. 12b) during the simulated three years are showed, respectively. The modeled surface temperature in QD decreases continuously rather than

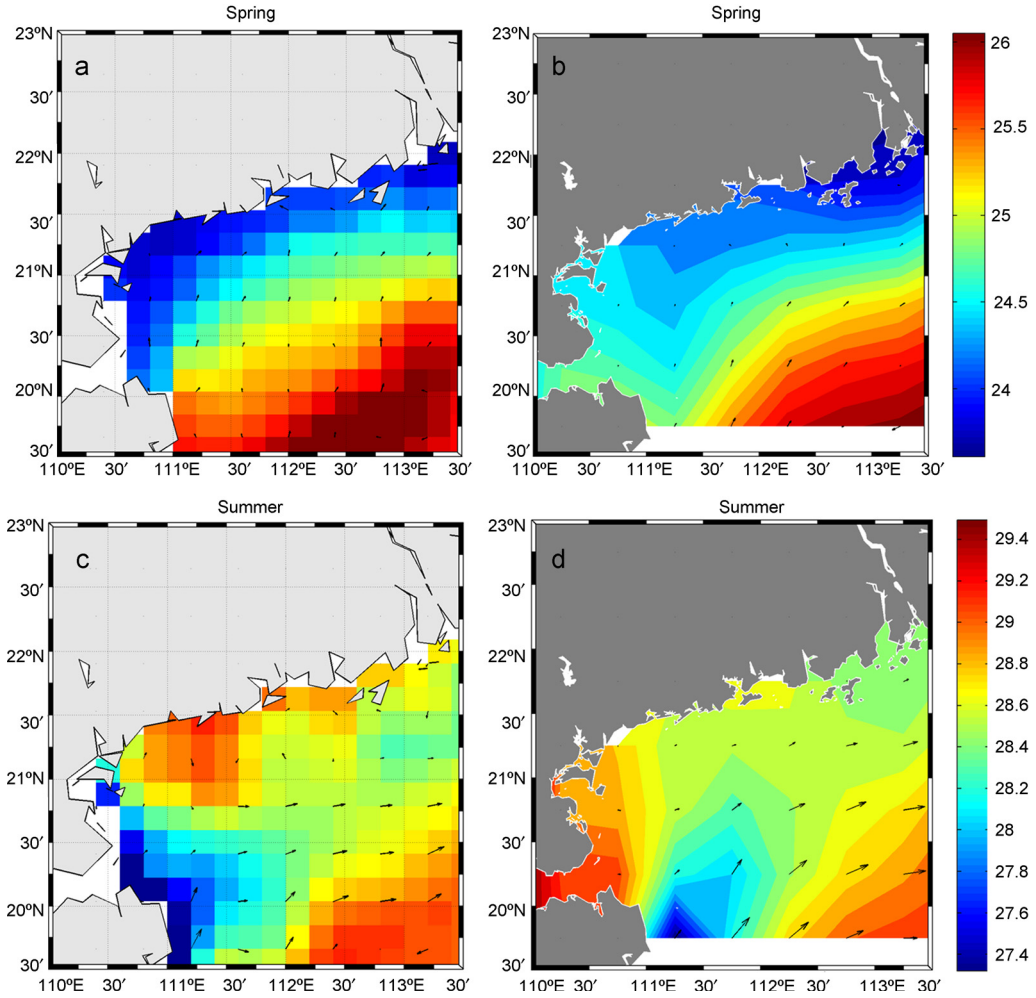

Figure 5 The seasonal changes of the sea surface temperature [°C] and the flow field in the Leizhou Peninsula (QD) simulated by our model (subplots a, c, e, g) and calculated from SODA (subplots b, d, f, h).

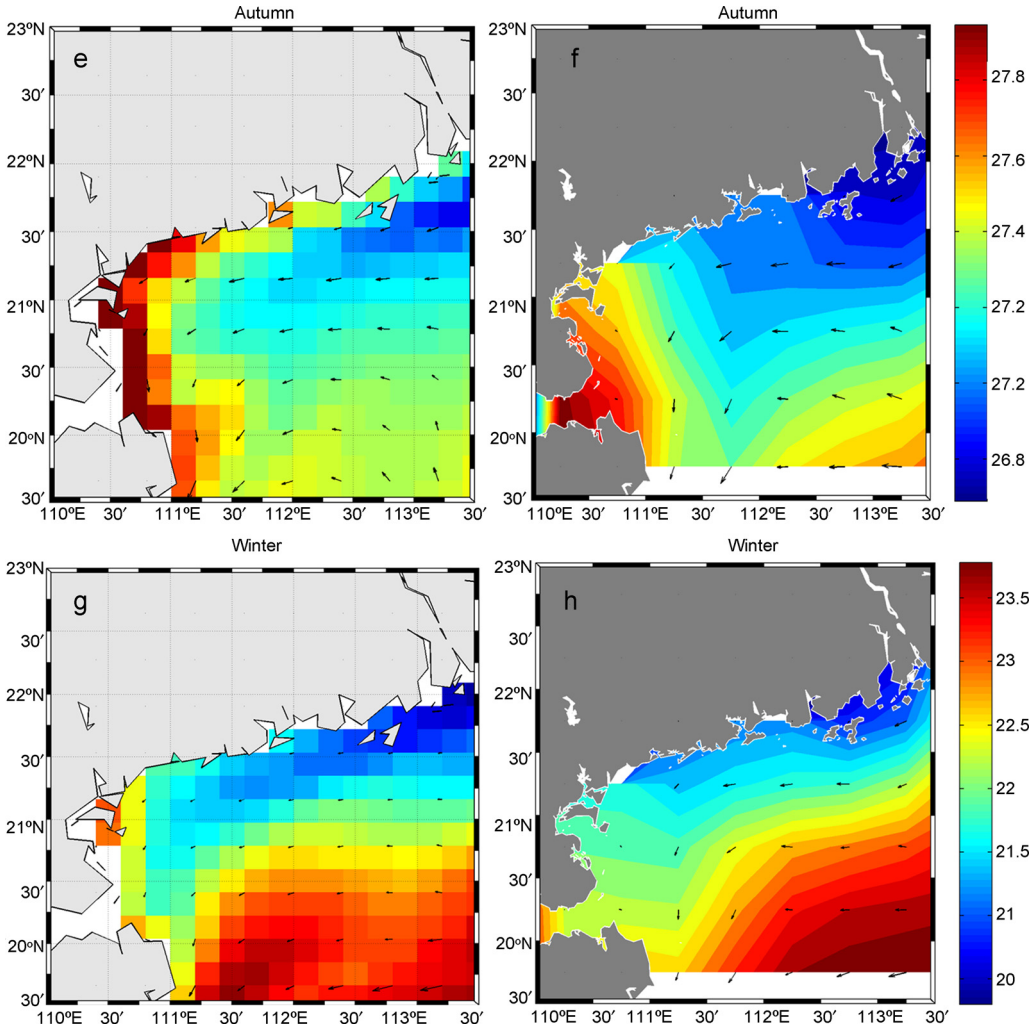

Figure 5. (*Continued*).

increases, and reaches the summer's lowest point in the middle of July, and then rises gradually to the second peak in the middle of September. Moreover, high salinity in the surface water can also be detected in both QD and YD (Figs. 12c and d, 13c and d). Three similar small salinity spikes can be found during every July of the three simulated years (Fig. 12c). The salinity during these periods of time is around 34, just the same as in the results of previous study (Li et al., 2012). However, there are no salinity spikes during the same period of time in the region around 113°E (Fig. 12d), and the salinity (about 32) is significantly lower than in QD.

5.2. Nutrients response to YDU and QDU

The distribution of nutrients in YDU and QDU follows the general pattern of coastal upwelling at other sea areas (Fernandes et al., 2014; Krishna, 2008), which has characteristics of higher concentrations near the subsurface layer of coastal waters and lower concentrations at the surface of offshore waters (Chenillat et al., 2012, 2013). However, the distribution of nutrients in these two regions also has its own characteristics.

It is obvious that the highest NO_3-N concentrations (<0.14 mmol m^{-3}) in the coast around the 115°E (Fig. 14a) are located between −50 m and −60 m water layer, and the NO_3-N concentrations of surface water are very low (<0.08 mmol m^{-3}), which reflects the impacts of stratification existing between the surface and sub-surface layer. And yet, the highest NO_3-N concentrations (>0.17 mmol m^{-3}) in YD appear between −20 m and −40 m water layer, and an enhanced vertical mixing can be found in this water layer (Fig. 14b). Meanwhile, the NO_3-N concentrations of surface water are much higher than in the water layer below −50 m. Compared with the coast around the 115°E, the water layer with the highest NO_3-N concentrations in YD moves up and the mean value of NO_3-N concentrations is much higher (Fig. 14a and b). According to the analysis above, the YDU is responsible for carrying nutrient-rich deeper water toward the surface. However, the NO_3-N concentrations in QD (Fig. 14d) and similar latitudes elsewhere (Fig. 14c) still show the strict vertical stratification, and the NO_3-N concentrations of surface water are much lower (<0.2 mmol m^{-3}). With the increase of water depth, the NO_3-N concentrations

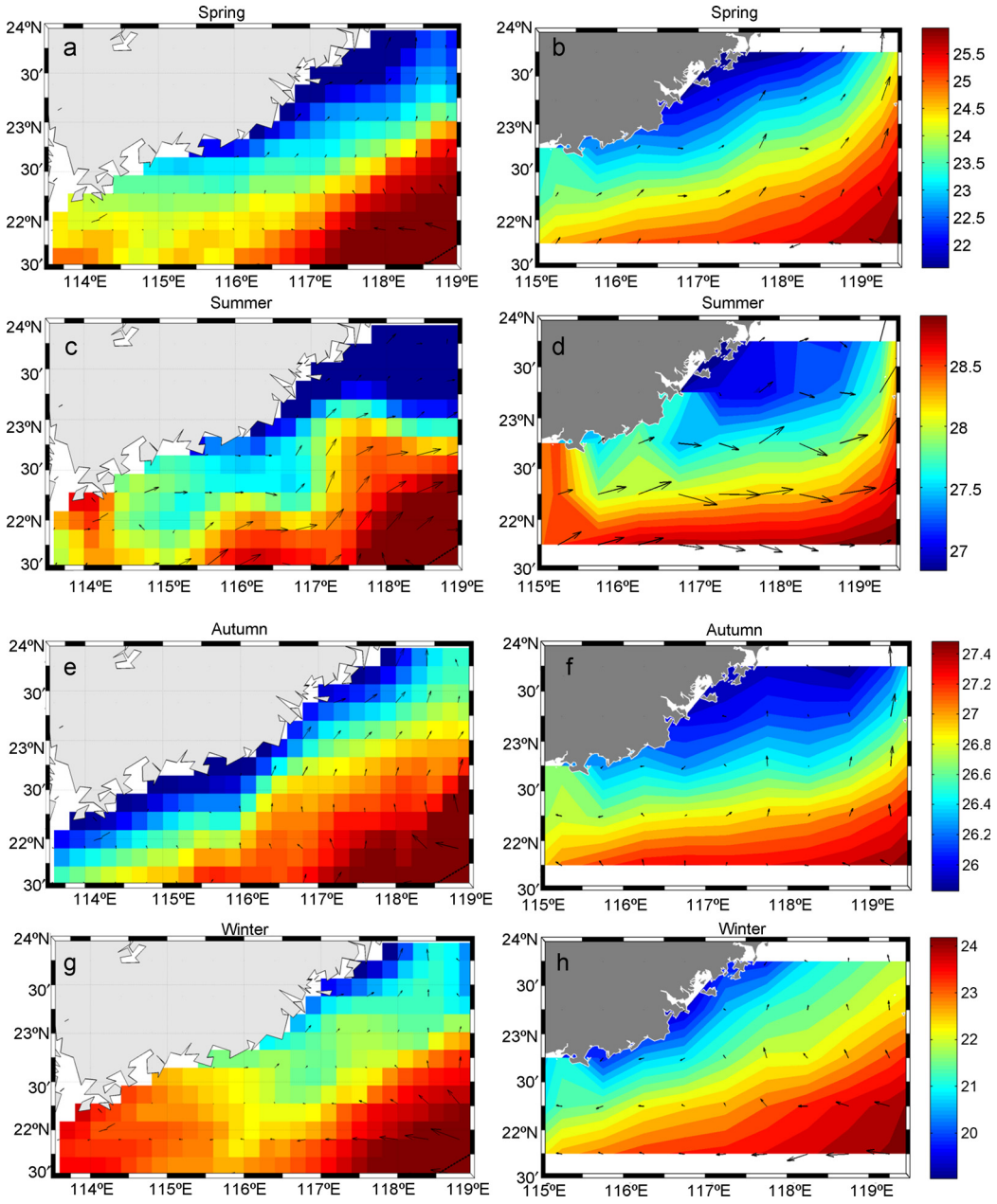

Figure 6 The seasonal changes of the sea surface temperature [°C] and the flow field in the Fujian Province (YD) simulated by our model (subplots (a), (c), (e), (g)) and calculated from SODA (subplots (b), (d), (f), (h)).

increase gradually until the water depth reaches about −70 m (>1.2 mmol m^{-3}).

Although the YDU and QDU are two main coastal upwellings in NSCS, their impacts on the distribution and concentrations of NO_3-N are different. There is an obvious upwelling triggered uplift of NO_3-N in YD, but only a slight upwelling triggered uplift in QD. In addition, the distributions and changes of nutrients may inevitably affect the primary productivity in YD like in the previous studies in other coastal upwelling areas (Hernández-Carrasco et al., 2014).

5.3. Phytoplankton response to YDU and QDU

Phytoplankton is an important bioindicator of chemical and biological modifications in natural ecosystems (Vilhena et al., 2014). It is also an important element of primary production, which is the key basic biological production in marine ecosystems (Song et al., 2010). It has been proposed that in NSCS the distribution of phytoplankton during summer time is closely related to the coupled processes driven by summer southwesterly monsoon induced upwelling (Ning et al., 2004), so are the YUD and QDU.

Table 2 RMSE and Corrcoef of the simulated results.

	Root mean squared error	Correlation coefficient
Chla	0.0989	0.7174
NO_3-N	1.8140	0.8236
u(YD)	0.1922	0.7269
v(YD)	0.0481	0.6507
u(QD)	0.1416	0.6945
v(QD)	0.0796	0.7654

In the middle of July, a great distribution and concentrations differences of phytoplankton exist between YD and the coast around the 115°E (Fig. 15a and b). It is obvious that the highest phytoplankton concentrations are located between −50 m and −70 m water layer (Fig. 15b) in the coast around the 115°E; however, the water column with the highest phytoplankton concentrations move up to −20 m to −40 m in YD (Fig. 15a). Beyond this uplift phenomenon, the phytoplankton concentrations in YD are also a lot higher than in the coast around the 115°E. The NSCS coastal upwelling driven by both upwelling favorable local wind and topography, which affects the distribution of nutrients, then would have an ultimate effect on the phytoplankton growth and standing stock. The YDU is just like a perfect nutrient pump for new production (Wang et al., 2014a,b).

The strongest coastal upwelling with the minimum temperature and the maximum nutrients in NSCS often occurs in the middle of July based on the previous study (Jing et al., 2008). This is the reason why we often use the simulation result of July 16th to illustrate our study. However, the similar rule cannot be applied to phytoplankton. The phytoplankton concentrations in the late July (>0.3 mmol m^{-3}) (Fig. 15c) are higher than in the middle of July (>0.2 mmol m^{-3}) (Fig. 15a). In addition, phytoplankton is advected to almost 30 km off the coast in the late July (Fig. 15c), which is much farther than 15 km in the middle of July (Fig. 15a). The intense YDU occurs in the middle of July, while the phytoplankton blooms in the late of July, which confirms that the maximum phytoplankton do not, in general, coincide with the minimum temperature (Santos et al., 2011; Sawant and Madhupratap, 1996), but are lagged in time, by about 10 days.

Different from YDU, QDU combined with the intensive seasonal thermocline makes the distribution of phytoplankton stratified and the phytoplankton concentrations still very low in the surface layer (Fig. 16a). Comparing with the region around 113°E (Fig. 16b), there is only a slight upwelling triggered uplift of phytoplankton in QD, and the maximum phytoplankton is located within the thermocline coupled to the nutricline. Due to this thermocline induced stratification, the surface productivity in QD may be held back.

5.4. Chlorophyll *a* response to YDU and QDU

At the initial stage, upwelled waters of YDU and QDU are characterized by low temperature, low chlorophyll *a* and

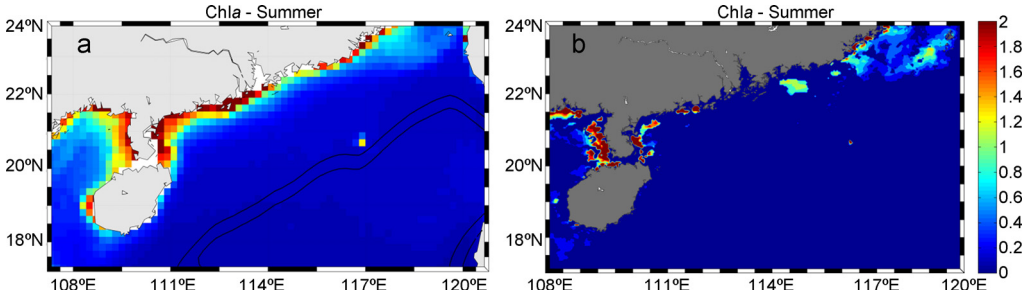

Figure 7 The simulated surface chlorophyll *a* [μg L^{-1}] (a) and satellite-derived high-resolution of surface chlorophyll *a* (b) from the Moderate Resolution Imaging Spectro-radiometer (MODIS).

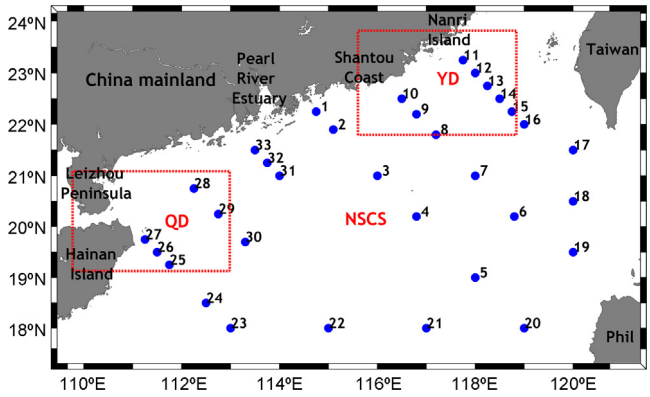

Figure 8 Stations of the measured experiment, which have been used to compare with the simulated results.

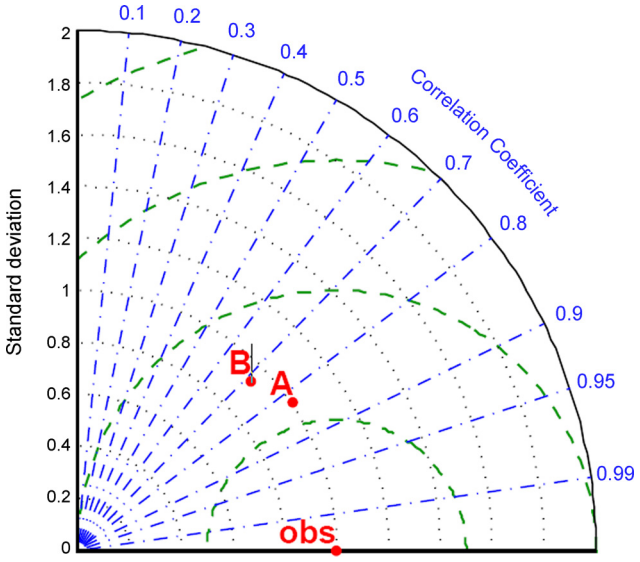

Figure 9 Taylor diagram for model skill assessments. Observations (obs) of stations include sea surface NO_3 (A) and sea surface chlorophyll *a* (B). The radial distance from the origin is proportional to the standard deviation of a pattern. The centered RMS difference between the simulations and obs is proportional to their distance apart (in the same units as the standard deviation). The correlation between the two fields is given by the azimuthal position of the test field.

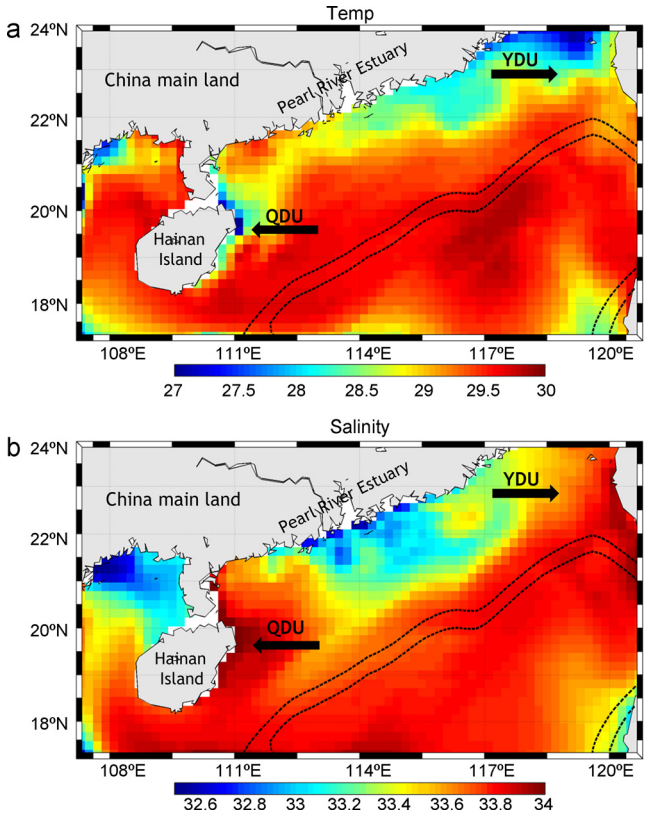

Figure 11 The climatological SST [°C] (a) and surface salinity (b) derived from CARS2009.

high nutrient concentrations (Joint et al., 2001). Afterwards, a fast growth of phytoplankton can take place coincided with the increase of chlorophyll *a* promoting a quick consumption of the available nutrients.

The concentrations of chlorophyll *a* are generally higher toward the inshore areas in YD and QD, and decrease to less than 0.2 ug L^{-1} at the offshore locations (Fig. 17). In YD, the maximum chlorophyll *a* (around 0.45 μg L^{-1}) is observed at −30 m to −20 m water layer in the middle of July (Fig. 17a). Then about 10 days later, the maximum chlorophyll *a* concentrations increase to 0.7 μg L^{-1} recorded at −20 m to lower than −10 m water layer (Fig. 17c). QD presents different distribution characteristics. Higher grazing pressure in the upper layer than at the thermocline may lead to the formation of the subsurface

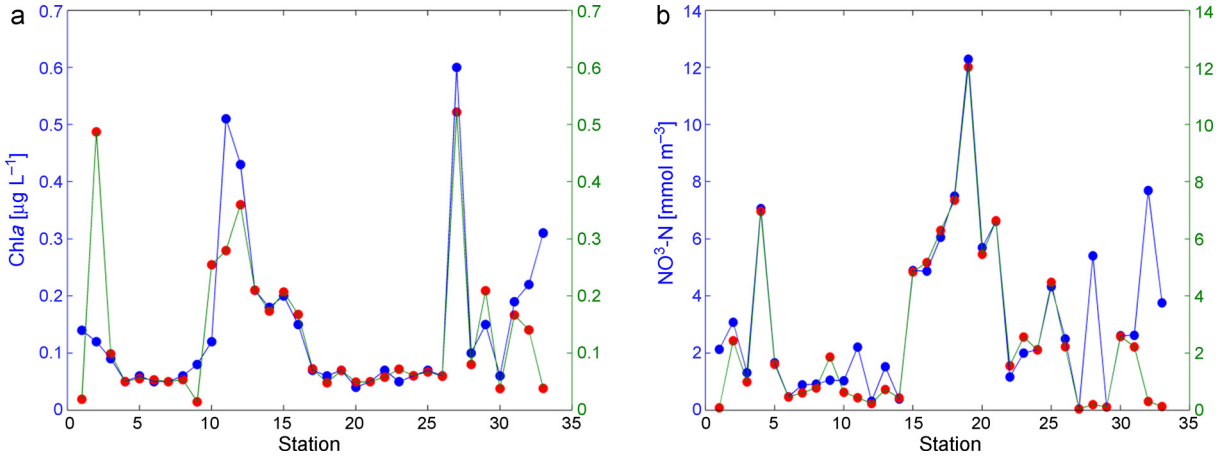

Figure 10 In (a), the blue dot line represents simulated Chl *a* concentrations [μg L^{-1}] and the red dot line represents measured Chl *a* concentrations; in (b), the blue dot line represents simulated NO_3-N concentrations [mmol m^{-3}] and the red dot line represents measured NO_3-N concentrations. (For interpretation of the references to color in this figure legend, the reader is referred to the web version of this article.)

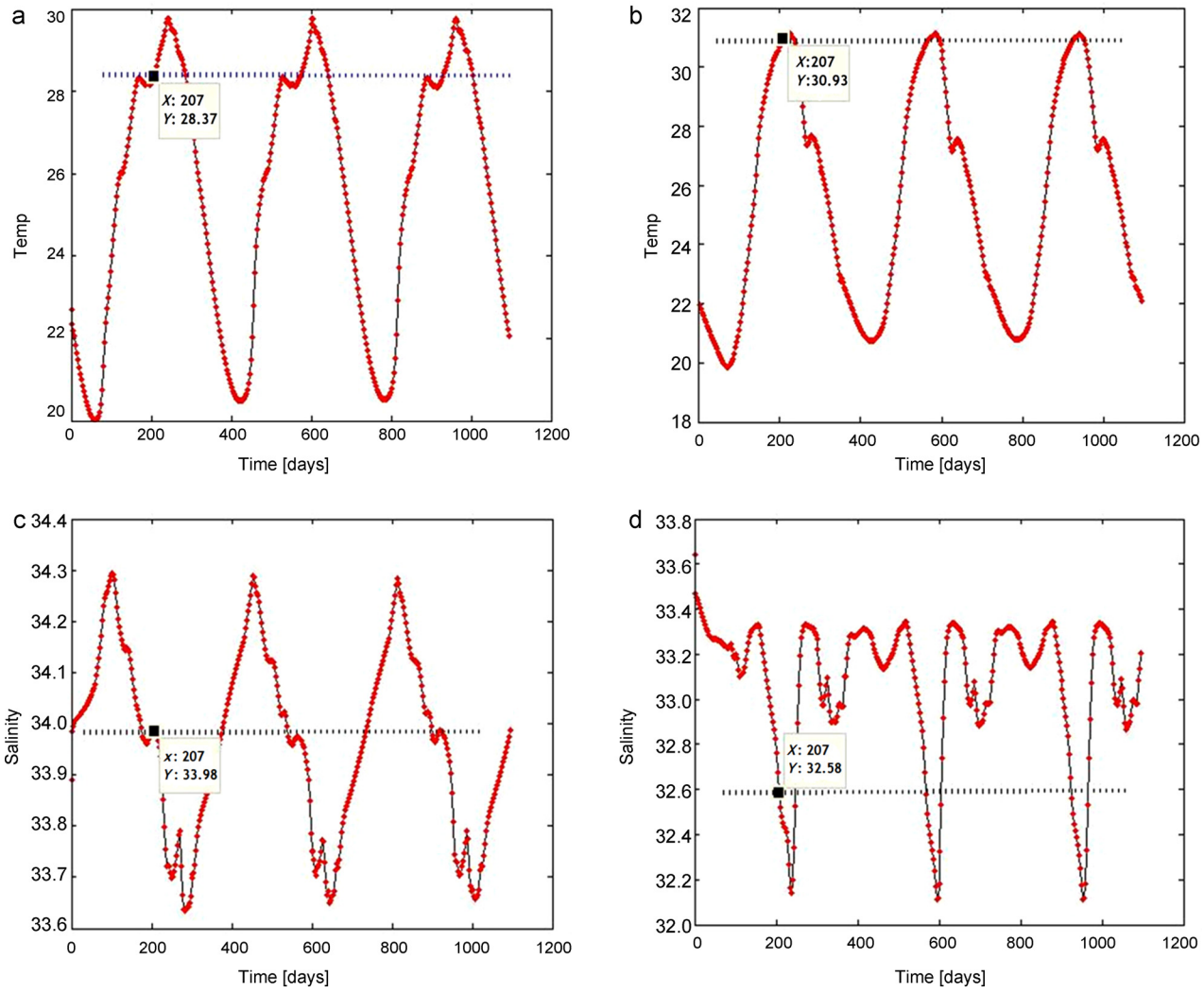

Figure 12 The time series of temperature [°C] in the Leizhou Peninsula (QD – a) and the region around the 113°E (b), the time series of salinity in QD (c) and the region around the 113°E (d).

maximum chlorophyll near the thermocline (Kononen et al., 1998). At QD, the maximum chlorophyll *a* (around 0.5 μg L^{-1}) is observed at −70 m to −60 m water layer in the middle of July (Fig. 17b). Then, about 10 days later, the chlorophyll *a* maxima rise to about 0.65 μg L^{-1} (Fig. 17d). The chlorophyll *a* maxima in YD and QD coincide with the phytoplankton maxima (Figs. 15–17). Similar to the phytoplankton, the maximum chlorophyll *a* does not, in general, coincide with the minimum temperature, which is lagged in time, by about 10 days.

Significant subsurface chlorophyll *a* maximum (SCM) exists in both YD and QD. SCM exists in YD at depth between −40 m and −10 m, and in QD between −70 m and −50 m. The results suggest that the locations of the SCM have close connection with the upward nutrients flux and downward light attenuation. The SCM appears in the same location with the maximum nutrients in the premise that the *PAR* is suitable (Fennel and Boss, 2003). The water layer between −70 m and −50 m in YD, there is not enough nutrients but enough *PAR*, the growth of phytoplankton is limited by nutrients, which leads to the low chlorophyll *a* concentrations. The similar low chlorophyll *a* concentrations phenomenon has also been observed by Lu et al. (2010).

6. Discussion

6.1. Hydrographic differences between YDU and QDU

In this paper, NPZD model rather successfully simulated the ecosystem response to distinctly intensified coastal upwelling over the widened shelf in the NSCS. As seen from model results, the surface water in YD and QD shows obvious continental shelf upwelling characteristics, such as low temperature, high salinity. However, comparing these two coastal upwelling regions, the salinity of YD is not as high as QD because of the effect from the Pearl River diluted

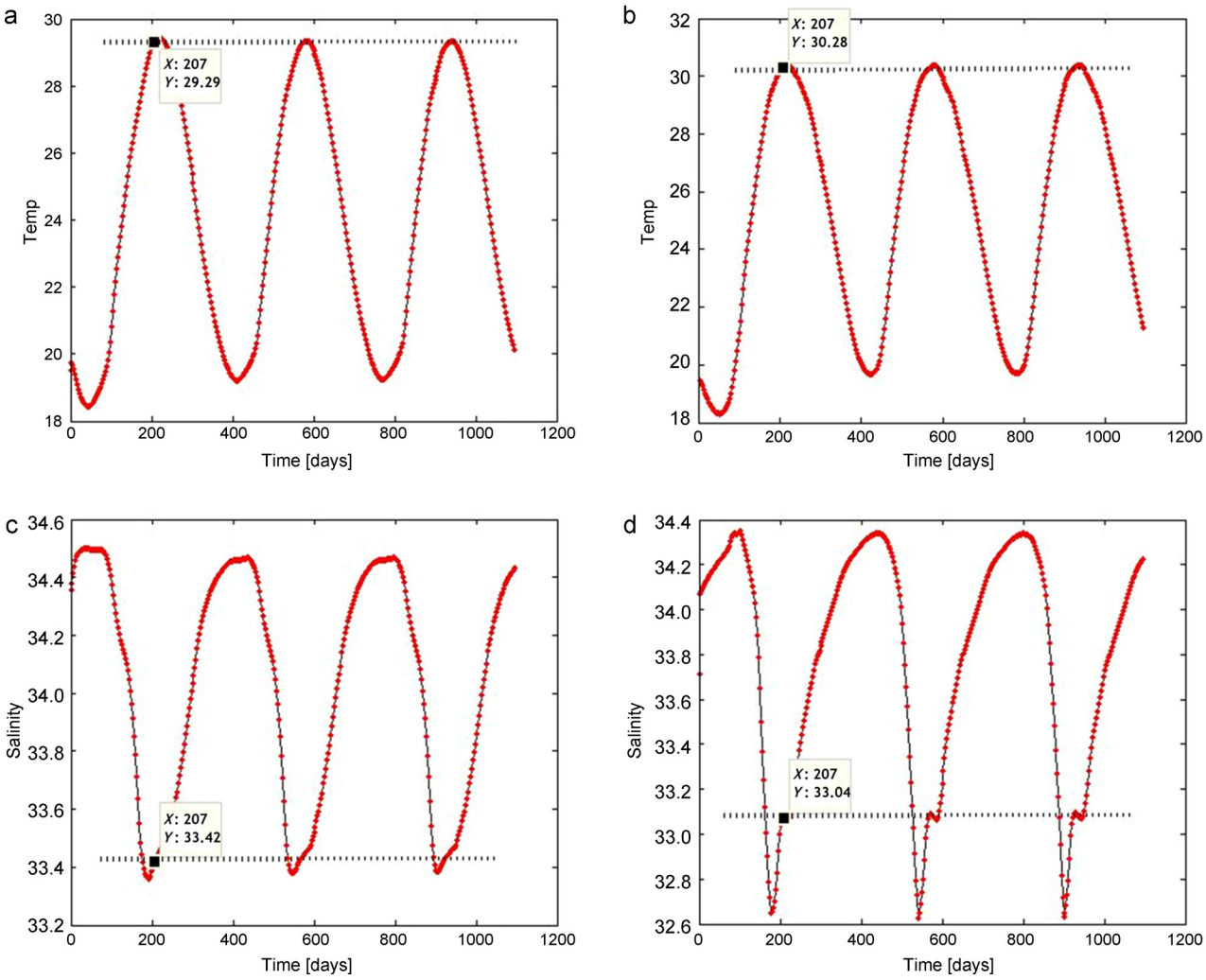

Figure 13 The time series of temperature [°C] in the Fujian Province (YD) (a) and the region around the 115°E (b), the time series of salinity in YD (c) and the region around the 115°E (d).

water (PRDW). The Pearl River is the largest river in south China and has the second largest annual runoff in China. The plume size of PRDW is at maximum in summer, and the southwest monsoon is conducive to the eastward and offshore expansion of the PRDW, which negatively influences the salinity of YD (Dong et al., 2004).

6.2. YDU and QDU acting as a nutrient pump

To comprehend the response of nutrients, the variation trend of nitrate (NO_3-N) was used as representative. According to 'Specification of Oceanographic Investigation', nutrients that include nitrate, nitrite (NO_2), ammonium, phosphate (PO_4-P) and silicate (SiO_3-Si) are often used to represent the main kind of nutrients in the SCS. Nevertheless, only NO_3-N has been simulated in our model study. The principal component analysis (PCA) was utilized to analyze nutrients in NSCS. Based on this former study, NO_3-N has positive correlations with NH_4-N and SiO_3-Si (Wu and Wang, 2007). Hence, NO_3-N has a certain degree of representativeness. In our study, there is an obvious upwelling triggered uplift of NO_3-N in YD, but only a slight upwelling triggered uplift in QD. Not only taking into account the summer coastal seasonal upwelling in NSCS, June to August is also a period of time, during which the most intensive thermocline happens in NSCS (Li and Jian, 2001). In some shallow waters of SCS, there exists the radiation-type seasonal thermocline, which is affected by gross radiation intensity and Ekman pumping (Liu et al., 2001). During every year from March to August, the seasonal thermocline appears in the southeast of the Hainan Island and the northwest of the Taiwan Island, which is almost in the same spot as QD and YD. From March to May is a sharp period of the thermocline in these two regions, and from June to August is the strongest period (Fan et al., 2014). The difference is that the seasonal thermocline in the southeast of Hainan Island is much stronger than in the northwest of Taiwan Island. At QD, prominent signatures providing evidence for the prevalence of upwelling are

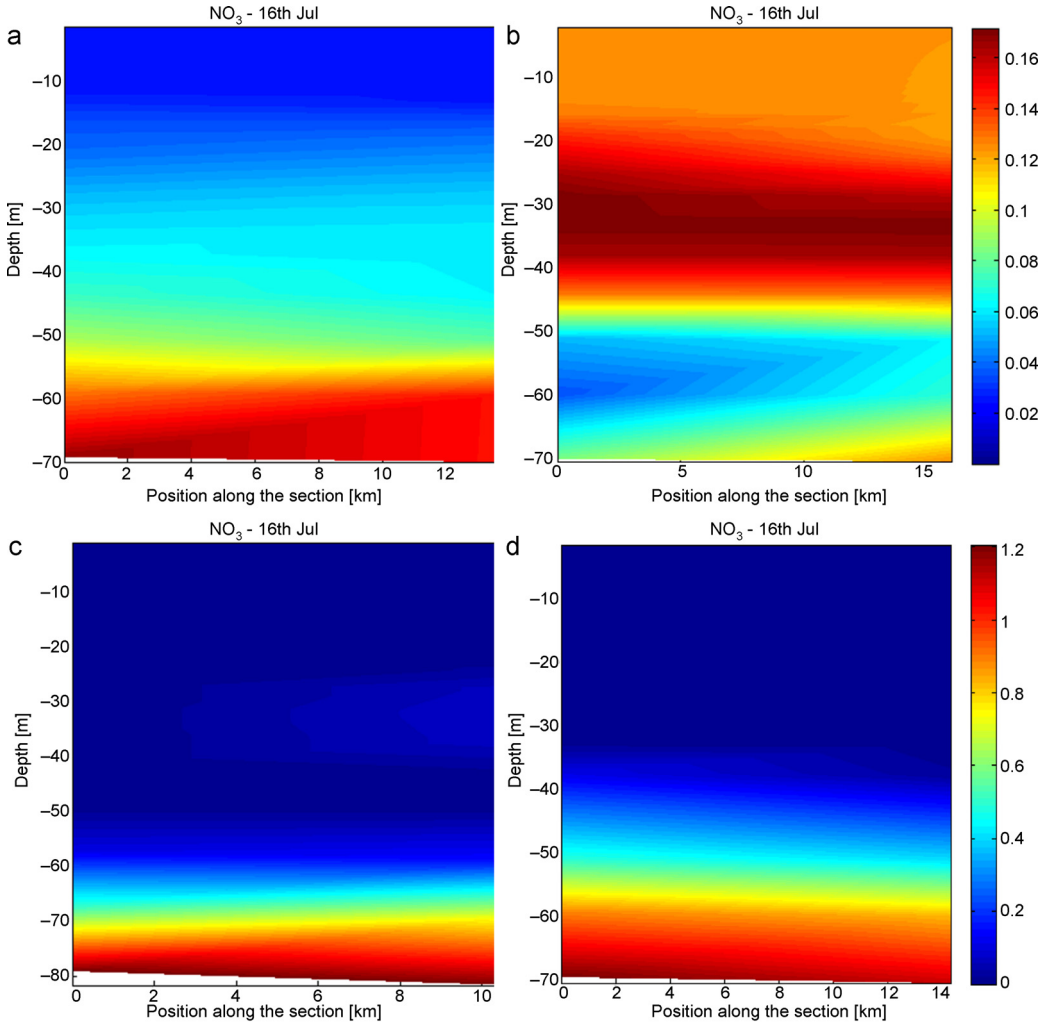

Figure 14 The vertical distribution of NO_3-N [mmol m^{-3}] with "interannual timescale" on the caption, "offshore distance" on the horizontal axis, and "depth" on the vertical axis. Subplots (a) represents the simulated results of the region around the 1158E; subplots (b) represents the simulated results of the Fujian Province (YD); subplots (c) represents the simulated results of the region around the 1138E; subplots (d) represents the model results of the Leizhou Peninsula (QD).

not only based on the sea surface temperature anomaly but also on the notable shoaling of the thermocline. The thermocline in the southeast of Hainan Island is too strong to break into surface by the QDU, hence there is only a slight upwelling triggered uplift of NO_3-N in QD. This thermocline leads to the shortage of nutrients in surface water, and may hold back the productivity in QD. Besides the impact of the thermocline, the water current and transport through Qiongzhou strait is very complicated in summer (Fig. 18) (Wang et al., 2014a,b), which also affects the variation trend of nutrients in QD.

6.3. Delay effects of phytoplankton and chlorophyll *a* in YD

The maximum amount of phytoplankton and chlorophyll *a* does not, in general, coincide with the minimum temperature and maximum nutrients (Santos et al., 2011), but is lagged in time, by nearly 10 days. In our study, the maximum amount appears (in July 28th) with lower upward water velocities (Fig. 19). This phenomenon is common in many upwelling systems in the world (Muller-Karger et al., 2001; Yokomizo et al., 2010) and it is related to the reaction time needed by phytoplankton to react to the sudden increase in nutrient concentrations, which can be about 8–10 days (MacIsaac et al., 1985). Following the previous study (Huete-Ortega et al., 2010), when upward water velocities are highest, together with relatively strong turbulence, they prevent the accumulation of large amounts of phytoplankton; for it takes time for phytoplankton communities to adjust to the new nutrients condition. On the other hand, the upwelling relaxation combining with increased water-column stability and reduced dispersion create appropriate conditions for the onset of the phytoplankton blooms (Lopes et al., 2014). In addition, the development rate

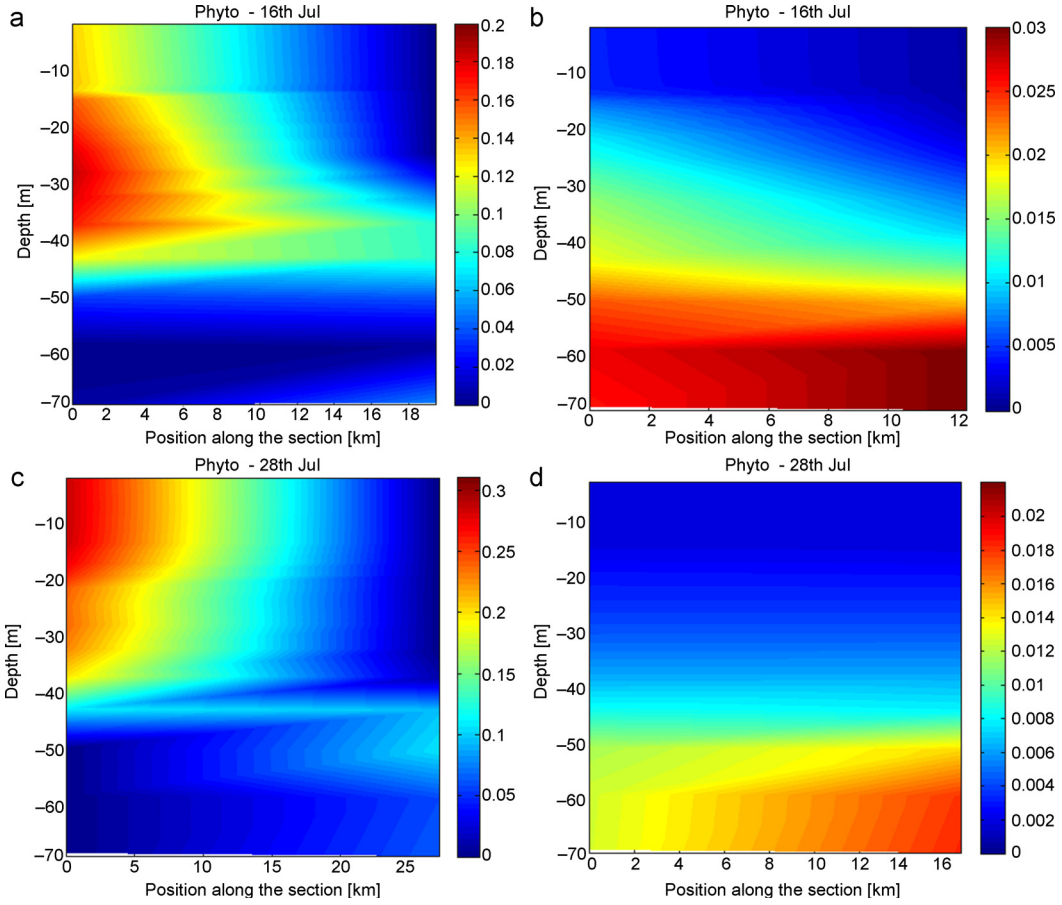

Figure 15 The vertical distribution of phytoplankton [mmol m^{-3}] with an "interannual timescale" on the caption, "offshore distance" on the horizontal axis, and "depth" on the vertical axis. Subplots (a) and (c) represent the model results of the Fujian Province (YD) in July 16 and July 28; subplots (b) and (d) represent the model results of the region around the 1158E in July 16 and July 28.

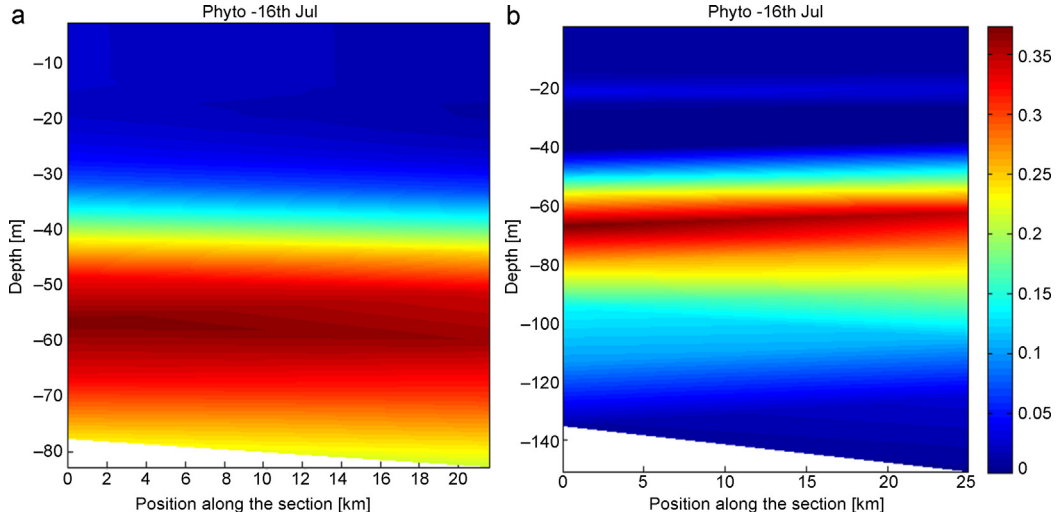

Figure 16 The vertical distribution of phytoplankton [mmol m^{-3}] with an "interannual timescale" on the caption, "offshore distance" on the horizontal axis, and "depth" on the vertical axis. Subplot (a) represents the model results of the Leizhou Peninsula (QD) in July 16, and subplot (b) presents the model results of the region around the 1138E in July 16.

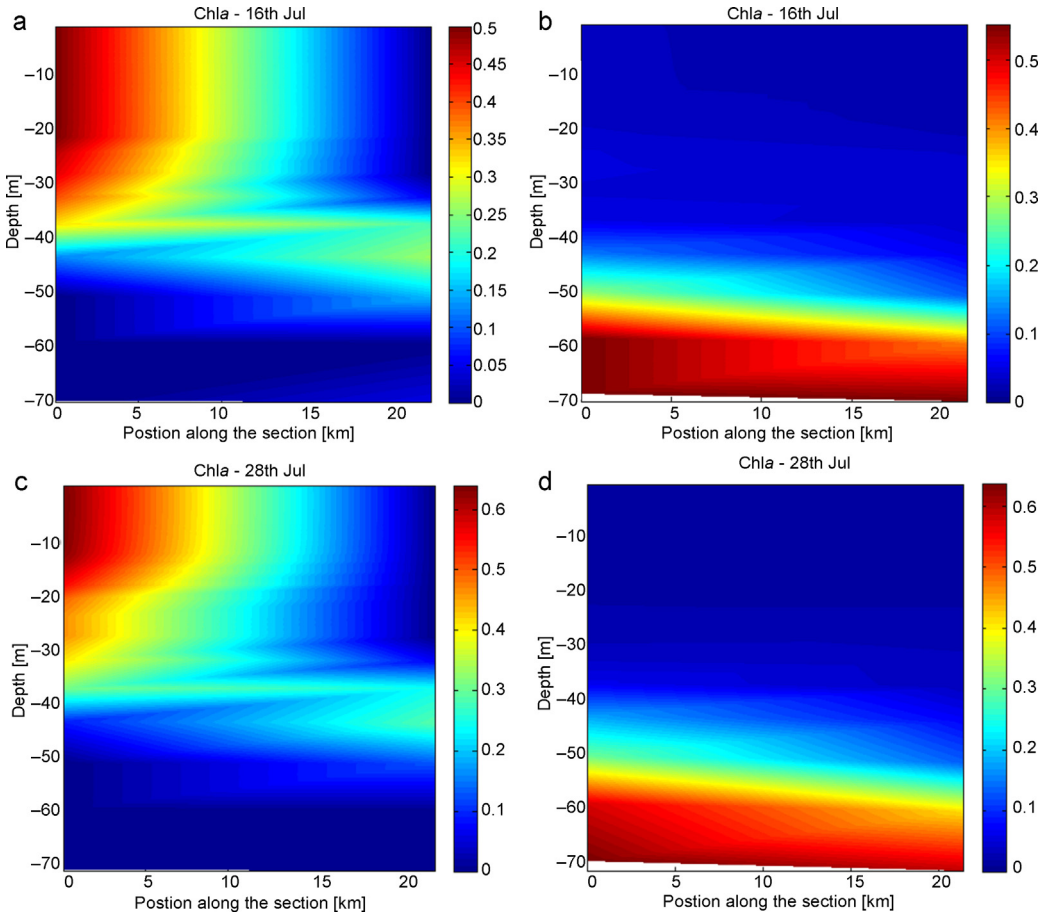

Figure 17 The vertical distribution of chlorophyll *a* [μg L^{-1}] with an "interannual timescale" on the caption, "offshore distance" on the horizontal axis, and "depth" on the vertical axis. Subplots (a) and (b) represent the model results of the Fujian Province (YD) and the Leizhou Peninsula (QD) in July 16; subplots (c) and (d) represent the model results of YD and QD in July 28.

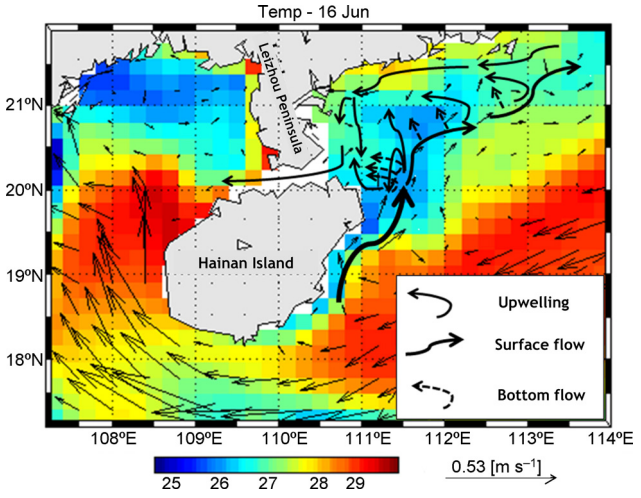

Figure 18 The water current, and its transport in the Leizhou Peninsula (QD).

of phytoplankton is closely related to the shelf width. The development rate changes from very wide (fast) to narrow (slow) (Botsford et al., 2003). The widened shelf off Shanwei and on the western flank of the Taiwan Banks intensifies the bottom friction, which is a key factor for topographically induced upwelling and also has a positive correlation to the development of phytoplankton. The phytoplankton production increases with lower wind strength, and in proportion to upwelled volume, but eventually begin to decrease as losses increase off the shelf (compared with Fig. 15c, Fig. 20 shows a remarkable decrease). Moreover, high offshore velocities on the seaward side advect the upwelling water off the coast, which leads to the strong phytoplankton concentrations at about −10 m to −40 m water layer extending seaward from the inner shelf to about 30 km into outer shelf (Fig. 15c).

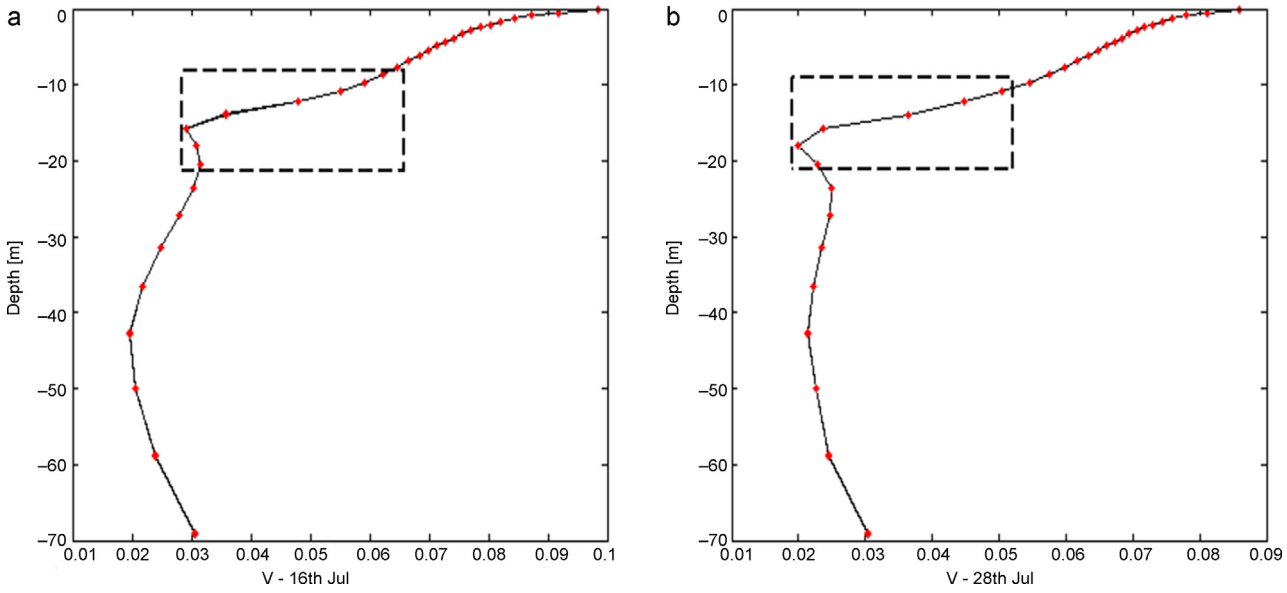

Figure 19 The upward water velocities [m s^{-1}] in the Fujian Province (YD). Subplot (a) represents the model results of YD in July 16, and subplot (b) represents the model results of YD in July 28.

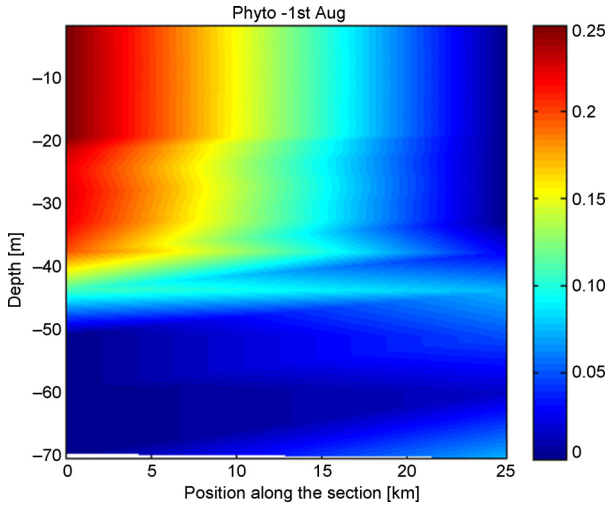

Figure 20 The vertical distribution of phytoplankton [mmol m^{-3}] of the Fujian Province (YD) in August 1st, with an "interannual timescale" on the caption, "offshore distance" on the horizontal axis, and "depth" on the vertical axis.

7. Conclusion

The coastal upwelling blooms common to the NSCS are captured by the model (ROMS-NPZD). Although in a simple framework, the results from our coupled biological-physical model are in qualitative agreement with the general characteristics of the NSCS coastal upwelling system. Based on our ecological model study, the ecosystem response to the summer coastal upwelling in NSCS can be summarized as follows.

YDU and QDU are physical processes which occur in sequential stages: (1) the first stage can be defined by the offshore transport of surface water and its replacement by cold, nutrient rich sub-surface water; (2) the second stage is the productive phase wherein an increase in phytoplankton and chlorophyll standing stock can be found.

During summer, YD and QD are characterized by nearshore cold and high salinity layer surrounded by an offshore warm and low salinity layer. The water temperature at YD and QD can be about 2—3°C lower than the offshore water, and the salinity is around 34 which is much higher than 32 in the offshore water. At YD and QD, the nutrients in the subsurface water layer also display high concentrations. There is an obvious upwelling triggered uplift of NO_3-N in YD. However, due to the impact of the intensive seasonal thermocline and the complex currents system, QD only display a slight upwelling triggered uplift of NO_3-N.

Similar to NO_3-N, an obvious upwelling triggered uplift of phytoplankton can also be found in YD. Unlike NO_3-N, the maximum phytoplankton do not, in general, coincide with the intense YDU, but is lagged in time, by about 10 days. Moreover, high offshore velocities on the seaward side advect the upwelled water off the coast, which leads to the strong phytoplankton concentrations at about −30 m to −40 m water layer extending seaward from the inner shelf to about 30 km into outer shelf. Nevertheless, being affected by the intensive seasonal thermocline, maximum phytoplankton in QD is located within the thermocline, coupled to the nutricline. The chlorophyll *a* concentrations and distribution in YD and QD are exactly similar to phytoplankton. The chlorophyll *a* maxima at YD and QD coincide with the phytoplankton maxima, and hence the maximum chlorophyll *a* does not, in general, coincide with the minimum temperature; but are lagged in time, by about 10 days.

It should be noted that the summer coastal upwelling system in the NSCS is too complicated to understand it fully. According to its impacts on the temperature, salinity, nutrients, phytoplankton and chlorophyll *a* presented in this paper, the summer coastal upwelling system must have a

significant effect on the distribution of marine organisms and the protection of NSCS coastal environment.

Acknowledgements

This research was supported by the Strategic Priority Research Program of the Chinese Academy of Sciences (XDA10020225), the research project of State Key Laboratory of Tropical Oceanography, the National Natural Science Foundation of China (41430966), National Key Research and Development Program of China (2017FY100700) and the Projects of Guangzhou Science and Technology (201504010006). We deeply appreciate the journal editors and the two anonymous reviewers for their constructive comments and suggestion.

References

Botsford, L.W., Lawrence, C.A., Dever, E.P., Hastings, A., Largier, J., 2003. Wind strength and biological productivity in upwelling systems: an idealized study. Fish. Oceanogr. 12 (4–5), 245–259, http://dx.doi.org/10.1046/j.1365-2419.2003.00265.x.

Cai, P.H., Huang, Y.P., Chen, M., Guo, L.D., Liu, G.S., Qiu, Y.S., 2002. New production based on Ra-228-derived nutrient budgets and thorium-estimated POC export at the intercalibration station in the South China Sea. Deep-Sea Res. Pt. I 49 (1), 53–66, http://dx.doi.org/10.1016/S0967-0637(01)00040-1.

Casey, K.S., Cornillon, P., 1999. A comparison of satellite and in situ-based sea surface temperature climatologies. J. Clim. 12 (6), 1848–1863, http://dx.doi.org/10.1175/1520-0442(1999)012<1848:ACOSAI>2.0.CO;2.

Chelton, D.B., DeSzoeke, R.A., Schlax, M.G., El Naggar, K., Siwertz, N., 1998. Geographical variability of the first baroclinic Rossby radius of deformation. J. Phys. Oceanogr. 28 (3), 433–460, http://dx.doi.org/10.1175/1520-0485(1998)028<0433:GVOTFB>2.0.CO;2.

Chen, C.C., Shiah, F.K., Chung, S.W., Liu, K.K., 2006. Winter phytoplankton blooms in the shallow mixed layer of the South China Sea enhanced by upwelling. J. Mar. Syst. 59 (1–2), 97–110, http://dx.doi.org/10.1016/j.jmarsys.2005.09.002.

Chenillat, F., Riviere, P., Capet, X., Di Lorenzo, E., Blanke, B., 2012. North Pacific Gyre Oscillation modulates seasonal timing and ecosystem functioning in the California Current upwelling system. Geophys. Res. Lett. 39 (1), L15606, 6 pp., http://dx.doi.org/10.1029/2011GL049966.

Chenillat, F., Riviere, P., Capet, X., Franks, P.J.S., Blanke, B., 2013. California coastal upwelling onset variability: cross-shore and bottom-up propagation in the planktonic ecosystem. PLOS ONE 8 (5), e66281, 15 pp., http://dx.doi.org/10.1371/journal.pone.0062281.

Cropper, W.P., DiResta, D., 1999. Simulation of a Biscayne Bay, Florida commercial sponge population: effects of harvesting after Hurricane Andrew. Ecol. Model. 118 (1), 1–15, http://dx.doi.org/10.1016/S0304-3800(99)00039-3.

Davenport, E.D., Fan, C., Govoni, J.J., Anderson, J., 2012. Description and application of a NPZD Model to forecast hurricane impacts to secondary production in coastal ecosystems. Proc. Environ. Sci. 13, 1569–1584, http://dx.doi.org/10.1016/j.proenv.2012.01.149.

Dong, L.X., Sun, J.L., Wong, L.A., Cao, Z.Y., Chen, J.C., 2004. Seasonal variation and dynamics of the Pearl River plume. Cont. Shelf. Res. 24 (16), 1761–1777, http://dx.doi.org/10.1016/j.csr.2004.06.006.

Ehlert, C., Grasse, P., Frank, M., 2013. Changes in silicate utilisation and upwelling intensity off Peru since the Last Glacial Maximum – insights from silicon and neodymium isotopes. Quater. Sci. Rev. 72 (4), 18–35, http://dx.doi.org/10.1016/j.quascirev.2013.04.013.

Fan, W., Song, J.B., Li, S., 2014. A numerical study on seasonal variations of the thermocline in the South China Sea based on the ROMS. Acta Oceanol. Sin. 33 (7), 56–64, http://dx.doi.org/10.1007/s13131-014-0504-8.

Fennel, K., Boss, E., 2003. Subsurface maxima of phytoplankton and chlorophyll: steadystate solutions from a simple model. Limnol. Oceanogr. 48 (4), 1521–1534, http://dx.doi.org/10.4319/lo.2003.48.4.1521.

Fasham, M.J.R., Ducklow, H.W., Mckelvie, S.M., 1990. A nitrogen-based model of plankton in the oceanic mixed layer. J. Mar. Res. 48 (3), 591–639, http://dx.doi.org/10.1357/002224090784984678.

Fernandes, S.O., Halarnekar, R., Malik, A., Vijayan, V., Kumari, R., Jineesh, V.K., Gauns, M.U., Nair, S., LokaBharathi, P.A., 2014. Nitrate reducing activity pervades surface waters during upwelling. J. Mar. Syst. 137 (3), 35–46, http://dx.doi.org/10.1016/j.jmarsys.2014.04.011.

Freon, P., Barange, M., Aristegui, J., 2009. Eastern boundary upwelling ecosystems: integrative and comparative approaches preface. Prog. Oceanogr. 83 (1–4), 1–15, http://dx.doi.org/10.1016/j.pocean.2009.08.001.

Gan, J.P., Cheung, A., Guo, X.G., Li, L., 2009a. Intensified upwelling over a widened shelf in the northeastern South China Sea. J. Geophys. Res. 114 (C9), 2157–2165, http://dx.doi.org/10.1029/2007JC004660.

Gan, J.P., Lu, Z.M., Dai, M.H., Cheung, A.Y.Y., Liu, H.B., Paul, H., 2009b. Biological response to intensified upwelling and a river plume in the northeastern South China Sea: a modeling study. J. Geophys. Res. 115 (C9), 292–295, http://dx.doi.org/10.1029/2009JC005569.

González-Gil, R., González Taboada, F., Höfer, J., Anadón, R., 2015. Winter mixing and coastal upwelling drive long-term changes in zooplankton in the Bay of Biscay (1993–2010). J. Plankton Res. 37 (2), 337–351, http://dx.doi.org/10.1093/plankt/fbv001.

Heinle, A., Slawig, T., 2013. Internal dynamics of NPZD type ecosystem models. Ecol. Model. 254, 33–42, http://dx.doi.org/10.1016/j.ecolmodel.2013.01.012.

Hernández-Carrasco, I., Rossi, V., Hernández-García, E., Garcon, V., López, C., 2014. The reduction of plankton biomass induced by mesoscale stirring: a modeling study in the Benguela upwelling. Deep-Sea Res. Pt. I 839 (1), 65–80, http://dx.doi.org/10.1016/j.dsr.2013.09.003.

Huete-Ortega, M., Marañón, E., Varela, M., Bode, A., 2010. General patterns in the size scaling of phytoplankton abundance in coastal waters during a 10-year time series. J. Plankton Res. 32 (1), 1–14, http://dx.doi.org/10.1093/plankt/fbp104.

Jing, Z.Y., Qi, Y.Q., Hua, Z.L., 2008. Numerical study on summer upwelling over northern continental shelf of South China Sea. J. Trop. Oceanogr. 30 (6), 1068–1081, (in Chinese).

Joint, I., Inall, M., Torres, R., Figueiras, F.G., Alvarez-Salgado, X.A., Andrew, P.R., Woodward, E.M.S., 2001. Two Lagrangian experiments in the Iberian Upwelling System: tracking an upwelling event and an off-shore filament. Prog. Oceanogr. 51 (2–4), 221–248, http://dx.doi.org/10.1016/S0079-6611(01)00068-4.

Kononen, K., Hallfors, S., Kokkonen, M., Kuosa, H., Laanemets, J., Pavelson, J., Autio, R., 1998. Development of a subsurface chlorophyll maximum at the entrance to the Gulf of Finland, Baltic Sea. Limnol. Oceanogr. 43 (6), 1089–1106, http://dx.doi.org/10.4319/lo.1998.43.6.1089.

Krishna, K.M., 2008. Coastal upwelling along the southwest coast of India – ENSO modulation. Ann. Geophys. 26 (6), 123–134, http://dx.doi.org/10.5194/angeo-26-1331-2008.

Li, B.H., Jian, Z.M., 2001. Evolution of planktonic foraminifera and thermocline in the southern South China Sea since 12 Ma (ODP-184, Site 1143). Sci. China Ser. D – Earth Sci. 44 (10), 889–896, http://dx.doi.org/10.1007/BF02907080.

Li, R.H., Liu, S.M., Li, Y.W., Zhang, G.L., Ren, J.L., Zhang, J., 2014. Nutrient dynamics in tropical rivers, lagoons, and coastal ecosystems of eastern Hainan Island, South China Sea. Biogeosciences 11 (2), 481–506, http://dx.doi.org/10.5194/bg-11-481-2014.

Li, Y.N., Peng, S.Q., Yang, W., Wang, D.X., 2012. Numerical simulation of the structure and variation of upwelling off the east coast of Hainan Island using QuikSCAT winds. Chin. J. Oceanol. Limnol. 30 (6), 1068–1081, http://dx.doi.org/10.1007/s00343-012-1275-8.

Li, Q.P., Wang, Y.J., Dong, Y., Gan, J.P., 2015. Modeling long-term change of planktonic ecosystems in the northern South China Sea and the upstream Kuroshio Current. J. Geophys. Res. 120 (6), 3913–3936, http://dx.doi.org/10.1002/2014JC010609.

Liu, Q.Y., Jia, Y.L., Liu, P.H., Wang, Q., Chu, P.C., 2001. Seasonal and intraseasonal thermocline variability in the Central South China Sea. Geophys. Res. Lett. 28 (23), 4467–4470, http://dx.doi.org/10.1029/2001GL013185.

Lopes, J.F., Ferreira, J.A., Cardoso, A.C., Rocha, A.C., 2014. Variability of temperature and chlorophyll of the Iberian Peninsula near coastal ecosystem during an upwelling event for the present climate and a future climate scenario. J. Mar. Syst. 129 (1), 271–288, http://dx.doi.org/10.1016/j.jmarsys.2013.07.002.

Lu, Z.M., Gan, J.P., Dai, M.H., Cheung, A.Y.Y., 2010. The influence of coastal upwelling and a river plume on the subsurface chlorophyll maximum over the shelf of the northeastern South China Sea. J. Mar. Syst. 82 (1–2), 35–46, http://dx.doi.org/10.1016/j.jmarsys.2010.03.002.

MacIsaac, J.J., Dugdale, R.C., Barber, R.T., Blasco, D., Packard, T.T., 1985. Primary production cycle in an upwelling center. Deep-Sea Res. Pt. I 32 (5), 503–529, http://dx.doi.org/10.1016/0198-0149(85)90042-1.

Morton, B., Blackmore, G., 2000. South China Sea. Mar. Pollut. Bull. 42 (12), 1236–1263, http://dx.doi.org/10.1016/S0025-326X(01)00240-5.

Muller-Karger, F., Varela, R., Thunell, R., Scranton, M., Bohrer, R., Taylor, G., Capelo, J., Astor, Y., Tappa, E., Ho, T.Y., Walsh, J.J., 2001. Annual cycle of primary production in the Cariaco Basin: response to upwelling and implications for vertical export. J. Geophys. Res. 106 (C3), 4527–4542, http://dx.doi.org/10.1029/1999JC000291.

Ning, X., Chai, F., Xue, H., Cai, Y., Liu, C., Shi, J., 2004. Physical–biological oceanographic coupling influencing phytoplankton and primary production in the South China Sea. J. Geophys. Res. 109 (C10), 215–255, http://dx.doi.org/10.1029/2004JC002365.

Ogasawara, H., 2010. Accurate distribution and its asymptotic expansion for the tetrachoric correlation coefficient. J. Multivariate-Anal. 101 (4), 936–948, http://dx.doi.org/10.1016/j.jmva.2009.12.011.

Park, T.Y., Jang, I.S., Ha, Y.H., 2009. Banding artifact reduction with interweaving dot dispersion based on probability model and human visual system weighted root mean squared error in blue noise multilevel dithering. J. Imaging Sci. Technol. 53 (6), 60504-1–60504-13, http://dx.doi.org/10.2352/J.ImagingSci.Technol.2009.53.6.060504.

Penven, P., Debreu, L., Marchesiello, P., McWilliams, J.C., 2006. Evaluation and application of the ROMS 1-way embedding procedure to the central california upwelling system. Ocean Model. 12 (1–2), 157–187, http://dx.doi.org/10.1016/j.ocemod.2005.05.002.

Powell, T.M., Lewis, C.V.W., Curchitser, E.N., Haidvogel, D.B., Hermann, A.J., Dobbins, E.L., 2006. Results from a three-dimensional, nested biological-physical model of the California Current System and comparisons with statistics from satellite imagery. J. Geophys. Res. 111 (C7), 520–522, http://dx.doi.org/10.1029/2004JC002506.

Prego, R., Guzmán-Zuñiga, D., Varela, M., de Castro, M., Gómez-Gesteira, M., 2007. Consequences of winter upwelling events on biogeochemical and phytoplankton patterns in a western Galician ria (NW Iberian peninsula). Estuar. Coast. Shelf Sci. 73 (3–4), 409–422, http://dx.doi.org/10.1016/j.ecss.2007.02.004.

Riley, G.A., Stommel, H., 1949. Quantitative ecology of the plankton of the Western North Atlantic. Bull. Bingham Oceanogr. Collect. 12 (3), 1–169.

Ruzicka, J.J., Brink, K.H., Gifford, D.J., Bahr, F., 2016. A physically coupled end-to-end model platform for coastal ecosystems: simulating the effects of climate change and changing upwelling characteristics on the Northern California Current ecosystem. Ecol. Model. 331, 86–99, http://dx.doi.org/10.1016/j.ecolmodel.2016.01.018.

Santos, F., Gesteira, M.G., Decastro, M., 2011. Coastal and oceanic SST variability along the western Iberian Peninsula. Cont. Shelf. Res. 31 (19), 2012–2017, http://dx.doi.org/10.1016/j.csr.2011.10.005.

Sawant, S.S., Madhupratap, M., 1996. Seasonality and composition of phytoplankton in the Arabian Sea. Curr. Sci. India 71 (11), 869–873.

Shchepetkin, A.F., McWilliams, J.C., 2005. The regional oceanic modeling system (ROMS): a split-explicit, free-surface, topography-following-coordinate oceanic model. Ocean Model. 9 (4), 347–403, http://dx.doi.org/10.1016/j.ocemod.2004.08.002.

Shchepetkin, A.F., McWilliams, J.C., 1998. Quasi-monotone advection schemes based on explicit locally adaptive dissipation. Mon. Weather Rev. 126 (6), 1541–1580, http://dx.doi.org/10.1175/1520-0493(1998)126<1541:QMASBO>2.0.CO;2.

Song, X.Y., Lai, Z.G., Ji, R.B., Chen, C.S., Zhang, J.L., Huang, L.M., Yin, J.Q., Wang, Y.S., Lian, S.M., Zhu, X.M., 2012. Summertime primary production in northwest South China Sea: interaction of coastal eddy, upwelling and biological processes. Cont. Shelf. Res. 48 (1), 110–121, http://dx.doi.org/10.1016/j.csr.2012.07.016.

Song, X.Y., Liu, H., Huang, L., 2010. Distribution characteristics of basic biological production and its influencing factors in the northern South China Sea in summer. Acta Ecol. Sin. 30 (23), 6409–6417, http://dx.doi.org/1000-0933(2010)30:23<6409:NHBBXJ>2.0.TX;2-G.

Taylor, K.E., 2001. Summarizing multiple aspects of model performance in a single diagram. J. Geophys. Res. 106 (D7), 7183–7192, http://dx.doi.org/10.1029/2000JD900719.

Turner, J.T., Tester, P.A., 1997. Toxic marine phytoplankton, zooplankton grazers, and pelagic food webs. Limnol. Oceanogr. 42 (5), 1203–1214, http://dx.doi.org/10.4319/lo.1997.42.5_part_2.1203.

Vilhena, M.D.S.P., Costa, M.L.D., Berrêdo, J.F., Paiva, R.S., Almeida, P.D., 2014. Chemical composition of phytoplankton from the estuaries of Eastern Amazonia. Acta Amazon. 44 (4), 513–526, http://dx.doi.org/10.1590/1809-4392201305244.

Wang, Y.S., 2013. Quantitative Marine Ecology. Sci. Press, Beijing, 328–334.

Wang, D.X., Shu, Y.Q., Xue, H.J., Hu, J.Y., Chen, J., Zhuang, W., Zu, T.T., Xu, J.D., 2014a. Relative contributions of local wind and topography to the coastal upwelling intensity in the northern South China Sea. J. Geophys. Res. 119 (4), 2550–2567, http://dx.doi.org/10.1002/2013JC009172.

Wang, Q.Y., Wang, X.W., Xie, L.L., Shang, Q.T., Lu, Y., 2014b. Observed water current and transport through Qiongzhou Strait during August 2010. Chin. J. Oceanol. Limnol. 32 (2), 703–708, http://dx.doi.org/10.1007/s00343-014-3159-6.

Waniek, J.J., 2003. The role of physical forcing in initiation of spring blooms in the northeast Atlantic. J. Mar. Syst. 39 (1–2), 57–82, http://dx.doi.org/10.1016/S0924-7963(02)00248-8.

Woodson, C.B., Eerkes-Medrano, D.I., Flores-Morales, A., Foley, M.M., Henkel, S.K., Hessing-Lewis, M., Jacinto, D., Needles, L., Nishizaki, M.T., O'Leary, J., Ostrander, C.E., Pespeni, M., Schwager, K.B., Tyburczy, J.A., Weersing, K.A., Kirincich, A.R., Barth, J.A., McManus, M.A., Washburn, L., 2007. Local diurnal upwelling driven by sea breezes in northern Monterey Bay. Cont. Shelf. Res. 27 (18), 2289–2302, http://dx.doi.org/10.1016/j.csr.2007.05.014.

Wu, M.L., Wang, Y.S., 2007. Using chemometrics to evaluate anthropogenic effects in Daya Bay, China. Estuar. Coast. Shelf Sci. 72 (4), 732—742, http://dx.doi.org/10.1016/j.ecss.2006.11.032.

Yokomizo, H., Botsford, L.W., Holland, M.D., Lawrence, C.A., Hastings, A., 2010. Optimal wind patterns for biological production in shelf ecosystems driven by coastal upwelling. Theor. Ecol. -Neth. 3 (1), 53—63, http://dx.doi.org/10.1007/s12080-009-0053-5.

Yu, W.Q., 1987. A preliminary approach of the upwelling for the northern South China Sea. Mar. Sci. 6, 7—10.

Oceanologia (2018) 60, 52—64

Available online at www.sciencedirect.com

ScienceDirect

journal homepage: www.journals.elsevier.com/oceanologia/

ORIGINAL RESEARCH ARTICLE

Identifying the main sources of silicate in coastal waters of the Southern Gulf of Valencia (Western Mediterranean Sea)

Javier Sospedra [a,*], L. Felipe H. Niencheski [b], Silvia Falco [a], Carlos F.F. Andrade [b], Karina K. Attisano [c], Miguel Rodilla [a]

[a] *Institut d'Investigació per a la Gestió Integrada de Zones Costaneres (IGIC), Universitat Politècnica de València, Grau de Gandia, Spain*
[b] *Instituto de Oceanografia, Universidade Federal do Rio Grande, Rio Grande, Brazil*
[c] *Centro CEP, Campus São Lourenço do Sul, Universidade Federal do Rio Grande, São Lourenço do Sul, Brazil*

Received 31 January 2017; accepted 17 July 2017
Available online 1 August 2017

KEYWORDS
Silicon;
Silicate flux;
Silicon balance;
Biogenic silica;
Submarine groundwater discharge;
Nutrient

Summary Silicon is a major nutrient for siliceous primary producers, which can become a potential limiting nutrient in oligotrophic areas. Most of the silicon inputs to the marine environment come from continental discharges, from both superficial and ground waters. This study analyses the main sources of silicon and their dynamics along the southernmost 43 km of shoreline in the Gulf of Valencia (Western Mediterranean Sea). The salinity and silicate concentration in the different compartments (springs, freshwater wells, beach groundwater, surf zone and coastal waters) in this coastal area were determined. In addition, chlorophyll *a* and phytoplankton community were analyzed in the surf zone and coastal waters. Silicate concentrations in freshwater wells ranged between 130 and 150 μM, whereas concentrations of this nutrient declined to 49 μM in freshwater—seawater mixture transects. At the same time, there was a positive gradient in silicate for both freshwater and coastal waters southward. An amount of 18.7 t of dissolved silicate was estimated in the nearest first kilometre nearest to the coastline, 6 t of this silicate belonged to the background sea level. On the other hand, the sum of the main

* Corresponding author at: Institut d'Investigació per a la Gestió Integrada de Zones Costaneres (IGIC), Universitat Politècnica de València, Grau de Gandia 46730, Spain. Tel.: +34 962849448.
E-mail address: jasoscis@epsg.upv.es (J. Sospedra).
Peer review under the responsibility of Institute of Oceanology of the Polish Academy of Sciences.

Production and hosting by Elsevier

http://dx.doi.org/10.1016/j.oceano.2017.07.004

rivers in the area supplies 1.6 t of dissolved silicate per day. This implies that a large amount of the remaining 11.1 t must derive from submarine groundwater discharges, which would thus represent 59% of the coastal dissolved silicate budget. Overall, it is suggested that a subterranean transport pathway must contribute considerably to silicate concentrations throughout this zone, which is characterized as permeable.

1. Introduction

The Mediterranean Sea is an oligotrophic sea as a consequence of general water circulation (Schroeder et al., 2010; Zenetos et al., 2002). High evaporation exceeds freshwater inputs due to surface water warming and to the low humidity of continental winds. A significant surface inflow enters the Mediterranean basin through the Strait of Gibraltar to compensate for evaporation losses, producing a water exchange as a deep layer of water flows from the Mediterranean Sea to the Atlantic Ocean (Bergamasco and Malanotte-Rizzoli, 2010). Consequently, the nutrient balance between the Atlantic Ocean and the Mediterranean Sea generates a deficit in the latter. The surface flow entering the Mediterranean basin is poor in nutrients. Conversely, the Mediterranean Sea is continuously losing a large amount of nutrients through the nutrient-rich deep current that heads into the Atlantic Ocean, since solutes tend to accumulate in deeper layers (Crispi et al., 2001; Hopkins, 1985). For example, in the Strait of Gibraltar, silicate concentrations in the surface (Atlantic) waters and in the deep (Mediterranean) waters are around 2.7 and 7.7 μM respectively (Dafner et al., 2003).

Regarding nutrients, the demand for silicon by primary producers is not as great as it is for phosphorus or nitrogen. Nevertheless, the cycle of this nutrient has acquired significant attention in relation to its role in marine primary production in recent decades (Dugdale and Wilkerson, 2001; Smetacek, 1999). Only diatoms, one of the most abundant taxonomic groups of phytoplankton which play an important role in organic matter export to the deep sea, require silicon as much as nitrogen and phosphorus for their development (Buesseler, 1998; Goldman, 1993; Nelson et al., 1995). Other planktonic groups that present silification are chrysophytes and silicoflagellates, but their quantitative importance in the silicon cycle is secondary. Silicon concentrations in the Mediterranean Sea are generally low, around 1–4 μM due to its oligotrophy (Marty et al., 2002; Ribera d'Alcalà et al., 2009; Schroeder et al., 2010), decreasing to 0.003 μM in the Northeastern Levantine basin (Aktan, 2011).

In the Northwestern sub-basin of the Mediterranean Sea, phosphorus is considered to be the potential limiting nutrient (Gadea et al., 2013; Lucea et al., 2005; Sala et al., 2002). However, when silicon is also taken into consideration as a limiting element, which is the case for siliceous primary producers, silicate limitation may have become a widespread phenomenon in the Mediterranean Sea (Ludwig et al., 2009). For instance, Olivos et al. (2002) concluded that silicate acts as a potential limiting nutrient in over 50% of cases, with percentages as high as 75% for stations sampled near the coast (0.5–2 km), in their study carried out in the Catalan Sea (Northwestern Mediterranean Sea). Gadea et al. (2013) noted that the phytoplankton community in the southern sector of the Gulf of Valencia was dominated by diatoms mainly in autumn, winter and summer. Furthermore, they considered phosphorus as a potential limiting nutrient in the area, although silicon could also act as a limiting nutrient in over 30% of cases during winter campaigns.

Currently, the most important sources of dissolved silicate in the global ocean come from the continental fluvial system and from groundwater discharges, according to Frings et al. (2016). These inputs are mainly: dissolved silicate in rivers (60%), the dissolution of river particulate matter (20%) and groundwater (7%). The remaining silicate reaches seawater from atmospheric depositions, and from seabed alterations, or is washed there.

Rivers are important sources of freshwater and nutrients for the Mediterranean Sea. Many studies have pointed out that Mediterranean rivers have suffered a significant reduction in freshwater discharges between 1960 and 2000 (Ludwig et al., 2009; MED-HYCOS, 2001; Vörösmarty et al., 1998). This is in part due to more severe hydrological droughts, but mainly to the construction of dams, reservoirs and hydroelectric power plants, and flow derivation (García-Ruiz et al., 2011; Nixon, 2003). A similar decrease could also be expected for the fluxes of dissolved silicate, which are highly dependent on water discharges and potentially reduced by river damming as well (Conley et al., 2008; Humborg et al., 1997). Contrariwise, the fluxes of nitrogen and phosphorus in the Mediterranean Sea, have been significantly enhanced by anthropogenic sources (Howarth et al., 1996; Ludwig et al., 2009).

Submarine groundwater discharge (SGD) has been recognized as one of the largest sources of macro- and micronutrients in the coastal environment (Krest et al., 2000; Moore, 1999; Niencheski et al., 2007; Santos et al., 2008; Windom et al., 2006). Generally, nutrient concentrations in SGD are much higher than in rivers, compensating for the lower flow of groundwater in comparison with superficial runoff. Consequently, SGD transports nutrient amounts into the ocean that are comparable to superficial runoff inputs, or even higher, as is the case for the coast of Southern Brazil (Niencheski et al., 2014), the Eastern Florida Bay (Corbett et al., 1999, 2000) and the salt marshes on the South Carolina coast (Krest et al., 2000). In particular, Rodellas et al. (2015) found that along the entire Mediterranean coast silica inputs associated with SGD are comparable, in magnitude, to those from rivers.

Globally, atmospheric inputs represent *ca.* 3% of silicon discharges into oceans (Frings et al., 2016). In the Mediterranean region, a great number of studies about atmospheric depositions and their implications for primary production have been carried out. However, most of these researches have focused on nitrogen, phosphorus and trace metal inputs into the sea (Carbo et al., 2005; Guerzoni et al., 1997, 1999; Koçak et al., 2004; Theodosi et al., 2010). With regard to silicon, Koçak et al. (2010) stipulate that atmospheric inputs of this nutrient can represent up to 10% in the Northeastern Levantine basin of the Eastern Mediterranean Sea. On the other hand, de Fommervault et al. (2015), studying the Northwestern area of the Mediterranean Sea, highlight the insufficient amount of data (post 1990) of atmospheric deposition in order to draw conclusions. A single dust deposition event of short duration could represent up to 30% of the total annual flux for Si (Bergametti et al., 1989) due to the proximity of the Sahara in this Western basin.

The southern sector of the Gulf of Valencia (Western Mediterranean Sea) is characterized by oligotrophic conditions (Gadea et al., 2013; Sebastiá et al., 2013; Sebastiá and Rodilla, 2013) so nutrient inputs from various sources play a key role in marine productivity. However, in the case of silicon, many questions still need to be investigated in our study area: what is its origin? Is the silicate discharged by rivers enough to supply diatom populations? Otherwise, what are the other sources? In order to answer these questions, the present study aims to investigate silicate concentrations along the coastal zone of the southern sector of the Gulf of Valencia, and to identify the main sources. For this purpose, silicate concentrations were analyzed in different compartments throughout the studied area: in groundwater, in the main rivers, and in the coastal marine area. Furthermore, the silica requirement by phytoplanktonic microorganisms in coastal waters was also explored.

2. Study area and methods

2.1. Study area

The study area falls within the southernmost sector of the Gulf of Valencia and covers about 43 km of coastline from Cullera Cape to about 5 km south of the Racons River (Fig. 1). The Gulf of Valencia is in the Balearic Sea, Western Mediterranean Sea, off the eastern coast of Spain. The coastal area of this gulf is characterized by the dominance of sand barriers and coastal lagoons (quaternary origin) in which sand spits have formed on both sides of river mouths (Albarracín et al., 2013). The material deposition carried out by rivers over time has augmented the silting of coastal lagoons in this area, until they have become shallow swamps (Dupré et al., 1988). Representative examples of these habitats in the southern sector of this gulf are (from north to south) Valencia Albufera, the Southern Júcar, Safor, and Pego-Oliva wetlands (represented in dotted shading in Fig. 1).

Sandy beaches along the southern sector of the Gulf of Valencia border with fertile lowlands that are dedicated to rice crops and irrigated agriculture (mainly citrus fruits and vegetables) (Rico-Amorós and Hernández-Hernández, 2008; Sebastiá et al., 2012b). However, much of the territory has suffered from the process of urbanization (this is one of the most densely inhabited and touristic areas in Spain), which has occupied the barrier dunes and some floodable areas (Zornoza-Gallego, 2013).

The rivers that discharge into the sea along these 43 km are (from north to south) the Júcar, Serpis, Vedat and Racons (Fig. 1).

The Júcar and Serpis Rivers, of 508.8 and 74.5 km in length respectively, have a Mediterranean regime characterized by high seasonality, with a dry period during the summer, and a wet period with torrential downpours mainly in autumn (Falco et al., 2007; Sebastiá et al., 2013). In addition to the Mediterranean climate, these rivers undergo artificial regulation and intensive water use, leading to a situation of no permanent flow in their final sections.

The Júcar River is strictly controlled by dams, due to intensive agricultural exploitation upstream. This results in a flow that decreases along the river, until it disappears completely during some periods of the year at the last gauging station (the Cullera irrigation dam) belonging to the Júcar Hydrographic Confederation (CHJ) situated 14 km from the river mouth. Júcar river flow data for the last 10 years (from January 2006 to January 2016) was obtained from the Cullera gauging station (CHJ, 2016). In addition, the volume of water destined to the Cullera Community of Irrigators (CHJ, 2015) has to be subtracted from the flows that come to this dam, resulting in an average flow to the sea of 1.42 $m^3 s^{-1}$, over the last 10 years (2006—2016). This value may still be overestimated due to the presence, downstream, of the Júcar-Vinalopó diversion (currently with operating problems) and two motors which are also able to pump water from the river for irrigation (Cullera Community of Irrigators, personal communication).

The Serpis River and its tributary the Vernissa River are artificially regulated by a complex system of weirs and irrigation channels that provide freshwater for the irrigated crops of the Safor County. The estimated average flow (from the union of these rivers (CHJ, 2016) minus the extraction for irrigation systems, CHJ, 2015) that reached the sea was 1.94 $m^3 s^{-1}$ for the period between 2006 and 2016.

The Racons and Vedat Rivers, unlike the previous waterways, are short rivers of about 7 km that drain water from the Pego-Oliva wetland. Both rivers are mainly fed by springs and pumping drainage. For the period of 2004—2011, mean flows were estimated as 1.62 and 1.93 $m^3 s^{-1}$ in the Vedat and Racons Rivers respectively (IGME and DPA, 2013).

Regarding aquifers, in the study area, the Betic and Iberic structural domains meet (Rey and Fumanal, 1996), creating contact between the south of the Plana Valencia hydrogeological system — which is part of the Iberic domain — and the Prebetic of Valencia-Alicante hydrogeological system — which belongs to the Betic domain (IGME, 1989). These two hydrogeological systems can be observed in Fig. 1. In the northernmost region within the study area, the aquifer of the Southern Júcar wetland (Cullera) belonging to the Plana Valencia hydrogeological system, borders the Mediterranean Sea. Various subsystems can be distinguished in the Prebetic of Valencia-Alicante hydrogeological system, although the Plana Gandia-Dénia is the only one that comes into contact with the Mediterranean Sea in our study area. In the Plana Gandia-Dénia subsystem (250 km^2 extension), two aquifers can be identified: Xeraco-Gandia and Oliva-Pego. All these detritic aquifers in the study area are rich in nitrate, with

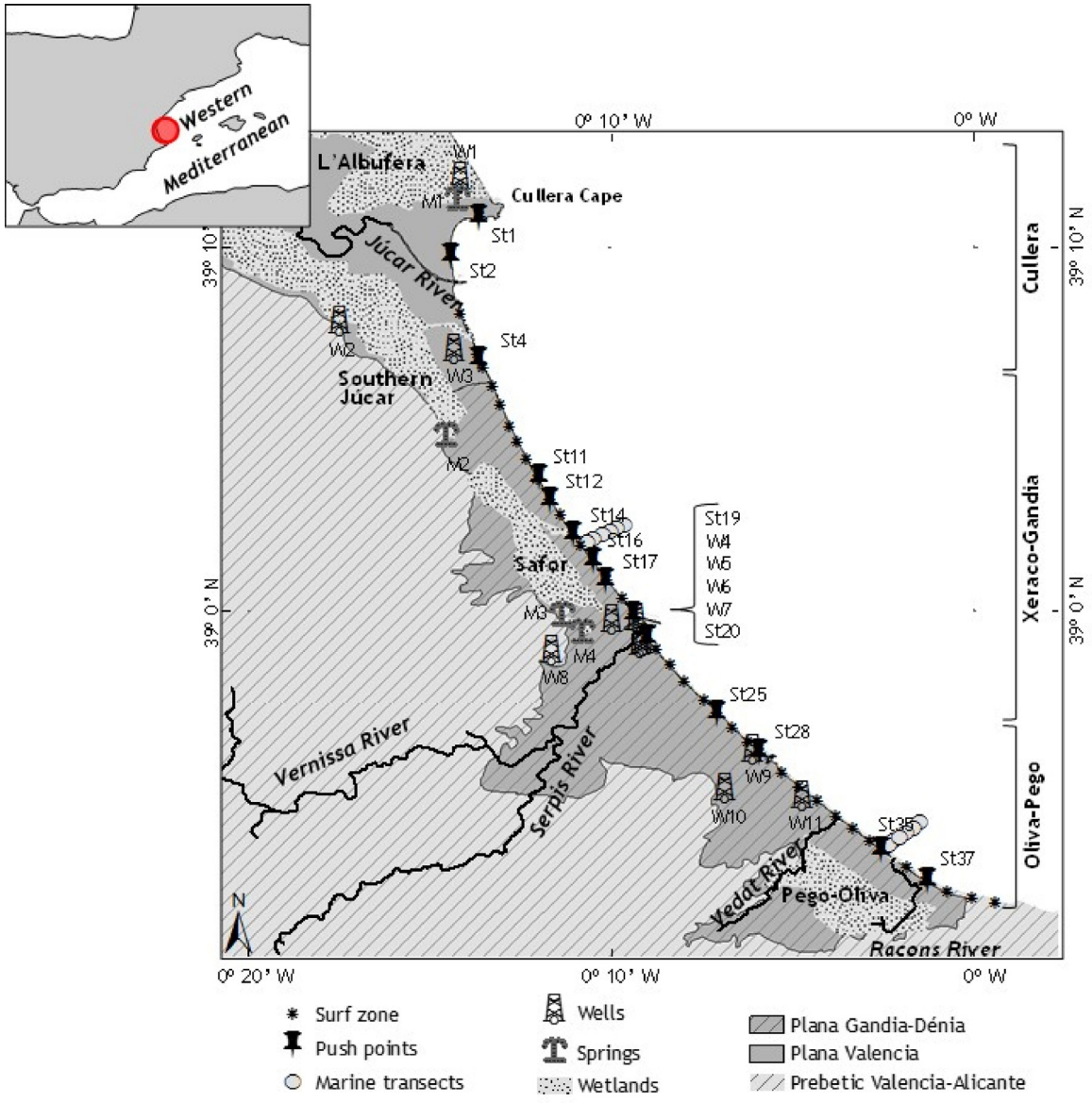

Figure 1 Study zone (asterisks and pins from St2 to St38: 2008 surf zone; pins: 2009 and 2013 push-point transects; circles: 2010 and 2013 sea transect; springs: 2013 springs; wells: 2013 permanent wells). St: sampled stations; W: sampled permanent freshwater wells; M: sampled springs.

values above 50 mg L^{-1} and even 200 mg L^{-1} in some zones (IGME and DPA, 2007; IGME, 1989; Pernía et al., 1996). The recommended nitrogen doses for citrus and horticultural crops have historically been exceeded in this area (MARM, 2010). In consequence, both surface runoff and groundwater flow are characterized by high nitrate concentrations and the areas have been declared as Nitrate Vulnerable Zones (MARM, 2010).

2.2. Field and laboratory methods

Various sampling campaigns were conducted in the study area between 2008 and 2013 (Table A in the online information). Sampling was designed taking into account that the Iberian Mediterranean rivers are characterized by high seasonality because of rainfall-based flow regime with maxima in autumn and spring and a minimum in summer (Sabater et al., 2009). For this reason, our sampling campaigns were carried out in autumn (two sampling campaigns in November 2008 and 2009), spring (June 2010 and March 2013) and the dry season (August 2012 and 2013).

The first sampling campaign was carried out in November 2008 (6th and 7th). Owing to the lack of a balanced spatial distribution of DSi data in the study area, 39 stations in the surf zone were sampled along 43 km of shoreline, approximately one at each kilometre along the entire shoreline, from St2, close to Cullera Cape, to St40, 5 km south of the Racons River (Fig. 1). These samples were analyzed for salinity, dissolved silicate (DSi) and chlorophyll *a* (Chl-*a*).

A new sampling campaign was designed in November 2009 (from 9th to 16th). The aim of this campaign was to cover the

entire study zone, with focus on the central area. Water samples were once again collected from the surf zone, in 11 of the previously sampled stations plus one more (St1) that was sampled for the first time at the northern part (pins St1, St2, St4, St11, St12, St14, St16, St17, St20, St25, St28 and St37 in Fig. 1). Perpendicular transects to the shoreline on the beach were also carried out in this campaign for sampling groundwater with a push-point piezometer system. Beach groundwater samples (1 m deep) were collected from the surf zone at 5, 10, 20, 30, 40, 50 and up to 70 m inland. This sampling strategy was aimed to obtain a groundwater salinity gradient, to verify if the biogeochemical processes behaved conservatively or not. Salinity and DSi were analyzed in all samples. Additionally, Chl-*a* and phytoplankton composition were determined in the surf zone samples.

In order to complete our dataset on the distribution of silicate in the coastal marine environment, two perpendicular transects to the coast (circles in St15 and St35, Fig. 1) were carried out in June 2010 (8th and 9th) at approximately 0, 400, 700, 1000, 1350, 1800 and 2100 m. Moreover, samples from the surf zone were collected in seven stations (St3, St8, St15, St22, St29, St35 and St40). Salinity, DSi and Chl-*a* were analyzed in all these samples.

In addition, in August 2012 and 2013, seawater samples were taken along 4 km of the southernmost shoreline, between the stations St32 and St37. In total, 13 points were collected: five at a distance of 200 m from shoreline, two points at 400 m, three at 600 m and three points at 800 m from the shore. Salinity, DSi, Chl-*a* and phytoplankton composition were analyzed in each sample.

The results acquired in the previous campaigns were decisive in the development of a more comprehensive sampling method in March 2013. This sampling campaign included 11 permanent groundwater wells (W1—W11), 4 springs (M1—M4) and 5 push-points (1 m deep) drilled at variable distances (between 20 and 40 m) across the beach to collect beach groundwater at intermediate salinity (between 10 and 15), at the stations St2, St15, St19, St25 and St35. Moreover, a perpendicular transect to the shoreline was sampled (at 0, 50, 100, 150, 200, 250, 300 m) in the sea at St19 (Fig. 1).

The surf zone water was sampled by wading to a depth of about 1 m and using a 2-L polyethylene bottle, and coastal water was sampled using a Niskin Teflon bottle.

A push-point piezometer system was used, similar to that used by Niencheski et al. (2007), to sample groundwater along the beach down to a depth of 1 m during the 2009 and 2013 sampling campaigns. The push-point system consisted of a stainless steel pipe through which a Teflon tube was passed and connected to the stainless steel, screened intake end. Samples were collected using a peristaltic pumping system.

Coastal water samples were collected in 2010, 2012 and 2013 across perpendicular transects to shore using a rubber boat. The first half metre below the sea surface was sampled using a Niskin Teflon bottle.

In the 2013 sampling campaign, groundwater from a permanent well and water from springs were collected using the same peristaltic pumping system described previously.

In the laboratory, salinity was determined by means of a multiparameter probe (Multi 340i/SET WTW). Water samples were filtered through a 0.45 μm pore diameter cellulose acetate filter and frozen in plastic bottles for later analysis. DSi was analyzed using the method described by Aminot and Chaussepied (1983). Chl-*a* was determined using the trichromatic method, based on spectrophotometry, according to APHA et al. (2012). The precision for Chl-*a* was 5%, whereas for DSi it was 3%.

Phytoplankton (Phyto) quantitative samples were placed in 125-mL jars and fixed *in situ* with 20% formaldehyde solution neutralized with hexamethylenetetramine (Throndsen, 1978). Sub-samples (50 mL) were allowed to settle for 24 h in HydroBios chambers and then counted and identified at ×400 magnifications with a Leica DMIL inverted microscope (Utermohl, 1958). Counts were made following the methodology of Andersen and Throndsen (2003). This did not include the small-size fraction of phytoplankton (picoplankton and some portion of the nanoplankton). The phytoplankton community was classified to the lowest taxonomic level possible, according to Tomas (1997).

2.3. Data processing and statistical analysis

In order to calculate the silicate budget in coastal waters, and to balance the data number along the 43 km of coastline, in addition to working with data collected at the surf zone and costal water in this study, we included more coastal water data. The coastal water data of DSi, Chl-*a* and the percentage of diatoms which cover a complete annual cycle (Falco et al., 2007; Gadea et al., 2013) were added to the northern and central sectors. Only data obtained from points located within the first kilometre of coastline were used, and those sites significantly influenced by fresh water (salinity <34.5 according to European Commission, 2013) were discarded from this calculation.

The biogenic silica estimate (biogenic Si) was explored according to Falco et al. (2010). It was based on the available percentage of diatoms within the phytoplankton community and the amount of chlorophyll *a*. An estimate of carbon content was made with reference to the relationship between carbon and chlorophyll (Ciotti et al., 1995). The average amount of silicate in the diatoms was calculated using the Redfield ratio (Redfield et al., 1963).

Non-parametric Kruskal—Wallis tests were conducted to assess statistically significant differences between regions (Cullera, Xeraco-Gandia and Oliva-Pego) for permanent wells, surf zone and coastal water samples. A *p*-value less than 0.05 was considered to indicate statistical significance. Multiple comparisons between groups were implemented using Bonferroni adjustment of *p*-values. Spearman—Rank correlation tests were performed in order to detect monotonic relationships between ranked variables in beach groundwater, surf zone and coastal water variables. These non-parametric tests were carried out with R statistical software.

3. Results

The main results presented below follow a chronological order within each subset.

3.1. Surf zone and beach groundwater

Table 1 presents the minimum, maximum and average values of salinity, DSi, Chl-*a* and phytoplankton density in the surf

Table 1 Minimum, maximum and average of salinity, dissolved silicate (DSi), chlorophyll *a* (Chl-*a*) and phytoplankton density and composition in the surf zone during 2008, 2009 and 2010. The name of the station is in parentheses.

Year		2008	2009	2010
Salinity	Min–Max	4.9(St20)–37.5(St3,St6,St23)	29.2(St4)–37.5(St14,St25)	33.4(St3)–36.7(St29)
	Avg.	35.1	35.9	35.9
DSi [μM]	Min–Max	1.8(St8)–47.4(St14)	2.7(St16)–42.5(St20)	3.3(St29)–19.6(St3)
	Avg.	8.9	11.5	7.9
Chl-*a* [μg L^{-1}]	Min–Max	0.41(St20)–12.78(St14)	0.76(St37)–5.60(St17)	–
	Avg.	1.90	1.91	–
Phyto [cells L^{-1}]	Min–Max	–	71,688(St4)–290,165(St20)	–
	Avg.	–	128,299	–
Diatom [%]	Min–Max	–	20(St20)–77(St14)	–
	Avg.	–	43	–

zone samples. In the 2008 campaign, it was observed that sampling stations with lower salinity values, St14 (5.6), St20 (4.9), St27 (34.9) and St36 (33.5), had the highest DSi concentration, 47.4, 32.2, 21.2 and 18.9 μM respectively. These low values of salinity were located, in most cases, in zones subject to the influence of rivers (St20 near to the Serpis River, St36 close to the Racons River) and to the drainage of irrigation channels. These variations were a consequence of the sampling strategy employed in this study. We tried to obtain a detailed study of the coast by collecting samples at every kilometre of shoreline, without taking into account the grouping of sampling stations based on freshwater input influence. Thus, Chl-*a* values ranged between 0.41 and 12.78 μg L^{-1} in St20 and St14 respectively, without any statistical correlation with salinity or DSi. On the other hand, when looking only at those samples with a salinity above 34.5 (assuming this value as a threshold between marine waters and those waters more influenced by continental discharges, as determined by the European Commission, 2013), a clear decrease in DSi average was observed for the surf waters (from 8.9 to 6.4 μM). The same trend was seen in Chl-*a*, with an average value of 1.6 μg L^{-1} in these high-salinity samples.

In the 2009 sampling campaign, Chl-*a* ranged between 0.76 and 5.60 μg L^{-1} (Table 1). As in the 2008 campaign, once again, no pattern was detected between salinity and Chl-*a*. In this campaign, the study of phytoplankton composition was added. On average, 43% of phytoplankton community was composed of diatoms. The two stations with the lowest salinity, St4 (29.2) and St20 (30.5), exhibited high DSi concentrations, 41.0 and 42.5 μM respectively. In the remaining 10 stations, salinity was greater than 34.5, and average DSi concentration decreased to 5.4 μM. This was remarkable, as DSi increased by one order of magnitude in those samples influenced by freshwater.

Thereby, we speculated that groundwater advection together with river contribution could be responsible for the high DSi concentrations. It should be emphasized that the rivers in this area exhibit a strong seasonal flow regime, producing a highly irregular contribution, whereas groundwater is discharged continuously. For this reason, beach piezometers were deployed along transects on the beach to collect groundwater at 1 m depth in the 12 stations sampled in 2009. Fig. 2A depicts salinity in beach groundwater at 1 m depth along the perpendicular transects from the coastline up to 70 m inland. This figure shows the existence of a subterranean estuary is clearly perceived, where permeable sediments provide a reaction zone in which freshwater and seawater are mixed in a similar way as occurs at the surface estuarine zone (Charette and Sholkovitz, 2006). Fig. 2B represents the DSi distribution along the saline gradient in the beach aquifer from the samples collected in these beach piezometers. It can be observed that there are greater DSi concentrations in freshwater samples than in marine waters, even more than one order of magnitude.

In 2010, the seven stations selected, among the 39 initially sampled stations, presented salinity and DSi concentrations within the intervals observed in preceding campaigns for surf zone samples (Table 1). In the same way as the 2008 and

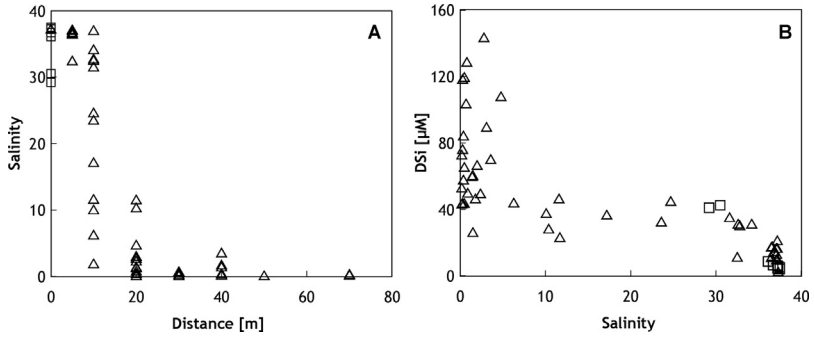

Figure 2 (A) Cross-beach profile in salinity from the surf zone (squares) and beach groundwater samples (triangles) collected in the 12 stations carried out in 2009. (B) Concentrations of dissolved silicate (DSi) in the surf zone (squares) and beach groundwater (triangles) in the 12 sampling stations, in samples from 2009.

2009 campaigns, there were samples with low salinity and high DSi (St03 with 33.4 and 9.6 μM). However, those samples with salinity above 34.5 — between 35.7 and 36.7 — showed an average DSi value of 5.9 μM, coinciding with the values previously observed, indicating a similar process.

3.2. Coastal waters

In the coastal marine environment, the two perpendicular transects to the coast carried out in Xeraco-Gandia (St15) and Oliva-Pego (St35) in 2010, showed negative gradients in DSi concentrations from the shoreline towards offshore. This is the pattern commonly found in other regions around the Mediterranean Sea (Aktan, 2011; Olivos et al., 2002), the continental influence on coastal waters being clearly visible.

Both sampling campaigns performed in coastal waters in Oliva-Pego during 2012 and 2013 were useful for increasing knowledge about DSi in the southern sector of the Gulf of Valencia. This nutrient showed an average value of 3.9 and 4.7 μM in 2012 and 2013 respectively. No sampling station presented salinity values influenced by freshwater surface inputs in these campaigns. Chl-*a* concentration was higher in 2012, with an average of 0.61 μg L^{-1}, while they were around 0.20 μg L^{-1} in 2013. In all stations sampled in these two campaigns, diatoms accounted for *ca*. 81% of the phytoplankton community.

In addition, another transect was made at St19 in 2013, where DSi values ranged from 0.7 to 11.2 μM, while there was not a clear DSi concentration gradient in coastal water, as was the case in 2010.

3.3. Groundwater in permanent wells and springs

The study area was divided into three regions, taking into account the different hydrogeological characteristics. From north to south, the first region, Cullera, is included within the hydrogeological system of Plana Valencia (from St1 to St5), while the other two regions, Xeraco-Gandia (from St6 to St26) and Oliva-Pego (from St27 to St40), belong to the Plana Gandia-Dénia hydrogeological subsystem (Fig. 1).

Table 2 depicts the average values of salinity and DSi in the sampled permanent wells. It is shown that groundwater DSi concentration was lower — but with higher salinity — in those permanent wells placed further north (130.2 μM), in Cullera. On the other hand, the highest DSi concentrations were determined towards the south, in the Oliva-Pego region (181.0 μM). Nonetheless, these differences were not statistically significant.

Regarding springs, it was not possible to detect any gradient among these data. The sample collected within the Cullera region presented a value of 180.3 μM and 3.0 for DSi and salinity respectively. The remaining three samples, collected in spring water bodies from Xeraco-Gandia, ranged between 98.7 and 149.8 μM of DSi and 0.1–0.2 for salinity.

4. Discussion

Fig. 3 shows all the water samples (surf zone, coastal area, push-points, permanent wells and springs) collected during the 2009, 2010, 2012 and 2013 campaigns. This figure depicts that DSi concentrations in aquifer groundwater — represented by permanent well samples (160.4 ± 51.6 μM) — are up to two orders of magnitude higher than in coastal waters, both in the surf zone (5.6 ± 1.9 μM) and in the coastal area (3.6 ± 1.9 μM). It is assumed that aquifer groundwater is able to supply high silicate amounts (a mean concentration in beach groundwater of 48.7 ± 32.5 μM) to the marine region by transporting submarine groundwater (SGD). This SGD can vary considerably due to rainfall and the hydrogeological features of aquifers (Tovar-Sánchez et al., 2014). For example, Tovar-Sánchez et al. (2014) observed that SGD from karstic aquifers is higher than SGD from detrital aquifers, being responsible for 75% of silicon fluxes in the Island of Majorca (Spain). In addition, aquifers in the study area supply springs with enriched silicate water (143.2 ± 33.7 μM) that may also reach the coastal environment through surface runoff.

Evident proof of water moving *via* a subterranean estuary is the distribution of DSi concentrations along the salinity gradient, supported by the superficial push-point piezometer transects on the sandy beach region (Fig. 2B). This pattern could also be observed beyond the beach zone from data collected in the central and southern coastal waters of the study area. Due to the lack of data in the northernmost region within the study area, it was necessary to resort to data obtained by Falco et al. (2007) to complete the knowledge of DSi distribution in the coastal marine environment.

With regard to the DSi sources in the coastal zone, rivers are an important source to take into consideration. In fact, rivers are responsible for 80% of dissolved silicate inputs to the ocean on a global scale. These sources include the dissolved silicate in river waters — which account for 60% of total inputs — and the subsequent dissolution of river particulate matter (20%) (Frings et al., 2016). Nonetheless, the river discharges into the sea are very low in the study area, amounting to zero throughout most of the year, due to the strict control of the main rivers by dams. Atmospheric inputs could be another source, although the lack of data concerning

Table 2 Salinity and dissolved silicate (DSi) in the permanent wells (*M*: mean and SD: standard deviation) sampled in 2013.

Region	Hydrogeological system/subsystem	Conductivity [μS cm^{-1}]		Salinity		DSi [μM]		Number of wells
		M	SD	*M*	SD	*M*	SD	
Cullera	Plana Valencia	1373	560	0.5	0.3	130.2	51.1	3
Xeraco-Gandia	Plana Gandia-Dénia	838	385	0.2	0.2	166.2	63.2	5
Oliva-Pego	Plana Gandia-Dénia	1142	797	0.4	0.5	181.0	24.9	3

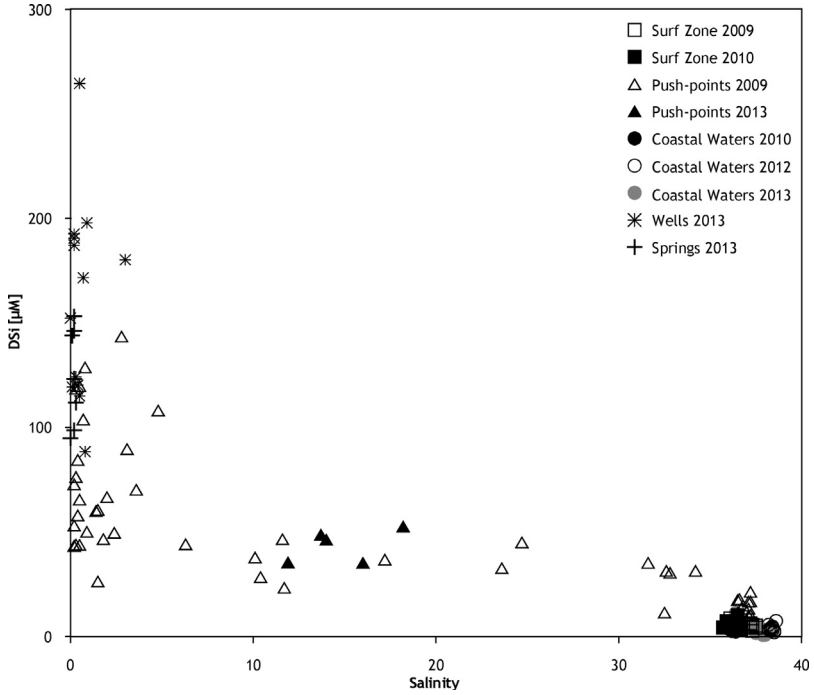

Figure 3 Scatter plot of dissolved silicate (DSi) concentrations in function of salinity from samples collected in the 2009, 2010, 2012 and 2013 campaigns (square: surf zone; triangle: push-point piezometer system; circle: coastal water; asterisk: permanent wells; cross: springs).

atmospheric fluxes of silicon in the Mediterranean do not allow for a proper assessment (Bartoli et al., 2005; de Fommervault et al., 2015). However, Koçak et al. (2010) calculated that silicon atmospheric fluxes could possibly account for as much as 10%, when comparing river inputs in the Northeastern Levantine basin. Marine bottoms could represent another source of silicate by means of benthic metabolism. The study area consists of permeable sands where Sospedra et al. (2015) determined that benthic silicate fluxes were not sufficient to supply the theoretical Si demand of microphytobenthos in a sampling station at 9 m depth. Thus, this nutrient must come from other sources. Therefore, it is assumed that there are other sources that could supply silicate to the coastal environment.

4.1. Submarine groundwater discharge

The conceptual model presented in Fig. 4 (modified from Niencheski et al., 2007) shows the silicate flux associated with the various water fluxes. These fluxes include: (1) fresh groundwater moving towards the ocean (F1), (2) SGD entering the ocean (F2), (3) seawater recirculating through permeable sediments (F3), and (4) the flux to the inner shelf (F4).

The groundwater flux pathway (F1) with a salinity end-member of 0.3, has an average DSi concentration of 160.4 µM (average in permanent wells). This groundwater is mixed with the coastal waters (F3) which have 36.8 of salinity and 5.6 µM of DSi (mean values in the 2009 and 2010 surf zone) as they advance towards the sea. It results in a conservative

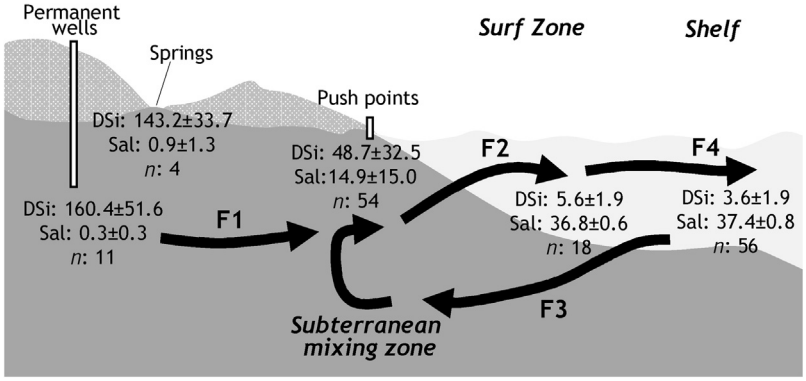

Figure 4 Conceptual model (not to scale) of silicate flux in the coastal surface water-groundwater system, based on Niencheski et al. (2007). The average and standard deviation of dissolved silicate (in µM), salinity and number of samples are shown for each compartment.

mixing process, therefore, the coastal region is supplied by continental groundwater enriched in silicate (F2) with an average concentration of 49 μM for an average salinity of 15 (values in 2009 and 2013 beach groundwater). Finally, the silicate-enriched water originating from this groundwater mixing zone is transported to the continental shelf (F4) with a mean of 37.4 and 3.6 μM of salinity and silicate respectively (values in the coastal waters of 2010, 2012 and 2013).

This conceptual model of how the submarine groundwater discharges Si flux is maintained as follows: there is a continual supply of silicate in fresh groundwater moving towards the coastline driven by local and/or regional hydraulic gradients. The Plana Valencia system and Plana Gandia-Dénia subsystem certainly provide local hydraulic gradients resulting in groundwater flow towards the Mediterranean Sea along a *ca*. 43 km length of coastline (IGME, 1989). The beach surface is dominated by sands – permeable sediments – where SGD is evident. It is suggested, however, that the dynamic circulation of seawater through the permeable beach sand allows a significant amount of silicate to escape into the surf zone with the SGD.

4.2. Silicate budget in coastal waters

As groundwater fluxes in this coastal area are unknown, it was investigated whether river contributions could be enough to support seawater silicate including silicate contained within phytoplankton. For this purpose, silicate fluxes (Si_DSi) for each river in the study area were calculated by multiplying mean river flows with the mean DSi concentrations and assuming that DSi concentrations were representative of conditions in these rivers. This method of flux calculation was selected because of the limited available data (GESAMP, 1987). Afterwards, silicate fluxes were multiplied by a conversion factor to express them in t d^{-1}. From these calculations, it was observed that silicate flux in the Júcar River was 0.3 t d^{-1}, whereas in the Serpis, Vedat and Racons Rivers these mass fluxes were *ca*. 0.4 t d^{-1} for each of them. In the case of the Júcar River, this value may still be overestimated due to the presence, downstream, of the Júcar-Vinalopó diversion (currently with operating problems) and two motors which are also able to pump water from the river for irrigation (Cullera Community of Irrigators, personal communication). The sum of these fluxes represents a total input towards the sea of 1.56 t d^{-1} in the whole study area (Table 3). In the Mediterranean Sea, other rivers with similar flows discharge similar amounts of Si to the sea. For example, the Pamisos River (Greece), the Rižana River (Slovenia) and the Lamas River (Turkey), with an average flow about 3 m^3 s^{-1}, deliver 0.9 t d^{-1} (Pavlidou et al., 2014), 0.5 t d^{-1} (from Cozzi and Giani, 2011) and 0.8 t d^{-1} (from Koçak et al., 2010), respectively.

Mean salinity, DSi, Chl-*a* concentrations and percentage of diatoms were estimated in each of the three regions for the first kilometre nearest to the coast and along the 43 km of coastline (Table 4) based on the work of Sebastiá et al. (2012a), which determined that the highest concentrations of chlorophyll *a* are observed in the 1000 m nearest to the coast. For this purpose, coastal water data from Cullera (Falco et al., 2007) and Gandia (Gadea et al., 2013) were also used. Those points significantly influenced by freshwater (salinity <34.5) were discarded. Regarding DSi, higher concentrations were clearly observed in Oliva-Pego, followed by Xeraco-Gandia and Cullera, showing statistically significant differences ($p < 0.01$) between the three regions. The increasing trend from north to south along the coastline might have matched with river DSi inputs, as higher discharges were displayed in the Oliva-Pego region (Table 3). Furthermore, this gradient could also correspond to the observed pattern for permanent wells (Table 2). This would suggest a connection between SGD and coastal waters where SGD could represent a significant percentage of Si contribution to the marine ecosystem.

The DSi content (t) for each region, could be estimated (Table 5) from the water volume (calculated from the shoreline length in each area (Table 4) and assuming that depth increases progressively up to 10 m at 1 km from the shoreline) and the DSi mean in each region (Table 4). Moreover, biogenic Si content was also calculated from the diatom percentage within the phytoplankton community (Table 4) and its corresponding Chl-*a* amount, assuming that all groups have similar levels of Chl-*a*. Diatom chlorophyll *a* was converted into carbon units using C:Chl-*a* 50: 1 ratio (Ciotti et al., 1995) and converted to Si moles according to the Redfield ratio (C:Si, 106:16) (Redfield et al., 1963) in order to estimate the biogenic Si belonging to diatoms in each of the three regions (Table 5). Finally, the total Si content for each region was obtained from the sum of dissolved Si and biogenic Si content. A total silicon amount of 21.3 t was estimated for the

Table 3 Mean discharges (*Q*) their corresponding period (*Q* period), mean dissolved silicate concentrations (DSi) and silicate fluxes (Si_DSi flux). The study region corresponding to each river is shown in parentheses.

Rivers (region)	*Q* period	*Q* [m^3 s^{-1}]	DSi [μM]	Si_DSi flux [t d^{-1}]
Júcar (Cullera)	2006–2016	1.42	87.8[a]	0.30
Serpis (Xeraco-Gandia)	2006–2016	1.94	93.3[b]	0.44
Vedat (Oliva-Pego)	2004–2011	1.62	96.0[c]	0.38
Racons (Oliva-Pego)	2004–2011	1.93	96.0[c]	0.45
Total				1.56

Sources:
[a] Falco et al. (2007).
[b] Sebastiá and Rodilla (2013).
[c] Values measured in 2010.

Table 4 Mean salinity, dissolved silicate (DSi) and chlorophyll *a* (Chl-*a*) concentrations and percentage of diatoms in the nearest kilometre to the coast in each region within the southern sector of the Gulf of Valencia.

	Cullera (n = 70)	Xeraco-Gandia (n = 101)	Oliva-Pego (n = 45)	Gulf of Valencia (southern sector)
Coastline [km]	10.0	21.3	11.9	43.2
Salinity	37.1	37.3	36.9	37.1
DSi [μM]	1.7	2.8	4.9	3.1
Chl-*a* [μg L^{-1}]	1.87	0.96	1.28	1.26
% Diatoms [%]	46.7	62.0	52.4	55.8

Values for the southern sector of the Gulf of Valencia were calculated as a weighted average from the three regions sampled, depending on their coastline length. These results are provided from data collected at the surf zone and coastal waters during 2008, 2009, 2010, 2012 and 2013 and Falco et al. (2007) and Gadea et al. (2013). The number of samples in each region are shown in brackets.

Table 5 Dissolved and biogenic Si content in the nearest kilometre to the coast in each study region and in the whole southern sector of the Gulf of Valencia.

	Cullera	Xeraco-Gandia	Oliva	Gulf of Valencia (southern sector)
Dissolved Si content [t]	2.4	8.2	8.1	18.7
Biogenic Si content [t]	0.8	1.1	0.7	2.6
Total Si content [t]	3.2	9.3	8.8	21.3

waterbody along the study area. Only 2.6 t were related with biogenic Si, which represent 13% of the total budget in the water column. This point implies that there is a sufficient amount of DSi to maintain diatom population in the study area, so the diatom community should have not been heavily dependent on continental inputs of this nutrient.

To study dissolved silicate sources within the nearest 1000 m to the coast in the study zone, the background level of this nutrient in seawater should be subtracted from the 18.7 t (Table 5). According to the data obtained by Sebastiá et al. (2013), which analyzed seawater quality in a sampling station placed in the central zone of the study area — approximately 9 km from the coastline — with low terrestrial input influence, a background level of 1 μM was assumed. Following this approach, there is a background level of 6 t within the study area (by multiplying the sea background concentration and the water volume in the first kilometre along the 43 km of shoreline), so it would be only necessary to justify an additional amount of 12.7 t of the 18.7 t dissolved. The local rivers in the study area — Júcar, Serpis, Vedat and Racons — discharge a total flux of 1.56 t d^{-1} into the sea (Table 3), requiring *ca.* 8 days to supply all this additional amount of Si through river inputs. The remaining 11.1 t (59% of dissolved silicate) could be related to SGD.

The amount discharged by local rivers — 1.56 t d^{-1} — must be increased by a groundwater flow enriched in silicate (F2, Fig. 4). This groundwater discharge, with mean values of 15 and 49 μM for salinity and DSi respectively, contributes to the increased Si concentration in the coastal region. Based on groundwater DSi content, it is speculated that the Plana Gandia-Dénia subsystem produces higher groundwater fluxes than the Plana Valencia system due to the higher Si concentrations found in southern sampling stations.

5. Conclusions

The coastal aquifers placed within the hydrogeological system of Plana Valencia and the subsystem of Plana Gandia-Dénia presented DSi values between 130 and 180 μM, displaying a positive gradient from north to south. The aquifers discharged into the coastal zone with an average salinity of 15 and a DSi concentration of 49 μM. Coastal waters have a mean DSi concentration of 3.1 μM, meaning that a continental influence is present when compared to concentrations obtained in Mediterranean Sea offshore waters. This continental influence could be more evident in those points located further south, where the highest DSi values were detected. The positive gradient observed corresponded with the DSi trend in coastal aquifers, so that SGD may represent an important percentage of Si inputs to the marine ecosystem. The silica requirement of diatoms in coastal waters was *ca.* 2.6 t, clearly lower than the amount dissolved (18.7 t). From this dissolved pool, nearly 6 t came from marine waters, 1.6 t from rivers and the rest must be provided by the SGD (59% of dissolved silicate in the first kilometre of the coast). There is obviously great uncertainty in these estimates because of the inherent heterogeneity of this system in time and space. This includes both temporal and spatial variability in silicon concentrations and advective transport. Constraining our estimates will require a considerable amount of additional work, including the use of isotopes of radium to assess SGD flux and cross-shelf transport.

Acknowledgments

The authors acknowledge the financial support for this study from the CNPq (Brazil — Grant 303672/2013-7). We are very

grateful for the valuable comments of anonymous reviewers on previous versions of the manuscript.

Appendix A. Supplementary data

Supplementary data associated with this article can be found, in the online version, at doi:10.1016/j.oceano.2017.07.004.

References

Aktan, Y., 2011. Large-scale patterns in summer surface water phytoplankton (except picophytoplankton) in the Eastern Mediterranean. Estuar. Coast. Shelf Sci. 91 (1), 551—558, http://dx.doi.org/10.1016/j.ecss.2010.12.010.

Albarracín, S., Alcántara-Carrió, J., Barranco, A., García, M.J.S., Bouzas, Á.F., Salgado, J.R., 2013. Seismic evidence for the preservation of several stacked Pleistocene coastal barrier/lagoon systems on the Gulf of Valencia continental shelf (western Mediterranean). Geo-Mar. Lett. 33 (2—3), 217—223, http://dx.doi.org/10.1007/s00367-012-0315-x.

Aminot, A., Chaussepied, M., 1983. Manuel des analyses chimiques en milieu marin. Centre National pour l'Explotation des Oceans, Brest, 396 pp.

Andersen, P., Throndsen, J., 2003. Estimating cell numbers. In: Hallegraef, G.M., Anderson, D.M., Cembella, A.D. (Eds.), Manual on Harmful Marine Microalgae. Intergovernmental Oceanographic Commission of UNESCO, Paris, 99—129.

APHA, AWWA, WEF, American Public Health, American Water Works Association, Water Environment Federation, 2012. Standard Methods for the Examination of Water and Wastewater, 22nd ed. American Public Health Association, Washington, 1360 pp.

Bartoli, G., Migon, C., Losno, R., 2005. Atmospheric input of dissolved inorganic phosphorus and silicon to the coastal northwestern Mediterranean Sea: fluxes, variability and possible impact on phytoplankton dynamics. Deep-Sea Res. Pt. I 52 (11), 2005—2016, http://dx.doi.org/10.1016/j.dsr.2005.06.006.

Bergamasco, A., Malanotte-Rizzoli, P., 2010. The circulation of the Mediterranean Sea: a historical review of experimental investigations. Adv. Oceanogr. Limnol. 1 (1), 11—28, http://dx.doi.org/10.1080/19475721.2010.491656.

Bergametti, G., Gomes, L., Remoudaki, E., Desbois, M., Martin, D., Buat-Ménard, P., 1989. Present transport and deposition patterns of African dusts to the north-western Mediterraneann. In: Leinen, M., Sarnthein, M. (Eds.), Paleoclimatology and Paleometeorology: Modern and Past Patterns of Global Atmospheric Transport. Kluwer Academic, Dordrecht, 227—252.

Buesseler, K.O., 1998. The decoupling of production and particulate export in the surface ocean. Glob. Biogeochem. Cycl. 12 (2), 297—310, http://dx.doi.org/10.1029/97GB03366.

Carbo, P., Krom, M.D., Homoky, W.B., Benning, L.G., Herut, B., 2005. Impact of atmospheric deposition on N and P geochemistry in the southeastern Levantine basin. Deep-Sea Res. Pt. II 52 (22—23), 3041—3053, http://dx.doi.org/10.1016/j.dsr2.2005.08.014.

Charette, M.A., Sholkovitz, E.R., 2006. Trace element cycling in a subterranean estuary: Part 2, Geochemistry of the pore water. Geochim. Cosmochim. Acta 70 (4), 811—826, http://dx.doi.org/10.1016/j.gca.2005.10.019.

CHJ, Confederación Hidrográfica del Júcar, 2015. Plan hidrológico de la demarcación hidrográfica del Júcar. Memoria-Anejo 3 Usos y demandas de agua, Ciclo de planificación hidrológica 2015—2021, Available from: http://www.chj.es/es-es/medioambiente/planificacionhidrologica/Paginas/PHC-2015-2021-Plan-Hidrologico-cuenca.aspx (accessed 01.04.16).

CHJ, Confederación Hidrográfica del Júcar, 2016. http://www.chj.es/es-es/ciudadano/modelossolicitud/Paginas/modelos-y-hojas-informativas.aspx (accessed 01.04.16).

Ciotti, A.M., Odebrecht, C., Fillmann, G., Möller Jr., O.O., 1995. Freshwater outflow and Subtropical Convergence influence on phytoplankton biomass on the southern Brazilian continental shelf. Cont. Shelf Res. 15 (14), 1737—1756, http://dx.doi.org/10.1016/0278-4343(94)00091-Z.

Conley, D.J., Likens, G.E., Buso, D.C., Saccone, L., Bailey, S.W., Johnson, C.E., 2008. Deforestation causes increased dissolved silicate losses in the Hubbard Brook Experimental Forest. Glob. Change Biol. 14 (11), 2548—2554, http://dx.doi.org/10.1111/j.1365-2486.2008.01667.x.

Corbett, D.R., Chanton, J., Burnett, W., Dillon, K., Rutkowski, C., Fourqurean, J., 1999. Patterns of groundwater discharge into Florida Bay. Limnol. Oceanogr. 44 (4), 1045—1055, http://dx.doi.org/10.4319/lo.1999.44.4.1045.

Corbett, D.R., Dillon, K., Burnett, W., Chanton, J., 2000. Estimating the groundwater contribution into Florida Bay via natural tracers ^{222}Rn and CH_4. Limnol. Oceanogr. 45 (7), 1546—1557, http://dx.doi.org/10.4319/lo.2000.45.7.1546.

Cozzi, S., Giani, M., 2011. River water and nutrient discharges in the Northern Adriatic Sea: current importance and long term changes. Cont. Shelf. Res. 31 (18), 1881—1893, http://dx.doi.org/10.1016/j.csr.2011.08.010.

Crispi, G., Mosetti, R., Solidoro, C., Crise, A., 2001. Nutrients cycling in Mediterranean basins: the role of the biological pump in the trophic regime. Ecol. Model. 138 (1—3), 101—114, http://dx.doi.org/10.1016/S0304-3800(00)00396-3.

Dafner, E.V., Boscolo, R., Bryden, H.L., 2003. The N:Si:P molar ratio in the Strait of Gibraltar. Geophys. Res. Lett. 30 (10), 1506, http://dx.doi.org/10.1029/2002GL016274.

de Fommervault, O.P., Migon, C., d'Alcalà, M.R., Coppola, L., 2015. Temporal variability of nutrient concentrations in the northwestern Mediterranean sea (DYFAMED time-series station). Deep-Sea Res. Pt. I 100, 1—12, http://dx.doi.org/10.1016/j.dsr.;1; 2015.02.006.

Dugdale, R.C., Wilkerson, F.P., 2001. Sources and fates of silicon in the ocean: the role of diatoms in the climate and glacial cycles. Sci. Mar. 65 (2), 141—152.

Dupré, M., Fumanal, M.P., Sanjaume, E., Santisteban, C., Usera, J., Viñals, M.J., 1988. Quaternary evolution of the Pego coastal lagoon (Southern Valencia, Spain). Palaeogeogr. Palaeoclimatol. Palaeoecol. 68 (2—4), 291—299, http://dx.doi.org/10.1016/0031-0182(88)90046-6.

European Commission, 2013. Commission Decision of 20 September 2013 establishing, pursuant to Directive 2000/60/EC of the European Parliament and of the Council, the values of the Member State monitoring system classifications as a result of the intercalibration exercise and repealing Decision 2008/915/EC. Off. J. Eur. Union L266, 1—47.

Falco, S., Hermosilla, Z., Romero, I., Martínez, R., Sierra, J.P., Mösso, C., Mestres, M., 2007. Spatial and temporal patterns of water quality in Cullera Bay. J. Coastal Res. 47 (SI), 40—47, http://dx.doi.org/10.2112/1551-5036-47.sp1.40.

Falco, S., Niencheski, L.F., Rodilla, M., Romero, I., del Río, J.G., Sierra, J.P., Mösso, C., 2010. Nutrient flux and budget in the Ebro estuary. Estuar. Coast. Shelf Sci. 87 (1), 92—102, http://dx.doi.org/10.1016/j.ecss.2009.12.020.

Frings, P.J., Clymans, W., Fontorbe, G., Christina, L., Conley, D.J., 2016. The continental Si cycle and its impact on the ocean Si isotope budget. Chem. Geol. 425, 12—36, http://dx.doi.org/10.1016/j.chemgeo.2016.01.020.

Gadea, I., Rodilla, M., Sospedra, J., Falco, S., Morata, T., 2013. Seasonal dynamics of the phytoplankton community in the Gandia coastal area, southern Gulf of Valencia. Thalassas 29 (1), 35—58.

García-Ruiz, J.M., López-Moreno, J.I., Vicente-Serrano, S.M., Lasanta-Martínez, T., Beguería, S., 2011. Mediterranean water resources in a global change scenario. Earth Sci. Rev. 105 (3—4), 121—139, http://dx.doi.org/10.1016/j.earscirev.2011.01.006.

GESAMP, Joint Group of Experts on the Scientific Aspects of Marine Environmental Protection, 1987. Land/Sea Boundary Flux of Contaminants: Contributions from Rivers, Report and Studies No. 32. UNESCO/GESAMP, 172 pp.

Goldman, J.C., 1993. Potential role of large oceanic diatoms in new primary production. Deep-Sea Res. Pt. I 40 (1), 159—168, http://dx.doi.org/10.1016/0967-0637(93)90059-C.

Guerzoni, S., Molinaroli, E., Chester, R., 1997. Saharan dust inputs to the western Mediterranean Sea: depositional patterns, geochemistry and sedimentological implications. Deep-Sea Res. Pt. II 44 (3—4), 631—654, http://dx.doi.org/10.1016/S0967-0645(96)00096-3.

Guerzoni, S., Chester, R., Dulac, F., Herut, B., Loÿe-Pilot, M.-D., Measures, C., Migon, C., Molinaroli, E., Moulin, C., Rossini, P., Saydam, C., Soudine, A., Ziveri, P., 1999. The role of atmospheric deposition in the biogeochemistry of the Mediterranean Sea. Prog. Oceanogr. 44 (1—3), 147—190, http://dx.doi.org/10.1016/S0079-6611(99)00024-5.

Hopkins, T.S., 1985. Physics of the sea. In: Margalef, R. (Ed.), Western Mediterranean. Pergamon Press, Oxford, 100—125.

Howarth, R.W., Billen, G., Swaney, D., Townsend, A., Jaworski, N., Lajtha, K., Downing, J.A., Elmgren, R., Caraco, N., Jordan, T., Berendse, F., 1996. Regional nitrogen budgets and riverine N & P fluxes for the drainages to the North Atlantic Ocean: natural and human influences. Biogeochemistry 35 (1), 75—139, http://dx.doi.org/10.1007/BF02179825.

Humborg, C., Ittekkot, V., Cociasu, A., Bodungen, B., 1997. Effect of Danube River dam on Black Sea biogeochemistry and ecosystem structure. Nature 386, 385—388, http://dx.doi.org/10.1038/386385a0.

IGME, Instituto Geológico y Minero de España, 1989. Las aguas subterráneas en la Comunidad Valenciana. Uso, calidad y perspectivas de utilización. IGME, Madrid, 298 pp.

IGME, Instituto Geológico y Minero de España, DPA, Diputación Provincial de Alicante, 2007. Determinación de la relación entre zonas húmedas y acuíferos asociados mediante modelos de flujos y transporte. Aplicación a la gestión sostenible del acuífero Pego-Dénia. IGME, Alicante, 241 pp.

IGME, Instituto Geológico y Minero de España, DPA, Diputación Provincial de Alicante, 2013. Modelo de densidad variable en régimen transitorio del acuífero Pego-Oliva. 110 pp.

Koçak, M., Nimmo, M., Kubilay, N., Herut, B., 2004. Spatio-temporal aerosol trace metal concentrations and sources in the Levantine Basin of the Eastern Mediterranean. Atmos. Environ. 38 (14), 213—2144, http://dx.doi.org/10.1016/j.atmosenv.2004.01.020.

Koçak, M., Kubilay, N., Tugrul, S., Mihalopoulos, N., 2010. Atmospheric nutrient inputs to the northern levantine basin from a long-term observation: sources and comparison with riverine inputs. Biogeosciences 7 (12), 4037—4050, http://dx.doi.org/10.5194/bg-7-4037-2010.

Krest, J.M., Moore, W.S., Gardner, L.R., Morris, J., 2000. Marsh nutrient export supplied by groundwater discharge: evidence from Ra measurements. Glob. Biogeochem. Cycl. 14 (1), 167—176, http://dx.doi.org/10.1029/1999GB001197.

Lucea, A., Duarte, C.M., Agustí, S., Kennedy, H., 2005. Nutrient dynamics and ecosystem metabolism in the Bay of Blanes (NW Mediterranean). Biogeochemistry 73 (2), 303—323, http://dx.doi.org/10.1007/s10533-004-0059-4.

Ludwig, W., Dumont, E., Meybeck, M., Heussner, S., 2009. River discharges of water and nutrients to the Mediterranean and Black Sea: major drivers for ecosystem changes during past and future decades? Prog. Oceanogr. 80 (3—4), 199—217, http://dx.doi.org/10.1016/j.pocean.2009.02.001.

MARM, Ministerio de Medio Ambiente, Medio Rural y Marino, 2010. Guía práctica de la fertilización racional de los cultivos en España, Ministerio de Medio Ambiente y Medio Rural y Marino, Secretaría General Técnica. Centro de publicaciones, 259 pp.

Marty, J.-C., Chiavérini, J., Pizay, M.-D., Avril, B., 2002. Seasonal and interannual dynamics of nutrients and phytoplankton pigments in the western Mediterranean Sea at the DYFAMED time-series station (1991—1999). Deep-Sea Res. Pt. II 49 (11), 1965—1985, http://dx.doi.org/10.1016/S0967-0645(02)00022-X.

MED-HYCOS, The Mediterranean Hydrological Cycle Observing System, 2001. MED-HYCOS period II, period 2002—2005, Rep. no. 17. p. 36.

Moore, W.S., 1999. The subterranean estuary: a reaction zone of groundwater and sea water. Mar. Chem. 65 (1—2), 111—126, http://dx.doi.org/10.1016/S0304-4203(99)00014-6.

Nelson, D.M., Tréguer, P., Brzezinski, M.A., Leynaert, A., Quéguiner, B., 1995. Production and dissolution of biogenic silica in the ocean: revised global estimates, comparison with regional data and relationship to biogenic sedimentation. Glob. Biogeochem. Cycl. 9 (3), 359—372, http://dx.doi.org/10.1029/95GB01070.

Niencheski, L.F.H., Windom, H.L., Moore, W.S., Jahnke, R.A., 2007. Submarine groundwater discharge of nutrients to the ocean along a coastal lagoon barrier, Southern Brazil. Mar. Chem. 106 (3—4), 546—561, http://dx.doi.org/10.1016/j.marchem.2007.06.004.

Niencheski, L.F.H., Windom, H.L., Moore, W.S., 2014. Controls on water column chemistry of the southern Brazilian continental shelf. Cont. Shelf. Res. 88, 126—139, http://dx.doi.org/10.1016/j.csr.2014.07.007.

Nixon, S.W., 2003. Replacing the Nile: are anthropogenic nutrients providing the fertility once brought to the Mediterranean by a great river? Ambio 32, 30—39.

Olivos, A., Masó, M., Camp, J., 2002. Continental runoff of nutrients and their possible influence over stoichiometric ratios (DIN:P:Si) in the northeastern Mediterranean waters of Spain (Catalan Sea). Cienc. Mar. 28, 393—406.

Pavlidou, A., Papadopoulos, V.P., Hatzianestis, I., Simboura, N., Patiris, D., Tsabaris, C., 2014. Chemical inputs from a karstic submarine groundwater discharge (SGD) into an oligotrophic Mediterranean coastal area. Sci. Total Environ. 488—489, 1—13.

Pernía, J.M., Cuesta, F., Ballesteros, B., Barba-Romero, J., García, E., 1996. Los recursos hídricos en la Comunidad Valenciana. IGME, p. 77.

Redfield, A.C., Ketchum, B.H., Richards, F.A., 1963. The influence of organisms on the composition of sea-water. In: Hill, M.N. (Ed.), The Sea, vol. 2. Wiley Interscience, New York, 26—77.

Rey, J., Fumanal, M.P., 1996. The Valencian coast (western Mediterranean): neotectonics and geomorphology. Quat. Sci. Rev. 15 (8—9), 789—802, http://dx.doi.org/10.1016/S0277-3791(96)00069-8.

Ribera d'Alcalà, M., Brunet, C., Conversano, F., Corato, F., Lavezza, R., 2009. Nutrient and pigment distributions in the southern Tyrrhenian Sea during mid-summer and late fall 2005. Deep-Sea Res. Pt. II 56 (11—12), 676—686, http://dx.doi.org/10.1016/j.dsr2.2008.07.028.

Rico-Amorós, M., Hernández-Hernández, M., 2008. Ordenación del territorio, escasez de recursos hídricos, competencia de usos e intensificación de las demandas urbano-turísticas en la Comunidad Valenciana. Doc. Anàl. Geogr. 51, 79—109.

Rodellas, V., Garcia-Orellana, J., Masqué, P., Feldman, M., Weinstein, Y., 2015. Submarine groundwater discharge as a major source of nutrients to the Mediterranean Sea. Proc. Natl. Acad. Sci. U. S. A. 112 (13), 3926—3930, http://dx.doi.org/10.1073/pnas.1419049112.

Sabater, S., Feio, M.J., Graça, M.A.S., Muñoz, I., Romaní, A.M., 2009. The Iberian rivers. In: Tockner, K., Uehlinger, U., Robinson, C.T. (Eds.), Rivers of Europe. Acad. Press, London, 113—150.

Sala, M.M., Peters, F., Gasol, J.M., Pedrós-Alió, C., Marrasé, C., Vaqué, D., 2002. Seasonal and spatial variations in the nutrient limitation of bacterioplankton growth in the northwestern Mediterranean. Aquat. Microb. Ecol. 27 (1), 47—56.

Santos, I.R., Machado, M.I.C.S., Niencheski, L.F., Burnett, W., Milani, I., Andrade, C., Peterson, R., Chanton, J., Baisch, P., 2008. Major ion chemistry in a freshwater coastal lagoon from Southern Brazil (Mangueira Lagoon): Influence of groundwater inputs. Aquat. Geochem. 14 (2), 133—146, http://dx.doi.org/10.1007/s10498-008-9029-0.

Schroeder, K., Gasparini, G.P., Borghini, M., Cerrati, G., Delfanti, R., 2010. Biogeochemical tracers and fluxes in the Western Mediter-

ranean Sea, spring 2005. J. Mar. Syst. 80 (1—2), 8—24, http://dx.doi.org/10.1016/j.jmarsys.2009.08.002.

Sebastiá, M.T., Rodilla, M., 2013. Nutrient and phytoplankton analysis of a Mediterranean Coastal area. Environ. Manage. 51 (1), 225—240, http://dx.doi.org/10.1007/s00267-012-9986-3.

Sebastiá, M.T., Estornell, J., Rodilla, M., Martí, J., Falco, S., 2012a. Estimation of chlorophyll «A» on the Mediterranean coast using a QuickBird image. Rev. Teledetec. 37, 23—33.

Sebastiá, M.T., Rodilla, M., Sanchis, J.A., Altur, V., Gadea, I., Falco, S., 2012b. Influence of nutrient inputs from a wetland dominated by agriculture on the phytoplankton community in a shallow harbour at the Spanish Mediterranean coast. Agric. Ecosyst. Environ. 152, 10—20, http://dx.doi.org/10.1016/j.agee.2012.02.006.

Sebastiá, M.T., Rodilla, M., Falco, S., Sanchis, J.A., 2013. Analysis of the effects of wet and dry seasons on a Mediterranean river basin: consequences for coastal waters and its quality management. Ocean Coast. Manage. 78, 45—55, http://dx.doi.org/10.1016/j.ocecoaman.2013.03.012.

Smetacek, V., 1999. Diatoms and the ocean carbon cycle. Protist 150 (1), 25—32, http://dx.doi.org/10.1016/S1434-4610(99)70006-4.

Sospedra, J., Falco, S., Morata, T., Gadea, I., Rodilla, M., 2015. Benthic fluxes of oxygen and nutrients in sublittoral fine sands in a north-western Mediterranean coastal area. Cont. Shelf. Res. 97, 32—42, http://dx.doi.org/10.1016/j.csr.2015.02.002.

Theodosi, C., Markaki, Z., Mihalopoulos, N., 2010. Iron speciation, solubility and temporal variability in wet and dry deposition in the Eastern Mediterranean. Mar. Chem. 120 (1—4), 100—107, http://dx.doi.org/10.1016/j.marchem.2008.05.004.

Throndsen, J., 1978. Preservation and storage. In: Sournia, A. (Ed.), Phytoplankton Manual. UNESCO, Paris, 69—74.

Tomas, C., 1997. Identifying Marine Phytoplankton. Acad. Press Inc., London, 858 pp.

Tovar-Sánchez, A., Basterretxea, G., Rodellas, V., Sánchez-Quiles, D., García-Orellana, J., Masqué, P., Jordi, A., López, J.M., Garcia-Solsona, E., 2014. Contribution of groundwater discharge to the coastal dissolved nutrients and trace metal concentration in Majorca Island: karstic vs detrital systems. Environ. Sci. Technol. 48, 11819—11827.

Utermohl, H., 1958. Zur wervollkommung der quantitative phytoplankton methodic. Mitteilungen-Internationale Vereininung für Limnology 9, 1—38.

Vörösmarty, C.J., Fekete, B.M., Tucker, B.A., 1998. Global River Discharge 1807—1991, RivDIS v1.1, Available from: https://daac.ornl.gov/cgi-bin/dsviewer.pl?ds_id=199.

Windom, H., Moore, W.S., Niencheski, L.F., Jahnke, R., 2006. Submarine groundwater discharge: a large, previously unrecognized source of dissolved iron to the South Atlantic Ocean. Mar. Chem. 102 (3—4), 252—266, http://dx.doi.org/10.1016/j.marchem.2006.06.016.

Zenetos, A., Siokou-Frangou, I., Gotsis-Skretas, O., 2002. The Mediterranean Sea — blue oxygen-rich, nutrient-poor waters. Europe's Biodiversity: biogeographical regions and seas. Eur. Environ. Agency 22.

Zornoza-Gallego, C., 2013. Crecimiento urbanístico en la zona costera de la Comunidad Valenciana (1987-2009): análisis y perspectivas de futuro, vol. 12. Universitat de València, Valencia, 117 pp.

Oceanologia (2018) 60, 65—75

Available online at www.sciencedirect.com

ScienceDirect

journal homepage: www.journals.elsevier.com/oceanologia/

ORIGINAL RESEARCH ARTICLE

Inherent optical properties and particulate matter distribution in summer season in waters of Hornsund and Kongsfjordenen, Spitsbergen

Sławomir Sagan *, **Mirosław Darecki**

Institute of Oceanology, Polish Academy of Sciences, Sopot, Poland

Received 23 July 2016; accepted 26 July 2017
Available online 12 August 2017

KEYWORDS
Optical properties;
Particles;
Hornsund;
Kongsfjordenen

Summary Two Spitsbergen fjords, Hornsund and Kongsfjorden, are known for being under different hydrological regimes. The first is cold, separated from warm Atlantic water by East Spitsbergen Current, while Kongsfjorden is frequently penetrated by relatively warm Atlantic water. On the other hand, both are under strong influence of water discharge from glaciers and land freshwater input. During the period of observation in both fjords a dominant water mass was Surface Water, which originates mainly from glacial melt. The presence of suspended matter introduced with melt water in Surface Water is reflected by highest values of light attenuation and absorption coefficients recorded in areas close to glacier both in Hornsund and Kongsfjorden. In Hornsund the maximum light attenuation coefficient $c_{pg}(555)$ was 5.817 m^{-1} and coefficient of light absorption by particles $a_p(676)$ = 0.10 m^{-1}. In Kongsfjorden the corresponding values were 26.5 m^{-1} and 0.223 m^{-1}. In Kongsfjorden suspended matter of the size class 20—200 μm dominated over fractions smaller than 20 μm while in Hornsund dominating size fraction was 2—20 μm. The results provide an evidence of considerable range of variability of the optical properties mainly due to glacial and riverine runoff. The scale of variability of particulate matter in Kongsfjorden is bigger than in Hornsund. Most of the variability in Hornsund can be attributed to glaciers discharge and a presence of particles of mineral origin, while in Kongsfjorden the organic and mineral particles contribute almost equally to defining the optical properties of water.

* Corresponding author at: Powstańców Warszawy 55, 81-712 Sopot, Poland. Tel.: +48 587311811.
E-mail address: sagan@iopan.gda.pl (S. Sagan).
Peer review under the responsibility of Institute of Oceanology of the Polish Academy of Sciences.

Production and hosting by Elsevier

http://dx.doi.org/10.1016/j.oceano.2017.07.006

1. Introduction

In recent years Spitsbergen fjords have received special attention as potentially sensitive areas to ongoing climate change and global warming (Pavlov et al., 2013; Węsławski et al., 2017; Wlodarska-Kowalczuk and Weslawski, 2001). Observed ice retreat and intensified glacier melt (Muckenhuber et al., 2016), discharging particulate matter to the surrounding waters affect light penetration and its availability, thus changing underwater light climate for photosynthetic processes. Rising air temperatures increase the supply of fresh water to the fjords, which increases local stratification and reduce vertical mixing (Kohler et al., 2007; Mortensen et al., 2013). This may have an effect on underwater light distribution, if particulate matter locked in upper surface layer prevents light penetration into deeper layers (Pegau, 2002). Changes in quantity and type of sediment discharged by retreating glaciers may alter biological climate in fjords and may also be interpreted as another sign of long term warming processes. The changes are expected to be especially visible while comparing the areas of known contrasting hydrological regimes, as in the case of Hornsund and Kongsfjorden, Spitsbergen (Ormańczyk et al., 2017; Piwosz et al., 2009). The first is relatively cold, separated from warm Atlantic water by East Spitsbergen Current (Rudels et al., 2005), while the latter is easily but irregularly penetrated by relatively warm Atlantic water (Cottier et al., 2010; Inall et al., 2015).

The aim of the study is to examine the differences and similarities of the optical properties and characteristics of particulate suspensions in fjords waters in relation to water masses and locations of sampling – vicinity of the glaciers, possibly affected by glacial runoff, inner and outer fjord areas, thus along the expected gradient of change. The study aims to set up a baseline of optical properties that may be used as a reference for future observation or modeling of effects of climate warming.

2. Material and methods

The presented material was collected in 2009 between 22nd and 26th of July in Hornsund and 30th of July to 1st of August in Kongsfjorden; in 2010 between 22nd and 25th of July in Hornsund, and 30th to 31st of July in Kongsfjorden. In both campaigns sampling was performed in the same locations. Altogether 11 stations were visited in Hornsund and 9 stations in Kongsfjorden in 2009–2010 (Fig. 1). Stations were grouped according to their location in fjords: glacier stations (H1, HR3, B1, B2, KB5, Ml2), inner stations in the middle of the fjords (H2, HR1, HR2, KB2, KB3) and outer stations, located at the entrance to the fjords (H4, Auk, KB1, KB0). The stations were sampled from the surface down to 110 m depth. Altogether 903 samples were collected in Kongsfjorden and 1002 samples in Hornsund.

Spectral light attenuation $c(\lambda)$ and absorption $a(\lambda)$ coefficients (inherent optical properties of water, IOP), salinity and temperature were measured in situ, with an instrument package consisting of an ac-9plus meter (WET Labs Inc., USA) and a Seabird SBE 49 FastCAT probe (Seabird Electronics, USA). Vertical sampling resolution was ~30 cm. Absorption a and beam attenuation c coefficients were measured at nine wavelengths; 412, 440, 488, 510, 532, 555, 650, 676 and 715 nm. Dynamic range of the meter is of 0.001–10.0 m^{-1}. Temperature and salinity corrections were applied to the signal, (Sullivan et al., 2006), as well as required correction for scattering (Zaneveld et al., 1994). The instrument was calibrated in ultrapure water and routinely checked for stability with air-readings. Every 3–6 casts all the optical elements of the sensors were routinely cleaned.

The light attenuation and absorption coefficients are linked by relation $c(\lambda) = a(\lambda) + b(\lambda)$, where $b(\lambda)$ is light scattering coefficient. Total absorption is a sum of absorption by pure water and water components, $a(\lambda) = a_w(\lambda) + a_p(\lambda) + a_g(\lambda)$, where index w denotes water, p – particles as a mixture of phytoplankton and non-pigmented particles, referred also as non-algal particles, *NAP*, and g, referred as *gelbstoff* – colored dissolved organic material (*CDOM*). Since ac-9plus meter is calibrated with pure water as a reference, output values of coefficients of absorption and attenuation do not account for the absorption or scattering by the water. Light absorption by dissolved organics and non-pigmented particles decay toward the red part of the light spectrum (Babin et al., 2003a; Bowers and Binding, 2006). In the investigated waters $a_g(676)$ and $a_{NAP}(676)$ may be considered negligible in case of the presence of phytoplankton, which absorbs light on 676 nm (Nima et al., 2016; Pavlov et al., 2015). In result, light absorption coefficient by particles $a_p(676)$ predominantly reflects the presence of the living organic.

Light scattering by particles, characterized by scattering coefficient $b_p(\lambda) = c_{pg}(\lambda) - a_{pg}(\lambda)$, depends on particles' size, shape, internal composition and origin – organic or mineral (Stramski et al., 2004). Light scattering in natural waters, which contain varying mixture of particles of different types and origin, is either weakly wavelength dependent (higher scattering in blue, lower in red) or spectrally neutral (Babin et al., 2003b). The contribution to scattering of organic particles, which have refraction index similar to that of surrounding water, is weaker than this of mineral particles. Model results suggest that all the planktonic components contribute to 17–20% of total scattering coefficient $b_p(\lambda)$ (Stramski et al., 2001). The value of $b_p(555)$ may be used as an indicator of a total particulate matter. The mid-spectrum wavelength of 555 nm is chosen to minimize dependency on type of particles and to avoid the effect of anomalous dispersion occurring around pigment absorption bands, (van de Hulst, 1957). Consequently, the ratio of $b_p(555)/a_p(676)$ was used as a proxy index of bulk particles composition where high/low ratio reflects the predomination of mineral/organic particles.

The particle volume concentration (PVC, microliter per liter [$\mu L\ L^{-1}$]) was measured with the Laser In Situ Scattering and Transmissometry (LISST), Sequoia Scientific, which was coupled with an optical probe. The instrument measures the light scattered by particles on 32 ring detectors arranged as to intercept light scattered at 32 different angles from a collimated laser beam (emission 670 nm) in 32 logarithmically spaced size classes ranging in diameter from 1.25 to 250 μm (Agrawal and Pottsmith, 2000). In this study, 32 discrete LISST size bins were grouped into three size classes. Without presumption about the actual origin of observed particles there was adopted classification proposed by Sieburth et al. (1978) for the separation of planktonic organisms into

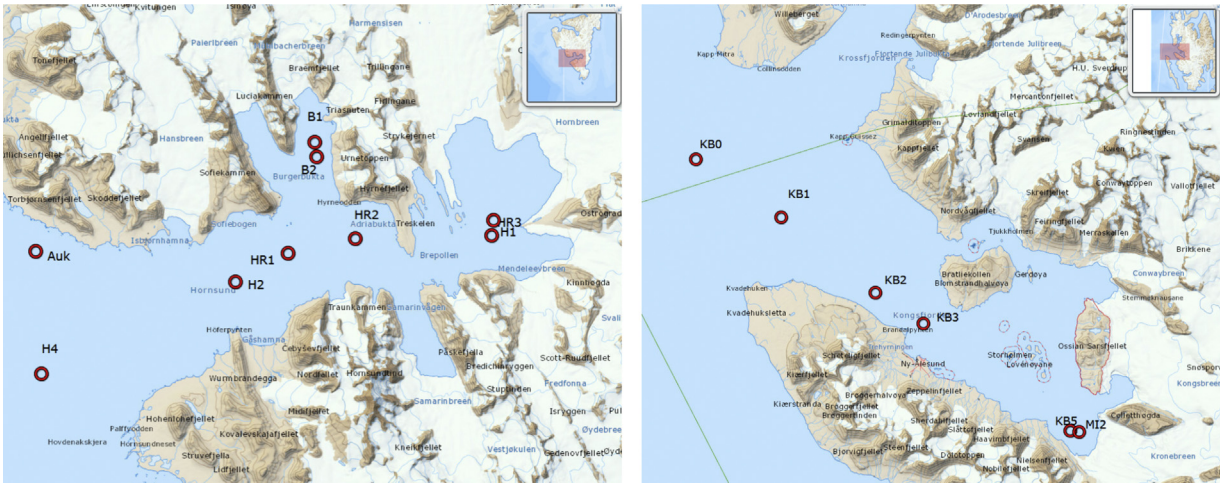

Figure 1 Sampling stations in Hornsund (left panel) and Kongsfjorden (right panel). Maps (http://toposvalbard.npolar.no/) were used with courtesy of Norwegian Polar Institute.

picoplankton (0.2–2 μm), nanoplankton (2–20 μm), and microplankton (20–200) μm.

3. Results and discussion

3.1. Hydrological background

Collected temperature and salinity data were plotted on the T–S diagram against a classification of Cottier et al. (2005) (Fig. 2). Classification, which was developed for water masses of Kongsfjorden, was applied also for Hornsund waters, as the physical processes governing water mass formation in different Arctic fjords are similar (Cottier et al., 2010). According to classification, the Surface Water (SW), which forms from glacial melt and is dominant in late spring and summer (Svendsen et al., 2002), is defined by salinity <34.00 and temperature >1.0. In Hornsund, on stations H1 and HR3, which were located close to the glacier, salinities in the water surface layer were below 33, so even if their temperatures were below 1°C, qualifying them for Local Waters (LW), these waters were also included in SW (Fig. 2). In all three groups of stations, located close to glacier, inner and outer stations, SW waters were found on depths from 0 m to 77 m in Hornsund, and from 0 m to 43 m in Kongsfjorden. Altogether, close to 50% of all recorded data of temperature and salinity were qualified as SW domain. Mean values of salinity in SW in Hornsund and Kongsfjorden were similar, 33.16 and 33.05, respectively, however mean values of temperature were higher in Kongsfjorden, 4.01°C compared to 1.58°C in Hornsund. This tally with numerous previous observations (as Cottier et al., 2010; Piwosz et al., 2009; Weslawski et al., 1991), categorizing Kongsfjorden as a 'warm' and Hornsund as a 'cold' fjord. Intermediate Water (IW) were found in Hornsund on inner stations on depths of 50–110 m, and on all stations in Kongsfjorden on depths 16–71 m. Waters of T–S characteristics of Local Water (LW), which apparently are formed during the autumn and winter (Cottier et al., 2005) were found on inner stations in Hornsund on depths of 40–110 m, and on all stations in Kongsfjorden on depths 40–110 m. Winter-cooled Water (WCW) was recorded in Kongsfjorden, on all stations on depths below 68 m, and in Hornsund on glacier stations on depths below 77 m. Many observations confirm frequent inflow of AW into Kongsfjorden (Cottier et al., 2005; Saloranta and Svendsen, 2001) and its relation with phytoplankton blooms (Hegseth and Tverberg, 2013), however during the period of observation AW and Transformed Atlantic Waters (TAW) were found only in 2010 in Kongsfjorden. About 16% of temperature and salinity recorded in Kongsfjorden fall in AW domain. AW was present on the outer stations KB0, depths > 40 m, KB1, depths > 65 m and inner station KB2, depths > 65 m. There were only 5 records of TAW, which were included to AW

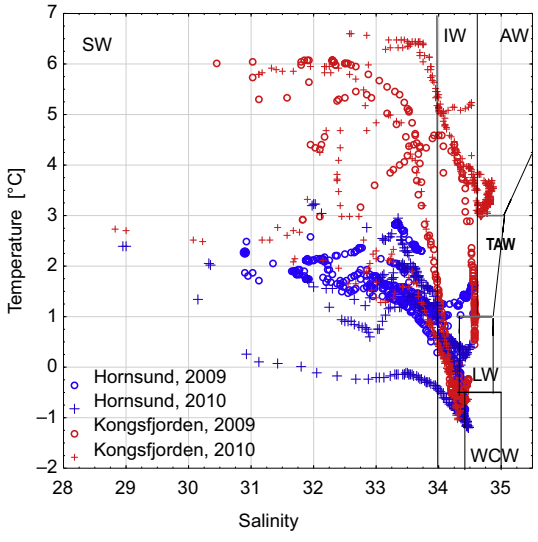

Figure 2 T–S diagram of the water masses that have been identified in Hornsund (blue) and Kongsfjorden (red) during campaigns in 2009 (rings) and 2010 (crosses). SW – Surface Water, IW – Intermediate Water, LW – Local Water, WCW – Winter-cooled Water, AW – Atlantic Water, TAW – Transformed Atlantic Water. The water mass classification applied was of Cottier et al. (2005). (For interpretation of the references to color in this figure legend, the reader is referred to the web version of the article.)

domain. No waters of characteristics of AW or TAW were found in Hornsund. As it is seen in Fig. 2, temperature and salinity in Hornsund (blue marks) and Kongsfjorden (red marks) display the same characteristics in 2009 and 2010, so in the further analyses optical and hydrological data from both years were clustered together.

3.2. Optical properties of the water masses in the inner and outer parts of the fjords

During the period of observation in both fjords a dominant water mass was Surface Water, which originates mainly from glacial melt. This is reflected by highest values of attenuation and absorption coefficients recorded in SW both in Hornsund and Kongsfjorden. In Hornsund the mean light attenuation coefficient $c_{pg}(555)$, mid-part of the light spectrum, is 1.155 m^{-1} with corresponding absorption $a_{pg}(555)$ = 0.038 m^{-1}, (Table 1). In SW in Kongsfjorden the values are 2.418 m^{-1} and 0.149 m^{-1}, respectively. Maximum values observed on stations close to the glacier in Kongsfjorden, exceeded 30.0 m^{-1}, which is well beyond the nominal dynamic range of the meter, 10.0 m^{-1}. Corresponding values of light absorption are of order of magnitude lower than attenuation (Table 1), which implies that the light attenuation is affected mainly by the process of light scattering by suspended particulate matter, induced by the melting glacier or river runoff. Due to the hydrological stratification, the process of sedimentation is slowed down,

Table 1 Median, mean, standard deviation, minimum and maximum values of light attenuation $c_{pg}(\lambda)$ [m^{-1}] and absorption $a_{pg}(\lambda)$ [m^{-1}] coefficients of visible light spectrum (λ = 412 nm to λ = 715 nm) in identified water masses in Hornsund and Kongsfjorden, July 2009 and 2010.

Water mass, number of samples	Wavelength [nm]	Hornsund									
		Light attenuation [m^{-1}]					Light absorption [m^{-1}]				
		Median	Mean	Std. dev	Min.	Max.	Median	Mean	Std. dev	Min.	Max.
Surface Water	412	1.081	1.602	1.339	0.273	7.853	0.300	0.295	0.149	0.076	0.822
N = 635	440	0.947	1.457	1.262	0.209	7.315	0.196	0.196	0.094	0.061	0.572
	488	0.872	1.323	1.155	0.181	6.636	0.096	0.105	0.059	0.018	0.343
	510	0.812	1.260	1.114	0.172	6.357	0.069	0.077	0.044	0.017	0.268
	532	0.783	1.204	1.069	0.150	6.089	0.048	0.060	0.034	0.012	0.195
	555	0.753	1.155	1.024	0.147	5.817	0.028	0.038	0.025	0.004	0.134
	650	0.647	0.993	0.885	0.122	4.978	0.021	0.022	0.011	0.007	0.069
	676	0.639	0.971	0.849	0.118	4.789	0.011	0.016	0.014	0.001	0.101
	715	0.602	0.913	0.809	0.106	4.531	0.000	0.000	0.000	0.000	0.000
Intermediate Water	412	0.421	0.418	0.041	0.341	0.526	0.108	0.107	0.005	0.095	0.116
N = 176	440	0.357	0.352	0.040	0.277	0.458	0.091	0.090	0.003	0.083	0.097
	488	0.325	0.320	0.038	0.248	0.421	0.044	0.044	0.002	0.037	0.050
	510	0.314	0.310	0.037	0.237	0.405	0.033	0.033	0.002	0.027	0.037
	532	0.289	0.285	0.037	0.213	0.377	0.031	0.031	0.002	0.027	0.035
	555	0.284	0.280	0.036	0.210	0.370	0.021	0.021	0.002	0.015	0.024
	650	0.255	0.251	0.033	0.187	0.335	0.009	0.009	0.001	0.007	0.011
	676	0.247	0.244	0.032	0.181	0.325	0.008	0.008	0.001	0.007	0.010
	715	0.233	0.230	0.031	0.167	0.310	0.000	0.000	0.000	0.000	0.000
Local Water	412	0.436	0.681	0.384	0.303	1.689	0.131	0.154	0.048	0.109	0.299
N = 178	440	0.417	0.620	0.337	0.283	1.534	0.080	0.104	0.038	0.066	0.209
	488	0.382	0.563	0.307	0.252	1.392	0.029	0.047	0.028	0.018	0.116
	510	0.355	0.532	0.303	0.221	1.328	0.027	0.038	0.018	0.019	0.091
	532	0.361	0.515	0.277	0.231	1.260	0.020	0.031	0.016	0.013	0.076
	555	0.351	0.498	0.266	0.223	1.210	0.012	0.020	0.013	0.004	0.056
	650	0.294	0.425	0.242	0.171	1.056	0.019	0.017	0.004	0.006	0.024
	676	0.311	0.427	0.221	0.191	1.025	0.006	0.007	0.002	0.003	0.015
	715	0.282	0.396	0.218	0.164	0.979	0.000	0.000	0.000	0.000	0.000
Winter-cooled Water	412	0.858	0.648	0.145	0.455	0.943	0.189	0.156	0.025	0.127	0.220
N = 41	440	0.791	0.602	0.117	0.429	0.832	0.122	0.103	0.022	0.079	0.159
	488	0.718	0.550	0.103	0.392	0.746	0.059	0.046	0.017	0.028	0.089
	510	0.681	0.518	0.104	0.385	0.713	0.049	0.040	0.010	0.027	0.063
	532	0.655	0.511	0.090	0.388	0.676	0.038	0.031	0.010	0.018	0.053
	555	0.633	0.495	0.085	0.376	0.657	0.026	0.020	0.008	0.010	0.038
	650	0.549	0.421	0.079	0.310	0.579	0.020	0.019	0.005	0.008	0.027
	676	0.544	0.429	0.069	0.322	0.561	0.006	0.005	0.002	0.002	0.009
	715	0.504	0.394	0.070	0.287	0.533	0.000	0.000	0.000	0.000	0.000

Water mass, number of samples	Wavelength [nm]	Kongsfjorden									
		Light attenuation [m^{-1}]					Light absorption [m^{-1}]				
		Median	Mean	Std. dev	Min.	Max.	Median	Mean	Std. dev	Min.	Max.
Surface Water	412	1.982	3.449	4.381	0.429	31.659	0.261	0.584	0.666	0.129	4.442
N = 276	440	1.595	3.083	4.202	0.374	30.248	0.199	0.432	0.494	0.101	3.276
	488	1.332	2.772	3.949	0.324	28.365	0.127	0.290	0.347	0.060	2.266
	510	1.209	2.637	3.845	0.310	27.600	0.096	0.235	0.290	0.045	1.867
	532	1.121	2.526	3.750	0.289	26.932	0.077	0.196	0.245	0.038	1.558
	555	1.037	2.418	3.647	0.274	26.255	0.056	0.149	0.192	0.026	1.210
	650	0.842	2.091	3.260	0.220	23.747	0.023	0.048	0.057	0.011	0.368
	676	0.814	2.040	3.176	0.240	23.289	0.026	0.037	0.033	0.011	0.223
	715	0.765	1.936	3.050	0.196	22.414	0.000	0.000	0.000	0.000	0.000
Intermediate Water	412	0.504	1.147	1.083	0.359	4.212	0.144	0.217	0.136	0.118	0.605
N = 176	440	0.450	1.053	1.041	0.303	4.032	0.111	0.173	0.116	0.089	0.507
	488	0.389	0.957	0.986	0.251	3.775	0.065	0.114	0.090	0.045	0.373
	510	0.378	0.927	0.960	0.241	3.655	0.051	0.094	0.080	0.034	0.324
	532	0.351	0.887	0.939	0.218	3.537	0.043	0.082	0.071	0.030	0.286
	555	0.339	0.857	0.914	0.208	3.424	0.031	0.064	0.058	0.020	0.229
	650	0.282	0.743	0.817	0.165	3.018	0.015	0.024	0.017	0.008	0.074
	676	0.310	0.753	0.800	0.188	2.975	0.013	0.019	0.011	0.009	0.048
	715	0.250	0.684	0.767	0.139	2.814	0.000	0.000	0.000	0.000	0.000
Local Water	412	1.471	1.867	0.769	1.159	3.662	0.201	0.328	0.247	0.173	0.945
N = 165	440	1.094	1.507	0.733	1.035	3.193	0.129	0.225	0.165	0.113	0.619
	488	0.845	1.263	0.701	0.787	2.837	0.071	0.137	0.110	0.059	0.391
	510	0.735	1.153	0.682	0.677	2.662	0.053	0.107	0.087	0.043	0.297
	532	0.657	1.074	0.670	0.602	2.542	0.041	0.087	0.071	0.034	0.235
	555	0.585	1.002	0.657	0.534	2.423	0.028	0.064	0.054	0.023	0.172
	650	0.437	0.827	0.593	0.394	2.077	0.012	0.022	0.015	0.008	0.049
	676	0.418	0.807	0.584	0.374	2.027	0.011	0.016	0.009	0.006	0.034
	715	0.385	0.754	0.561	0.342	1.930	0.000	0.000	0.000	0.000	0.000
Winter-cooled Water	412	1.462	3.204	0.591	1.421	3.866	0.203	0.696	0.206	0.172	0.946
N = 37	440	1.064	2.785	0.549	1.034	3.396	0.129	0.483	0.120	0.111	0.621
	488	0.810	2.477	0.510	0.785	3.042	0.069	0.316	0.074	0.058	0.394
	510	0.700	2.330	0.489	0.678	2.835	0.051	0.251	0.055	0.042	0.304
	532	0.624	2.225	0.475	0.603	2.722	0.040	0.206	0.043	0.033	0.240
	555	0.556	2.123	0.459	0.535	2.600	0.028	0.155	0.032	0.023	0.176
	650	0.420	1.825	0.403	0.396	2.232	0.011	0.045	0.009	0.009	0.051
	676	0.399	1.779	0.392	0.377	2.165	0.008	0.029	0.005	0.007	0.032
	715	0.367	1.691	0.375	0.345	2.059	0.000	0.000	0.000	0.000	0.000
Atlantic Water	412	0.384	0.407	0.058	0.345	0.573	0.121	0.128	0.014	0.112	0.160
N = 149	440	0.344	0.356	0.050	0.291	0.505	0.090	0.096	0.010	0.085	0.120
	488	0.290	0.301	0.048	0.239	0.443	0.050	0.052	0.008	0.043	0.070
	510	0.287	0.294	0.045	0.233	0.428	0.039	0.041	0.007	0.032	0.056
	532	0.263	0.270	0.044	0.209	0.400	0.034	0.035	0.006	0.028	0.048
	555	0.251	0.259	0.043	0.201	0.387	0.025	0.025	0.005	0.019	0.036
	650	0.200	0.208	0.041	0.157	0.329	0.013	0.012	0.003	0.007	0.016
	676	0.195	0.220	0.051	0.167	0.359	0.010	0.010	0.001	0.007	0.012
	715	0.171	0.179	0.039	0.130	0.295	0.000	0.000	0.000	0.000	0.000

so high values of IOP, higher than in other water masses, are observed in SW in all stations in both fjords. On stations located in inner and outer part of fjords and in water masses of IW, LW, WCW the optical properties are within the same range of values in both fjords. Values of light scattering $b_p(555)$ were in range of 0.30—0.60 m^{-1} and absorptions $a_{pg}(412)$ were close to minimum values observed, 0.20 m^{-1} (Table 1, Fig. 3). In most cases the means of $b_p(555)$ or $a_{pg}(412)$ between inner and outer stations are not statistically different (post hoc Tukey HSD test). This reflects processes of horizontal and vertical hydrological mixing which transform waters in the annual cycle (Cottier et al., 2005, 2010). It is noticeable, however, that mean values of light attenuation and absorption in Atlantic Water (AW) in Kongsfjorden, $b_p(555) = 0.30\ m^{-1}$, $a_{pg}(412) = 0.13\ m^{-1}$, (Table 1), are of typical of Atlantic Water in West Spitsbergen Current

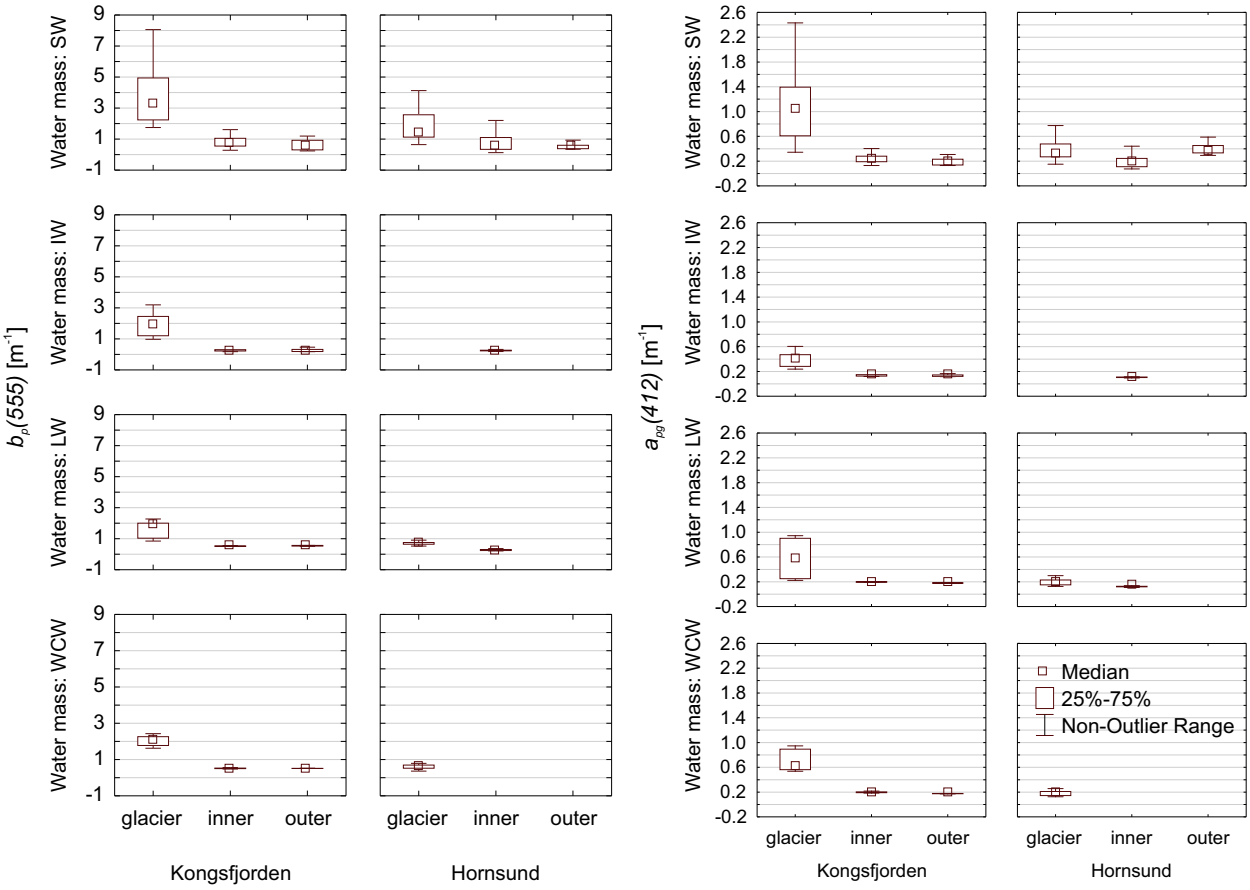

Figure 3 Median statistics of light scattering $b_p(555)$ by particulate matter (left panel) and absorption $a_{pg}(412)$ by sum of non-pigmented particles (*NAP*) and dissolved organic matter (*CDOM*), (right panel), aggregated over location of samples: glacier, inner fjord and outer fjord areas and over identified water masses in Hornsund and Kongsfjorden, July 2009 and 2010; box — 25—75% quartiles, whiskers — non-outlier range.

outside the Kongsfjorden (Pavlov et al., 2015). This leads to a conclusion that in the period of observation optical properties of fjords' waters (SW, LW, IW, WCW) were shaped by a local process, such as glacial or river runoff or local production of organic matter, rather than induced by advection of AW.

One of the distinct features seen in Table 1, common for all water masses in both fjords, is high light absorption in the blue part of the spectrum, 412—488 nm, which is the effect of absorption by colored dissolved organic matter (*CDOM*) and particles, (Babin et al., 2003a). Since absorption by *NAP* is usually one order of magnitude smaller than by *CDOM*, (Babin et al., 2003a; Nima et al., 2016), observed high values of absorption are mainly the effect of the presence of *CDOM*. In both fjords the highest values of $a_{pg}(412)$ were recorded on glacier stations in Surface Water, 0.82 m^{-1} in Hornsund and 4.44 m^{-1} in Kongsfjorden. The absorption values $a_{pg}(412)$ are comparable with observed in coastal waters in temperate regions, as Baltic Sea (Kowalczuk, 1999). Elevated level of *CDOM* in glacier areas tally with observations of Hood et al. (2009) of possible release of organic carbon from glaciers and ice sheets, and Kuliński et al. (2014) on the role of glaciers as a source of particulate organic material. It is known that increased load of dissolved organic matter, of which *CDOM* is an important part, may lead to serious implication in the Arctic Ocean biogeochemistry, heat budget and underwater light filed (Granskog et al., 2007; Pegau, 2002; Stedmon et al., 2011), so the presence of *CDOM* should be considered in further studies of fjords' environment.

3.3. Particulate matter in the inner and outer parts of the fjords

Similarly to optical data, data of particle volume concentration were aggregated according to the sampling location in the fjords, and in respect to identified water masses. Table 2 presents basic statistics of particle volume concentration of suspended matter in Hornsund and Kongsfjorden. Values of median, mean, standard deviation, minimum and maximum of PVC were calculated over size classes of 20—200 μm, 2.0—20 μm, 1.5—2.0 μm, as a sum the PVCs in all water masses found in a given location: glacier, inner fjord and outer fjord areas.

Based on all parameters and statistics that were applied, the waters in a glacier area in Kongsfjorden were the richest in particles, compared to other areas, including Hornsund glacier area. Median size of particles in Kongsfjorden was 110.4 μm vs 79.38 μm in Hornsund and in terms of PVC, 11.77 μL L^{-1} in Kongsfjorden and 3.63 μL L^{-1} in Hornsund

Table 2 Median, mean, standard deviation, minimum and maximum values of particle volume concentration of suspended matter in size classes 20—200, 2.0—20, 1.5—2.0 μm aggregated over location of samples: glacier, inner fjord and outer fjords areas and over identified water masses in Hornsund and Kongsfjorden, July 2009 and 2010.

Particle size class [μm]	Hornsund					Kongsfjorden				
	Particle volume concentration [μL L^{-1}]									
	Median	Mean	Std. dev	Min.	Max.	Median	Mean	Std. dev	Min.	Max.
Glacier area										
	Median size = 79.38 μm; n = 408					Median size = 110.44 μm; n = 262				
20—200	2.55	3.63	3.45	0.21	35.40	6.40	11.77	17.29	0.89	137.83
2.0—20	0.52	0.79	0.72	0.22	3.89	0.87	1.38	2.42	0.30	29.31
1.5—2.0	0.02	0.07	0.13	0.00	0.84	0.05	0.13	0.47	0.00	6.46
Inner fjord										
	Median size = 35.62 μm; n = 460					Median size = 44.84 μm; n = 324				
20—200	0.63	1.39	3.07	0.01	54.37	0.16	0.45	0.96	0.00	6.46
2.0—20	0.37	0.53	0.46	0.13	2.14	0.14	0.21	0.23	0.02	1.17
1.5—2.0	0.01	0.04	0.10	0.00	1.28	0.01	0.03	0.08	0.00	0.69
Outer fjord										
	Median size = 26.13 μm; n = 134					Median size = 37.01 μm; n = 317				
20—200	0.09	0.22	0.52	0.00	4.77	0.04	0.34	1.56	0.00	18.58
2.0—20	0.14	0.26	0.31	0.03	1.77	0.14	0.20	0.18	0.01	0.97
1.5—2.0	0.01	0.02	0.02	0.00	0.12	0.01	0.02	0.05	0.00	0.40
Surface Water										
	Median size = 46.61 μm; n = 635					Median size = 90.64 μm; n = 276				
20—200	1.59	2.72	3.96	0.00	54.37	1.48	9.07	17.87	0.00	137.83
2.0—20	0.50	0.75	0.70	0.03	3.89	0.66	1.17	2.42	0.01	29.31
1.5—2.0	0.02	0.07	0.14	0.00	1.28	0.05	0.15	0.46	0.00	6.46
Intermediate Water										
	Median size = 19.15 μm; n = 68					Median size = 56.66 μm; n = 176				
20—200	0.63	0.64	0.08	0.51	1.02	0.05	1.72	3.17	0.00	12.34
2.0—20	0.40	0.39	0.03	0.33	0.42	0.19	0.32	0.30	0.03	1.36
1.5—2.0	0.00	0.00	0.00	0.00	0.01	0.01	0.03	0.02	0.00	0.14
Local Water										
	Median size = 50.88 μm; n = 178					Median size = 65.59 μm; n = 165				
20—200	0.71	1.08	1.12	0.01	4.90	0.33	1.81	2.58	0.00	7.69
2.0—20	0.31	0.33	0.15	0.13	0.64	0.15	0.31	0.31	0.02	1.06
1.5—2.0	0.01	0.01	0.01	0.00	0.03	0.00	0.02	0.02	0.00	0.08
Winter-cooled Water										
	Median size = 86.00 μm; n = 121					Median size = 54.77 μm; n = 135				
20—200	1.37	1.54	0.84	0.21	3.69	0.23	1.69	2.32	0.00	0.23
2.0—20	0.35	0.34	0.08	0.22	0.50	0.14	0.32	0.33	0.02	0.14
1.5—2.0	0.00	0.01	0.01	0.00	0.03	0.01	0.02	0.02	0.00	0.01
Atlantic Water										
	—					Median size = 16.79 μm; n = 151				
20—200	—	—	—	—	—	0.00	0.02	0.07	0.00	0.00
2.0—20	—	—	—	—	—	0.13	0.13	0.03	0.05	0.13
1.5—2.0	—	—	—	—	—	0.01	0.01	0.00	0.00	0.01

(Table 2). In both fjords, PVC of suspended matter of the size class 20—200 μm dominated over fractions smaller than 20 μm. The characteristics of particle distribution, as PVC in mean or median size, are defined more by location in the fjords than by the water mass they are measured in. As it is seen in Fig. 4 and Table 2, the median size of particulate content is of the same range of 60—90 μm in water masses in the glacier area. This may reflect the sedimentation process along the water column (Görlich, 1986).

In inner and outer areas of fjords mean values of PVC were considerably lower than those observed close to the glacier: 0.34—0.45 μL L^{-1} in Kongsfjorden and 0.22—1.39 μL L^{-1} in Hornsund (Table 2), while their range of variability is of an order of magnitude smaller than in waters close to the glacier. In respect of water masses, in Surface Water an opposite patterns of distribution of median of particle size was noted along the fjords. While in both fjords value of median particle size decreases toward the fjord entrance, in

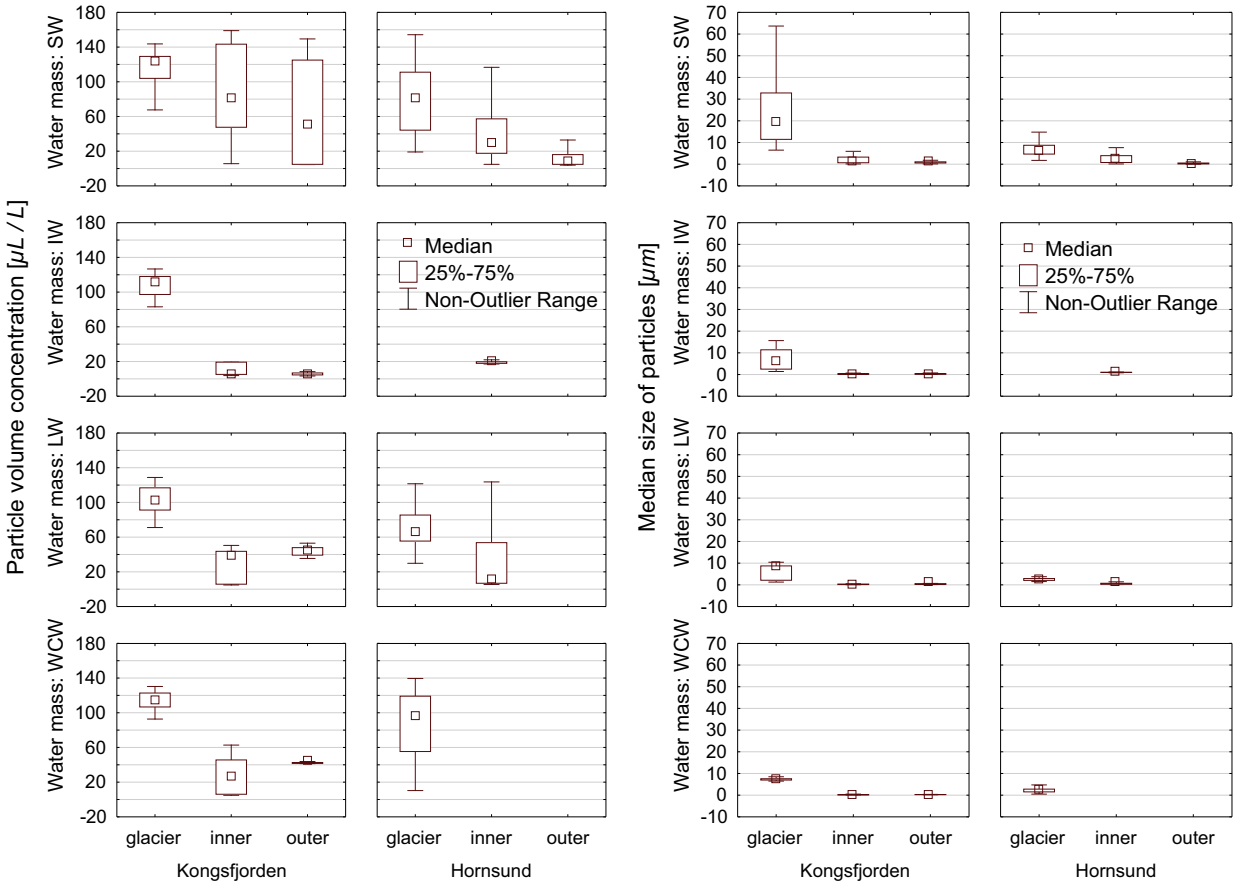

Figure 4 Median statistics of particle volume concentration (left panel) and median size of particles of range of 0.15—200 μm (right panel), aggregated over location of samples: glacier, inner fjord and outer fjord areas and over identified water masses in Hornsund and Kongsfjorden, July 2009 and 2010; box — 25—75% quartiles, whiskers — non-outlier range.

Kongsfjorden its variability, measured with a span of 25—75% quartiles, increases toward the entrance of the fjords from 110 to 130 μm in the fjord end to 20—130 μm at the outer area (Fig. 4, right upper panel). In Hornsund an opposite trend was observed; the median of particle size variability decreased from a 60—110 μm to 10—20 μm. This detected difference in particles median size characteristics along the fjords may indicate differences between the fjords in terms of the processes of particles dynamics, such as sinking, aggregation, trophic interactions within the planktonic community or particle composition.

3.4. Relations between light absorption and particles content

Coefficients of correlation between light scattering by particulate matter $b_p(555)$, light absorption by sum of particles and dissolved organic matter $a_{pg}(412)$, light absorption in chlorophyll band $a_p(676)$ and particle volume concentration in size classes of 20—200 μm, 2—20 μm and 0.15—2 μm are presented in Table 3. In Kongsfjorden light scattering by particulate matter $b_p(555)$ is strongly correlated both with absorptions in 412 nm and 676 nm, $r > 0.92$, which suggests that close to 90% of observed variance of $b_p(555)$ may be explained by the dominating presence of particles of organic origin. In Hornsund the correlation coefficients for the same parameters are lower, $r = 0.65$—0.76, which suggests equal influence on water optical properties of particles of mineral and organic origin. Fjords also differ by the dominating particle size fraction. In Kongsfjorden coefficient of correlation of scattering and absorption with particles volume concentration of size 20—200 μm is of range of 0.90—0.96. In Hornsund dominating size fraction is 2—20 μm, and its high correlation with $b_p(555)$, $r = 0.95$, but lower correlation with $a_p(676)$, $r = 0.75$ confirms the notion of higher content of particles of mineral origin.

Further evidence that optical properties of fjords are considerably controlled by particulate matter composition is provided by statistics of the ratio $b_p(555)/a_p(676)$. The ratio largely removes first order dependency on particle concentration, and is thus expected to mainly reflect changes in bulk composition and size distribution of the particle assemblage (Neukermans et al., 2016). Median statistics of $b_p(555)/a_p(676)$ are presented in Fig. 5, with the values of ratio aggregated over location of samples: glacier, inner fjord and outer fjords areas, and over identified water masses in Hornsund and Kongsfjorden. In all derived categories, location or water mass, the ratio, as well as a range of variability of quartiles are lower in Kongsfjorden, $b_p(555)/a_p(676) \approx 60 - 70$, compared to 100—120 in Hornsund (Fig. 5). All values of the ratio are also statistically different in fjords in respective categories.

Table 3 Coefficients of correlation between light scattering by particulate matter $b_p(555)$, light absorption by sum of particles and dissolved organic matter $a_{pg}(412)$, light absorption in chlorophyll band $a_p(676)$ and particle volume concentration in size classes of 20–200 μm, 2–20 μm and 0.15–2 μm in Kongsfjorden and Hornsund, July 2009 and 2010.

	Kongsfjorden					
N = 903	$b_p(555)$	$a_{pg}(412)$	$a_p(676)$	PVC (20–200 μm)	PVC (2–20 μm)	PVC (0.15–20 μm)
$b_p(555)$	1.000	0.923	0.961	0.929	0.893	0.728
$a_{pg}(412)$		1.000	0.923	0.905	0.785	0.597
$a_p(676)$			1.000	0.907	0.838	0.654
PVC (20–200 μm)				1.000	0.806	0.617
PVC (2.0–20 μm)					1.000	0.939
PVC (0.15–20 μm)						1.000
	Hornsund					
N = 1002	$b_p(555)$	$a_{pg}(412)$	$a_p(676)$	PVC (20–200 μm)	PVC (2–20 μm)	PVC (0.15–20 μm)
$b_p(555)$	1.000	0.760	0.650	0.689	0.949	0.818
$a_{pg}(412)$		1.000	0.576	0.505	0.673	0.630
$a_p(676)$			1.000	0.562	0.750	0.625
PVC (20–200 μm)				1.000	0.670	0.513
PVC (2.0–20 μm)					1.000	0.826
PVC (0.15–20 μm)						1.000

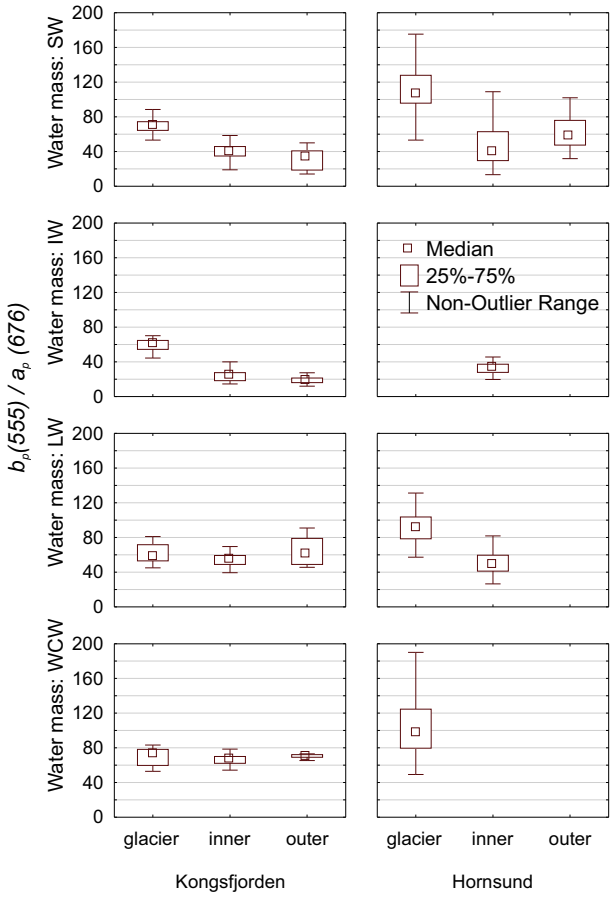

Figure 5 Median statistics of $b_p(555)/a_p(676)$ as a proxy index of bulk composition of particles, aggregated over location of samples: glacier, inner fjord and outer fjord areas and over identified water masses in Hornsund and Kongsfjorden, July 2009 and 2010; box – 25–75% quartiles, whiskers – non-outlier range.

Coefficients of light attenuation $c(\lambda)$ and scattering $b(\lambda)$ in both fjords were highly correlated for all wavelengths, with the r coefficient exceeding 0.98 in both fjords, with no statistical difference between the areas or water masses. Similarly high correlations, r = 0.93, were observed between $a(\lambda)$ and $b(\lambda)$ in Kongsfjorden, and lower, but sill statistically significant, in Hornsund, r = 0.62–0.90. These high spectral correlations are characteristic for waters with substantial content of suspended particulate matter (Levin et al., 2013; Voss, 1992). This feature was not explored there in the context of differences between fjords, but points to a combination of coefficients of light scattering in 555 nm and absorption in 676 nm as a proxy for suspended particulate matter content, reflecting the varying proportions between organic and inorganic particles. This potentially allows to narrow the observations to reduced number of wavelengths of $c(\lambda)$, $b(\lambda)$ or $a(\lambda)$ (i.e. with use of simpler and cheaper instrumentation) while still being able to resolve the basic optical properties of the waters in the areas.

4. Conclusions

In both fjords the optical parameters, as well as particulate matter distribution, are mainly driven by vertical structure which, through density field, constrains the presence and residence time of the optically active components. Considering possibility of relatively rapid changes in hydrological stratification and distribution of water masses in fjords due to changes of winds, currents and atmospheric pressure (Cottier et al., 2005), presented statistics are perhaps closer to a summer season snapshot than a long term regularity. Nevertheless, the study presents the first insight into spatial distribution and range of variability of spectral light attenuation and absorption, in relation to particulate matter volume concentrations and size of particles in water masses in Kongsfjorden and Hornsund. The results provide an evidence of considerable range of variability of the optical properties of the water column mainly due to glacial and riverine runoff.

The scale of variability of particulate matter in Kongsfjorden is bigger than in Hornsund. Most of the variability in Hornsund can be attributed to glaciers discharge and a presence of particles of mineral origin, while in Kongsfjorden the organic particles contribute almost equally to defining the optical properties of water. This increasing inflow of suspended matter affects underwater light field, a key factor for water biological processes. The result of increasing presence of suspended or dissolved matter, termed as a 'darkening' of waters, may implicate mesopelagic regime shifts in fjords (Aksnes et al., 2009). Presented in this study detailed spectral statistics of optical properties and particulate matter of fjords' water masses may be used as basic or boundary conditions for modeling underwater light field for a range of other studies.

Acknowledgments

This work was carried out in frame of GAME project of National Science Center nr DEC-2012/04/A/NZ8/00661. Data of 2009 and 2010 were collected under ALKEKONGE project, Norway Grants, PNRF-234-AI-1/07.

References

Agrawal, Y.C., Pottsmith, H.C., 2000. Size and settling velocity observations in sediment transport. Mar. Geol. 168, 114–890.

Aksnes, D., Dupont, N., Staby, A., Fiksen, Ø., Kaartvedt, S., Aure, J., 2009. Coastal water darkening and implications for mesopelagic regime shifts in Norwegian fjords. Mar. Ecol. Prog. Ser. 387, 39–49.

Babin, M., Stramski, D., Ferrari, G.M., Claustre, H., Bricaud, A., Obolensky, G., Hoepffner, N., 2003a. Variations in the light absorption coefficients of phytoplankton, nonalgal particles, and dissolved organic matter in coastal waters around Europe. J. Geophys. Res. 108 (C7), 3211, 4-1–4-20.

Babin, M., Morel, A., Fournier-Sicre, V., Fell, F., Stramski, D., 2003b. Light scattering properties of marine particles in coastal and open ocean waters as related to the particle mass concentration. Limnol. Oceanogr. 48, 843–859, http://dx.doi.org/10.4319/lo.2003.48.2.0843.

Bowers, D.G., Binding, C.E., 2006. The optical properties of mineral suspended particles: a review and synthesis. Estuar. Coast. Shelf Sci. 67, 219–230.

Cottier, F., Tverberg, V., Inall, M., Svendsen, H., Nilsen, F., Griffiths, C., 2005. Water mass modification in an Arctic fjord through cross-shelf exchange: the seasonal hydrography of Kongsfjorden. Svalbard. J. Geophys. Res. 110 (C12), C12005, 18 pp.

Cottier, F.R., Nilsen, F., Skogseth, R., Tverberg, V., Skarðhamar, J., Svendsen, H., 2010. Arctic fjords: a review of the oceanographic environment and dominant physical processes. Geol. Soc. Lond. Spec. Publ. 344, 35–50.

Görlich, K., 1986. Glacimarine sedimentation of muds in Hornsund Fjord, Spitsbergen. Ann. Soc. Geol. Pol. 56, 433–477.

Granskog, M.A., Macdonald, R.W., Mundy, C.-J., Barber, D.G., 2007. Distribution, characteristics and potential impacts of chromophoric dissolved organic matter (CDOM) in Hudson Strait and Hudson Bay, Canada. Cont. Shelf Res. 27, 2032–2050.

Hegseth, E.N., Tverberg, V., 2013. Effect of Atlantic water inflow on timing of the phytoplankton spring bloom in a high Arctic fjord (Kongsfjorden, Svalbard). J. Mar. Syst. 113–114, 94–105, http://dx.doi.org/10.1016/j.jmarsys.2013.01.003.

Hood, E., Fellman, J., Spencer, R.G.M., Hernes, P.J., Edwards, R., D'Amore, D., Scott, D., 2009. Glaciers as a source of ancient and labile organic matter to the marine environment. Nature 462, 1044–1047, http://dx.doi.org/10.1038/nature08580.

Inall, M.E., Nilsen, F., Cottier, F.R., Daae, R., 2015. Shelf/fjord exchange driven by coastal-trapped waves in the Arctic. J. Geophys. Res. 120, 8283–8303.

Kohler, J., James, T.D., Murray, T., Nuth, C., Brandt, O., Barrand, N. E., Aas, H.F., Luckman, A., 2007. Acceleration in thinning rate on western Svalbard glaciers. Geophys. Res. Lett. 34 (18), L18502, http://dx.doi.org/10.1029/2007GL030681 5 pp.

Kowalczuk, P., 1999. Seasonal variability of yellow substance absorption in the surface layer of the Baltic Sea. J. Geophys. Res. 104 (C12), 30047–30058.

Kuliński, K., Kędra, M., Legeżyńska, J., Gluchowska, M., Zaborska, A., 2014. Particulate organic matter sinks and sources in high Arctic fjord. J. Mar. Syst. 139, 27–37.

Levin, I., Darecki, M., Sagan, S., Radomyslskaya, T., 2013. Relationships between inherent optical properties in the Baltic Sea for application to the underwater imaging problem. Oceanologia 55 (1), 11–26, http://dx.doi.org/10.5697/oc.55-1.011.

Mortensen, J., Bendtsen, J., Motyka, R.J., Lennert, K., Truffer, M., Fahnestock, M., Rysgaard, S., 2013. On the seasonal freshwater stratification in the proximity of fast-flowing tidewater outlet glaciers in a sub-Arctic sill fjord. J. Geophys. Res. 118, 1382–1395.

Muckenhuber, S., Nilsen, F., Korosov, A., Sandven, S., 2016. Sea ice cover in Isfjorden and Hornsund, Svalbard (2000–2014) from remote sensing data. Cryosphere 10, 149–158.

Neukermans, G., Reynolds, R.A., Stramski, D., 2016. Optical classification and characterization of marine particle assemblages within the western Arctic Ocean. Limnol. Oceanogr. 61, 1472–1494.

Nima, C., Frette, Ø., Hamre, B., Erga, S.R., Chen, Y.-C., Zhao, L., Sørensen, K., Norli, M., Stamnes, K., Stamnes, J.J., 2016. Absorption properties of high-latitude Norwegian coastal water: the impact of CDOM and particulate matter. Estuar. Coast. Shelf Sci. 178, 158–167, http://dx.doi.org/10.1016/j.ecss.2016.05.012.

Ormańczyk, M.R., Gluchowska, M., Olszewska, A., Kwasniewski, S., 2017. Zooplankton structure in high latitude fjords with contrasting oceanography (Hornsund and Kongsfjorden, Spitsbergen). Oceanologia 59 (4), 508–524, http://dx.doi.org/10.1016/j.oceano.2017.06.003.

Pavlov, A.K., Tverberg, V., Ivanov, B.V., Nilsen, F., Falk-Petersen, S., Granskog, M.A., 2013. Warming of Atlantic Water in two west Spitsbergen fjords over the last century (1912–2009). Polar Res. 32 (1), 11206, http://dx.doi.org/10.3402/polar.v32i0.11206 14 pp.

Pavlov, A.K., Granskog, M.A., Stedmon, C.A., Ivanov, B.V., Hudson, S. R., Falk-Petersen, S., 2015. Contrasting optical properties of surface waters across the Fram Strait and its potential biological implications. J. Mar. Syst. 143, 62–72, http://dx.doi.org/10.1016/j.jmarsys.2014.11.001.

Pegau, W.S., 2002. Inherent optical properties of the central Arctic surface waters. J. Geophys. Res. 107 (C10), http://dx.doi.org/10.1029/2000JC000382 16 pp.

Piwosz, K., Walkusz, W., Hapter, R., Wieczorek, P., Hop, H., Wiktor, J., 2009. Comparison of productivity and phytoplankton in a warm (Kongsfjorden) and a cold (Hornsund) Spitsbergen fjord in midsummer 2002. Polar Biol. 32, 549–559, http://dx.doi.org/10.1007/s00300-008-0549-2.

Rudels, B., Björk, G., Nilsson, J., Winsor, P., Lake, I., Nohr, C., 2005. The interaction between waters from the Arctic Ocean and the Nordic Seas north of Fram Strait and along the East Greenland Current: results from the Arctic Ocean-02 Oden expedition. J. Mar. Syst. 55 (1–2), 1–30, http://dx.doi.org/10.1016/j.jmarsys.2004.06.008.

Saloranta, T.M., Svendsen, H., 2001. Across the Arctic front west of Spitsbergen: high-resolution CTD sections from 1998–2000. Polar Res. 20, 177–184.

Sieburth, J.M., Smetacek, V., Lenz, J., 1978. Pelagic ecosystem structure: heterotrophic compartments of the plankton and their relationship to plankton size fractions. Limnol. Oceanogr. 23, 1256—1263.

Stedmon, C., Amon, R.M.W., Rinehart, A.J., Walker, S.A., 2011. The supply and characteristics of colored dissolved organic matter (CDOM) in the Arctic Ocean: Pan Arctic trends and differences. Mar. Chem. 124, 108—118.

Stramski, D., Bricaud, A., Morel, A., 2001. Modeling the inherent optical properties of the ocean based on the detailed composition of the planktonic community. Appl. Opt. 40, 2929—2945.

Stramski, D., Boss, E., Bogucki, D., Voss, K.J., 2004. The role of seawater constituents in light backscattering in the ocean. Progr. Oceanogr. 61, 27—56.

Sullivan, J.M., Twardowski, M.S., Zaneveld, J.R.V., Moore, C.M., Barnard, A.H., Donaghay, P.L., Rhoades, B., 2006. The hyperspectral temperature and salt dependencies of absorption by water and heavy water in the 400—750 nm spectral range. Appl. Opt. 45, 5294—5309, http://dx.doi.org/10.1364/AO.45.005294.

Svendsen, H., Beszczynska-Moller, A., Hagen, J.O., Lefauconnier, B., Tverberg, V., Gerland, S., Orback, J.B., Bischof, K., Papucci, C., Zajaczkowski, M., Azzolini, R., Bruland, O., Wiencke, C., Winther, J.-G., Dallmann, W., 2002. The physical environment of Kongsfjorden-Krossfjorden, an Arctic fjord system in Svalbard. Polar Res. 21, 133—166.

van de Hulst, H.C., 1957. Light Scattering by Small Particles. John Wiley & Sons, New York, 470 pp.

Voss, K.J., 1992. A spectral model of the beam attenuation coefficient in the ocean and coastal areas. Limnol. Oceanogr. 37 (3), 501—509.

Weslawski, J.M., Jankowski, A., Kwasniewski, S., Swerpel, S., Ryg, M., 1991. Summer hydrology and zooplankton in two Svalbard Fjords. Pol. Polar Res. 12, 445—460.

Węsławski, J.M., Buchholz, F., Głuchowska, M., Weydmann, A., 2017. Ecosystem maturation follows the warming of the Arctic fjords. Oceanologia 59 (4), http://dx.doi.org/10.1016/j.oceano.2017.02.002 (in press).

Wlodarska-Kowalczuk, M., Weslawski, J.M., 2001. Impact of climate warming on Arctic benthic biodiversity: a case study of two Arctic glacial bays. Clim. Res. 18, 127—132.

Zaneveld, J.R.V., Kitchen, J.C., Moore, C., 1994. The scattering error correction of reflecting-tube absorption meters. In: Ocean Optics XII, Proc. SPIE, vol. 2258. 44—55.

Oceanologia (2018) 60, 76—85

Available online at www.sciencedirect.com

ScienceDirect

journal homepage: www.journals.elsevier.com/oceanologia/

ORIGINAL RESEARCH ARTICLE

Spatio-temporal variability in the Brazil-Malvinas Confluence Zone (BMCZ), based on spectroradiometric MODIS-AQUA chlorophyll-*a* observations

Luciano Telesca [a,*], **Jorge O. Pierini** [b], **Michele Lovallo** [c], **Eduardo Santamaría-del-Angel** [d]

[a] *National Research Council, Institute of Methodologies for Environmental Analysis, Tito, PZ, Italy*
[b] *Comisión de Investigaciones Científicas (CIC) — IADO-CONICET, Bahía Blanca, Argentina*
[c] *ARPAB, Potenza, Italy*
[d] *Universidad Autónoma de Baja California, Baja California, Mexico*

Received 28 March 2017; accepted 7 August 2017
Available online 26 August 2017

KEYWORDS
MODIS;
Ocean color spectroradiometric chlorophyll-*a*;
Remote sensing oceanography;
Statistics

Summary The Brazil—Malvinas Confluence Zone (BMCZ) is characterized by high environmental variation, which could be reflected in several optical types of water, from one containing only phytoplankton and sea water to other optically more complex. In this paper, we analyze the spatio-temporal variability of the Chlorophyll-*a* detected by the ocean color sensor ($CHLA_{sat}$) in BMCZ in order to understand its environmental variability. We use the MODIS-Aqua $CHLA_{sat}$ monthly composites imagery from 2002 to 2015, and applied two statistical methods: the correlogram-based robust periodogram to identify, over a broad spectrum of temporal, the most significant periodicities, and the pixel gradient distribution to study the spatial-temporal gradients within the BMCZ and variations over the continental shelf and coastal waters. Our results point out to the predominance of the annual cycle over most of the investigated area, although an area from latitude 37°S in direction NE, alongshore of Uruguay to Brazil, evidences interannual periodicities, possibly related to variations in the discharge of the Rio de la Plata associated with the El Niño phenomena. The ocean color spectroradiometric signature in terms of

* Corresponding author at: C.da S. Loja, 85050 Tito, PZ, Italy. Tel.: +39 0971427277; fax: +39 0971427271.
E-mail address: luciano.telesca@imaa.cnr.it (L. Telesca).

Peer review under the responsibility of Institute of Oceanology of the Polish Academy of Sciences.

ELSEVIER Production and hosting by Elsevier

http://dx.doi.org/10.1016/j.oceano.2017.08.002

pixel gradient presents a relatively high variability (~0.0 to 0.65 mg m^{-3}); in particular the high values of the pixel gradient correspond to saline front of the estuarine system of Rio de la Plata, and to the strip of the platform that extends along the isobaths of 80 m (coast of Uruguay), especially in the center and south of the study area.

1. Introduction

Ocean fronts over continental shelf are closely linked to bathymetric features. Besides these, other important fronts are associated with the discharge of large rivers: Rio de la Plata, for instance, represents a clear example over our study area (Brazil-Malvinas Confluence Zone). The discharge of this river is one of the largest in the southern hemisphere and the second largest after that of the Amazon River, contributing to an average of about 24,000 $m^3 s^{-1}$ of fresh nutrient-rich water of the Atlantic Ocean. Furthermore, seasonal rainfalls, especially intense during El Niño periods, contribute to increase the discharge of Rio de la Plata up to about 80,000 $m^3 s^{-1}$ (Acha et al., 2004; Depetris and Kempe, 1990; Guerrero et al., 1997; Huret et al., 2005; Mechoso and Iribarren, 1992). The fresh water plume travels over the continental shelf mainly responding to the bottom topography and seasonal characteristics of the main winds and can extend its influence to northern Uruguay – South Brazil or move south until reaching Mar del Plata city (Braga et al., 2008). The ocean waters are also influenced by contributions from warm waters of subtropical origin (Brazil Current) and cold waters of subantarctic origin (Malvinas current). These two water masses converge on the edge of the continental shelf, creating what is known as the Brazil-Malvinas confluence (BMCZ) (Gordon, 1989).

This region contrasts with the low phytoplankton concentrations of the Brazilian current (nutrient scarcity affects the growth of the primary producers) and the Malvinas current, although they are rich in nutrients, due to the presence of permanent winds, these vertically mix the water column and prevent the production of phytoplankton. Phytoplankton accumulation is observed only along narrow strips on the ocean surface, and its productivity is due to the fact that both currents provide elements that favor their growth and concentration. If the Malvinas Current brings nutrient-rich water, the Brazil Current makes phytoplankton growth quite stable and thanks to such stability of subtropical warm waters, the growth of phytoplankton is very significant (Carreto et al., 1995; Romero et al., 2006).

The frontal areas coincide with the geographical location of phytoplankton blooms. Marine phytoplankton abundance and productivity are subject to complex set of relationships between physical and biological patterns that appear to be different in physically distinct regions. Several ocean studies, in which ocean color satellite images were used, have shown high chlorophyll-*a* concentration structures in the BMCZ (Piola et al., 2000), but on the other hand, still few studies have been carried out on its space-time variability in such important area of the confluence (Machado et al., 2013).

The availability of remote sensing technology has enabled the identification of physical and biological synoptic patterns over the BMCZ. Most studies have been based on the analysis of the seasonal variability of in situ Chlorophyll-*a*, while the interannual variability remains still less approached due to the relatively short length of time series (Garcia and Garcia, 2008; Lutz et al., 2010; Machado et al., 2013; Romero et al., 2006).

Changes in ecosystems have already been reported by other authors, and the abrupt and nonlinear potential can again be more likely future changes (Machado et al., 2013). To understand these changes in marine ecosystems, with essential data sets with lots of information, thus, the satellite ocean color data are valuable assets. The global coverage provided by satellites provides a long time series of records of concentration of Chlorophyll-*a* detected by ocean color sensor ($CHLA_{sat}$), which is especially suited to identify patterns of temporal variability (Brandini et al., 2000; Piola et al., 2008), not only of phytoplankton biomass but also of all the optical components present in seawater, which absorb the same wavelengths as chlorophyll in optical complex water.

Argentina's continental shelf is a highly productive area; with values of phytoplankton abundance around three times the average for the rest of the oceans. Phytoplankton find not evenly distributed, but has a higher concentration in certain regions associated with ocean fronts (Marrari et al., 2016). In our study, we aim at describing quantitatively the temporal variations of the $CHLA_{sat}$ in the BMCZ by using two statistical approaches the robust periodogram and the pixel gradient distribution, never used to investigate the variability of the $CHLA_{sat}$, up to our knowledge.

2. Data analysis

The satellite data we used in our study are provided by the polar orbiting satellite AQUA, which carries the Moderate Resolution Imaging Spectrophotometer (MODIS). AQUA has a sun-synchronous circular orbit, overpasses any given location on Earth twice a day (one night time and one day time pass) and it orbits the Earth every 98.8 min, crossing the equator from south to north each day. Modis Aqua imagery were building at level 3 GLO (4 km resolution) in the Ocean color laboratory in the Facultad de Ciencias Marinas (Universidad Autonoma de Baja California). The level 1b data were obtained from the NASA Ocean Color Data web page (http://oceandata.sci.gsfc.nasa.gov/). The level 1b to level 2 conversion was made carried out using the SEADAS 6 using the specifically atmospherically data form each scene. The level 2 to level 3 monthly GLO imagery processing was made

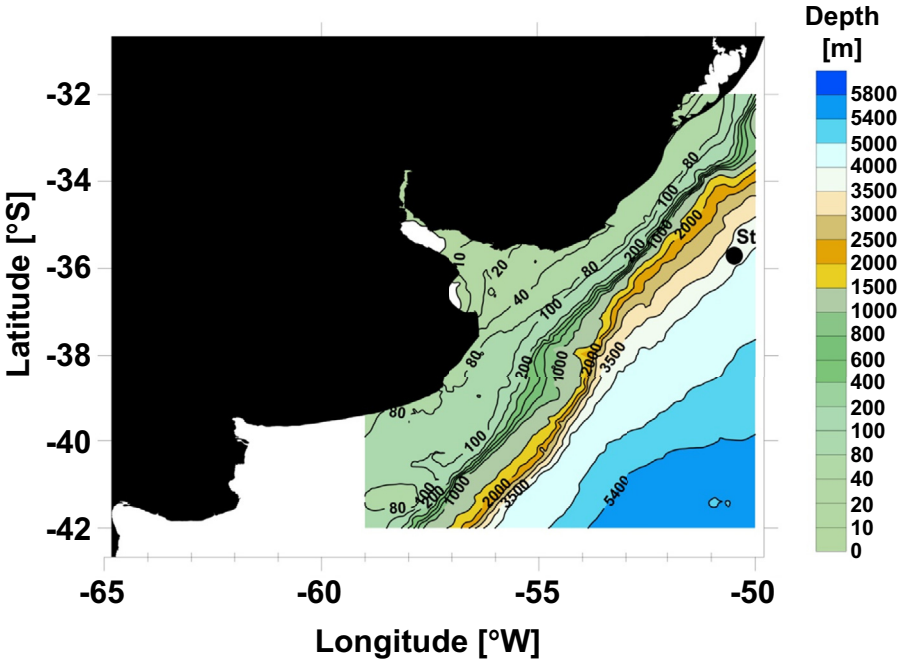

Figure 1 The BMCZ. The black circle St marks the pixel whose time variation is plotted in Fig. 2.

using a WIM software (http://wimsoft.com/) with the WIM automation Module (WAM) ver. 9.10.

The area of interest extends from 50°W to 60°W and from 32°S to 42°S including the BMCZ (Fig. 1). We used the monthly MODIS AQUA images from July 2002 to April 2015; the length of each pixel time series is 154.

Before analyzing the time variation of each pixel in the area (Fig. 1), we pre-processed the data to remove outliers. Fig. 2a shows, as an example, the time variation of $CHLA_{sat}$ corresponding to the pixel (Lat = −35.945833, Lon = −50.8087963), and it is clearly visible the presence of outliers. We applied a third-order one-dimensional median filter to the data and removed all the values whose absolute difference from the filtered signal is above 1. Fig. 2b shows the same time series plotted in Fig. 2a but with the outliers removed ($CHLA_{s,f}$).

Fig. 3 shows the mean $CHLA_{s,f}$ only for pixel time series longer than 50 samples. The data suggest a high concentration of mean $CHLA_{s,f}$ in the nearshore region, alongshore of Uruguay, that reflect the longitudinal gradients within these coastal waters. Such high concentration does not mean a real increase in chlorophyll, but it may be a response to the pulses of sediment and other substances that drag the river during discharges or by the waves, forced by storms, that could generate sediments resuspension favoring the vertical mixture.

For each filtered pixel, we computed the standardized anomaly $CHLA_d = (CHLA_{s,f} - \langle CHLA_{s,f}\rangle)/std(CHLA_{s,f})$, where the $\langle CHLA_{s,f}\rangle$ is the calendar mean, that is calculated for each calendar month, *e.g.* January, by averaging over all years in the record (Pierini et al., 2016) and $std(CHLA_{s,f})$ is the calendar standard deviation. Fig. 4 shows the anomaly $CHLA_d$ for the same pixels shown in Fig. 2.

The most of pixel time series present from low to high percentage of missing data; since the size of the time series is rather small, the presence of missing data reduces further such size, preventing us calculating the power spectral density by using the classical Fourier Transform. For this reason, we used a recently developed algorithm based on the correlogram to robustly calculate the periodogram and, therefore, obtain information about the spectral content of the $CHLA_d$ time series and identify their most significant periodicity. Furthermore, we applied the pixel gradient distribution analysis to evaluate the spatial-temporal gradients within the study region and the variations over continental shelf and coastal waters.

2.1. Robust periodogram method

Among the several complex features a natural phenomenon is characterized by, the robust identification of periodicities are the first type of time fluctuations that are necessary to be detected and investigated. Observational data are generally affected by noise, gaps, spikes; furthermore they could also be very short, making crucial the use of efficient algorithms to obtain as much information as possible.

Wichert et al. (2004) introduced a formal statistical testing procedure for the detection of periodicities, based on the so-called Fisher's g-statistic for which the exact null-distribution can be derived under the Gaussian noise assumption. Considering the following simple model of periodic series:

$$y_n = \beta\cos(\omega t + \phi) + \epsilon_n, \tag{1}$$

where $\beta > 0$, $0 < \omega < \pi$, ϕ uniformly distributed in $(-\pi, \pi]$, and $\{\varepsilon_n\}$ is a sequence of uncorrelated random variables with mean 0 and variance σ^2, independent of ϕ.

Then, the classical periodogram is given by the following formula:

$$I(\omega) = \frac{1}{N}\left|\sum_{n=1}^{N} y_n e^{-i\omega n}\right|^2, \quad 0 \le \omega \le \pi \tag{2}$$

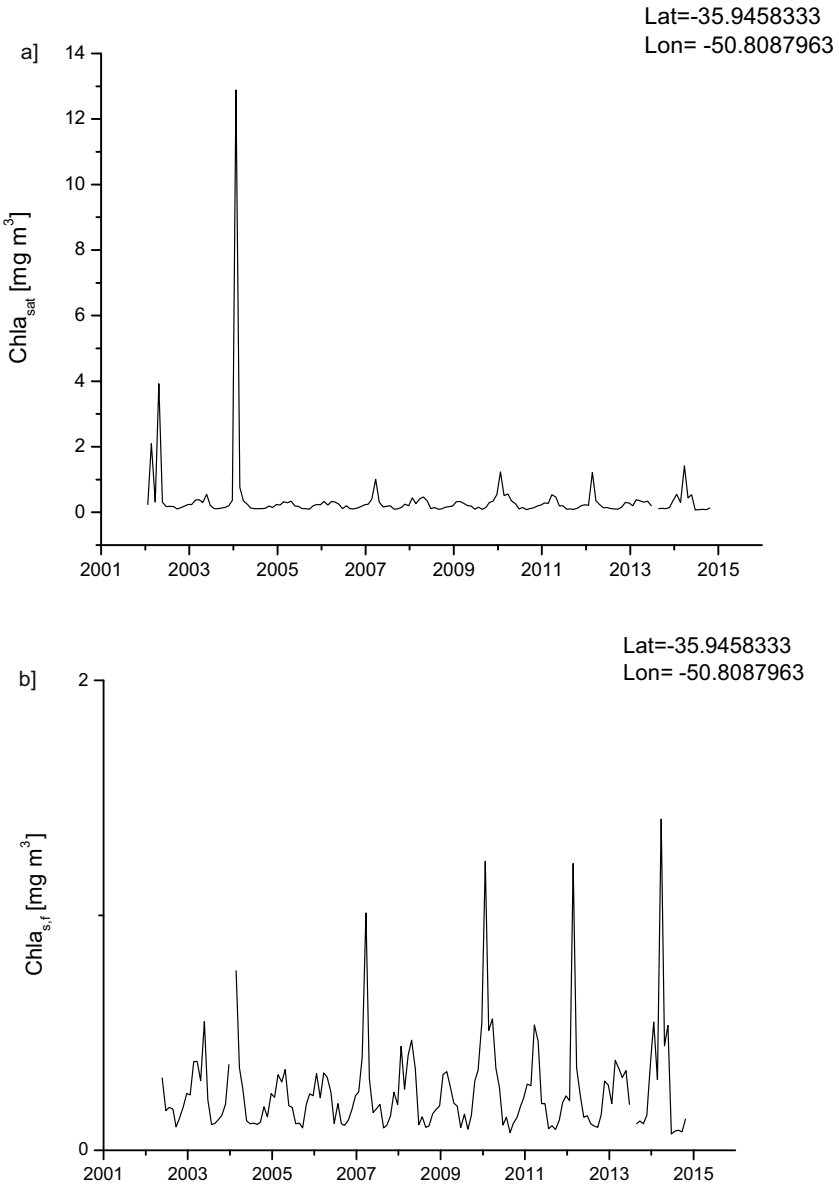

Figure 2 Time variation of $CHLA_{sat}$ (a) and $CHLA_{s,f}$ (b) corresponding to the pixel (Lat = −35.945833, Lon = −50.8087963).

where N is the length of the time series. The periodogram is further evaluated at normalized frequencies

$$\omega_l = \frac{2\pi l}{N}, \quad l = 0, 1, \ldots, a \tag{3}$$

where $a = [(N-1)/2]$ and $[x]$ indicates the integer part of x. If the signal has a significant cycle with frequency ω_0, then the periodogram has a high probability to exhibit a peak centered at that frequency. While, if the time series is a purely random process, which means $\beta = 0$ in Eq. (1), then the periodogram is uniform appearing flat for any frequency bands (Priestley, 1981).

The main periodicity (as argued by the highest peak in the periodogram) can be tested by using the g-statistics (Ahdesmäki et al., 2005):

$$g = \frac{\max_{1\le l\le a} I(\omega_l)}{\sum_{l=1}^{a} I(\omega_l)}, \tag{4}$$

which is the maximum periodogram ordinate divided by the sum of all periodogram ordinates for $l = 1, \ldots, a$. Large value of g indicates strong periodicity and leads to the rejection of the null hypothesis.

Wichert et al. (2004) calculated the exact p-value for a realization of the g-statistics, under the Gaussian noise assumption:

$$P(g > x) = a(1-x)^{a-1} - \frac{a(a-1)}{2}(1-2x)^{a-1} + \cdots + (-1)^b \frac{a!}{b!(a-b)!}(1-bx)^{a-1}, \tag{5}$$

where b is the largest integer less than $1/x$ and x is the observed value of the g-statistic. Eq. (5), then, provides the exact significance value for a realization of the g-statistic under the assumption of Gaussian distribution of the noise.

Ahdesmäki et al. (2005) developed a robust detection of periodic time series based on the estimation of the

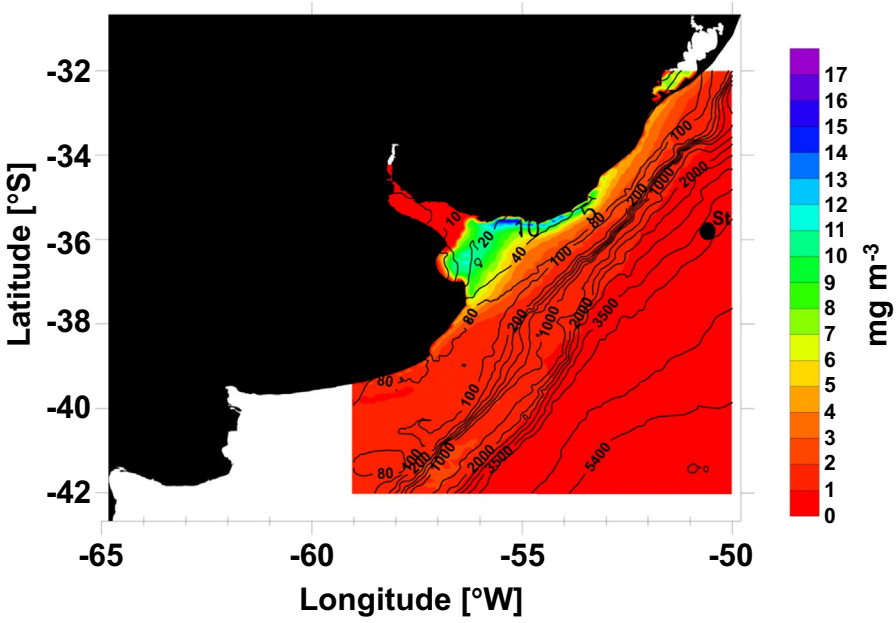

Figure 3 Spatial distribution of the mean $CHLA_{s,f}$. The black circle St marks the pixel whose time variation is plotted in Fig. 2.

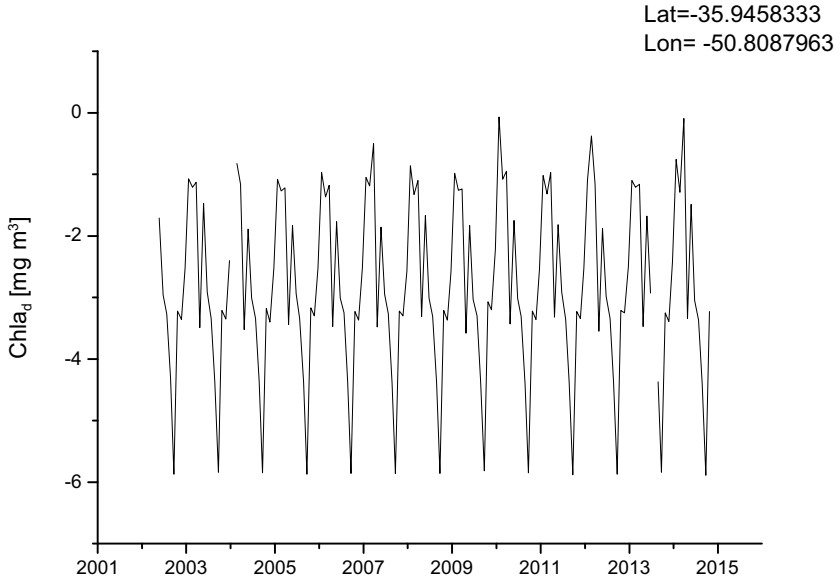

Figure 4 Standardized anomaly $CHLA_d$ for the same pixel shown in Fig. 2.

autocorrelation function. Since the periodogram $I(\omega)$ is equivalent to the correlogram spectral estimator

$$S(\omega) = \sum_{k=-N+1}^{N-1} \hat{r}(k) e^{-i\omega k}, \tag{6}$$

where

$$\hat{r}(m) = \frac{1}{N} \sum_{k=1}^{N-m} y_k y_{k+m} \tag{7}$$

is the biased estimator of the autocorrelation function, the g-statistics in Eq. (5) and the significance test in Eq. (6) can be calculated using $S(\omega)$ instead of $I(\omega)$. Recalling that the sample correlation function between two sequence with length N is given by

$$\rho(m) = \frac{\frac{1}{N}\sum_{i=1}^{N}(x_i - \overline{x})(y_i - \overline{y})}{\sigma_x \sigma_y}, \tag{8}$$

where the bar over the symbol indicates the mean; Ahdesmäki et al. (2005) obtained the following robust spectral estimator on the base of the relationship between the estimator of the autocorrelation function $\hat{r}(m)$ and the estimator of correlation function $\tilde{\rho}(m)$ between the sequences $\{y_k\}$ and $\{y_{k+m}\}$:

$$\tilde{S}(\omega) = 2\Re\left(\sum_{k=0}^{L}\tilde{\rho}(k)e^{-i\omega k}\right) - \tilde{\rho}(0), \quad (9)$$

where $\Re(x)$ indicates the real part of x, L is the maximum lag for which the correlation coefficient $\tilde{\rho}(k)$ is computed.

The g-statistics test can be modified as follows to test the significance of any frequency ω:

$$g = \frac{|\tilde{S}(\omega_l)|}{\sum_{l=1}^{a}|\tilde{S}(\omega_l)|}. \quad (10)$$

The significance values can be computed with the simulation-based method (Ahdesmäki et al., 2005): given the model as in Eq. (1) a set of P random time series are generated under the null hypothesis. The test statistics shown in Eq. (10) is evaluated for each index on each of the P time series. The obtained g-values are used to estimate the distribution of g-statistics under the null hypothesis and, therefore, the p-value.

Fig. 5 shows, as an example, the robust periodogram (Fig. 5a) of $CHLA_d$ time series corresponding to the pixel (Lat = −35.945833, Lon = −50.8087963) (Station 10001) and the p-value (Fig. 5b). The lowest p-value corresponds to the periodicity of about 12 months, which is the most significant.

For each pixel we calculated the robust periodogram and identified the most significant periodicity (the one corresponding to the lowest p-value). Since several pixel time series present data missings, we computed the robust periodogram only for those pixel time series whose amount of data missing is lower than 2/3 of the total length of the time series. Furthermore, we considered valid only those significant periodicities whose value was smaller than half of the overall period of the time series, thus only periodicities less than 77 months.

Fig. 6 shows the spatial variation of the most significant periodicity of $CHLA_d$. It is visible that relatively short period oscillations (up to 24 months) are spread almost all over the investigated area. However, predominant frequencies of relatively long period (above 24 months) extend around from latitude 37°S and longitude 56°W in direction NE, alongshore of Uruguay, where the impingement is on interannual temporal scales and variability slides along the bathymetry until Brazil.

2.2. Pixel gradient distribution

We investigated the mean $CHLA_d$ gradient distribution. For each pixel, at a specified time, the gradient magnitude is calculated using centered differences as (Saraceno et al., 2005):

$$\|grad(CHLA_d(i))\| = \sqrt{\left(\frac{CHLA_d(ix+1)-CHLA_d(ix-1)}{dist(ix+1,ix-1)}\right)^2 + \left(\frac{CHLA_d(iy+1)-CHLA_d(iy-1)}{dist(iy+1,iy-1)}\right)^2}, \quad (11)$$

where $(ix-1)$ and $(ix+1)$ are the neighbors of the ith pixel in the X (analogously in Y) direction; $dist$ is the distance in the X (analogously in Y) direction. Then, the time average of all the gradients for each pixel is calculated and the mean gradient distribution of $CHLA_d$ is computed only if the number of quadruples (two neighbors of ith pixel in X direction and two in Y direction, as indicated in formula (11)) is above 50 (Fig. 7). The pixel gradient distribution of $CHLA_d$ mainly varies between ∼0.0 and ∼0.65 mg m^{-3}. The influence of highly turbid waters of Río de La Plata can be clearly seen in the MODIS in Fig. 7. The highest chlorophyll gradient is found

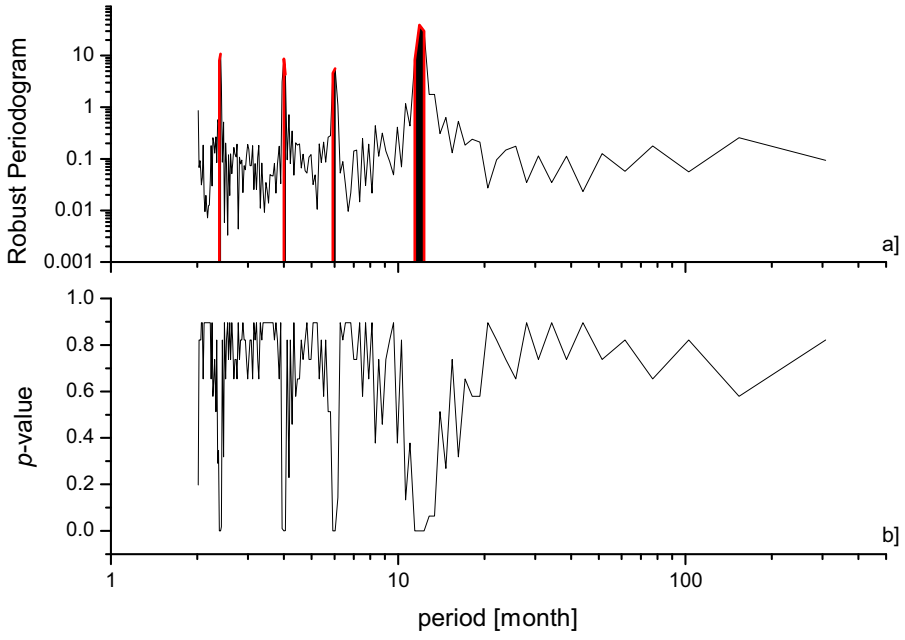

Figure 5 Robust periodogram of $CHLA_d$ time series corresponding to the pixel (Lat = −35.945833, Lon = −50.8087963) (a) and its p-value (b). The bold red part of the robust periodogram correspond to the frequencies that are significant with $p < 0.001$: the annual cycle and its higher harmonics (6 months, 4 months, 2.4 months) are clearly identified. (For interpretation of the references to color in this figure legend, the reader is referred to the web version of this article.)

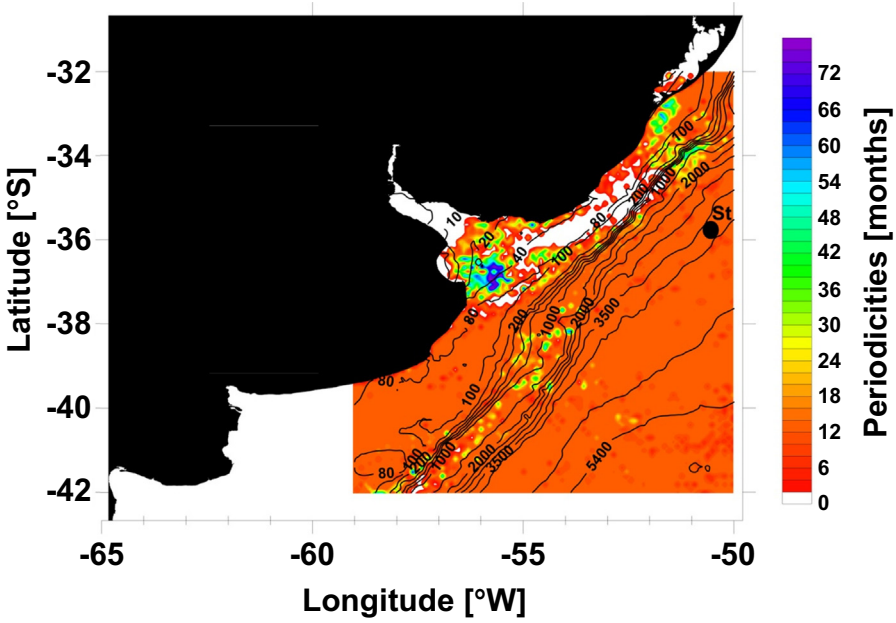

Figure 6 Spatial distribution of the most significant periodicity (months) of $CHLA_d$. The black circle St marks the pixel whose time variation is plotted in Fig. 2.

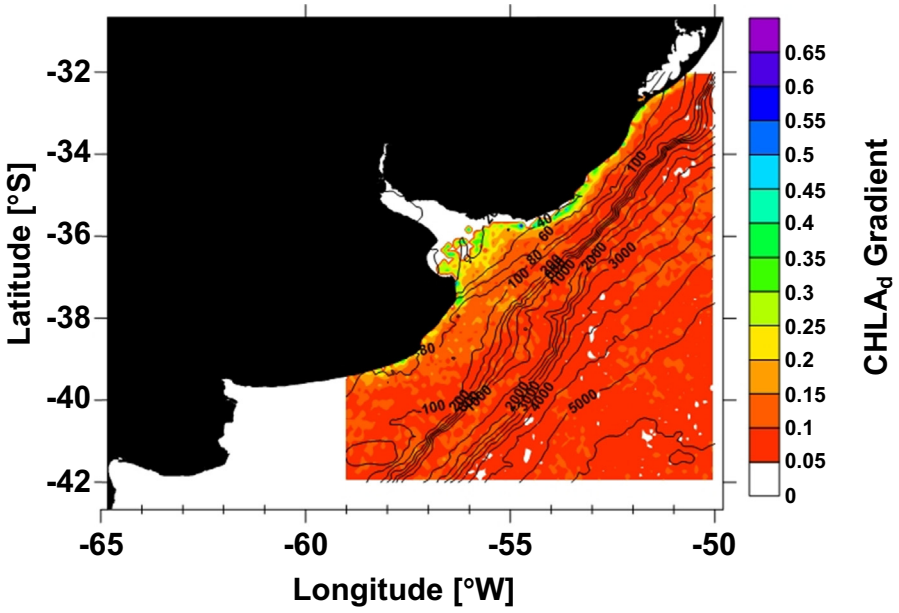

Figure 7 Pixel $CHLA_d$ gradient distribution.

near coastal regions. The pixel gradient map shows a spatial distribution of chlorophyll consistent with known patterns and expected values in the outer region of the Rio de la Plata. In fact, the highest gradient values can be observed along the northern tip of Samborombón Bay and the 15 and 45 m isobaths along south-north direction, showing a north-eastward discharge along the Uruguayan coast as also found by Calliari and Gomez (2005), Romero et al. (2006) and Simionato et al. (2004). The fluvial and estuarine domains in the West and the Oceanic domains in the East are divided by the thermohaline front, near isobaths 45 m along south-north direction. The discharge of the Río de la Plata registers low values of $CHLA_d$ due to the unfavorable conditions for the development of phytoplankton related to the low availability of light, being within the limit of salt intrusion (maximum turbidity); however a clear relationship with the gradient that measures the relative space-time variation of $CHLA_d$ cannot be established, due to the gaps in the time series of the pixels of that area (white zones in Fig. 7). In addition, a high gradient region is observed

near the coast and outer shelf area between 40° and 34°S, where, in addition, Malvinas slope water intrusion plays an important role in phytoplankton blooms (Piola et al., 2010; Romero et al., 2006).

3. Discussion

It is well known that at the mouth of Rio de la Plata estuarine highly variable, complex and unpredictable ecosystems exist (Day et al., 1989), where different forcing interact with geomorphologic configuration, depth, dimension of the estuary. Around the 30 m isobath, the chlorophyll variability is influenced mostly by local scale processes, such as river and estuarine outflow, wave effects, and nearshore circulation (Campos et al., 1999; Simionato et al., 2004, 2005). Nearshore coastal areas tend to exhibit high CHLA levels due to increased nutrient inputs from land runoff, riverine and estuarine flux, resuspension of sediments, pore water nutrients and recycling of nutrients. Nutrient loads of terrestrial origin to the nearshore waters of the Rio de la Plata increased by an order of magnitude (Martinez and Ortega, 2015). This is most likely due to the increase urbanization and agricultural use in the watersheds of the study area. These large freshwater flows can also set up salinity fronts, which may have the ability to inhibit the cross-shelf exchange of dissolved and suspended materials (Acha et al., 2004), thereby affecting the residence time of nutrients and phytoplankton growth limited by light availability on the inner shelf (Martinez and Ortega, 2015).

Several heterogeneous factors contribute to determine the high spatial-temporal variability of chlorophyll. The Rio de la Plata estuary, in fact, is of large scale type, characterized by large freshwater discharge; it also represents a very important area in the Argentine Platform Continental Shelf, featured by biophysical and biogeochemical processes related to the complex pattern of regional variability (Calliari and Gomez, 2005; Garcia and Garcia, 2008). These processes are mainly characterized by a strong annual cycle in most of the study area, although an area from latitude 37°S in direction NE, alongshore of Uruguay to Brazil, interannual periodicities are also evidenced (Fig. 6). Such periodicities may be the effect of variations in the discharge of the Rio de la Plata mainly associated with the El Niño phenomena, characterized by episodic hydro-meteorological phenomena (pulsatile) whose extreme manifestation are the floods, that cause significant impacts on the population (Acha et al., 2008; Depetris et al., 1996; Mechoso and Iribarren, 1992), that along with other external factors (wind, etc.) can introduce unstable conditions on CHLA (Gonzalez-Silvera et al., 2006; Piola et al., 2005; Sathicq et al., 2015).

The chlorophyll gradients presents a relatively high variability from 0.02 to 0.65 mg m^{-3}. The high values, indicating regions of high concentration, are assumed on two areas, isolated from each other. These two areas of increased phytoplankton abundance correspond to: (a) the saline front of the estuarine system of Rio de la Plata, and to (b) the strip of the platform that extends along the isobaths of 80 m (coast of Uruguay), especially in the center and south of the study area, which also occupies sectors of the intermediate platform sector (Acha et al., 2004). The results of the analysis of chlorophyll gradients suggest that this variable is closely linked with hydrodynamics processes. Indeed, at the mouth of the Rio de la Plata a marked increase gradient of chlorophyll can be seen, probably linked with the temperature and the amount of light hours (Framiñan and Brown, 1986). This phenomenon is expected considering that there abundant nitrogen and water clarity are enhanced by the sedimentation of particles in suspension, allowing penetration of light (Calliari and Gomez, 2005; Lasta et al., 1996). Chlorophyll gradients increase along the Uruguay coast of the Rio de la Plata and decrease outside along the coast of Argentina (Nagy et al., 1987). This could be correlated with the average displacement of fresh water plume in response to external forcings (wind, geometry depth, etc.). In the frontal domain (frontal region and marine adjacent zone) CHLA gradients are distributed as spots reaching maximum values of 0.65 mg m^{-3}. Rather high values of CHLA gradients are observed over the Samborombón Bay (37°S and 57°W), due to the geometry of the area. In the center and south of the deepest region of the platform sector, the CHLA gradient is less than that observed in the saline front at the mouth of the Rio de la Plata ($<$0.2 mg m^{-3}) and shows a more homogeneous spatial distribution.

4. Conclusions

By using the monthly AQUA MODIS satellite images from July 2002 to April 2015 we analyzed the spatial and temporal variability of CHLA data in the Brazil–Malvinas Confluence Zone, which represents one of the most productive oceanic areas worldwide. The spatial distribution of the average of CHLA over the investigated area indicates a high concentration in the nearshore region reflecting the longitudinal gradients within these coastal waters. Due to the short length of each pixel time series (only 154 values) that become even shorter in presence of missing data, we used a robust method for the identification of the most significant periodicities over the investigated area. A predominance of the annual periodicity was found over the most of the area, but even longer periodicities were identified from latitude 37°S in direction NE, alongshore of Uruguay to Brazil, possibly related to discharge fluctuations of Rio de la Plata associated with the El Niño phenomena. The analysis of pixel gradient distribution reveals increased phytoplankton abundance corresponding to the saline front of the estuarine system of Rio de la Plata, and to the strip of the platform that extends along the isobaths of 80 m (coast of Uruguay), especially in the center and south of the study area. Our findings, obtained by using robust statistical methods could contribute to deepen our comprehension of the complex biophysical processes that govern the space-time dynamics of the variability of Chlorophyll-*a* data within the BMCZ.

Acknowledgements

Two anonymous referees are acknowledged for their constructive review. Moderate Resolution Imaging Spectrophotometer (MODIS) data were distributed by the NASA Ocean Biology Processing Group (http://oceancolor.gsfc.nasa.gov/). This study was partially funded by Mincyt-MAE Project 1302.

References

Acha, E.M., Mianzan, H.W., Guerrero, R.A., Favero, M., Bava, J., 2004. Marine fronts at the continental shelves of austral South America, physical and ecological processes. J. Mar. Syst. 44 (1—2), 83—105, http://dx.doi.org/10.1016/j.jmarsys.2003.09.005.

Acha, M., Mianzan, H., Guerrero, R., Carreto, J., Giberto, D., Montoya, N., Carignan, M., 2008. An overview of physical and ecological processes in the Rio de la Plata Estuary. Cont. Shelf Res. 28 (13), 1579—1588, http://dx.doi.org/10.1016/j.csr.2007.01.031.

Ahdesmäki, M., Lähdesmäki, H., Pearson, R., Huttunen, H., Yli-Harja, O., 2005. Robust detection of periodic time series measured from biological systems. BMC Bioinform. 6, 117, http://dx.doi.org/10.1186/1471-2105-6-117 18 pp.

Brandini, F., Boltovskoy, D., Piola, A., Kocmur, S., Rottgers, R., Abreu, P.C., Lopes, R., 2000. Multiannual trends in fronts and distribution of nutrients and chlorophyll in the southwestern Atlantic (30-23S). Deep-Sea Res. Pt. I 47 (6), 1015—1033, http://dx.doi.org/10.1016/S0967-0637(99)00075-8.

Braga, E., Chiozzini, V.C., Glaucia, B.B., Maluf, J.C.C., Aguiar, V.M. C., Charo, M., Molina, D., Romero, S.I., Eichler, B.B., 2008. Nutrient distributions over the Southwestern South Atlantic continental shelf from Mar del Plata (Argentina) to Itajaí (Brazil): winter—summer aspects. Cont. Shelf Res. 28 (13), 1649—1661, http://dx.doi.org/10.1016/j.csr.2007.06.018.

Calliari, D., Gomez, N., 2005. Biomass and composition of the phytoplankton in the Río de la Plata: large-scale distribution and relationship with environmental variables during a spring cruise. Cont. Shelf Res. 25 (2), 197—210, http://dx.doi.org/10.1016/j.csr.2004.09.009.

Campos, J.D., Lentini, C.A., Miller, J.L., Piola, A.R., 1999. Interannual variability of the Sea Surface Temperature in the South Brazilian Bight. Geophys. Res. Lett. 26 (14), 2061—2064, http://dx.doi.org/10.1029/1999GL900297.

Carreto, J.I., Lutz, V.A., Carignan, M.O., Colleoni, A.D.C., Marcos, S.G. D., 1995. Hydrography and chlorophyll *a* in a transect from the coast to the shelf-break in the Argentinian Sea. Cont. Shelf Res. 15 (2—3), 315—336, http://dx.doi.org/10.1016/0278-4343(94)E0001-3.

Day Jr., J.W., Hall, C.A.S., Kemp, W.M., Yáñez-Arancibia, A., 1989. Estuarine Ecology. Wiley, New York, 576 pp.

Depetris, P.J., Kempe, S., 1990. The impact of the El Niño 1982 event on the Parana River, its discharge and carbon transport. Palaeogeogr. Palaeocl. 89 (3), 239—244, http://dx.doi.org/10.1016/0921-8181(90)90019-9.

Depetris, P., Kempe, S., Latif, M., Mook, W., 1996. ENSO-controlled flooding in the Paranti River (1904—1991). Naturwissenschaften 83 (3), 127—129, http://dx.doi.org/10.1007/BF01142177.

Framiñan, M., Brown, O., 1986. Study of the Rio de la Plata turbidity front. Part I: spatial and temporal distribution. Cont. Shelf Res. 16 (10), 1259—1283, http://dx.doi.org/10.1016/0278-4343(95)00071-2.

Garcia, C., Garcia, V.T., 2008. Variability of chlorophyll-*a* from ocean color images in the La Plata continental shelf region. Cont. Shelf Res. 28 (13), 1568—1578, http://dx.doi.org/10.1016/j.csr.2007.08.010.

Gonzalez-Silvera, A., Santamaria del Angel, E., Millan-Nuñez, R., 2006. Spatial and temporal variability of the Brazil-Malvinas Confluence and the La Plata Plume as seen by SeaWiFS and AVHRR imagery. J. Geophys. Res. 111, C06010, http://dx.doi.org/10.1029/2004JC002745.

Gordon, A., 1989. Brazil-Malvinas confluence — 1984. Deep-Sea Res. Pt. A 36 (3), 359—384, http://dx.doi.org/10.1016/0198-0149(89)90042-3.

Guerrero, R.A., Acha, E.M., Framiñan, M.B., Lasta, C.A., 1997. Physical oceanography of the Río de la Plata estuary, Argentina. Cont. Shelf Res. 17 (7), 727—742, http://dx.doi.org/10.1016/S0278-4343(96)00061-1.

Huret, M., Dadou, I., Dumas, F., Lazure, P., Garçon, V., 2005. Coupling physical and biogeochemical processes in the Río de la Plata plume. Cont. Shelf Res. 25 (5—6), 629—653, http://dx.doi.org/10.1016/j.csr.2004.10.003.

Lasta, C., Gagliardini, D., Milovich, J., Acha, E., 1996. Seasonal variation observed in surface water temperature of Samborombón Bay, Argentina, using NOAA-AVHRR and field data. J. Coast. Res. 12 (1), 18—25.

Lutz, V., Segura, V., Dogliotti, A., Gagliardini, D., Bianchi, A., Balestrini, C., 2010. Primary production in the Argentine Sea during spring estimated by field and satellite models. J. Plankton Res. 32 (2), 181—195, http://dx.doi.org/10.1093/plankt/fbp117.

Machado, I., Barreiro, M., Calliari, D., 2013. Variability of chlorophyll-*a* in the Southwestern Atlantic from satellite images: seasonal cycle and ENSO influences. Cont. Shelf Res. 53, 102—109, http://dx.doi.org/10.1016/j.csr.2012.11.014.

Marrari, M., Piola, A., Valla, D., Wilding, J., 2016. Trends and variability in extended ocean color time series in the main reproductive area of the Argentine hake, *Merluccius hubbsi* (Southwestern Atlantic Ocean). Remote Sens. Environ. 177, 1—12, http://dx.doi.org/10.1016/j.rse.2016.02.011.

Martinez, A., Ortega, L., 2015. Delimitation of domains in the external Río de la Plata estuary, involving phytoplanktonic and hydrographic variables. Braz. J. Oceanogr. 63 (3), 217—227, http://dx.doi.org/10.1590/S1679-87592015086106303.

Mechoso, C.R., Iribarren, G.P., 1992. Streamflow in southeastern South America and the southern oscillation. J. Climate 5, 1535—1539, http://dx.doi.org/10.1175/1520-0442(1992)005<1535:SISSAA>2.0.CO;2.

Nagy, G., Lopez Laborde, J., Anastasia, L., 1987. Caracterización de ambientes en el Río de la Plata exterior (salinidad y turbiedad óptica). Investigación Oceanol. 1 (1), 31—56.

Pierini, J.O., Lovallo, M., Gómez, E.A., Telesca, L., 2016. Fisher-Shannon analysis of the time variability of remotely sensed sea surface temperature at the Brazil-Malvinas Confluence. Oceanologia 58, 187—195.

Piola, A.R., Campos, E.J., Moller Jr., O., Charo, M., Martinez, C.M., 2000. Subtropical shelf front off eastern South America. J. Geophys. Res. 105 (C3), 6566—6578, http://dx.doi.org/10.1029/1999JC000300.

Piola, A.R., Matano, R., Palma, E., Moller Jr., O., Campos, E., 2005. The influence of the Plata River discharge on the western South Atlantic shelf. Geophys. Res. Lett. 32 (1), 1603—1606, http://dx.doi.org/10.1029/2004GL021638.

Piola, A., Martinez, N., Guerrero, R., Jardón, F., Palma, E., Romero, S., 2010. Malvinas-slope water intrusions on the northern Patagonia continental shelf. Ocean Sci. 6, 345—359, http://dx.doi.org/10.5194/os-6-345-2010.

Piola, A., Romero, S., Zajaczkovski, U., 2008. Space time variability of the Plata plume inferred from ocean color. Cont. Shelf Res. 28 (13), 1556—1567, http://dx.doi.org/10.1016/J. Csr.2007.02.013.

Priestley, M., 1981. Spectral Analysis and Time Series, Two-Volume Set, Volume 1-2. Elsevier.

Romero, S., Piola, A., Charo, M., Garcia, C.A.E., 2006. Chlorophyll-*a* variability off Patagonia based on SeaWiFS data. J. Geophys. Res. 111 (C5), 1—11, http://dx.doi.org/10.1029/2005JC003244.

Saraceno, M., Provost, C., Piola, A., 2005. On the relationship between satellite retrieved surface temperature fronts and chlorophyll-*a* in the Western South Atlantic. J. Geophys. Res. 110 (C11), http://dx.doi.org/10.1029/2004JC002736.

Simionato, C., Dragani, W., Meccia, V., Nuñez, M., 2004. A numerical study of the barotropic circulation of the Río de la Plata estuary: sensitivity to bathymetry, the Earth's rotation and low frequency wind variability. Estuar. Coast. Shelf Sci. 61 (2), 261—273, http://dx.doi.org/10.1016/j.ecss.2004.05.005.

Simionato, C., Vera, C., Siegismund, F., 2005. Surface wind variability on seasonal and interannual scales over Río de la Plata Area.

J. Coast. Res. 21 (4), 770—783, http://dx.doi.org/10.2112/008-NIS.1.

Sathicq, M., Bauer, D., Gomez, N., 2015. Influence of El Nino Southern Oscillation phenomenon on coastal phytoplankton in a mixohaline ecosystem on the southeastern of South America: Rio de la Plata estuary. Mar. Pollut. Bull. 98 (1—2), 26—33, http://dx.doi.org/10.1016/j.marpolbul.2015.07.017.

Wichert, S., Fokianos, K., Strimmer, K., 2004. Identifying periodically expressed transcripts in microarray time series data. Bioinformatics 20 (1), 5—20.

Oceanologia (2018) 60, 86—96

Available online at www.sciencedirect.com

ScienceDirect

journal homepage: www.journals.elsevier.com/oceanologia/

ORIGINAL RESEARCH ARTICLE

Laboratory measurements of remote sensing reflectance of selected phytoplankton species from the Baltic Sea

Monika Soja-Woźniak [a,b,c,*], **Mirosław Darecki** [d], **Bożena Wojtasiewicz** [a,e], **Katarzyna Bradtke** [a]

[a] *Institute of Oceanography, University of Gdańsk, Poland*
[b] *Department of Space, Earth and Environment, Chalmers University of Technology, Gothenburg, Sweden*
[c] *CSIRO Oceans & Atmosphere, Hobart, TAS, Australia*
[d] *Institute of Oceanology Polish Academy of Sciences, Sopot, Poland*
[e] *CSIRO Oceans & Atmosphere, Crawley, WA, Australia*

Received 19 May 2017; accepted 8 August 2017
Available online 26 August 2017

KEYWORDS
Phytoplankton monoculture;
Laboratory measurements;
Remote sensing reflectance

Summary Results of unique laboratory measurements of remote sensing reflectance (R_{rs}) of several phytoplankton species typically occurring in high abundances in the Baltic Sea waters are presented. Reflectance spectra for diatoms: *Cyclotella meneghiniana* and *Skeletonema marinoi* and cyanobacteria: *Dolichospermum* sp., *Nodularia spumigena* and *Synechococcus* sp. were analysed in terms of assessment of their characteristic features and the differences between them. These species contain similar pigments, which results in general similarities of reflectance spectra, i.e. decrease of reflectance magnitude in the blue and red spectrum regions. However, hyper-spectral resolution of optical measurements let us find differences between optical signatures of diatoms and cyanobacteria groups and between species belonging to one group as well. These differences are reflected in location of local maxima and minima in the reflectance spectrum and changes in relative height of characteristic peaks with changes of phytoplankton concentration. Wide ranges of phytoplankton concentrations were analysed in order to show the persistence of R_{rs} characteristic features. The picoplankton species, *Synechococcus* sp. show the

* Corresponding author at: CSIRO Oceans & Atmosphere, Hobart, TAS 7000, Australia. Tel.: +61 362 32 5163.
E-mail addresses: monika@soja-wozniak.com (M. Soja-Woźniak), darecki@iopan.gda.pl (M. Darecki), bozena.wojtasiewicz@ug.edu.pl (B. Wojtasiewicz), katarzyna.bradtke@ug.edu.pl (K. Bradtke).
Peer review under the responsibility of Institute of Oceanology of the Polish Academy of Sciences.

ELSEVIER | Production and hosting by Elsevier

http://dx.doi.org/10.1016/j.oceano.2017.08.001

most distinct optical signature, which let to distinguish separate cluster in hierarchical cluster analysis (HCA). The results can be used to calibrate input data into radiative transfer model, e.g. phase function or to validate modelled R_{rs} spectra.

1. Introduction

Harmful algal blooms that can vary in terms of their harmfulness, causal organisms, biomass distribution, and many other factors affecting the marine environment occur frequently in many marine and freshwater reservoirs. In the Baltic Sea massive phytoplankton blooms affecting its entire ecosystem are observed almost every year during spring, summer and early autumn (Kahru, 1997; Klais et al., 2013; Kutser et al., 2006; Pliński et al., 2007). From this point of view monitoring of these blooms, especially with cost effective methods like optical indirect measurements carried out in situ or remotely, e.g. by satellites, is in the interest of many environmental agencies and institutions. There is a strong demand for remote sensing algorithms which enable distinguishing between different phytoplankton species (IOCCG, 2014; Sathyendranath et al., 2016). Some of published studies use look up tables (LUT) (Xi et al., 2015) or optical indexes (Kim et al., 2016) based on modelled R_{rs} characteristics for individual species, but output of these models has not been validated against measured R_{rs}. The results presented here can be a significant contributions to that goal.

The spectral characteristic of the water leaving radiance (L_w) can be linked to the optically significant components of seawater. Thus the spectra of remote sensing reflectance (R_{rs}), being the ratio between the upwelling radiance just above the water and the downwelling irradiance at the sea surface, can be a useful tool which relates optical measurements to desired optically active seawater constituents (e.g. Darecki et al., 2008; Kratzer et al., 2008; Soja-Woźniak et al., 2017; Woźniak et al., 2008). For last two decades both in situ and remote sensing radiometry has developed significantly. Improved in situ techniques enabled measurement of L_w with hyperspectral resolution while bio-optical studies gave increasingly better understanding of the interaction between water components and the light field (Evers-King et al., 2014). Nowadays, retrieval of the phytoplankton pigments concentration based on R_{rs} can be obtained with reasonable accuracy (Darecki and Stramski, 2004; Darecki at al., 2008; Simis et al., 2005; Soja-Woźniak et al., 2017; Woźniak et al., 2016), but identification of single phytoplankton species or even entire phytoplankton functional groups by means of R_{rs} still remains a challenge (Craig et al., 2006; Hunter et al., 2008; Lubac et al., 2008; Shang et al., 2014; Torrecilla et al., 2011; Xi et al., 2015).

Phytoplankton species are characterised by their unique light absorption and backscattering properties resulting from differences in cell sizes and shapes, inner structure and composition of the pigments (e.g. Aguirre-Gómez et al., 2001; Vaillancourt et al., 2004; Whitmire et al., 2010) that all influence the shape of the R_{rs} spectra. The main pigments occurring in cyanobacteria and diatoms together with their absorptive properties are given in Table 1. Analysis of remote sensing reflectance of the Baltic Sea phytoplankton was carried out in the previous studies in order to detect and characterise algal blooms and to differentiate phytoplankton taxonomic groups (e.g. Kutser et al., 2006; Xi et al., 2015). However, the R_{rs} has been determined using either the R_{rs} dependence on the absorption and backscattering given by Gordon et al. (1975) or radiative transfer simulations. This approach can lead to some errors resulting from the applied assumptions, e.g. the assumption of the shape of the scattering function which for the phytoplankton cultures can be much different from the average Petzold particle scattering function as shown by Volten et al. (1998). There have been several studies performed in which the R_{rs} spectra of various phytoplankton taxonomic were measured under controlled laboratory or semi-laboratory conditions (Table 2).

Table 1 Main pigments occurring in cyanobacteria and diatoms with the location of main absorption peaks (based on Roy et al., 1989). The "+" sign indicates the presence of the chosen pigment.

Pigment	Cyanobacteria	Diatoms	Location of main absorption peaks [nm]
Chlorophylls			
a	+	+	430–432, 662–666
c		+	442–457, 628–634
Carotenoids			
β-Carotene	+	+	451–454, 475–480
Myxoxanthophyll	+		472–478, 502–510
Zeoxanthin	+		449–454, 475–481
Diadinoxanthin		+	445–449, 475–479
Diatoxanthin		+	451–453, 478–480
Fucoxanthin		+	444–449, 467–475
Phycobilins			
Phycocyanin	+		620
Phycoerythrin	+		550
Allophycocyanin	+		650

Table 2 Overview of previous laboratory and semi-laboratory studies on the characteristics of remote sensing reflectance spectra of selected phytoplankton species.

Group	Species	Tank volume [m^3]	Light conditions	Chl-*a* [mg m^{-3}]	Reference
Chlorophyte	*Chlorella* sp.	80	Outdoor, clear sky	0.5–60	[a]
Chlorophyte	*Chlorella* sp. (with small amounts of other species)	9.5	Outdoor, clear sky	34–439	[a]
Cyanophyte	*Anabaena* sp.	0.57	500 W halogen lamp	12.7–58.3	[a]
Bacillariophyte	*Novicula minima*	30	1000 W halogen lamp	3–77	[a]
Dinophyte	*Prorocentrum minimum*	0.05	Outdoor, clear sky	785	[b]
Cyanophyte	*Synechococcus* sp.	0.05	Outdoor, clear sky	29.9	[b]
Cyanophyte	*Planktothrix agardhii*	0.002	500 W halogen lamp	0–105	[c]
Cyanophyte	*Microcystis aeruginosa*	0.002	500 W halogen lamp	0–95.6	[c]
Cyanophyte	*Anabaena flos-aquae*	0.002	500 W halogen lamp	0–136	[c]
Chlorophyte	*Scenedesmus* sp.	0.002	500 W halogen lamp	0–122	[c]
Bacillariophyte	*Cyclotella meneghiniana*	0.002	500 W halogen lamp	0–127	[c]

[a] Gitelson et al. (1999).
[b] Warner and Fan (2013).
[c] Oyama et al. (2010).

In this study we characterised the reflectance spectra for five phytoplankton species commonly present in the Baltic Sea, diatoms: *Cyclotella meneghiniana* and *Skeletonema marinoi* and cyanobacteria: *Dolichospermum* sp., *Nodularia spumigena* and *Synechococcus* sp. The aim of the study was to find the characteristic features of R_{rs} spectra which can be observed for selected species over a wide range of phytoplankton concentrations. The results can be used to calibrate input data into radiative transfer model, e.g. phase function (Woźniak, 2014) or to validate modelled R_{rs} spectra. Moreover, they can be used as reference data to compare with in situ measured R_{rs} spectra in order to find a dominant species in algal assemblages. Analysis of variability of R_{rs} spectra as a response to changes in the phytoplankton growth conditions (e.g. nutrient availability, light, temperature, etc.) affecting pigment composition as well as cell sizes was out of scope of this study, therefore further investigation is necessary.

2. Material and methods

2.1. Selected phytoplankton species

Five phytoplankton species were chosen for this study. *C. meneghiniana* is a cosmopolitan diatom species in the euphotic surface waters of the whole Baltic Sea. It exists seasonally in the Southern Baltic in algal communities in autumn and winter, and is a quantitatively important component of the blooming species (Lewandowska and Kosakowska, 2004; Pankow et al., 1990). *S. marinoi* is a centric diatom species with worldwide distribution, which blooms mainly in the temperate sea waters. It is highly abundant also in the Baltic Sea especially during the spring bloom. *S. marinoi* has an important role as a primary producer in the Baltic Sea and serves as a valuable source of energy for higher trophic levels. Therefore, studying this organism has a high ecological relevance (Godhe et al., 2006). *N. spumigena* and *Dolichospermum* sp. are filamentous, nitrogen-fixing cyanobacteria species that can float near the water surface and form dense algal blooms which can be seen from satellite level (Walsby et al., 1995). *N. spumigena* is one of dominant species in summer algal blooms in the Baltic Sea. Moreover, this species produces nodularin, a hepatotoxin which has a negative impact on other organisms (Mazur and Pliński, 2003; Mazur-Marzec et al., 2006). *Dolichospermum* sp. (before known as *Anabaena* sp.) is a co-occurring species during cyanobacteria blooms and can contribute significantly to the total biomass, especially in the northern part of the Baltic Sea. *Dolichospermum* sp. can produce microcystin and is potentially toxic (Kanoshina et al., 2003; Karlsson et al., 2005; Seppälä et al., 2007; Suikkanen et al., 2007). *Synechococcus* sp. is a non-motile and non-nitrogen fixing cosmopolitan picocyanobacteria species which is a significant contributor to phytoplankton biomass and primary productivity (Albertano et al., 1997).

Synechococcus sp. (AA-0091), *C. meneghiniana* (BA-0010) and *S. marinoi* (BA-0098) were taken from the Culture Collection of Baltic Algae. They were grown in batch cultures in F/2 medium in a culture chamber under controlled conditions at the temperature of 18°C and 16/8 h light/dark cycle. *N spumigena* (CCNP1403), and *Dolichospermum* sp. (CCNP1405) strains were taken from the Culture Collection of Northern Poland. The strains were cultured in BG11 medium with salinity of 7 PSU in a phytotron chamber under the irradiance of 14 $\mu E\ m^{-2}\ s^{-1}$ in 12/12 h light/dark cycle with constant temperature of 22°C. All analysed phytoplankton species are characterised in Table 3.

2.2. Experimental setup and radiometric measurements

A series of radiometric measurements of water containing phytoplankton monocultures were undertaken in a large circular tank ($Ø = 1.2$ m, $h = 1.4$ m, $V = 1.6\ m^3$) under controlled darkroom conditions (Fig. 1). The size of the tank and its inner mat black colour minimised the influence of light

Table 3 Size, shape and main characteristic pigments (PC – phycocyanin, PE – phycoerythrin, Fuco – fucoxanthin) of studied phytoplankton species.

Species	Diameter [μm]	Height [μm]	Shape	Marker pigment
Nodularia spumigena	6–12	<100	Cylinder	PC
Dolichospermum sp.	4.5–11	<100	Chain of spheres	PC
Synechococcus sp.	2	–	Sphere	PC, PE
Cyclotella meneghiniana	10–35	8.4–22.4	Cylinder	Fuco
Skeletonema marinoi	2–10	4–21	Cylinder	Fuco

All size and shape data taken from Annex 1 in Olenina et al. (2006).

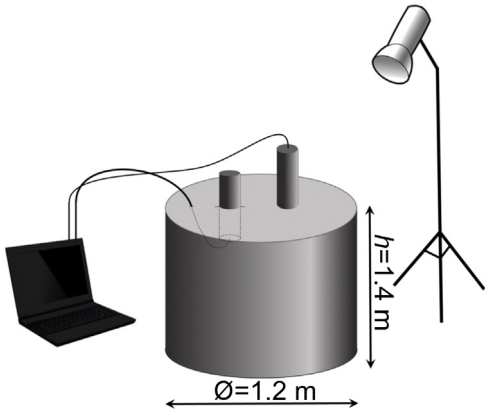

Figure 1 The experimental setup.

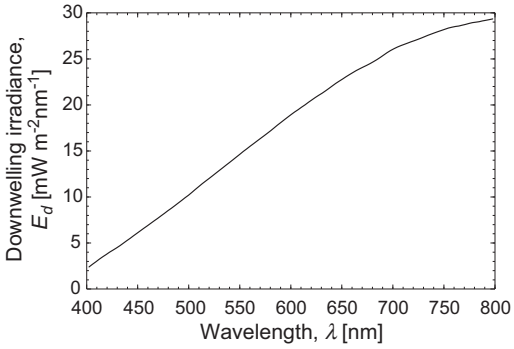

Figure 2 The irradiance spectrum of the lamp used during the measurements.

reflection from tank's sides and bottom on measurement results.

The experimental setup was illuminated only by an incandescent 2000 W lamp with smooth spectrum as an irradiance source (Fig. 2). It enabled to eliminate the influences of the variable contribution of the natural light in the background, moreover all measurements were taken under the same light conditions making the results comparable. The light intensity during the experiments was approximately 30 times lower compared to the daylight. Nevertheless, it was similar to the conditions in the culture chamber and therefore prevented formation of additional photo-protective pigments during the experiments.

During each series of measurements portions of phytoplankton monoculture were being added to brackish water (7 PSU equal to average salinity of the Baltic Sea surface waters; Feistel et al., 2010) in order to obtain increasing concentration of phytoplankton. Radiometric measurements were performed right after putting and carefully mixing the monocultures into the experimental tank. Downwelling irradiance (E_d) [W m^{-2} nm^{-1}] above (0^+) and below (at 0^-, 15 and 50 cm) the water surface and upwelling radiance (L_u) [W m^{-2} nm^{-1} sr^{-1}], just below water surface were measured with sampling intervals of 3.3 nm and a spectral resolution of ~ 10 nm by means of hand–held hyperspectral sensors RAMSES ACC–VIS (Trios) and RAMSES MRC (Trios), respectively (Hommersom et al., 2012). The radiometers have been mounted on the small frame to provide repeatability of sampling conditions. To minimise the self-shading effect, the MRC radiometer was custom designed with effective sensor diameter of 1 cm at the side of the optical window. The measurements were repeated five times for each concentration. The variability within these consecutive measurements varied among the species with the coefficient of variation (CV) (calculated separately for each wavelength as a ratio of standard deviation to mean value) ranging from 0.1 to 0.2% for E_d and 0.1 to 20% for L_u. The largest variability for L_u was observed between 450 nm and 470 nm and above 700 nm. In the range between 500 nm and 700 nm CV for L_u was lower than 10%. In further calculations mean values of E_d and L_u were used. In order to calculate the remote sensing reflectance, the upwelling radiance measured below the water surface $L_u(0^-)$ was transferred into the $L_u(0^+)$ by using immersion factor (I_f) determined for that radiometer in the paper (Zibordi and Darecki, 2006). Then remote sensing reflectance R_{rs} [sr^{-1}] in spectral range between 450 nm and 750 nm was derived as the ratio between L_u and E_d at the water surface (0^+). The diffuse attenuation coefficient of the downward irradiance $K_d(\lambda)$ [m^{-1}] was calculated as:

$$K_d(\lambda)(z_1, z_2) = -\frac{1}{z_2 - z_1} \ln\left(\frac{E_d(\lambda, z_2)}{E_d(\lambda, z_1)}\right), \quad (1)$$

where $E_d(z_i)$ is downwelling irradiance measured at z_i depth.

The transparency of water was characterised by K_d(PAR) calculated within the photosynthetically active radiation spectrum.

2.3. Pigment concentration

For each concentration of all analysed phytoplankton monoculture water samples were taken for further spectrophotometric analysis of chlorophyll-*a* (chl-*a*) (Jeffrey and Humphrey, 1975) and total carotenoids (TCar) concentrations (Parsons et al., 1984). Spectrophotometer Shimadzu UV-1202

UV–VIS was used. The pigment (chlorophyll-*a* and total carotenoids) concentration was calculated as follows:

$$C = (X \cdot E) \cdot V^{-1} (\mu g\, dm^{-3}), \quad (2)$$

where C is the chlorophyll *a* (chl-*a*) or total carotenoids (TCar) concentration, X is amount of pigment in μg per ml extract, E is the volume of acetone in ml (here 10 ml), and V is the volume of filtered water in litres. To calculate chlorophyll *a* (chl-*a*) concentration X was derived from the following equation:

$$X = (11.85 \cdot OD_{664} - 1.54 \cdot OD_{647} - 0.08 \cdot OD_{630}) \cdot L^{-1}, \quad (3)$$

where OD_λ stands for the optical density at particular wavelength corrected by subtracting OD_{750}. While to calculate total carotenoids (TCar) concentration X was derived from:

$$X = (7.6 \cdot (OD_{480} - 1.49 \cdot OD_{510})) \cdot L^{-1}, \quad (4)$$

where OD_{480} is the optical density at 480 nm corrected by subtracting $3 \cdot OD_{750}$, OD_{510} is the optical density at 510 nm corrected by subtracting $2 \cdot OD_{750}$. L is the pathlength of the cuvette in centimetres, here it was 1 cm.

2.4. Statistical approach

R_{rs} spectra measured for the highest phytoplankton biomass for each species were used as reference spectra to analyse how characteristic features change with decrease of phytoplankton concentration. The degree of similarity between the reference spectrum, and R_{rs} spectrum for each concentration of the same phytoplankton species was quantified with similarity index (SI) (e.g. Millie et al., 1997, 2002), which is given by:

$$SI = 1 - \frac{2\arccos(A)}{\pi}, \quad (5)$$

where A is a cosine of the angle between two vectors that comprise the fourth derivative of the two R_{rs} spectra (450–750 nm) smoothed with Savitsky–Golay filter. The SI calculation yields a number from zero to one, where zero indicates no similarity between reference and derived spectra, and one indicates absolute similarity between them. SI reflects mainly the differences in the spectral shape of optical data rather than magnitude.

The agglomerative hierarchical cluster analysis (HCA) was used in order to test which of the examined phytoplankton species gives an optical signal which is unique enough to differentiate this species from another one at different concentrations. This statistical method links entities (here, spectra derived from each species at different concentrations) characterised by similar properties into groups (clusters) (Jain et al., 1999; Townend, 2002). We tested R_{rs} and the 4th derivative of R_{rs} spectra as an input data in cluster analysis separately. The cluster tree was generated using Ward's method which ensures homogeneity (variance minimum) within a single group together with heterogeneity (variance maximum) among clusters (Nowacki and Jarosz, 1998). The similarity between groups is calculated from relative distance of linkage (Euclidean distance). The highest distance means 0% of similarity.

3. Results and discussion

E_d measured at three depths (0^- cm, 15 cm, 50 cm) were used to calculate K_d. For clear water three spectra of attenuation coefficient at different depth overlapped in the range between 415 nm and 740 nm. For shorter and longer wavelengths it showed minimal variation with a coefficient of variation (CV) not higher than 4% for all wavelengths. This allows us to assume that the results in studied range were not influenced by limited diameter of the tank. Together with increasing concentration of chlorophyll *a* the values of attenuation coefficient were increasing as well. However, the spectra of K_d for the layer between 0^- and 15 cm gave slightly lower values than for the layer between 0^- and 50 cm, or between 15 cm and 50 cm, what can be assigned to phytoplankton cells settling down during the radiometric measurements though carefully mixing. For all analysed phytoplankton species the highest coefficient of variation of K_d values measured in three layers was found for wavelengths around 550 nm and it was about 15%. Except *Cyclotella marinoi* which showed slightly higher values of CV, close to 20%, probably due to larger cell size comparing to other studied species. In further analysis K_d between 0^- and 50 cm was showed.

All analysed species contained chl-*a* and carotenoids but in different proportions (Table 4). The highest content of TCar was observed in *Synechococcus* sp. and *C. meneghiniana*, the lowest for *N. spumigena*. Attenuation coefficient at 490 nm ($K_d(490)$) showed good agreement ($R^2 = 0.82$) with chl-*a* concentration regardless phytoplankton species (Fig. 3). Therefore $K_d(490)$ or $K_d(\lambda)$ at any other wavelength could not be a good candidate here for distinction between phytoplankton species. The transparency of water characterised by K_d(PAR) ranged from 1.1 to 7 m^{-1} (Table 4). Inverse of K_d(PAR) suggests that even for our lowest chl-*a* concentration the bottom effect can be omitted.

R_{rs} spectra measured for all species showed characteristic shape with decrease of reflectance in the blue and red regions. Different pigment composition for diatoms and cyanobacteria (Table 1) results in different location of local

Table 4 The range of measured parameters: concentration of chlorophyll *a* (chl-*a*) and carotenoids (TCar), ratio between concentration of carotenoids and chlorophyll *a* (chl-*a*:TCar), and attenuation coefficient within PAR (K_d(PAR)).

Species	Chl-*a* [mg m^{-3}]	TCar [mg m^{-3}]	Chl-*a*:TCar	K_d(PAR) [m^{-1}]
Nodularia spumigena	3–23	0.2–2	~10	1.6–2.7
Dolichospermum sp.	20–80	3–12	~7	1.7–5
Synechococcus sp.	25–60	10–26	~2.5	1.1–7
Cyclotella meneghiniana	9–23	4–10	~2.5	1.6–2.9
Skeletonema sp.	15–50	~4	~4.5–12	1.8–3.2

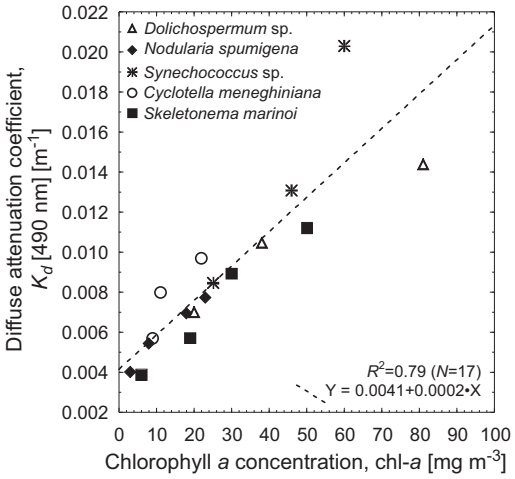

Figure 3 Relationship between chlorophyll *a* concentration and attenuation coefficient at 490 nm based on laboratory measurements.

maxima and minima in the reflectance spectrum (Fig. 4). Maximum of R_{rs} measured for cyanobacteria was located around 530–550 nm, whereas for diatoms could be seen around 570 nm what has been observed in previous studies (Metsamaa et al., 2006). $K_d(\lambda)$ spectra showed wider minimum for diatoms than for cyanobacteria (Fig. 4). Both groups contain pigments strongly absorbing in the range of 400–520 nm, as chl-*a* and carotenoids, which explains decrease of R_{rs} in this region. Additionally diatoms contain fucoxanthin with very wide absorption band from 450 to 540 nm (Wright and Jeffrey, 1987) and the maximum absorption between 450 and 470 nm. It resulted in a wider pigment absorption band for diatoms and R_{rs} maximum shifted towards longer wavelengths in comparison to cyanobacteria species. Among cyanobacteria, only R_{rs} spectrum of *Synechococcus* had a narrower peak around 530–550 nm. It also needs to be noted that it is a common feature that the position of phytoplankton pigment absorption minima and maxima in vivo are slightly shifted towards longer wavelengths relative to their position in solvents (Rabinowitch and Govindjee, 1969). This shift is not the same for different species. Therefore the location of R_{rs} minima and maxima for the analysed species was not the same, although most often being caused by the presence of the same pigments. Similarly to Gitelson et al. (1999) we observed a slight shift in the position of peaks with increasing phytoplankton concentration (Figs. 5 and 6).

In all analysed cyanobacteria a local minimum of R_{rs} at about 620 nm caused by absorption maximum of phycocyanin (PC) could be observed (Fig. 5). It was the most distinct for *Synechococcus* sp. Most probably *Synechococcus* sp. had very high PC to chl-*a* ratio among the analysed cyanobacteria species (Wojtasiewicz and Stoń-Egiert, 2016). This local minimum of R_{rs} was followed by local maximum, near 650 nm, very clearly seen by the peak in the 4th derivative spectrum (Fig. 5). It appeared mainly because it is located between two strong absorption bands (PC at 620 nm and chl-*a* at 670 nm). However, it could also be affected by PC fluorescence at 650 nm (e.g. Sobiechowska-Sasim et al., 2014). Such distinct peak was not observed in the diatom species we analysed. However, a small increase in this region could be seen, especially for the highest concentration of *S. marinoi* (Fig. 6). Most likely the occurrence of this peak was caused by the presence of chlorophyll $c_1 + c_2$ characterised by similar location of the second absorption peak to that of phycocyanin (Table 1). Similar differences in the spectral shape of R_{rs} were observed in the modelled results obtained by Metsamaa et al. (2006). In all analysed species a clear local minimum of R_{rs} accompanied by an increase in $K_d(\lambda)$ could be seen at 670 nm, which results from the presence of chl-*a* (Fig. 4). This minimum was followed by a maximum at about 700 nm which has been observed for both phytoplankton monocultures (e.g. Gitelson et al., 1999; Warner and Fan, 2013) and natural samples (e.g. Shang et al., 2014; Warner and Fan, 2013). This feature resulted from an interaction between light scattering by suspended particles and light absorption by water and chlorophyll *a* and its position was strongly correlated with chlorophyll *a* concentration moving towards longer wavelengths with increasing chl-*a* (e.g. Gitelson, 1992; Gitelson et al., 1999). Then the magnitude of R_{rs} decreased rapidly accompanied by an increase in $K_d(\lambda)$ which was caused by strong increase in pure water absorption in this part of the spectrum (Smith and Baker, 1981). In all our experiments we also observed a peak around 810 nm (data not shown). This feature was previously used to retrieve water constituents from remotely sensed data in turbid waters (Kutser et al., 2016), but in this study we mainly focused on the visible spectral range.

In the blue–green part of spectra the magnitude of R_{rs} decreased with increasing concentration of pigments (chl-*a* and TCar) in the case of the diatom *S. marinoi* (Fig. 6) and

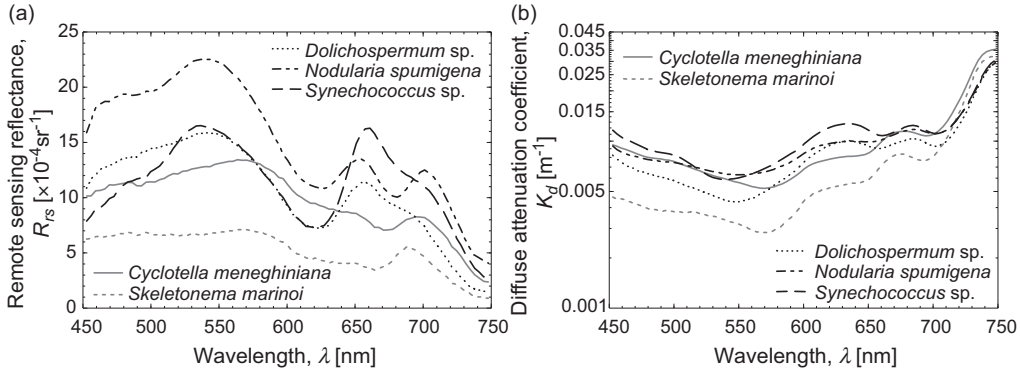

Figure 4 R_{rs} (*a*) and $K_d(\lambda)$ (*b*) spectra for studied phytoplankton species, chl-*a* for each was ~20 mg m^{-3}.

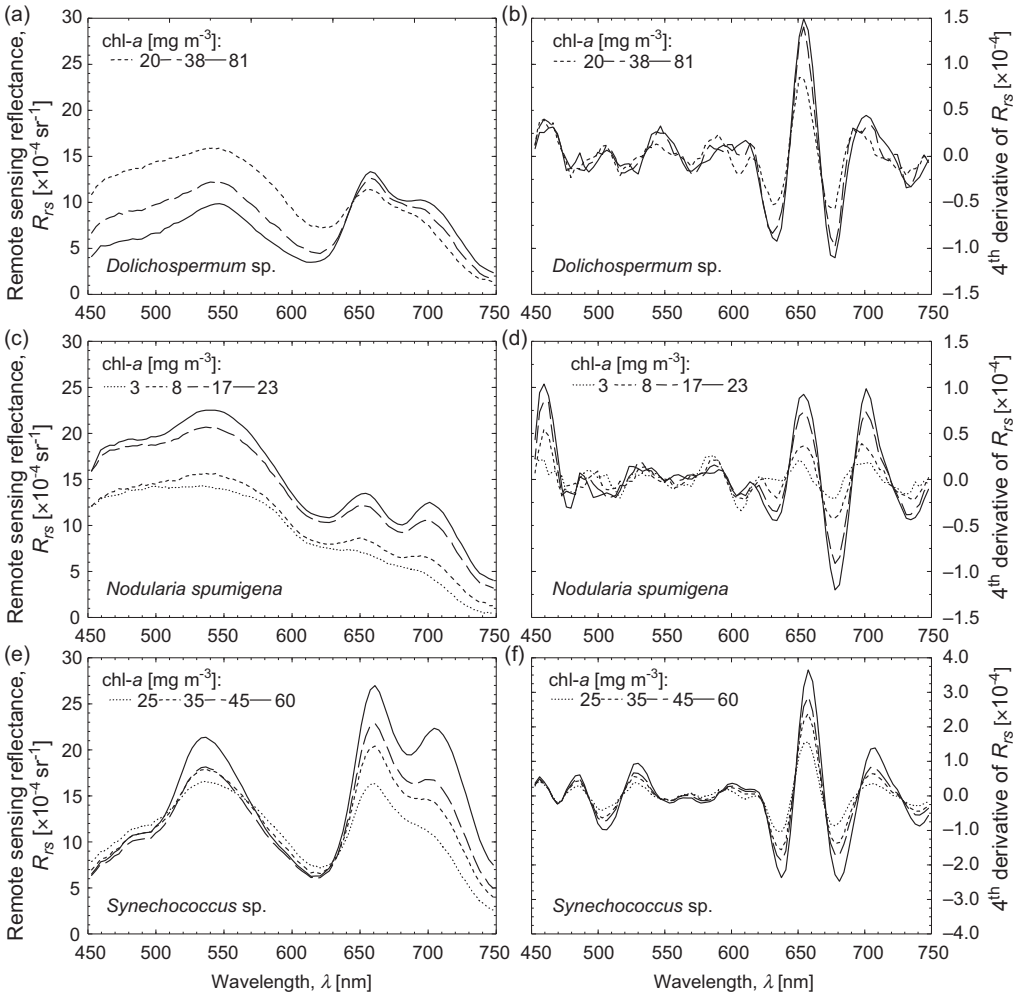

Figure 5 R_{rs} spectra and its 4th derivative for *Dolichospermum* sp. (a, b), *Nodularia spumigena* (c, d), and *Synechococcus* sp. (e, f), respectively.

cyanobacteria *Dolichospermum* sp. (Fig. 5), which suggests that absorption by pigments is a dominant process influencing shape of R_{rs} spectra. On the other hand, for the remaining species the scattering by particles played the dominant role in shaping the R_{rs} spectra causing the increase of the R_{rs} within this region with increasing chl-*a* concentration (Figs. 5 and 6). It needs to be noted that the increase in the phytoplankton concentration leads to increase of the impact of nonlinear effects on R_{rs}. Contribution of multiple scattering to radiance reflectance can be as high as 94% in turbid waters (Chami et al., 2006) what explains the changes in the spectral shape of R_{rs} observed with the increasing chl-*a* concentration (Figs. 5 and 6).

Besides the differences between the two phytoplankton groups, the R_{rs} spectra showed some differences between species belonging to the same group (Figs. 5 and 6). Among the diatoms the 700 nm peak in the R_{rs} is much more pronounced for *S. marinoi* compared to *C. meneghiniana* (Fig. 6). This was caused by differences in the scattering of light by these organisms resulting mainly from differences in their size and structure (Table 3). In the case of *S. marinoi* the shape of the R_{rs} spectrum changed distinctly with increasing chl-*a* concentration. It is probable that the number of cells was too small to have a sufficient impact on the R_{rs} spectrum. The differences observed among cyanobacteria strains (Fig. 5) resulted from the differences in their light scattering properties. For example, *N. spumigena* is characterised by almost wavelength independent scattering spectrum with low values of the chlorophyll-specific scattering coefficient (Metsamaa et al., 2006; Wojtasiewicz and Stoń-Egiert, 2016; Wojtasiewicz and Stramski, 2010). On the other hand, *Synechococcus* sp. cells are small therefore the scattering spectrum for this species is very steep and the scattering coefficient values are high (Wojtasiewicz and Stoń-Egiert, 2016). This can be the reason for a different shape of R_{rs} spectrum of *Synechococcus* sp. compared to the remaining ones.

Characteristic features of R_{rs} spectra for each species were the most evident for samples with the highest biomass of phytoplankton (chl-*a* as an indicator), what can clearly be seen by its 4th derivative changes (Figs. 5 and 6). These features were kept very well, with the SI $>$ 0.95, over concentrations of chl-*a* higher than 50% of maximum (Fig. 7). Higher dilution resulted in less distinct peaks, however SI for all analysed concentrations was higher than 0.6. The spectra which maintain their major features within wide range of chl-*a* concentration are suitable for developing model spectra for particular species. It is worth to note that characteristic shape of R_{rs} spectra for *N. spumigena* could be seen even if the

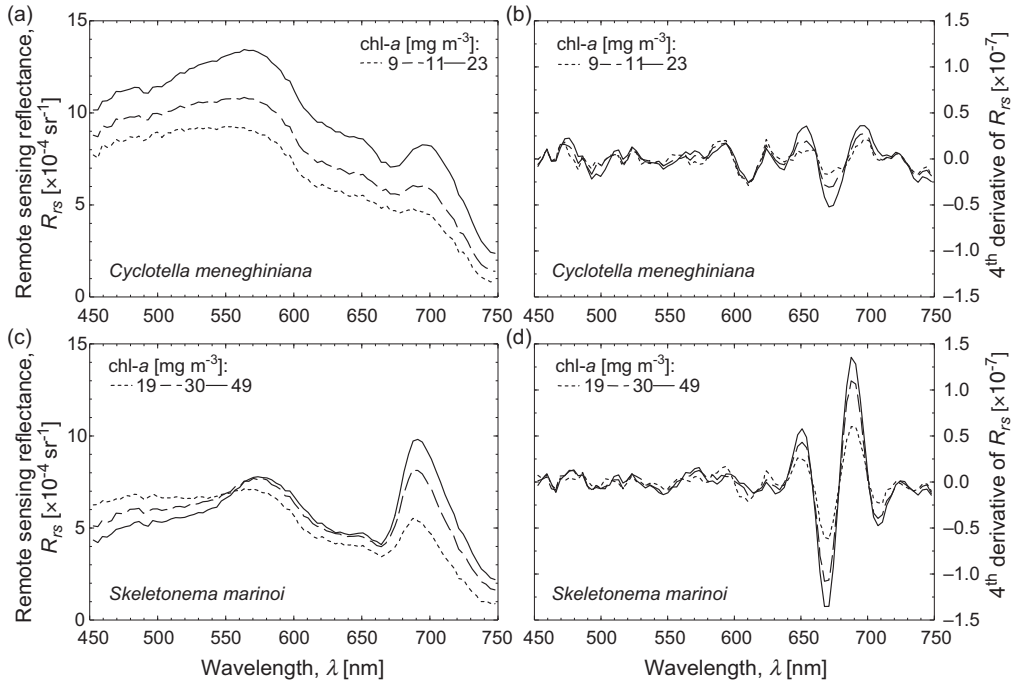

Figure 6 R_{rs} spectra and its 4th derivative for *Cyclotella meneghiniana* (a, b) and *Skeletonema marinoi* (c, d), respectively.

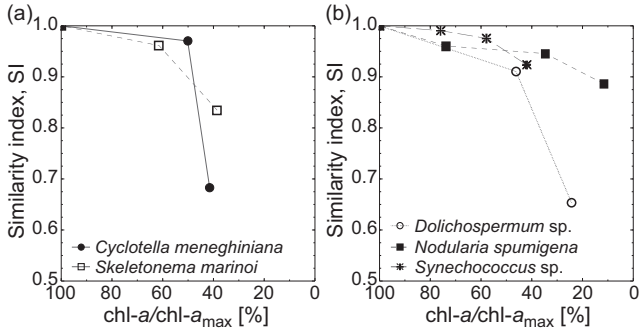

Figure 7 Similarity index between the R_{rs} spectra of phytoplankton species with increasing chl-*a* concentration.

concentration of chlorophyll *a* was relatively low, here it was only 13% of the reference concentration. It is due to the fact, that dilution of phytoplankton cells for this species results in changes of R_{rs} spectra magnitude rather than its shape (Fig. 5), despite slight shifts in the main peak positions. Similarly high dilution of cyanobacteria *Dolichospermum* or diatoms *S. marinoi* showed lower similarity to their references, with SI of about 0.65 (Fig. 7). This is a consequence of changes in relative height of peaks in blue-green and red portions of the R_{rs} spectra characteristic for these species (Figs. 5 and 6).

Characteristic features of R_{rs} spectra for different phytoplankton species described above are located at different bands over the whole analysed spectral range. Therefore to evaluate which phytoplankton species have the most unique optical signature, HCA between 450 nm and 750 nm was used. Fig. 8 illustrates the results from cluster analysis (HCA) applied to R_{rs} spectra presented in the left panels of Figs. 5 and 6. The spectra of picoplankton species, *Synechococcus* sp., for all concentration belonged to one cluster (Fig. 8), suggesting that those species have a distinct optical signature. The shape of R_{rs} spectra differed significantly from the other species. Two main peaks (close to 540 nm and 660 nm) were stable and similarly high for all studied concentrations. The second peak was shifted towards longer wavelengths compared to the other species, which had it around 650 nm. The second cluster (Fig. 8) included all *N. spumigena* spectra. However, it also contained one *Dolichospermum* sp. spectrum (lowest measured concentration) and one *C. meneghiniana* spectrum (highest measured concentration). Those spectra were characterised by three main peaks, where the second and the third peaks were significantly lower than the first one. Spectra of higher concentration of *Dolichospermum* sp. were characterised by higher second peak than the first one, and spectra of lower concentration of *C. meneghiniana* were flatter without distinct peaks. For those reasons they were not included in that group. The third cluster (Fig. 8) contained spectra of two diatom species, *C. meneghiniana* and *S. marinoi* and one cyanobacteria species, *Dolichospermum* sp. It is difficult to find any common features in the shape of their spectra except they are generally characterised by the lowest values of reflectance. However, if we considered clusters with similarity above 85% (the linkage distance decrease) the third cluster would be splitted into three separate groups, one for each species.

Summarising above, results of the HCA analysis based on R_{rs} showed that spectral signatures of *Synechococcus* sp., *N. spumigena* and *S. marinoi* were unique enough to separate each of them into different clusters regardless concentration. *Dolichospermum* sp. and *C. meneghiniana* showed similarity to *N. spumigena* or *S. marinoi*, depending on concentration (Fig. 8). Results of similar HCA analysis based on the 4th derivative of R_{rs} spectra gave worst results of

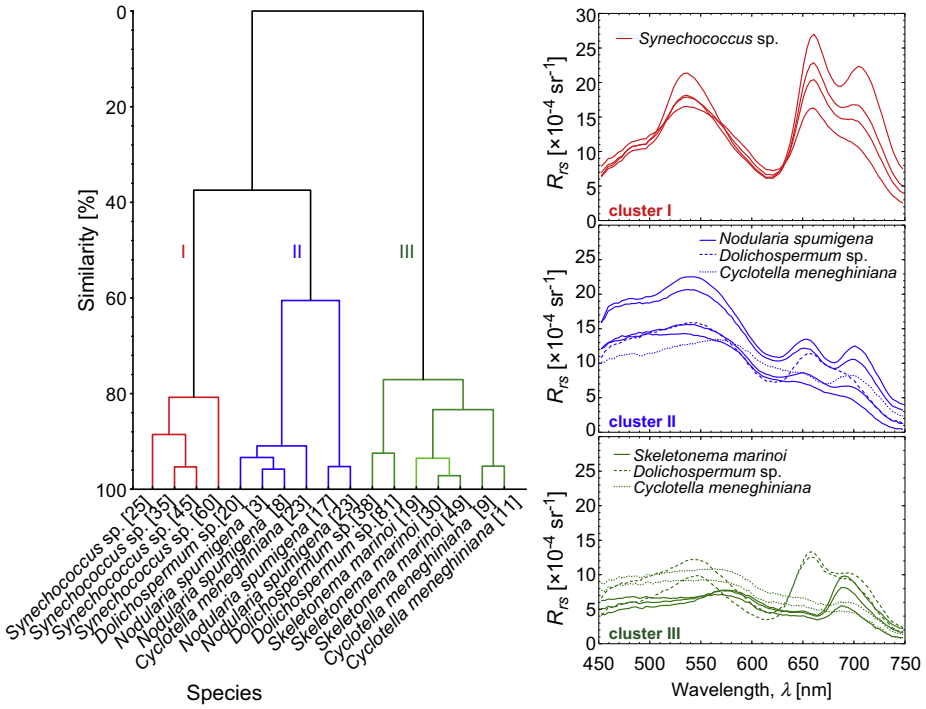

Figure 8 Cluster tree of all analysed phytoplankton species at different concentrations (chlorophyll *a* concentration in [mg m^{-3}] is given in parenthesis) generated by using $R_{rs}(\lambda)$ spectra in the range of 450—750 nm (left) and $R_{rs}(\lambda)$ spectra belonging to each cluster (right).

species separation. Although clusters in this case were characterised by higher inner similarity (three main clusters at level of 70% of similarity), spectra derived for the same species but with different chl-*a* concentration were placed in different clusters (*Synechococcus*, *Dolichospermum* sp. and *N. spumigena*) or if not, they belonged to one big cluster consisting spectra of different species (all *S. marinoi* and all *C. meneghiniana* together with some spectra of *N. spumigena* and *Dolichospermum* sp.). This fact showed that not only shape of R_{rs} spectrum (emphasised by the 4th derivative) but also its magnitude is an important feature. The clusters did not change if blue part of the spectrum (up to 525 nm) was excluded from the HCA analysis (525—750 nm analysed). In the blue part of a spectrum, R_{rs} is expected to be strongly modified in Baltic Sea waters, rich in dissolved organic matter.

4. Conclusions

The results from the unique experiments designed to study specific apparent optical properties of selected phytoplankton species of the Baltic Sea are shown in our paper. Presented reflectance spectra can be used in calibration and validation of radiative transfer models for water dominated by specific phytoplankton species. They can be successfully applied to modelling of the volume scattering function for phytoplankton assemblages (Woźniak, 2014). Moreover, the spectral shape characteristic for each species can be used as a reference spectrum for comparison with in situ measured reflectance spectra by means of similarity index (cosine similarity) or root-mean-square deviation. This can help to assess the water quality and distinguish the dominant phytoplankton type. There is a need for those data in development, calibration and validation of Earth Observation algorithms (Sathyendranath et al., 2016). We analysed the R_{rs} spectra of 5 phytoplankton species commonly occurring in the Baltic Sea. As expected, the pigment composition as well as size structure were responsible for differences in spectral shape of R_{rs} spectra. Beside the differences between the two phytoplankton groups, the R_{rs} spectra showed some differences between species belonging to one group. Their characteristic features, e.g. location of peaks and their relative heights, for each species were kept over wide range of phytoplankton concentrations with the similarity index (SI) higher than 0.6. The picoplankton species *Synechococcus* sp. showed the most distinct optical signature, which allowed to distinguish a separate cluster in HCA analysis. Presented study enlarges the database of existing specific optical properties of phytoplankton species in the Baltic Sea and shows the first step towards knowing the variability of R_{rs} within phytoplankton species. In further studies different phytoplankton growth phases and different conditions (light, temperature, nutrients, etc.) need to be accounted for.

Acknowledgements

The authors would like to thank colleagues from Division of Marine Biotechnology, and Division of Marine Ecosystems Functioning, both at the University of Gdańsk, for growing phytoplankton monocultures needed for experiments.

The work was supported as part of the Institute of Oceanography University of Gdańsk statutory research (DS/530-G210-D425) and the SatBaltyk project funded by the European Union through European Regional Development Fund (contract No. POIG.01.01.02-22-011/09 entitled 'The Satellite Monitoring of the Baltic Sea Environment'). M.S.-W. and B.W. were funded by CSIRO OCE Postdoctoral Fellowship Programme.

References

Aguirre-Gómez, R., Weeks, A.R., Boxall, S.R., 2001. The identification of phytoplankton pigments from absorption spectra. Int. J. Remote Sens. 22 (2–3), 315–338, http://dx.doi.org/10.1080/014311601449952.

Albertano, P., Somma, D.D., Capucci, E., 1997. Cyanobacterial picoplankton from the Central Baltic Sea: cell size classification by image-analyzed fluorescence microscopy. J. Plankton Res. 19 (10), 1405–1416, http://dx.doi.org/10.1093/plankt/19.10.1405.

Chami, M., McKee, D., Leymarie, E., Khomenko, G., 2006. Influence of the angular shape of the volume-scattering function and multiple scattering on remote sensing reflectance. Appl. Opt. 45 (36), 9210–9220, http://dx.doi.org/10.1364/AO.45.009210.

Craig, S.E., Lohrenz, S.E., Lee, Z., Mahoney, K.L., Kirkpatrick, G.J., Schofield, O.M., 2006. Use of hyperspectral remote sensing reflectance for detection and assessment of the harmful alga, *Karenia brevis*. Appl. Opt. 45 (21), 5414–5425, http://dx.doi.org/10.1364/AO.45.005414.

Darecki, M., Stramski, D., 2004. An evaluation of MODIS and SeaWiFS bio-optical algorithms in the Baltic Sea. Remote Sens. Environ. 89 (3), 326–350, http://dx.doi.org/10.1016/j.rse.2003.10.012.

Darecki, M., Ficek, D., Krężel, A., Ostrowska, M., Majchrowski, R., Woźniak, S.B., Bradtke, K., Dera, J., Woźniak, B., 2008. Algorithms for the remote sensing of the Baltic ecosystem (DESAMBEM). Part 2: Empirical validation. Oceanologia 50 (4), 509–538.

Evers-King, H., Bernard, S., Robertson-Lain, L., Probyn, T.A., 2014. Sensitivity in reflectance attributed to phytoplankton cell size: forward and inverse modelling approaches. Opt. Express 22 (10), 11536–11551, http://dx.doi.org/10.1364/OE.22.011536.

Feistel, R., Weinreben, S., Wolf, H., Seitz, S., Spitzer, P., Adel, B., Nausch, G., Schneider, B., Wright, D.G., 2010. Density and absolute salinity of the Baltic Sea 2006–2009. Ocean Sci. 6 (1), 3–24, http://dx.doi.org/10.5194/os-6-3-2010.

Gitelson, A., 1992. The peak near 700 nm on radiance spectra of algae and water: relationships of its magnitude and position with chlorophyll concentration. Int. J. Remote Sens. 13 (17), 3367–3373, http://dx.doi.org/10.1080/01431169208904125.

Gitelson, A.A., Schalles, J.F., Rundquist, D.C., Schiebe, F.R., Yacobi, Y.Z., 1999. Comparative reflectance properties of algal cultures with manipulated densities. J. Appl. Phycol. 11 (4), 345–354, http://dx.doi.org/10.1023/A:1008143902418.

Godhe, A., McQuoid, M.R., Karunasagar, I., Karunasagar, I., Rehnstam-Holm, A.-S., 2006. Comparison of three common molecular tools for distinguishing among geographically separated clones of the diatom *Skeletonema marinoi* Sarno et Zingone (Bacillariophyceae). J. Phycol. 42 (2), 280–291, http://dx.doi.org/10.1111/j.1529-8817.2006.00197.x.

Gordon, H.R., Brown, O.B., Jacobs, M.M., 1975. Computed relationships between the inherent and apparent optical properties of a flat, homogeneous ocean. Appl. Opt. 14 (2), 417–427, http://dx.doi.org/10.1364/AO.14.000417.

Hommersom, A., Kratzer, S., Laanen, M., Ansko, I., Ligi, M., Bresciani, M., Giardino, C., Beltrán-Abaunza, J.M., Moore, G., Wernand, M., Peters, S., 2012. Intercomparison in the field between the new WISP-3 and other radiometers (TriOS Ramses, ASD FieldSpec, and TACCS). J. Appl. Remote Sens. 6 (1), 063615, http://dx.doi.org/10.1117/1.JRS.6.063615 21pp.

Hunter, P.D., Tyler, A.N., Présing, M., Kovács, A.W., Preston, T., 2008. Spectral discrimination of phytoplankton colour groups: the effect of suspended particulate matter and sensor spectral resolution. Remote Sens. Environ. 112 (4), 1527–1544, http://dx.doi.org/10.1016/j.rse.2007.08.003.

IOCCG, 2014. Phytoplankton functional types from space. In: Sathyendranath, S. (Ed.), Reports of the International Ocean-Colour Coordinating Group, No. 15. IOCCG, Dartmouth, Canada, Phytoplankton functional types from Space, 156 pp.

Jain, A.K., Murty, M.N., Flynn, P.J., 1999. Data clustering: a review. ACM Comput. Surv. 31 (3), 264–323, http://dx.doi.org/10.1145/331499.331504.

Jeffrey, S.W., Humphrey, G.F., 1975. New spectrophotometric equations for determining chlorophylls *a*, *b*, *c1*, and *c2* in higher plants, algae and natural phytoplankton. Biochem. Physiol. Pflanz. 167, 191–194, http://dx.doi.org/10.1016/S0015-3796(17)30778-3.

Kahru, M., 1997. Using satellites to monitor large-scale environmental change: a case study of cyanobacteria blooms in the Baltic Sea. In: Kahru, M., Brown, C.W. (Eds.), Monitoring Algal Blooms: New Techniques for Detecting Large-scale Environmental Change. Springer, Berlin/New York, 43–61.

Kanoshina, I., Lips, U., Leppänen, J.-M., 2003. The influence of weather conditions (temperature and wind) on cyanobacterial bloom development in the Gulf of Finland (Baltic Sea). Harmful Algae 2 (1), 29–41, http://dx.doi.org/10.1016/S1568-9883(02)00085-9.

Karlsson, K.M., Kankaanpää, H., Huttunen, M., Meriluoto, J., 2005. First observation of microcystin-LR in pelagic cyanobacterial blooms in the northern Baltic Sea. Harmful Algae 4 (1), 163–166, http://dx.doi.org/10.1016/j.hal.2004.02.002.

Kim, Y., Yoo, S., Son, Y.B., 2016. Optical discrimination of harmful *Cochlodinium polykrikoides* blooms in Korean coastal waters. Opt. Express 24 (22), A1471, http://dx.doi.org/10.1364/OE.24.0A1471, 18 pp.

Klais, R., Tamminen, T., Kremp, A., Spilling, K., An, B.W., Hajdu, S., Olli, K., 2013. Spring phytoplankton communities shaped by interannual weather variability and dispersal limitation: mechanisms of climate change effects on key coastal primary producers. Limnol. Oceanogr. 58 (2), 753–762, http://dx.doi.org/10.4319/lo.2013.58.2.0753.

Kratzer, S., Brockmann, C., Moore, G., 2008. Using MERIS full resolution data to monitor coastal waters – a case study from Himmerfjärden, a fjord-like bay in the north-western Baltic Sea. Remote Sens. Environ. 112 (5), 2284–2300, http://dx.doi.org/10.1016/j.rse.2007.10.006.

Kutser, T., Metsamaa, L., Strömbeck, N., Vahtmäe, E., 2006. Monitoring cyanobacterial blooms by satellite remote sensing. Estuar. Coast. Shelf Sci. 67 (1–2), 303–312, http://dx.doi.org/10.1016/j.ecss.2005.11.024.

Kutser, T., Paavel, B., Verpoorter, C., Ligi, M., Soomets, T., Toming, K., Casal, G., 2016. Remote sensing of black lakes and using 810 nm reflectance peak for retrieving water quality parameters of optically complex waters. Remote Sens. 8 (6), 497, http://dx.doi.org/10.3390/rs8060497, 15 pp.

Lewandowska, J., Kosakowska, A., 2004. Effect of iron limitation on cells of the diatom *Cyclotella meneghiniana* Kutzing. Oceanologia 46 (2), 269–287.

Lubac, B., Loisel, H., Guiselin, N., Astoreca, R., Artigas, L.F., Mériaux, X., 2008. Hyperspectral and multispectral ocean color inversions to detect *Phaeocystis globosa* blooms in coastal waters. J. Geophys. Res. 113 (C6), http://dx.doi.org/10.1029/2007JC004451, 17 pp.

Mazur, H., Pliński, M., 2003. *Nodularia spumigena* blooms and the occurrence of hepatotoxin the Gulf of Gdańsk. Oceanologia 45 (1), 305–316.

Mazur-Marzec, H., Krężel, A., Kobos, J., Pliński, M., 2006. Toxic *Nodularia spumigena* blooms in the coastal waters of the Gulf of Gdańsk: a ten-year survey. Oceanologia 48 (2), 255–273.

Metsamaa, L., Kutser, T., Strömbeck, N., 2006. Recognising cyanobacterial blooms based on their optical signature: a modelling study. Boreal Environ. Res. 11, 493–506, 14 pp.

Millie, D.F., Schofield, O.M., Kirkpatrick, G.J., Johnsen, G., Tester, P.A., Vinyard, B.T., 1997. Detection of harmful algal blooms using photopigments and absorption signatures: a case study of the FLorida red tide dinoglagellate, *Gymnodinium breve*. Limnol. Oceanogr. 42 (5), 1240–1251, http://dx.doi.org/10.4319/lo.1997.42.5_part_2.1240.

Millie, D.F., Schofield, O.M.E., Kirkpatrick, G.J., Johnsen, G., Evens, T.J., 2002. Using absorbance and fluorescence spectra to

discriminate microalgae. Eur. J. Phycol. 37 (3), 313–322, http://dx.doi.org/10.1017/S0967026202003700.

Nowacki, J., Jarosz, E., 1998. The hydrological and hydrochemical division of the surface waters in the Gulf of Gdańsk. Oceanologia 40 (3), 261–272.

Olenina, I., Hajdu, S., Edler, L., Andersson, A., Wasmund, N., Busch, S., Göbel, J., Gromisz, S., Huseby, S., Huttunen, M., Jaanus, A., Kokkonen, P., Ledaine, I., Niemkiewicz, E., 2006. Biovolumes and size-classes of phytoplankton in the Baltic Sea (Proceedings No. 106). In: HELCOM Baltic Sea Environment Proceedings. HELCOM, Helsinki, 144 pp.

Oyama, Y., Matsushita, B., Fukushima, T., Chen, J., Nagai, T., Imai, A., 2010. Testing the spectral decomposition algorithm (SDA) for different phytoplankton species by a simulation based on tank experiments. Int. J. Remote Sens. 31 (6), 1605–1623, http://dx.doi.org/10.1080/01431160903475365.

Pankow, H., Kell, V., Wasmund, N., Zander, B., 1990. Ostsee-Algenflora. G. Fischer Verl, Jena, 85 pp.

Parsons, T.R., Maita, Y., Lalli, C.M., 1984. A Manual of Chemical and Biological Methods for Seawater Analysis. Pergamon Press, Oxford, 173 pp.

Pliński, M., Mazur-Marzec, H., Jóźwiak, T., Kobos, J., 2007. The potential causes of cyanobacterial blooms in Baltic Sea estuaries. Oceanol. Stud. 36 (1), 125–137, http://dx.doi.org/10.2478/v10009-007-0001-x.

Rabinowitch, E., Govindjee, 1969. Photosynthesis. John Wiley and Sons, Inc., New York/London/Sydney/Toronto, 273 pp.

Roy, S., Llewellyn, C.A., Skarstad-Egeland, E., Johnsen, G., 1989. Phytoplankton Pigments Characterization, Chemotaxonomy and Applications in Oceanography (Cambridge Environmental Chemistry Series). Cambridge Univ. Press, Cambridge, New York, 845 pp.

Sathyendranath, S., Bracher, A., Brockmann, C., Platt, T., Ramon, D., Regner, P., 2016. Colour and Light in the Ocean (CLEO) 2016: A Scientific Roadmap from the CLEO Workshop Organised by ESA and PML. Frascati, Italy, 77 pp.

Seppälä, J., Ylöstalo, P., Kaitala, S., Hällfors, S., Raateoja, M., Maunula, P., 2007. Ship-of-opportunity based phycocyanin fluorescence monitoring of the filamentous cyanobacteria bloom dynamics in the Baltic Sea. Estuar. Coast. Shelf Sci. 73 (3–4), 489–500, http://dx.doi.org/10.1016/j.ecss.2007.02.015.

Shang, S., Wu, J., Huang, B., Lin, G., Lee, Z., Liu, J., Shang, S., 2014. A new approach to discriminate dinoflagellate from diatom blooms from space in the East China Sea. J. Geophys. Res. Oceans 119 (7), 4653–4668, http://dx.doi.org/10.1002/2014JC009876.

Simis, S.G.H., Peters, S.W.M., Gons, H.J., 2005. Remote sensing of the cyanobacterial pigment phycocyanin in turbid inland water. Limnol. Oceanogr. 50 (1), 237–245, http://dx.doi.org/10.4319/lo.2005.50.1.0237.

Smith, R.C., Baker, K.S., 1981. Optical properties of the clearest natural waters (200–800 nm). Appl. Opt. 20 (2), 177–184, http://dx.doi.org/10.4319/lo.2007.52.1.0217.

Sobiechowska-Sasim, M., Stoń-Egiert, J., Kosakowska, A., 2014. Quantitative analysis of extracted phycobilin pigments in cyanobacteria – an assessment of spectrophotometric and spectrofulorometric methods. J. Appl. Phycol. 26 (5), 2065–2074, http://dx.doi.org/10.1007/s10811-014-0244-3.

Soja-Woźniak, M., Craig, S., Kratzer, S., Wojtasiewicz, B., Darecki, M., Jones, C., 2017. A novel statistical approach for ocean colour estimation of inherent optical properties and cyanobacteria abundance in optically complex waters. Remote Sens. 9 (4), 343, http://dx.doi.org/10.3390/rs9040343, 22 pp.

Suikkanen, S., Laamanen, M., Huttunen, M., 2007. Long-term changes in summer phytoplankton communities of the open northern Baltic Sea. Estuar. Coast. Shelf Sci. 71 (3–4), 580–592, http://dx.doi.org/10.1016/j.ecss.2006.09.004.

Torrecilla, E., Stramski, D., Reynolds, R.A., Millán-Núñez, E., Cannizzaro, J., 2011. Cluster analysis of hyperspectral optical data for discriminating phytoplankton pigment assemblages in the open ocean. Remote Sens. Environ. 115 (10), 2578–2593, http://dx.doi.org/10.1016/j.rse.2011.05.014.

Townend, J., 2002. Practical Statistics for Environmental and Biological Scientists. Wiley, Chichester/New York, 276 pp.

Vaillancourt, R.D., Brown, C.W., Guillard, R.R.L., Balch, W.M., 2004. Light backscattering properties of marine phytoplankton: relationships to cell size, chemical composition and taxonomy. J. Plankton Res. 26 (2), 191–212, http://dx.doi.org/10.1093/plankt/fbh012.

Volten, H., de Haan, J.F., Hovenier, J.W., Schreurs, R., Vassen, W., Dekker, A.G., Hoogenboom, H.J., Charlton, F., Wouts, R., 1998. Laboratory measurements of angular distributions of light scattered by phytoplankton and silt. Limnol. Oceanogr. 43 (6), 1180–11970, http://dx.doi.org/10.4319/lo.1998.43.6.1180.

Walsby, A.E., Hayes, P.K., Boje, R., 1995. The gas vesicles, buoyancy and vertical distribution of cyanobacteria in the Baltic Sea. Eur. J. Phycol. 30 (2), 87–94, http://dx.doi.org/10.1080/09670269500650851.

Warner, R.A., Fan, C., 2013. Optical spectra of phytoplankton cultures for remote sensing applications: focus on harmful algal blooms. Int. J. Environ. Sci. Dev. 4 (2), 94–98, http://dx.doi.org/10.7763/IJESD.2013.V4.312.

Whitmire, A.L., Pegau, W.S., Karp-Boss, L., Boss, E., Cowles, T.J., 2010. Spectral backscattering properties of marine phytoplankton cultures. Opt. Express 18 (14), 15073–15093, http://dx.doi.org/10.1364/OE.18.015073.

Wojtasiewicz, B., Stoń-Egiert, J., 2016. Bio-optical characterization of selected cyanobacteria strains present in marine and freshwater ecosystems. J. Appl. Phycol. 28 (4), 2299–2314, http://dx.doi.org/10.1007/s10811-015-0774-3.

Wojtasiewicz, B., Stramski, D., 2010. Chlorophyll-specific absorption and scattering coefficients of selected cyanobacteria. In: Proceedings of Ocean Optics XX.

Woźniak, M., 2014. Identification of the dominant phytoplankton groups in the algal blooms in the waters of the Baltic Sea using remote sensing methods. (PhD). Univ. Gdańsk, Gdynia, 153 pp. (in Polish).

Woźniak, B., Krężel, A., Darecki, M., Woźniak, S.B., Majchrowski, R., Ostrowska, M., Kozłowski, Ł., Ficek, D., Olszewski, J., Dera, J., 2008. Algorithms for the remote sensing of the Baltic ecosystem (DESAMBEM). Part 1: Mathematical apparatus. Oceanologia 50 (4), 451–508.

Woźniak, M., Bradtke, K.M., Darecki, M., Krężel, A., 2016. Empirical model for phycocyanin concentration estimation as an indicator of cyanobacterial bloom in the optically complex coastal waters of the Baltic Sea. Remote Sens. 8 (3), http://dx.doi.org/10.3390/rs8030212, 23 pp.

Wright, S.W., Jeffrey, S.W., 1987. Fucoxanthin pigment markers of marine phytoplankton analysed by HPLC and HPTLC. Mar. Ecol.-Prog. Ser. 38, 259–266.

Xi, H., Hieronymi, M., Röttgers, R., Krasemann, H., Qiu, Z., 2015. Hyperspectral differentiation of phytoplankton taxonomic groups: a comparison between using remote sensing reflectance and absorption spectra. Remote Sens. 7 (11), 14781–14805, http://dx.doi.org/10.3390/rs71114781.

Zibordi, G., Darecki, M., 2006. Immersion factor for the RAMSES series of hyperspectral underwater radiometers. J. Opt. Pure Appl. Opt. 8, 252–258.

Oceanologia (2018) 60, 97—100

Available online at www.sciencedirect.com

ScienceDirect

journal homepage: www.journals.elsevier.com/oceanologia/

SHORT COMMUNICATION

Live autochthonous benthic diatoms on the lower depths of Arctic continental shelf. Preliminary results

Elena Druzhkova *, **Anatoliy Oleinik, Pavel Makarevich**

Murmansk Marine Biological Institute, Kola Scientific Centre, Russian Academy of Sciences, Murmansk, Russia

Received 6 April 2017; accepted 4 July 2017
Available online 21 July 2017

KEYWORDS
Microphytobenthos;
Arctic continental shelf;
Diatoms

Summary An autochthonous community of benthic diatoms was discovered in June 2015 in the upper sediment layer at depths of 170, 205, and 245 m in the central Barents Sea. At least three benthic microalgae species (*Gyrosigma fasciola*, *Pleurosigma angulatum*, and *Pleurosigma* sp. 1) were detected in the sediment but not the upper water column. Analyses revealed that these benthic microalgae represent a depleted fragment of Arctic littoral microphytobenthos. Compared with the littoral flora, the deep-water assemblage is less diverse and displays low abundance. The data reported here challenge the generally accepted belief that the presence of certain microalgae at significant depths results from vertical or horizontal transfer.

Microphytobenthos, together with phytoplankton and ice algae, are important components of the primary production potential in Arctic marine ecosystems. The importance of benthic microalgae in the littoral and sublittoral coastal zones is well established (Cahoon and Laws, 1993). However, the entire current database of microphytobenthic production in Arctic waters comprises only 10 published studies, according to which the benthic production in Arctic coastal waters exceeds the pelagic production by a factor of ca. 1.5 (reviewed in Glud et al., 2009, see Fig. 1). An overview study conducted by Cahoon (1999) directly indicated that there is substantial underestimation of the benthic microalgal contribution to the productivity of marine ecosystems, especially for oligotrophic (including Arctic) waters. This underestimation results from the narrowness of the generally accepted approach to such investigations, which are often conducted at sites that presuppose the presence of the object under investigation. Consequently, an important unresolved issue is the depth distribution of benthic microalgae. According to the common point of view, sustainable existence of algal communities is governed by the availability

* Corresponding author at: Murmansk Marine Biological Institute, Kola Scientific Centre, Russian Academy of Sciences, 17 Str. Vladimirskaya, Murmansk 183010, Russia. Tel.: +7 8152 23 95 55; fax: +7 8152 25 39 94.
E-mail address: druzhkova.elena@yandex.ru (E. Druzhkova).
Peer review under the responsibility of Institute of Oceanology of the Polish Academy of Sciences.

Production and hosting by Elsevier

http://dx.doi.org/10.1016/j.oceano.2017.07.001

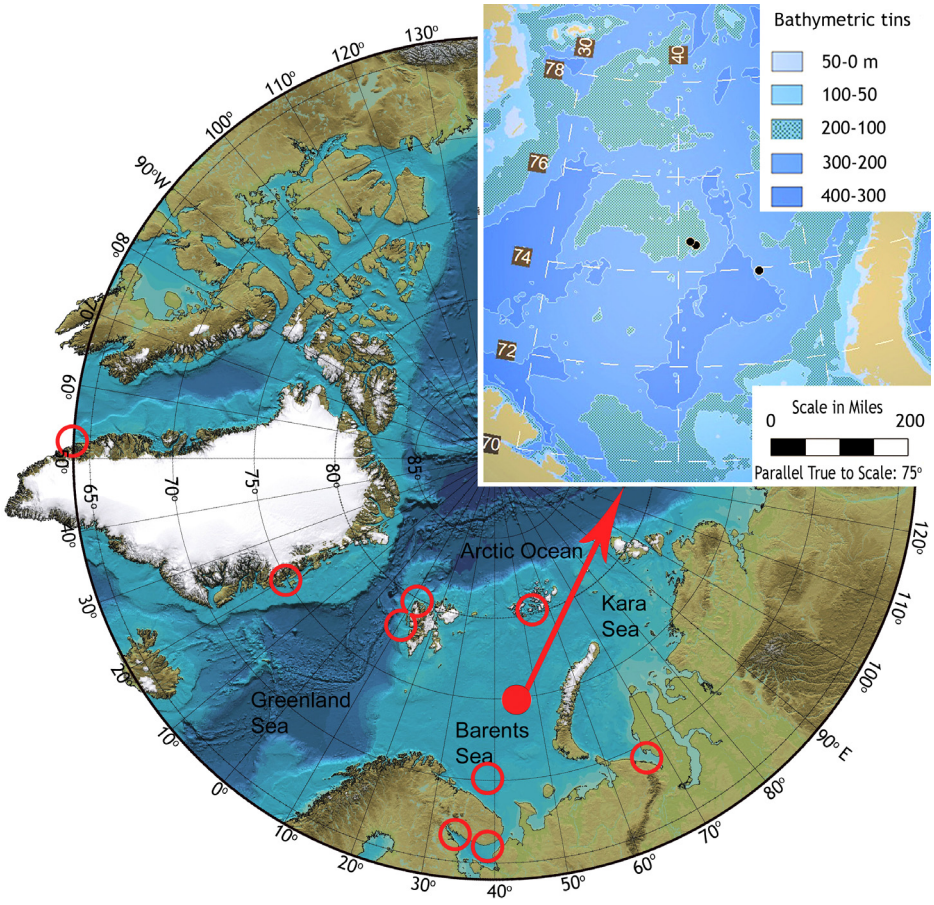

Figure 1 Locations of sampling stations in the Barents Sea, June 2015 (filled red dot). The figure of Arctic region is modified from Glud et al. (2009).

of photosynthetically active radiation and in aquatic habitats is limited by the compensation depth (i.e. the depth at which the energy of incoming light balances the metabolic costs), which constitutes the first tens of meters for continental shelf seas and 100—300 m for oceanic water areas (Raymont, 1980). The zone of the World Ocean below 200 m is considered to be free of floral organisms (Kiselev, 1969). However, there have been several studies indicating the presence of living microalgae at depths below 100 m (Cahoon, 1999), e.g. chlorophyll-*a* was reported from sediments of the continental shelf at depths down to 222 m (Cahoon et al., 1990; Cahoon and Cooke, 1992), and even to 2000 m (Cahoon et al., 1994), indicating that benthic microalgae may exist at significant depths. However, this hypothesis has not been verified, as previous investigations were conducted using indirect and/or calculation methods (Karsten et al., 2011). Although such data extend the lower distribution limits of live benthic microalgae, the lack of direct observations renders the conclusions questionable. We have found only one previous study in which indirect measurements of the biomass of deep-sea benthic microalgae using chlorophyll-*a* values were directly verified. In October 2003 in Onslow Bay, McGee et al. (2008) collected sediment samples at depths of 67—191 m and discovered 11 species of live benthic diatoms by direct microscopy. Moreover, that study indicated and substantiated an autochthonous origin for the species found.

The objective of this study was to investigate the surface sediments of the Barents Sea Continental Shelf to determine whether microphytobenthic assemblages are present at depth.

The study was conducted on the Central Plateau of the Barents Sea (Fig. 1) during a cruise by the Murmansk Marine Biological Institute on board the r/v *Dalnie Zelentsy* in June 2015. Samples were obtained at three stations (74.56°N, 41.41°E, depth 205 m; 74.64°N, 40.96°E, depth 174 m; 73.94°N, 46.15°E, depth 245 m) at a distance of 130—240 miles from the nearest shore.

The sediment consisted of red mud with some inequigranular sand. The depth of photic zone (45—75 m) was determined as 3 times the Secchi depth for case 2 water (Abakumov, 1983; Jerlov, 1968).

A Van Veen grab device was used to collect sediment from the surface layer in triplicate. Each subsample (ca. 30 ml volume and 1 cm depth) was obtained from a separate sediment sample. All three subsamples, taken from one station, were placed together into one sample cup (total volume ca. 100 ml) and preserved in 40% formaldehyde (final concentration of 2%). Water samples were gathered with a bathometer ("Hidro-bios", 5l) from the surface water layer, the pycnocline (30 m), the intermediate layer (100 and 120 m water depths), and the near-bottom layer, and by a small-meshed plankton net with a mesh size of 29 μm × 29 μm from the 150—50 m water layer.

For cell count analyses sediment subsamples of 1–1.5 ml were taken from the mixed total sediment sample, then placed in a test tube and diluted with certain volume of water (V_{H_2O}) up to the mark of 10 ml ($V_{\sum}$ = 10 ml). Exact volume of sediment subsample ($V_{sed} \pm 0.02$ ml) is a difference between $V_{\sum}$ and V_{H_2O}. After resuspension of a subsample solid particles settled within 5 min were removed. Diluted in such a way subsample of the volume $V'_{\sum}$ corresponds to the sediment of the volume V'_{sed} as

$$V'_{sed} = V_{sed} \times \left(\frac{V'_{\sum}}{V_{\sum}} \right).$$

Then cells were enumerated (n, cells ml^{-1}) in a Nageotte counting chamber using a generally accepted method and recalculated per volume of sediment (N, cells cm^{-3}):

$$N = \frac{n}{V'_{sed}}.$$

The number of cells per cm^2 (R) can be expressed as

$$R = N \times h,$$

where N is the number of cells per cm^3, H is the height of sampled sediment layer (1 cm).

Enumeration of microalgae was conducted by direct light microscopy (at a magnification of 400×) using Nageotte counting chambers. Taxonomic identifications were based on descriptions in Proshkina-Lavrenko (1950) and Hendey (1964). Some small forms could not be identified to species level because of the limitations of the methods used. Division into dead and live cells was conducted by visual assessment of undamaged state of cell content (Woelfel et al., 2010).

Each cell was measured individually with an ocular micrometer. Best fitting geometric shape and matching equations were used to determine cell biomass in μg (Olenina et al., 2006).

Living cells of at least ten species of diatoms were detected in the sediment samples (Table 1), of which seven species were identified as mass forms of spring or summer plankton represented by spore-bearing or vegetative cells.

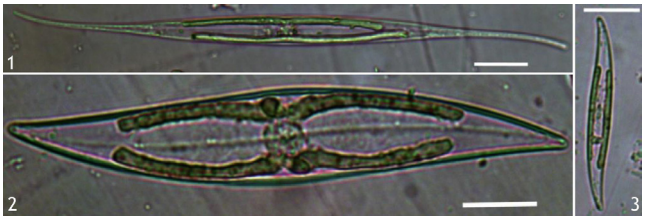

Figure 2 Typical species of microphytobenthos (1 – *Gyrosigma fasciola* Griffith & Henfrey, 2 – *Pleurosigma angulatum* Smith, 3 – *Pleurosigma* sp. 1) from sediment samples. Scale bar represents 20 μm.

Cells of all these planktonic species were abundant in the pelagic layer throughout the whole water area studied. In the benthic community under investigation, this assemblage of pelagic species is an allochthonous component introduced directly from the water column. However, three species of pennate diatoms, *Gyrosigma fasciola*, *Pleurosigma angulatum*, and *Pleurosigma* sp. 1 (Fig. 2), only occurred in the sediment samples.

Direct examination of the bathometric and net samples demonstrated the absence of these three species throughout the whole vertical profile of the pelagic zone at a lower threshold of detectability of 0.6–1.0 cells cm^{-2}, whereas in bottom sediments the average density (in total for cells of the three species) was ca. 600 cells cm^{-2} (Table 1), but empty frustules and damaged cells were rare. Therefore, the presence of these forms in the benthic zone cannot be explained by settling out from the water column, i.e. direct derivation from pelagic assemblages. Members of genus *Gyrosigma* and *Pleurosigma* are common in the Barents Sea coastal algal communities, where they co-occur with typical dominant microphytobenthic species such as *Melosira juergensii*, *Melosira moniliformis*, *Melosira nummuloides*, *Rhabdonema minutum*, *Synedra pulchella*, and *Synedra tabulata* (Kuznetsov and Shoshina, 2003; Makarevich and Druzhkova, 2010; Makarevich et al., 2015). If direct transport had occurred, for example with shore ice from the littoral

Table 1 Abundance and biomass of microalgae in surface sediments (average values for the three stations).

Taxon	Abundance [cells cm^{-2}]	Biomass [μg cm^{-2}]
Amphiprora hyperborea Grunow	99	0.99
Chaetoceros contortus Schütt (spores)	13	0.01
Chaetoceros furcillatus Bailey (spores)	5233	2.62
Chaetoceros socialis Lauder (spores)	60,333	6.03
Fragilariopsis oceanica Hasle	33	0.01
Gyrosigma fasciola Griffith & Henfrey	365	2.85
Pleurosigma angulatum W. Smith	67	0.53
***Pleurosigma* sp. 1**	202	0.30
Pseudo-nitzschia seriata complex	13	0.01
Thalassiosira gravida Cleve (spores)	147	0.01
Centrales 15–20 μm	160	0.16
Pennales <30 μm	926	0.28
Pennales 30–50 μm	3890	1.95
Pennales 50–60 μm	186	0.19
Total	71,667	15.9

zones of neighboring archipelagoes, the bottom sediments under investigation would be expected to contain a microalgae diversity similar in composition to that of coastal waters. No such assemblage was detected. Hence, the horizontal transport hypothesis fails to explain the presence of single components of the littoral benthic microalgae assemblage in the sediments with a background of the absence of the majority of species. A similar pattern of a difference in taxonomic composition from the planktonic microalgae community and a similarity with the littoral one was reported for deep-sea microphytobenthos on the North Carolina Continental Shelf (Cahoon and Laws, 1993).

This presence of viable microalgae cells much deeper than the location of the possible compensation depth, where photosynthesis cannot be the main source of energy, does not contradict existing knowledge of the physiology of these organisms. The possible mechanism of life support in such conditions is the capability for heterotrophic metabolism, which is widespread among diatoms (Hellebust and Lewin, 1977; Lewin, 1953; Tuchman et al., 2006; Veuger and van Oevelen, 2011), and/or storage and utilization of energy reserves at a reduced metabolic rate (Zhang et al., 1995).

Finally, the occurrence of a considerable number of cells of small pennate diatoms, which were not identified to species level during study of the sediment samples, suggests that *G. fasciola*, *P. angulatum*, and *Pleurosigma* sp. 1 represent only part of a specific algal community inhabiting the lower depths of the Barents Sea Continental Shelf.

This discovery of an autochthonous microalgal community in the benthic zone of the central Barents Sea represents a depleted fragment of Arctic littoral assemblages of benthic microalgae. At present, a depth of at least 245 m may be regarded as the lower habitat limit of the microphytobenthic community on the Barents Sea Continental Shelf. The formation of such a deep-sea algal community may be considered to result from loss of species incapable of adopting heterotrophic feeding from the microphytobenthos during transport from the littoral zone to below the compensation depth.

Findings of live autochthonous algal communities in bottom habitats suggests that the occurrence of viable microalgae at similar depths in the pelagic zone (Agusti et al., 2015) (optionally as Deep Chlorophyll Maxima/Deep Biomass Maxima; Fennel and Boss, 2003) in some cases might not be directly related to the overlying surface waters.

References

Abakumov, V.A., 1983. Manual on Methods of Surface Water and Sediments Hydrological Analysis. Hydrometeoisdat, Leningrad, 240 pp. (in Russian).

Agusti, S., González-Gordillo, J.I., Vaqué, D., Estrada, M., Cerezo, M. I., Salazar, G., Gasol, J.M., Duarte, C.M., 2015. Ubiquitous healthy diatoms in the deep sea confirm deep carbon injection by the biological pump. Nat. Commun. 6, 8608–8616.

Cahoon, L.B., 1999. The role of benthic microalgae in neritic ecosystems. Oceanogr. Mar. Biol. Annu. Rev. 37, 47–86.

Cahoon, L.B., Cooke, J.E., 1992. Benthic microalgal production in Onslow Bay, North Carolina, USA. Mar. Ecol.-Prog. Ser. 84, 185–195.

Cahoon, L.B., Laws, R.A., 1993. Benthic diatoms from the North Carolina continental shelf: inner and mid shelf. J. Phycol. 29, 257–263.

Cahoon, L.B., Redman, R.S., Tronzo, C.R., 1990. Benthic microalgal biomass in sediments of Onslow Bay, North Carolina. Estuar. Coast. Shelf Sci. 31, 805–815.

Cahoon, L.B., Laws, R.A., Thomas, C.J., 1994. Viable diatoms and chlorophyll *a* in continental slope sediments off Cape Hatteras, North Carolina. Deep-Sea Res. 41, 767–782.

Fennel, K., Boss, E., 2003. Subsurface maxima of phytoplankton and chlorophyll: steady-state solutions from a simple model. Limnol. Oceanogr. 48 (4), 1521–1534.

Glud, R.N., Woelfel, J., Karsten, U., Kühl, M., Rysgaard, S., 2009. Benthic microalgal production in the Arctic: applied methods and status of the current database. Bot. Mar. 52, 559–571.

Hellebust, J.A., Lewin, J., 1977. Heterotrophic nutrition. In: Warner, D. (Ed.), Biology of Diatoms. Univ. California Press, Berkeley, 169–197.

Hendey, N.I., 1964. An Introductory Account of the Smaller Algae of British Coastal Waters, Part V: Bacillariophyceae (Diatoms). H.M. S.O., London, 317 pp.

Jerlov, N.G., 1968. Optical Oceanography. Elsevier, Amsterdam, 194 pp.

Karsten, U., Schlie, C., Woelfel, J., Becker, B., 2011. Benthic diatoms in arctic seas – ecological functions and adaptations. Polarforschung 81 (2), 77–84.

Kiselev, I.A., 1969. The Plankton of Seas and Continental Waterbodies. Science, Leningrad, 658 pp. (in Russian).

Kuznetsov, L.L., Shoshina, E.V., 2003. Phytocenoses of the Barents Sea (*physiological and structural characteristics*). KSC RAN Press, Apatity, 308 pp. (in Russian).

Lewin, J.C., 1953. Heterotrophy in diatoms. J. Gen. Microbiol. 9, 305–313.

Makarevich, P.R., Druzhkova, E.I., 2010. Seasonal Processes in Coastal Planktonic Algocenoses of Northern Seas. Publ. SSC RAS, Rostov-on-Don, 280 pp. (in Russian).

Makarevich, P.R., Vodopyanova, V.V., Oleinik, A.A., 2015. Floral Communities in the Pelagic Zone of Kola Bay. Structure and Functional Characteristics. Publ. SSC RAS, Rostov-on-Don, 190 pp. (in Russian).

McGee, D., Laws, R.A., Cahoon, L.B., 2008. Live benthic diatoms from the upper continental slope: extending the limits of marine primary production. Mar. Ecol.-Prog. Ser. 356, 103–112.

Olenina, I., Hajdu, S., Edler, L., Andersson, A., Wasmund, N., Busch, S., Göbel, J., Gromisz, S., Huseby, S., Huttunen, M., Jaanus, A., Kokkonen, P., Ledaine, I., Niemkiewicz, E., 2006. Biovolumes and size-classes of phytoplankton in the Baltic Sea. HELCOM Balt. Sea Environ. Proc. 106 pp.

Proshkina-Lavrenko, A.I., 1950. Analyses of Diatoms. Book 3. Identifying of Fossil and Modern Diatom Algae. Order Pennales. State Publishing House of Geological Literature, Leningrad, 633 pp. (in Russian).

Raymont, J.E.G., 1980. Plankton and Productivity in the Oceans. Phytoplankton, 2nd ed. Pergamon Press, Oxford, 496 pp.

Tuchman, N.C., Schollett, M.A., Rier, S.T., Geddes, P., 2006. Differential heterotrophic utilization of organic compounds by diatoms and bacteria under light and dark conditions. Hydrobiologia 561, 167–177.

Veuger, B., van Oevelen, D., 2011. Long-term pigment dynamics and diatom survival in dark sediment. Limnol. Oceanogr. 56 (3), 1065–1074.

Woelfel, J., Schumann, R., Peine, F., Flohr, A., Kruss, A., Tegowski, J., Blondel, P., Wiencke, C., Karsten, U., 2010. Microphytobenthos of Arctic Kongsfjorden (Svalbard Norway): biomass and potential primary production along the shore line. Polar Biol 33, 1239–1253.

Zhang, Q., Gradingerfaud, R., Spindler, M., 1995. Dark survival of marine microalgae in the high arctic (Greenland Sea). Polarforschung 65 (3), 111–116.

Oceanologia (2018) 60, 101—105

Available online at www.sciencedirect.com

ScienceDirect

journal homepage: www.journals.elsevier.com/oceanologia/

SHORT COMMUNICATION

First records of two planktonic Indo-Pacific diatoms: *Chaetoceros bacteriastroides* and *C. pseudosymmetricus* in the Adriatic Sea

Marijeta Čalić [a,*], Stijepo Ljubimir [a], Sunčica Bosak [b], Ana Car [a]

[a] *Institute for Marine and Coastal Research, University of Dubrovnik, Dubrovnik, Croatia*
[b] *Department of Biology, Faculty of Science, University of Zagreb, Zagreb, Croatia*

Received 21 April 2017; accepted 18 July 2017
Available online 3 August 2017

KEYWORDS
Bacillariophyta;
Chaetoceros;
Introduced species;
Mediterranean;
Phytoplankton;
Tropical

Summary Unusual occurrence of planktonic diatom species, *Chaetoceros bacteriastroides* and *Chaetoceros pseudosymmetricus*, was noticed in three different marine ecosystems of Adriatic Sea: the Krka Estuary and Telaščica Bay in the Central Adriatic, and in southern Adriatic offshore. From 2010 to 2015, these two *Chaetoceros* species were recorded in heterogeneous environmental conditions and in a very low abundances. Both species are regarded as very rare in world oceans, and consequently knowledge of their distribution and ecology is rather poor. Primarily described from tropical waters and showing Indo-Pacific distribution, *C. bacteriastroides* and *C. pseudosymmetricus* findings in Adriatic represent the northernmost records in world's oceans and seas. For *C. pseudosymmetricus* this is also the first occurrence in European seas. Areal expansion and introduction of new phytoplankton species in the Adriatic Sea might be related to different circulation regimes in the Ionian Sea and the concurrent rise in sea temperature in the Mediterranean in the last decade. Recent investigations have shown that entering currents, of either Atlantic/Western Mediterranean or Eastern Mediterranean origin, modify the composition of the plankton community in the Adriatic by bringing different newcomers.

* Corresponding author at: Kneza Damjana Jude 12, 20000 Dubrovnik, Croatia. Tel.: +385 20 323484; fax: +385 20 323872.
E-mail address: marijeta.calic@unidu.hr (M. Čalić).
Peer review under the responsibility of Institute of Oceanology of the Polish Academy of Sciences.

ELSEVIER Production and hosting by Elsevier

http://dx.doi.org/10.1016/j.oceano.2017.07.005

The genus *Chaetoceros* Ehrenberg (Bacillariophyta) is one of the most important diatom genera, with a great variety of species found worldwide (Malviya et al., 2016). In the Adriatic Sea the genus is ecologically very significant and represented with ca. 50 species (Viličić et al., 2002). Its identification is often problematic due to the large morphological variability within the species, the frequent occurrence of intermediate forms and the fact that some of the characters used for delineation can only be observed using electron microscopy (Bosak, 2013). In general, this genus is characterized by an extension of the valve named setae and the formation of chains that are joined in various structures associated mainly with the form and position of setae (Hasle and Syvertsen, 1997). One of their most conspicuous characteristics is the possession of four setae per cell in the majority of species (Round et al., 1990). In spite of these taxonomic characteristics *Chaetoceros bacteriastroides* Karsten has a larger number of setae making it morphologically different from other *Chaetoceros* species. *C. bacteriastroides* has been rarely recorded from the Indian Ocean (Karsten, 1907; Paul et al., 2007; Simonsen, 1974), the Pacific Ocean (Fryxell, 1978; Guilard and Kilham, 1977; Hernández-Becerril, 1993), Chinese seas (Ke et al., 2012; Liu, 2008) and the Tyrrhenian Sea (Sarno and Zingone, 2008). The chains are straight, usually long and robust. The cells are cylindrical, in girdle view appear rectangular with smooth corners and long pervalvar axis. Each cell contains numerous small chloroplasts. Each intercalary valve possesses six setae of which two are long and robust while four are shorter and very strongly spirally undulated (Hernández-Becerril, 1993). Another recorded diatom, *Chaetoceros pseudosymmetricus* Steemann-Nielsen is a very rare species, reported only three times from the Indian Ocean (Hernández-Becerril, 2000; Steemann-Nielsen, 1931; Thorrington-Smith, 1970). The cells form straight and short chains of three to seven cells that are rectangular in girdle view and narrowly elliptical in valve view. The cells are delicate, and lacking chloroplasts within the setae, therefore belonging to the subgenus *Hyalochaete*. The intercalary setae emerge from the apices of the valves and fuse immediately to the sibling setae. After fusion, they become inflated for a short distance and then gradually taper to the tip (Hernández-Becerril, 2000).

Findings of *C. bacteriastroides* and *C. pseudosymmetricus* in the Adriatic Sea add to the scarce information on the geographical and ecological features of these rare diatoms. Also, these unusual reports for the whole Mediterranean contribute to the knowledge of phytoplankton biodiversity and checklists of European seas.

The Adriatic Sea is an elongated basin in the northern part of the Mediterranean, with three distinctive sections, the northern, central and southern parts where different water masses can be recognized (Viličić et al., 2002). Adriatic ecosystems are influenced by the regular exchange of water with the Eastern Mediterranean through the Strait of Otranto. Levantine Intermediate Water (LIW) and Ionian Surface Water (ISW) flow into the Adriatic along the sea's eastern border. The volume of this flow is greater in winter but, depending on climatic oscillations that occur from the Atlantic to the south-east Mediterranean, varies year-to-year (Grbec et al., 2002). Studies where previously unrecorded *C. bacteriastroides* and *C. pseudosymmetricus* were found have been made in three different marine ecosystems of the Adriatic Sea: the Krka Estuary and Telaščica Bay in the Central Adriatic, and in the southern Adriatic offshore. Karstic river Krka is a salt-wedge, highly stratified estuary (Žutić and Legović, 1987), characterized by small tidal amplitudes and permanently brackish surface water (Svensen et al., 2007). Telašćica Bay is located about 32 nautical miles north-west from the Krka Estuary and it is a poorly investigated, semi-enclosed oligotrophic marine ecosystem that is formed by Dugi Otok island. Finally, the South Adriatic is the deepest and the widest part of the basin, characterized by the oligotrophic offshore and circular, 1243 m deep South Adriatic Pit.

The records of *C. bacteriastroides* and *C. pseudosymmetricus* in the Adriatic Sea are the results of 4 different research projects that were carried out from 2009 to 2016. Altogether, 24 research cruises were undertaken and in total 41 net samples (Krka Estuary and Telaščica Bay) and 272 bottle samples (South Adriatic) were analyzed. In the Krka Estuary (at 4 stations in June 2010) and Telaščica Bay (at 5 stations in March 2012) only net samples were collected by vertical hauling from 20 m to surface. Mesh plankton net (20 μm-pore-sized) samples were observed using an inverted Zeiss Axio Observer Z1 microscope and Mira II FE LMU scanning electron microscope (Bosak, 2013). Phytoplankton samples in South Adriatic were collected by 5-L Niskin bottles at 4 stations along the Dubrovnik-Bari transect monthly from February 2009 to February 2013 and at 12 stations from December 2015 to April 2016, both at standard oceanographic depths (0–200 m). Niskin samples were preserved in neutralized formaldehyde (2.5% final concentration) and observed using an Olympus IX-71 inverted microscope according to the Utermöhl method (Utermöhl, 1958). Subsamples (100 mL) were settled for 48 h in counting chambers (HydroBios) before analyses. Observations were made over the entire area of the counting chamber base plate to obtain the most accurate estimation. The phytoplankton abundances are expressed as number of cells per liter (cells L^{-1}). Temperature and salinity profiles were taken by CTD multiparametric probe (SBE 911 plus, SeaBird Electronics Inc., USA). Identification of *C. bacteriastroides* and *C. pseudosymmetricus* was carried out following Fryxell (1978) and Hernández-Becerril (1993, 2000). In all examined samples from Krka Estuary, at Telašćica Bay and along the Dubrovnik-Bari transect *C. bacteriastroides* and *C. pseudosymmetricus* were encountered only in 7 cases (Fig. 1, Table 1). Particular records with locations and abundances as well as temperature and salinity conditions of *C. bacteriastroides* and *C. pseudosymmetricus* in Adriatic Sea are shown in Table 1. *C. bacteriastroides* (Fig. 2) was recorded for 6 times from 2010 to 2015, while *C. pseudosymmetricus* (Fig. 3) was recorded just once in 2015. Abundance of both species did not exceed 10^2 cells L^{-1}.

The migration of new planktonic species from tropical and subtropical areas to the temperate seas is a regular process that has changed the dynamic of Mediterranean and Adriatic biodiversity in the last decade (Batistić et al., 2014; Gómez, 2006; Halim, 1990; Pećarević et al., 2013; Zenetos et al., 2005). The opening of the Suez Canal slowly allowed some Indo-Pacific species to migrate north into the eastern Mediterranean while, at the other end of the basin, Atlantic water entering via the Straits of Gibraltar carries into the western Mediterranean species that are prevalently of (sub)

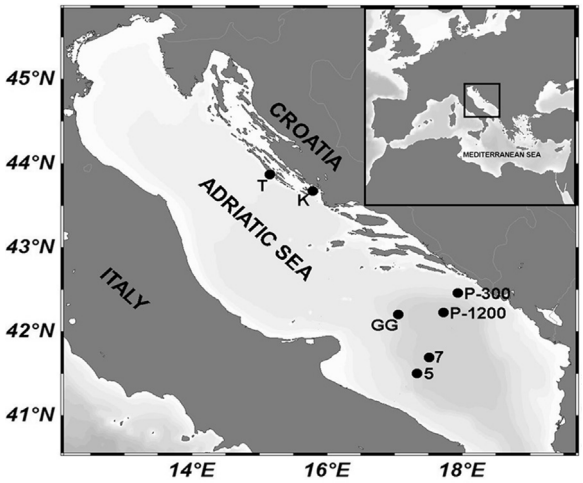

Figure 1 Map of the 7 station locations in the Adriatic Sea where *Chaetoceros bacteriastroides* and *C. pseudosymmetricus* have been recorded. Krka Estuary (K), Telašćica Bay (T) and Dubrovnik-Bari transect (GG, 5, 7, P-1200 and P-300).

tropical affinity (Bianchi, 2007; Gómez et al., 2000; Por, 1990). Spreading of warm water species has been speeded up by the increase of sea temperature in the Mediterranean which enhances the survival of newcomers (Parravicini et al., 2015). The exact path of introduction of *C. bacteriastroides* and *C. pseudosymmetricus* into the Adriatic Sea is difficult to reconstruct. Regarding other introduced species in the Eastern Adriatic, possible vectors of introduction could be aquaculture activities and shipping (Pećarević et al., 2013). But most likely it might be related to the regular inflow of Levantine Intermediate Water (LIW) and Ionian Surface Water (ISW). The surface and subsurface temperature and salinity in the South Adriatic ($T > 14.5$°C, $S > 38.5$) seem to be a signature of the cyclonic regime of circulation that brings warm and more saline Eastern Mediterranean Water (Batistić et al., 2012; Civitarese et al., 2010). However, both species have never been reported in the eastern Mediterranean but occurrence of *C. bacteriastroides* was noted in the Western Mediterranean, in Gulf of Naples (Southern Tyrrhenian Sea) in 2002 (Sarno and Zingone, 2008). Since then it has been found at the same site on other dates, but at relatively low abundances (Zingone, 2015). Remarkable is that occurrence of rarely reported *C. pseudosymmetricus* was observed for the first time in European seas. Both species were defined tentatively as Indo-Pacific in origin (Hernández-Becerril, 1993, 2000) with scarce information about their ecology. Those findings in Adriatic represent the northernmost records in world's oceans and seas. Although rare, it is obvious that *C. bacteriastroides* found their ecological niche in the Adriatic Sea as it is recorded in different areas over a span of several years, being adaptive enough to survive. Thus, in the Adriatic it was recorded in different environmental conditions; from the estuarine waters with lower salinity to the South Adriatic offshore with a high salinity influence. However, if we compare the environmental conditions of warmer seas in which *C. bacteriastroides* was reported such as the Bay of Bengal ($T = 27$–29°C, $S = 29$–33) and the China Sea ($T = 29$–32°C, $S = 32$–33), this species in the Adriatic shows an expanded tolerance limits for temperature and salinity (Ke et al., 2012; Paul et al., 2007). It is certain that both newly recorded *Chaetoceros* in the Adriatic prefer oligotrophic conditions (Čalić et al., 2010; Šupraha et al., 2014; Viličić et al., 2002). For now it is still unknown whether the record of *C. pseudosymmetricus* is a temporary appearance in the Adriatic or will adapt and become a common taxon of the Mediterranean phytoplankton communities. As it was first described from below 50 m (Steemann-Nielsen, 1931) and at 50 m in this study, *C. pseudosymmetricus* is considered as a more oceanic 'shade' form. Huge and sparsely studied area of the Mediterranean and the Adriatic open waters offers the possibility that those taxa have been being overlooked or misidentified in the past as is the case with numerous other phytoplankton species (Gómez, 2008; Hamsher et al., 2013). However, for *C. bacteriastroides* and *C. pseudosymmetricus* misidentification is highly unlikely considering their peculiar morphology (Hernández-Becerril, 1993, 2000).

Recent records of these unusual *Chaetoceros* species in Adriatic Sea should be considered as an example of the expansion of thermophilic phytoplankton species. Although such sporadic events do hardly allow trend analyses they nevertheless provide useful information on environmental alteration and the global distribution of species. We can expect the spreading of warm-water phytoplankton species in the Mediterranean associated with sea warming in present day. The future regular studies are necessary to verify if new *Chaetoceros* species establish a healthy population in the Adriatic Sea. These findings will facilitate the identification of *C. bacteriastroides* and *C. pseudosymmetricus*, and possibly further records in Mediterranean.

Table 1 Spatio-temporal data of new *Chaetoceros* species in Adriatic Sea – abundances (A), temperature (T) and salinity (S).

Species	Location	Station	Date	Sample	Depth [m]	A [cell L^{-1}]	T [°C]	S
Chaetoceros bacteriastroides	43°41′N/15°49′E	Krka (K)	9.6.2010	Net	0–20	+[a]	15.4–22	34.9–37.9
	43°50′N/15°12′E	Telaščica (T)	1.3.2012	Net	0–20	+[a]	12–12.5	38.7–38.8
	42°13′N/17°42′E	P-300	12.1.2012	Bottle	100	140	14.3	38.7
	42°27′N/17°56′E	P-1200	12.1.2012	Bottle	75	180	14.7	38.7
	41°29′N/17°12′E	7	13.12.2015	Bottle	2	70	16.2	38.8
	42°58′N/17°04′E	GG	14.12.2015	Bottle	50	160	14.2	38.8
Chaetoceros pseudosymmetricus	41°19′N/17°07′E	5	13.12.2015	Bottle	50	80	14.2	38.8

[a] +, present in net samples.

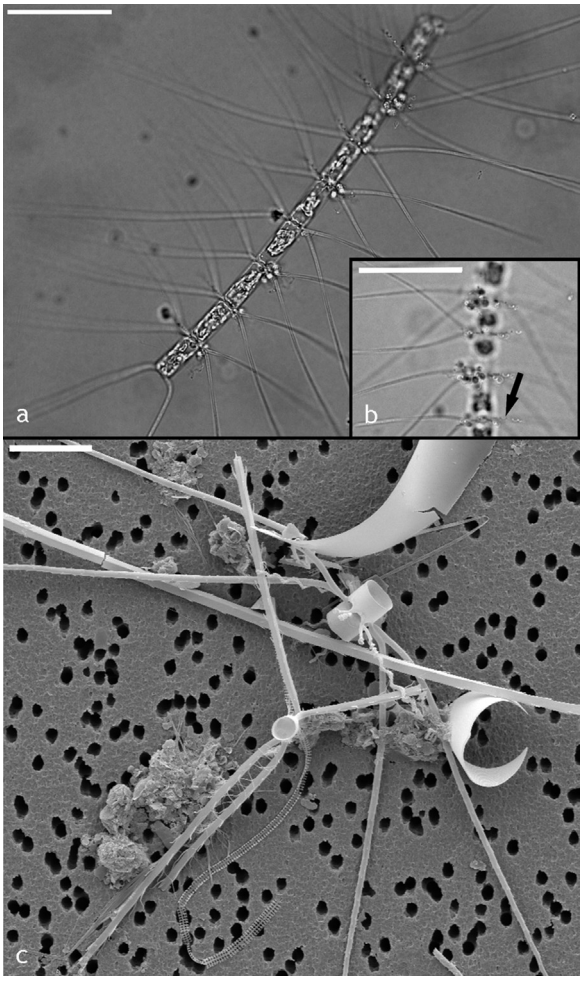

Figure 2 LM (a, b) and SEM (c) micrographs of *Chaetoceros bacteriastroides* from the South Adriatic (station P-1200) and Krka Estuary: Complete chain showing orientation of the setae (a); Detail of the intercalary valves and setae showing reduced spirally undulated setae (b); sibling valves in girdle view showing two pairs of reduced spirally undulated setae and two pairs of common intercalary setae (c). Scale bar = 50 μm (a, b) and 20 μm (c).

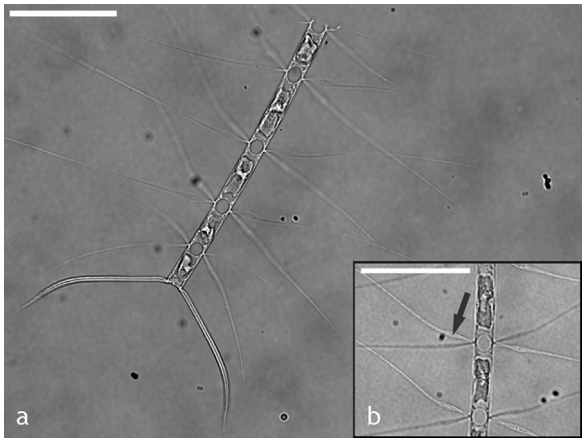

Figure 3 LM micrographs of *Chaetoceros pseudosymmetricus* from the South Adriatic (station 5): Terminal part of the chain with intercalary and terminal setae (a); detail of the intercalary valves and setae, showing inflation of intercalary setae (b). Scale bar = 50 μm.

Acknowledgements

This study was fully supported by the Croatian Science Foundation under the project 'Influence of thermohaline circulation variations in the Eastern Mediterranean on the plankton community of the South Adriatic: ecological and genetical approach' (AdMedPLan, 2014-09-2945) and by Eurofleets 2 under the 7th Framework Programme of the European Commission, project 'Evolution and spreading of the Southern Adriatic Waters' (ESAW, 312762). The authors are grateful to Dr. Zrinka Ljubešić for providing of data from the Krka Estuary and Telašćica Bay and acknowledge the support by the HRZZ project BIOTA UIP-2013-11-6433. We wish to express our appreciation to the reviewers in-depth comments, suggestions, and corrections, which have greatly improved the manuscript.

References

Batistić, M., Jasprica, N., Carić, M., Čalić, M., Kovačević, V.A., Garić, R., Njire, J., Mikuš, J., Bobanović-Ćolić, S., 2012. Biological evidence of a winter convection event in the South Adriatic: a phytoplankton maximum in the aphotic zone. Cont. Shelf Res. 44, 57—71, http://dx.doi.org/10.1016/j.csr.2011.01.004.

Batistić, M., Garić, R., Molinero, J.C., 2014. Interannual variations in Adriatic Sea zooplankton mirror shifts in circulation regimes in the Ionian Sea. Clim. Res. 61 (3), 231—240, http://dx.doi.org/10.3354/cr01248.

Bianchi, C.N., 2007. Biodiversity issues for the forthcoming tropical Mediterranean Sea. Hydrobiologia 580, 7—21, http://dx.doi.org/10.1007/s10750-006-0469-5.

Bosak, S., 2013. Taxonomy and ecology of the planktonic diatom family Chaetocerotaceae (Bacillariophyta) from the Adriatic Sea. (PhD dissertation). Department of Biology, Univ. Zagreb, 256 pp.

Čalić, M., Carić, M., Jasprica, N., 2010. Seasonality of dinoflagellates in oligotrophic ecosystem of Middle Adriatic. Rapp. Comm. Int Mer. Médit. 39 339 pp.

Civitarese, G., Gačić, M., Lipizer, M., Eusebi Borzelli, G.L., 2010. On the impact of the bimodal oscillating system (BIOS) on the biogeochemistry and biology of the Adriatic and Ionian Seas (Eastern Mediterranean). Biogeosciences 7 (12), 3987—3997, http://dx.doi.org/10.5194/bg-7-3987-2010.

Fryxell, G.A., 1978. Chain-forming diatoms: three species of *Chaetoceraceae*. J. Phycol. 14 (1), 62—71, http://dx.doi.org/10.1111/j.1529-8817.1978.tb00633.x.

Gómez, F., 2006. Endemic and Indo-Pacific plankton in the Mediterranean Sea: a study based on dinoflagellate records. J. Biogeogr. 33 (2), 261—270, http://dx.doi.org/10.1111/j.1365-2699.2005.01373.x.

Gómez, F., 2008. Phytoplankton invasions: comments on the validity of categorizing the non-indigenous dinoflagellates and diatoms in European seas. Mar. Poll. Bull. 56 (4), 620—628, http://dx.doi.org/10.1016/j.marpolbul.2007.12.014.

Gómez, F., Echevarría, F., Garcia, C.M., Prieto, L., Ruiz, J., Reul, A., Jiménez-Gómez, F., Varela, M., 2000. Microplankton distribution in the Strait of Gibraltar: coupling between organisms and hydrodynamic structures. J. Plankton. Res. 22 (4), 603—617, http://dx.doi.org/10.1093/plankt/22.4.603.

Grbec, B., Dulčić, J., Morović, M., 2002. Long-term changes in landings of small pelagic fish in the eastern Adriatic — possible influence of climate oscillations over the Northern Hemisphere.

Clim. Res. 20 (3), 241—252, http://dx.doi.org/10.3354/cr020241.

Guilard, R.R.L., Kilham, P., 1977. The ecology of marine planktonic diatoms. In: Werner, D. (Ed.), The Biology of Diatoms. Univ. California Press, Berkeley/New York, 410 pp.

Halim, Y., 1990. On the potential migration of the Indo-Pacific plankton through the Suez Canal. In: Godeaux, J. (Ed.), A Propos Des Migrations Lessepsiennes, vol. 7. Bull. Inst. Oceanogr. (Monaco), 11—27.

Hamsher, S.E., LeGresley, M.M., Martin, J.L., Saunders, G.W., 2013. A comparison of morphological and molecular-based surveys to estimate the species richness of *Chaetoceros* and *Thalassiosira* (Bacillariophyta), in the Bay of Fundy. PLoS ONE 8 (10), e73521, http://dx.doi.org/10.1371/journal.pone.0073521.

Hasle, G.R., Syvertsen, E.E., 1997. Marine diatoms. In: Tomas, C.R. (Ed.), Identifying Marine Phytoplankton. Acad. Press, San Diego, 5—385.

Hernández-Becerril, D.U., 1993. Note on the morphology of two planktonic diatoms: *Chaetoceros bacteriastroides* and *C. seychellarus*, with comments on their taxonomy and distribution. Bot. J. Linn. Soc. 111 (2), 117128, http://dx.doi.org/10.1111/j.1095-8339.1993.tb01894.x.

Hernández-Becerril, D.U., 2000. Morphology and taxonomy of three littleknown marine planktonic *Chaetoceros* species (Bacillariophyceae). Eur. J. Phycol. 35 (2), 183—188, http://dx.doi.org/10.1080/09670260010001735771.

Karsten, G., 1907. Das Indische Phytoplankton nach dem Material der deutschen Tiefsee-Expedition 1898—1899. Wissenschaftliche Ergebnisse der Deutschen Tiefsee-Expedition auf dem Dampfer 'Valdivia' 1898—1899 2, 221—548, http://dx.doi.org/10.5962/bhl.title.2171.

Ke, Z., Tan, Y., Huang, L., Zhang, J., Lian, S., 2012. Relationship between phytoplankton composition and environmental factors in the surface waters of southern South China Sea in early summer of 2009. Acta Oceanol. Sin. 31 (3), 109—119, http://dx.doi.org/10.1007/s13131-012-0211-2.

Liu, J.Y., 2008. In: Liu, J.Y. (Ed.), Checklist of Biota of Chinese Seas. Sci. Press, Acad. Sinica, Beijing, 1—1267.

Malviya, S., Scalco, E., Audic, S., Vincent, F., Veluchamy, A., Poulain, J., Wincker, P., Iudicone, D., De Vargas, C., Bittner, L., Zingone, A., Bowler, C., 2016. Insights into global diatom distribution and diversity in the world's ocean. Proc. Natl. Acad. Sci. U. S. A. 113 (11), 1516—1525, http://dx.doi.org/10.1073/pnas.1509523113.

Parravicini, V., Mangialajo, L., Mousseau, L., Peirano, A., Morri, C., Montefalcone, M., Francour, P., Kulbicki, M., Bianchi, C.N., 2015. Climate change and warm-water species at the north-western boundary of the Mediterranean Sea. Mar. Ecol. 36 (4), 897—909, http://dx.doi.org/10.1111/maec.12277.

Paul, J.T., Ramaiah, N., Gauns, M., Fernandes, V., 2007. Preponderance of a few diatom species among the highly diverse microphytoplankton assemblages in the Bay of Bengal. Mar. Biol. 152 (1), 63—75.

Pećarević, M., Mikuš, J., Bratoš-Cetinić, A., Dulčić, J., Čalić, M., 2013. Introduced marine species in Croatian waters (Eastern Adriatic Sea). Mediterr. Mar. Sci. 14 (1), 224—237, http://dx.doi.org/10.12681/mms.383.

Por, F.D., 1990. Lessepsian migration. An appraisal and new data. In: Godeaux, J. (Ed.), A Propos Des Migrations Lessepsiennes, vol. 7. Bull. Inst. Oceanogr. (Monaco), 1—10.

Round, F.E., Crawford, R.M., Mann, D.G., 1990. The Diatoms. Biology and Morphology of the Genera. Cambridge Univ. Press, Cambridge, 747 pp.

Sarno, D., Zingone, A., 2008. MARECHIARA-phytoplankton Long-term Time-series (1984—2006) at the Fixed Coastal Station in the Gulf of Naples, Southern Tyrrhenian Sea, http://dx.doi.org/10.1594/PANGAEA.701471.

Simonsen, R., 1974. The diatom plankton of the Indian Ocean expedition of RV 'Meteor' 1964—1965. Meteor Forschungsergebnisse 19, 1—107.

Steemann-Nielsen, E., 1931. Einige Planktonalgen aus den warmen Meeren. Dansk Bot. Ark. 6, 1—13.

Šupraha, L., Bosak, S., Ljubešić, Z., Mihanović, H., Olujić, G., Mikac, I., Viličić, D., 2014. Cryptophyte bloom in a Mediterranean estuary: High abundance of Plagioselmis cf. prolonga in the Krka River estuary (eastern Adriatic Sea). Sci. Mar. 78 (3), 329—338, http://dx.doi.org/10.3989/scimar.03998.28C.

Svensen, C., Viličić, D., Wassmann, P., Arashkevich, E., Ratkova, T., 2007. Plankton distribution and vertical flux of biogenic matter during high summer stratification in the Krka Estuary (Eastern Adriatic). Estuar. Coast. Shelf. Sci. 71 (3—4), 381—390, http://dx.doi.org/10.1016/j.ecss.2006.07.022.

Thorrington-Smith, M., 1970. Some new and little-known planktonic diatoms from the West Indian Ocean. Nova Hedwigia Beih. 31, 815—835.

Utermöhl, H., 1958. Zur Vervollkommnung der quantitativen Phytoplankton-Metodik. Mitt. Int. Ver. Theor. Angew. Limnol. 9, 1—38.

Viličić, D., Marasović, I., Mioković, D., 2002. Checklist of phytoplankton in the eastern Adriatic Sea. Acta Bot. Croat. 61 (1), 57—91.

Zenetos, A., Çinar, M.E., Pancucci-Papadopoulou, M.A., Harmelin, J. G., Furnari, G., Andaloro, F., Bellou, N., Streftaris, N., Zibrowius, H., 2005. Annotated list of marine alien species in the Mediterranean with records of the worst invasive species. Medit. Mar. Sci. 6 (2), 63—118, http://dx.doi.org/10.12681/mms.186.

Zingone, A., 2015. Evaluation on the NIS From the Assessment Areas Ionian Sea and Western Mediterranean Sea, http://www.marinespecies.org/aphia.php?p=sourcedetails&id=198224 (accessed 13.03.17).

Žutić, V., Legović, T., 1987. A film of organic matter at the freshwater/sea-water interface of an estuary. Nature 328, 612—614, http://dx.doi.org/10.1038/328612a0.